DROP-TUBE INVESTIGATION OF ANOMALOUS EUTECTIC FORMATION IN UNDERCOOLED MELTS

Yisheng Yu

A thesis submitted for the degree of Doctor of Philosophy

March 2018

The candidate confirms that the work submitted is his own, except where work which has formed part of jointly-authored publications has been included. The candidate confirms that appropriate credit has been given within the thesis where reference has been made to the work of others.

1. Yu, Y., A. M. Mullis and R. F. Cochrane (2016). "Rapidly solidified Ag-Cu eutectics: A comparative study using drop-tube and melt fluxing techniques." IOP Conference Series: Materials Science and Engineering 117(1): 012053.

ACKNOWLEDGEMENTS

I would like to give my deepest gratitude to my supervisors, Prof Andy Mullis for his constant supervision, guidance and encouragement throughout this work.

I would like to thank Diane Cochrane and Rob Simpson not only for their help on training me using the equipments but also for their patients on equipments maintenance and repairs.

Finally, I would like to thank my parents, my sisters, brother and relatives, and particularly my parents. Thank you very much for your unwavering support through the whole adventure. I could not have done it without you.

Thank you.

Yisheng Yu

ABSTRACT

The rapid solidification of the Ag – 40at %Cu alloys was studied by the drop tube technique, aiming to investigate the formation of anomalous eutectic and morphology transitions at different cooling rates. The droplets of different diameters with 38 ~ 850 μm droplets were obtained. Several characteristic techniques were used to analyse the as-solidified samples, including SEM and DTA.

The drop-tube processed Ag – 40at %Cu alloys formed anomalous eutectic as the dominant phase in all ranges of droplets, with either lamellar eutectic or lamellar eutectic and single phase dendrite being present. Among those droplets, certain large degrees of undercooling can theoretically be attained, either by the avoidance or at least the reduction of heterogeneous nucleation on container walls, or by the great amount of cooling rate to hinder the nucleation event in response. Three typical morphologies were observed: (1) lamellar and anomalous eutectic at undercooling 10 ~ 60 K; (2) lamellar eutectic and single phase dendrite at > 60 K; and (3) lamellar and anomalous eutectic and single phase dendrite at ~ 60 K.

Unfortunately, the drop tube technique has not yet been developed a proper experimental measurement of neither the nucleation temperature nor the undercooling directly. Therefore the indirect method by using heat transfer modelling is used to quantitatively predict the thermal history with regard to time and the size of the as-solidified droplets. Furthermore, the 2D unsteady convection heat transfer model is developed to better numerically estimate the thermal extraction situation during the solidification, in which minimum value of Nusselt number Nu no longer stays at 2 as a portion of the heat transferred from the leading part of sphere is return to the rear part. Thus, the Nu changing along the surface of sphere gives rise to the temperature gradient inside droplet, regardless of its size.

To further prove the temperature gradient existed in droplet, the *ImageJ* macro scripting is developed to analyse the BSE images quantitatively. It is found that the distribution of anomalous eutectic due to temperature gradient, is changed with the droplet size. With the increase of droplet size, the greater amount of anomalous eutectic is retained in the centre of droplet than the surface of droplet.

Contents

List of Figures

List of Tables

NOMENCLATURE

$f(\theta')$	contact angle factor, where wetting angle $\theta' \in [0, \pi]$
r^*	critical radius of nucleus

Physics

ΔH	enthalpy
ΔS	entropy
$\dot{q}$	heat flux
ϵ	emissivity
κ	thermal conductivity
σ	the Stefan-Boltzmann constant $= 5.670 \times 10^{-8}\,\mathrm{W/m^2\,K^4}$
σ_{SL}	solid/liquid interface energy
L	latent heat

Subscripts

F	fusion
i	interface
L	liquid
m	melting point
p	constant pressure
S	solid
v	volume

CHAPTER 1

BACKGROUND

1.1 THERMODYNAMICS

1.1.1 EQUILIBRIUM

A phase transformation from one phase at T_l to another phase at T_s occurs, giving rise to the negative change in Gibbs free energy ΔG under certain conditions. Accordingly, the principle driving force for phase transformation, such as solidification, is examined by

$$\Delta G = \Delta H - T\,\Delta S < 0 \tag{1.1.1}$$

where the changes in enthalpy ΔH and entropy ΔS are expressed respectively by

$$\Delta H = L_f - \int_{T_s}^{T_l} \Delta c_p \ \mathrm{d}T \tag{1.1.2a}$$

$$\Delta S = \Delta S_f - \int_{T_s}^{T_l} \frac{\Delta c_p}{T} \ \mathrm{d}T \tag{1.1.2b}$$

In Eq. (1.1.2a), the difference of between heat capacity $c_{p,l}$ at T_l and $c_{p,s}$ at T_s under constant pressure is

$$\Delta c_p = c_{p,l} - c_{p,s} \tag{1.1.3}$$

Although the decrease in Gibbs free energy is possible to drive new phase transformation, the existence of Gibbs activation energy barrier thermodynamically prevents the transition between the metastable phase and another new stable equilibrium phase from happening as shown in Fig. 1.1.1 [1]. In nature, few raw metastable materials such as diamond can last at room temperature and pressure. But the well-designed forming processes, such as the containerless technique*, that can successfully attain high undercooling, might trap a large amount of metastable phases after solidification.

* the detail review of containerless technique shall refer Section 2.2 and the operation of drop tube is introduced in Section 5.1.2.

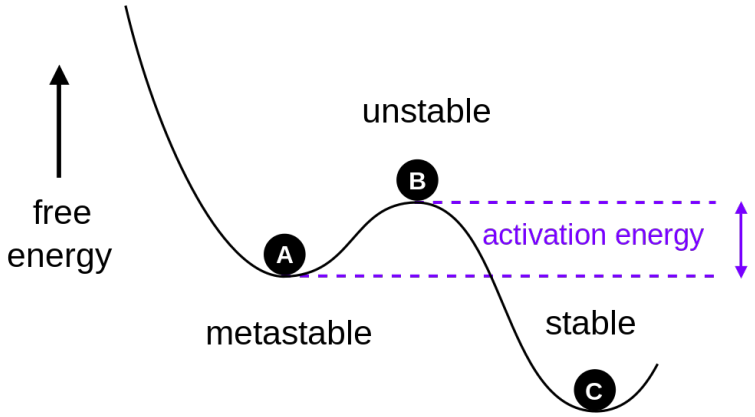

Figure 1.1.1: Schematic representation of the principles of thermodynamic stability due to variation in Gibbs free energy, where a certain activation energy is between the metastable A and the stable C

1.1.2 NUCLEATION

In solidification, heat transmission from the melt to the surroundings changes the amount of Gibbs free energy such that the relative thermodynamic stability of present phase might be interpreted by its driving force due to Eq. (1.1.1). The rearrangement of the atoms in matrix then causes some irreversible departure from its previous equilibrium, followed by an embryo may be created by those thermal fluctuations. This embryo might be unstable when the initial occurrence appears at the temperatures higher than the melting point T_m. After a critical temperature is reached in the cooling process, the unstable embryo changes to metastable and eventually to stable. Once nucleations are generated, atom transfer would continue to ensure the crystal growth afterwards.

CONDITIONS FOR NUCLEATION

For an initial embryo of atoms to form a crystal nucleus in the beginning of solidification, the activation energy, introduced in Section 1.1.1, is conquered by generating nucleus accident with the critical radius r^*, which is related to

$$\frac{\mathrm{d}(\Delta G)}{\mathrm{d}r} = 0 \tag{1.1.4}$$

where

$$\Delta G = \Delta G_i + \Delta G_v = \sigma_{sl}\, A + \Delta g\, V \tag{1.1.5}$$

In Eq. (1.1.5), the interface term ΔG_i is the thermal fluctuations that leads to the creation of interface between the liquid and the solid, and the volume term ΔG_v attributes the Gibbs free energy to the creation of variously sized crystal embryos.

Providing a nucleus initiates as a spherical form with radius r, the surface-area (A) dependent G_i and the volume (V) dependent G_v in Eq. (1.1.5), can be given as

$$\Delta G = \sigma_{sl}\left(4\pi r^2\right) + \Delta g\left(\frac{4}{3}\pi r^3\right) \tag{1.1.6}$$

where the Gibbs free energy difference between the liquid and the solid per unit volume is by

$$\Delta g = -\Delta S_f \Delta T = -\frac{L_f}{T_m}\Delta T \tag{1.1.7}$$

It should be noted that the unit of latent heat L_f in Eq. (1.1.7) is J/m^3 since the Gibbs free energy ΔG is with regards to radius r in Eq. (1.1.6). Because L_f is more likely to be characteristic with the unit of either J/kg or J/mol in Eq. (1.1.7) in the reference book [2], the extra care is necessary in application of L_f.

The free energy change of both ΔG_i and ΔG_v in Eq. (1.1.6) increases monotonically with the increment of spherical radius r at negative undercooling ($\Delta T = T_m - T < 0$). When temperature T is cooled down to less than T_m, negative ΔG_v decreases the total amount of Gibbs free energy ΔG. Once the absolute value of ΔG_v becomes equal to or greater than that of the quadratic term, ΔG_i, ΔG_v prevails in the nucleation-controlled solidification at the expense of a large excess energy to weight the balance against surface creation of an interface between the liquid and the solid phases. In the following cooling process, the subsequent growth-controlled solidification is dominant, which will be further introduced in Section 1.2)

In the most cases, the nucleation would be assisted with the external inclusions such as the solid particle, or the crystalline crucible or oxide layer to reduce the barrier energy, which is also known as heterogeneous nucleation. The relationship between the homogeneous nucleation and the heterogeneous nucleation is

$$\Delta G_{\text{het}} = \Delta G_{\text{hom}} \cdot f(\theta) \tag{1.1.8}$$

where the magnitude of the effect on heterogeneous nucleus accident is well defined in [3]

$$f(\theta) = \frac{(2+\cos\theta)(1-\cos\theta)^2}{4} = \frac{1}{4}\left(2 - 3\cos\theta + \cos^3\theta\right) \tag{1.1.9}$$

With the assistance of a foreign solid, the barrier energy required for heterogeneous nucleation ΔG_{het}, dependent on the contact angle factor $f(\theta)$ which is no greater than 1, should be lower than that for homogeneous nucleation ΔG_{hom}.

Furthermore, the relationship between undercooling ΔT and the critical radius r^* can be generated by combining Eq. (1.1.6) with Eq. (1.1.4) and Eq. (1.1.7)

$$\frac{\mathrm{d}}{\mathrm{d}r}(\Delta G) = 8\pi r\sigma_{sl} + 4\pi r^2 \Delta g = 0 \Rightarrow r^* = -\frac{2\sigma_{sl}}{\Delta g} = \frac{2\sigma_{sl}}{\Delta S_f \Delta T} \tag{1.1.10}$$

The smaller the undercooling ΔT, the larger the size of the critical radius r^* for nucleation and so the lower probability the occurrence of nucleation event.

RATE OF NUCLEATION

Considering there is no external enthalpy ΔH_n due to the existence of an mixture between crystal clusters N_n and liquid atoms N_l, the condition to reach the equilibrium concentration of cluster is similar with Eq. (1.1.4) as

$$\frac{\mathrm{d}(\Delta G)}{\mathrm{d}N_n} = 0 \tag{1.1.11}$$

and the free enthalpy change of such a system is

$$\Delta G = N_n \Delta G_n^* - T \Delta S_n \tag{1.1.12}$$

where ΔG_n^* stands for the activation energy for the nucleation of the critical number of clustered atoms at temperature T.

Combining Eq. (1.1.8) with Eq. (1.1.6) and Eq. (1.1.10),

$$\begin{aligned}
\Delta G_n^* &= \left\{\sigma_{sl}\left(4\pi\,(r^*)^2\right) + \Delta g\left(\frac{4\pi}{3}\,(r^*)^3\right)\right\}\cdot f(\theta) \\
&= \left\{4\pi\,\sigma_{sl}\left(-\frac{2\,\sigma_{sl}}{\Delta g}\right)^2 + \frac{4\pi}{3}\,\Delta g\left(-\frac{2\,\sigma_{SL}}{\Delta g}\right)^3\right\}\cdot f(\theta) \\
&= \frac{16\pi}{3}\,\frac{\sigma_{sl}^3}{\Delta g^2}\cdot f(\theta)
\end{aligned} \tag{1.1.13}$$

The mixing entropy ΔS_n in Eq. (1.1.12) is

$$\Delta S_n = k_B \ln\left[\frac{(N_l + N_n)!}{N_n!\,N_l!}\right] \tag{1.1.14}$$

Applying *Stirling's approximation* for large N as $\ln(N!) = N\ln(N) - N$ in Eq. (1.1.12) in Eq. (1.1.14), then the condition in Eq. (1.1.11) can be derived as

$$\frac{\mathrm{d}\Big\{N_n\,\Delta G_n^* - k_B\,T\left[(N_l+N_n)\ln(N_l+N_n) - (N_l+N_n)\right] + k_B\,T\left[N_n\ln(N_n) - N_n\right] + k_B\,T\left[N_l\ln(N_l) - N_l\right]\Big\}}{\mathrm{d}N_n}$$

$$\Rightarrow \frac{\mathrm{d}\Big\{N_n\,\Delta G_n^* - k_B\,T\left[(N_l+N_n)\ln(N_l+N_n)\right] + k_B\,T\,N_n\ln(N_n) + k_B\,T\,N_l\ln(N_l)\Big\}}{\mathrm{d}N_n}$$

$$\Rightarrow \Delta G_n^* - k_B\,T\left[\ln(N_l+N_n)+1\right] + k_B\,T\left[\ln(N_n)+1\right]$$

$$\Rightarrow \Delta G_n^* - k_B\,T\ln\left[\frac{N_l+N_n}{N_n}\right] = 0 \tag{1.1.15}$$

Because the atoms of liquid is predominant in the undercooled melt ($N_l \gg N_n$), the number of critical clusters in equilibrium is obtained by neglecting N_n in Eq. (1.1.15) as

$$N_n^* = N_l \exp\left[-\frac{\Delta G_n^*}{k_B\,T}\right] \tag{1.1.16}$$

When there are N_n^* clusters achieve the activation energy ΔG_n^* to pass through the barrier energy, the thermal fluctuations might still move the cluster with critical radius r^* backwards and forwards to decrease their energy. So the nucleation rate J_v is not characteristic only with the number of critical cluster (N_n^*) in Eq. (1.1.16), but also with the rate of random additions to, or removals of atoms from the unstable nucleus ($\mathrm{d}n/\ \mathrm{d}t$) as

$$J_v = N_n^* \cdot \frac{\mathrm{d}n}{\mathrm{d}t} \tag{1.1.17}$$

where the adsorption rate according to [4] can be expressed

$$\frac{\mathrm{d}n}{\mathrm{d}t} = v_0\, p\, n_s^* \exp\left[-\frac{\Delta G_d}{k_B\, T}\right] \tag{1.1.18}$$

Combining Eq. (1.1.17) with Eq. (1.1.16) and Eq. (1.1.18),

$$J_v = K_v \exp\left[-\frac{\Delta G_n^* + \Delta G_d}{k_B\, T}\right] = K_v \exp\left[-\frac{\Delta G_n^*}{k_B\, T}\right] \exp\left[-\frac{\Delta G_d}{k_B\, T}\right] \tag{1.1.19}$$

For metals, the exact value of K_v is unimportant in Eq. (1.1.19) and is approximated in [3] as

$$K_v = N_l \cdot v_0\, p\, n_s^* \approx 10^{42} \tag{1.1.20}$$

Moreover, the attachment of atomic on the non-faceted interface is easy and largely independent of crystal orientation. As a result, it is more likely for atomically rough interface to grow at low undercooling ΔT, which leads to the second exponential function in Eq. (1.1.19) [4]

$$\exp\left[-\frac{\Delta G_d}{k_B\, T}\right] \approx 0.01 \tag{1.1.21}$$

Therefore, the nucleation rate combined with Eq. (1.1.13), Eq. (1.1.20) and Eq. (1.1.21) becomes

$$J_v = 10^{40} \exp\left[-\frac{\Delta G_n^*}{k_B\, T}\right] = 10^{40} \exp\left[-\frac{16\pi}{3\, k_B\, T}\, \frac{\sigma_{SL}^3}{\Delta g^2} \cdot f(\theta)\right] \tag{1.1.22}$$

The further substitution of Eq. (1.1.7) with Δg in Eq. (1.1.22) reveals the relationship between J_v and $T\,\Delta T^2$ as

$$J_v \propto -\frac{1}{T\,\Delta g^2} \propto -\frac{1}{T\,\Delta T^2} \tag{1.1.23}$$

When the melt cools down a small amount of temperature below the melting point, the change of nucleation rate J_v is firstly controlled by undercoolings ΔT, resulting in more numerous and smaller nucleus of critical radius, also in agreement with Eq. (1.1.10). On the other hand, when ΔT becomes large in the further cooling process, J_v is then temperature-controlled, since most of atoms frozen at the low temperature cause fewer atoms having enough energy to transfer from the liquid to the nucleus.

1.2 SOLIDIFICATION

1.2.1 SOLID/LIQUID INTERFACE

Once a nucleus with critical radius r^* is formed in the nucleation-controlled solidification, the following growth-controlled solidification is mainly determined by the interface growth. Such growth has three main factors to determine the growth morphology: **(a)** the kinetics of atom attachment to the interface **(b)** diffusion of heat and mass **(c)** capillarity

KINETICS

For metals, value of dimensionless entropy α calculated in Eq. (1.2.1) is as low as ~ 2.

$$\alpha = \frac{\Delta S_f}{R} = \frac{L_f}{T_m R} \tag{1.2.1}$$

which leads to a negligible kinetics of transfer of atoms from the liquid to the crystal in non-faceted crystal growth.

DIFFUSION

In the simple assumption, only diffusion-dependent morphology is assumed under the maximum growth rate or minimum undercooling. The excess solute is rejected from the solid and piles up ahead of the interface during the solidification. Once a steady-state growth is reached after a transient diffusion, a fully developed boundary layer (C_0 for solid and C_0/k for liquid) is established as

$$D\nabla^2 C = \frac{\partial C}{\partial t} = 0 \tag{1.2.2}$$

Considering the local interface is moving with respect to time (t) under the growth velocity ($V = \mathrm{d}s/\mathrm{d}t$) in z' direction, the location of interface $z'(s) = z(0)$ at any instant of time.

$$z = z' - V\,t \Longrightarrow \quad \frac{\partial z}{\partial t} = \frac{\partial z'}{\partial t} - V\,, \quad \frac{\partial z}{\partial z'} = 1 \tag{1.2.3}$$

In unidirectional diffusion, Eq. (1.2.2) is simplified

$$\begin{aligned} D\frac{\partial^2 C}{\partial z'^2} &= \frac{\partial C}{\partial t} \\ D\frac{\partial^2 C}{\partial z^2} = \frac{\partial C}{\partial z}\cdot\frac{\partial z}{\partial t} &= -V\frac{\partial C}{\partial z} + \frac{\partial C}{\partial t} \Rightarrow D\frac{\partial^2 C}{\partial z^2} + V\frac{\partial C}{\partial z} = \frac{\partial C}{\partial t} = 0 \end{aligned} \tag{1.2.4}$$

The general solution of Eq. (1.2.4) is in the form of exponential function as

$$C(z) = A + B\exp\left(-\frac{V}{D}z\right) \tag{1.2.5}$$

In the steady-state situation, there are two boundary conditions applied in Eq. (1.2.5) as

$$\text{BC1:} \quad C_{z=0} = \frac{C_0}{k} \tag{1.2.6}$$

$$\text{BC2:} \quad -D\left(\frac{\mathrm{d}C}{\mathrm{d}z}\right)_{z=0} = \left(\frac{C_0}{k} - C_0\right) V \tag{1.2.7}$$

where BC2 represents the rate of solute rejection must be equal to the diffusional flux from solid to liquid at the interface $z = 0$.

Combining Eq. (1.2.5) with Eq. (1.2.6) and Eq. (1.2.7),

$$A = C_0$$

$$B = \frac{C_0}{k} - C_0 = \Delta C_0$$

and the complete solution is

$$C(z) = C_0 + \Delta C_0 \exp\left(-\frac{V}{D}z\right) \tag{1.2.8}$$

Then the local equilibrium liquidus temperature ahead of interface expressed in Eq. (1.2.9) can generate the curve line in Fig. 1.2.1.

$$T_l = T_l(C_0) - m\left(C_0 - C_l\right) = T_l(C_0) - m\,\Delta C_0 \exp\left(-\frac{V}{D}z\right) \tag{1.2.9}$$

where m is the liquidus slope in the binary diagram.

For practical estimation of concentration boundary layer δ_c ahead of interface, the area of triangle MON is assumed to equal to that of the grey region as shown in Fig. 1.2.2

$$\frac{1}{2}\Delta C_0\,\delta_c = \int_0^\infty \left(C(z) - C_0\right)\mathrm{d}z = \int_0^\infty \Delta C_0 \exp\left(-\frac{V}{D}z\right)\mathrm{d}z = \Delta C_0\,\frac{D}{V}$$

$$\delta_c = \frac{2D}{V} \tag{1.2.10}$$

When the actual temperature gradient due to heat flux (T_1 in Fig. 1.2.1) is lower than the equilibrium temperature gradient due to the concentration change ahead of interface (T_L), a zone of constitutional undercooling (the pink region in Fig. 1.2.1) is formed and the melt in this zone is undercooled so as to outbreak the dendritic microstructure.

In order to predict the interface stability, the difference between the heat-flux-imposed temperature gradient (mG_c) and the liquidus temperature gradient (G) at the interface is further concerned

$$\phi = \left(\frac{\mathrm{d}T_l}{\mathrm{d}z} - \frac{\mathrm{d}T_q}{\mathrm{d}z}\right)_{z=0} = mG_c - G \tag{1.2.11}$$

where the concentration gradient is obtained by differentiating Eq. (1.2.8) at $z = 0$

$$G_c = \left(\frac{\mathrm{d}C}{\mathrm{d}z}\right)_{z=0} = -\Delta C_0\,\frac{V}{D} \tag{1.2.12}$$

It is apparent to note in Eq. (1.2.11) that the limiting condition for constitutional undercooling occurs at $\phi = 0$. If a high temperature gradient (G) is imposed to induce $\phi < 0$ as T_2 in Fig. 1.2.1, the solid/liquid interface shall remain the planar growth and be restricted from unstable microstructures, such as dendrite that will be introduced in Section 1.2.3.

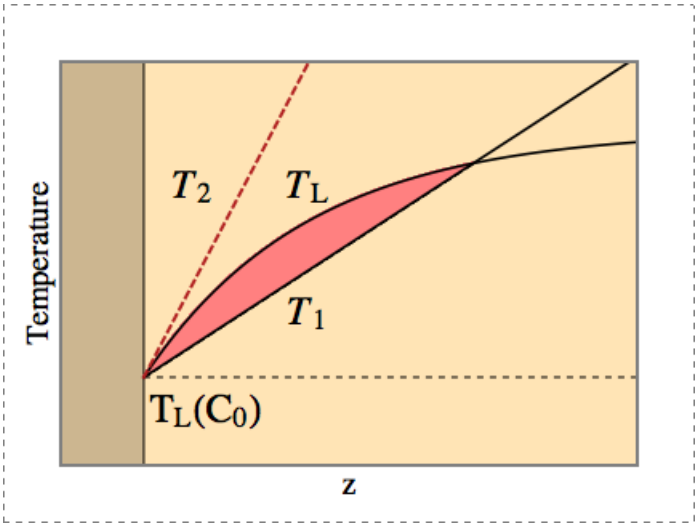

Figure 1.2.1: schematic diagram of constitutional undercooling, in which the local equilibrium temperature T_L expressed in Eq. (1.2.9) is higher than the actual interface temperature T_1 and the tangent line T_2 extended from $T_L(C_0)$ has greater liquidus slope despite $T_L(C_0) = T_1$ at the interface $z = 0$

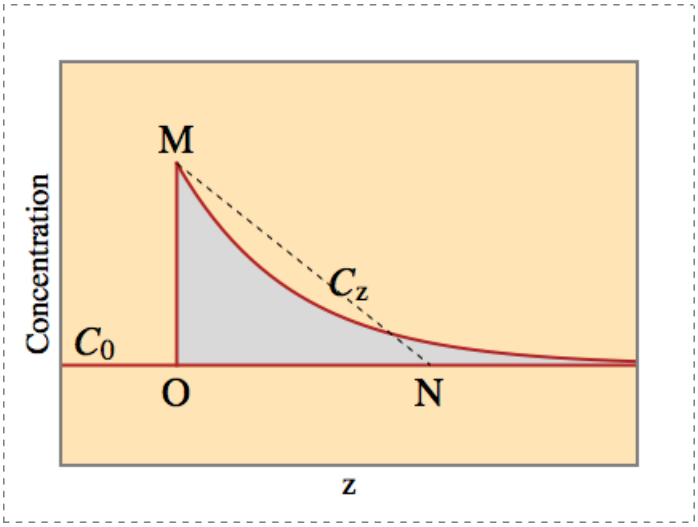

Figure 1.2.2: schematic diagram of steady-state boundary layer δ_c along the direction of the solid/liquid interface growth, which is obtained by assuming the triangle area of MON identical to that of the grey region as $\int_0^\infty \left(C(z) - C_0\right) \mathrm{d}z$ in Eq. (1.2.10)

CAPILLARITY

Once the interface becomes unstable ($\phi \geq 0$ in Eq. (1.2.11)), perturbations on the interface will form and influence the form and scale of the resultant morphology. Thus the effect of the surface tension along the solid/liquid interface also plays a significant role in interface stability.

A simple method in consideration of perturbation in the interface stability is to introduce a purely mathematical perturbations (see in Fig. 1.2.3) as

$$z = \varepsilon \sin(\omega y) \tag{1.2.13}$$

where ε is the amplitude and $\omega = 2\pi/\lambda$.

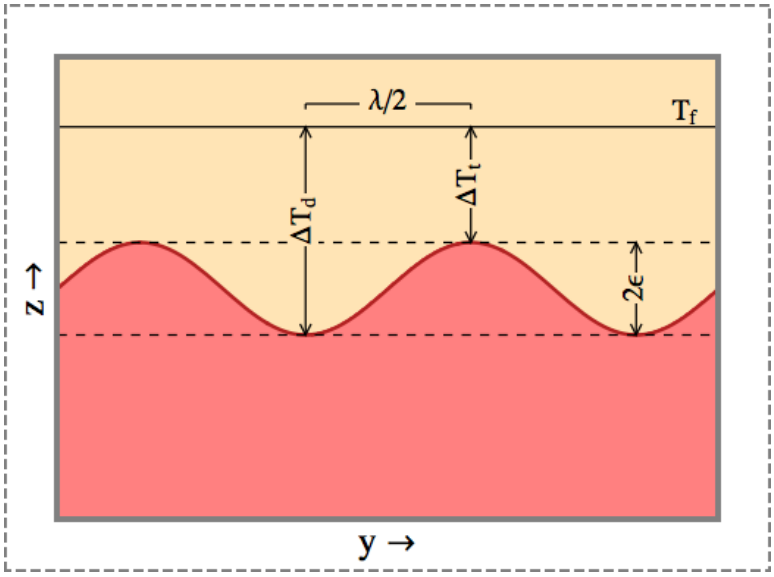

Figure 1.2.3: schematic diagram of perturbations at a solid/liquid interface

First of all, because the perturbation is two-dimensional dependent, Eq. (1.2.4) should be extended as

$$\left(\frac{\partial^2 C}{\partial y^2} + \frac{\partial^2 C}{\partial z^2}\right) + \frac{V}{D}\frac{\partial C}{\partial z} = 0 \tag{1.2.14}$$

Assumed the solution of Eq. (1.2.14) is formed by the product of separate function

$$C(y,z) = Y(y) \cdot Z(z) \tag{1.2.15}$$

then the relevant expression of Eq. (1.2.14) after inserting Eq. (1.2.15) is

$$-\frac{1}{Y} \cdot \frac{\mathrm{d}^2 Y}{\mathrm{d}y^2} = \frac{1}{Z} \cdot \frac{\mathrm{d}^2 Z}{\mathrm{d}z^2} + \frac{V}{D}\frac{1}{Z} \cdot \frac{\mathrm{d}Z}{\mathrm{d}z} = A \tag{1.2.16}$$

The general solution of each separated variable to Eq. (1.2.16)[†] is

$$\frac{\mathrm{d}^2 Z}{\mathrm{d}z^2}+\frac{V}{D}\cdot\frac{\mathrm{d}Z}{\mathrm{d}z}-A\cdot Z=0\Rightarrow Z=\exp\left\{-z\frac{V}{2D}-z\left[\left(\frac{V}{2D}\right)^2+A\right]^{1/2}\right\} \tag{1.2.17a}$$

$$\frac{1}{Y}\cdot\frac{\mathrm{d}^2 Y}{\mathrm{d}y^2}+A\,Y=0\Rightarrow Y=B_1\cos(A^{1/2}\,y)+B_2\sin(A^{1/2}\,y) \tag{1.2.17b}$$

Thus,

$$C(y,z)=\left(B_1\cos(A^{1/2}\,y)+B_2\sin(A^{1/2}\,y)\right)\exp\left\{-z\frac{V}{2D}-z\left[\left(\frac{V}{2D}\right)^2+A\right]^{1/2}\right\} \tag{1.2.18}$$

Provided the assumption introduced in Eq. (1.2.13) satisfy the general solution of two-dimensional diffusion in Eq. (1.2.18), the arbitrary constant $A=\omega^2$, $B_1=0$ and $B_2=a\varepsilon$ is needed to meet the perturbation morphology. As a result, the external diffusion C_r regarding the perturbed interface is expressed by

$$C_r(y,z)=a\varepsilon\sin(\omega\,y)\exp\left\{-z\frac{V}{2D}-z\left[\left(\frac{V}{2D}\right)^2+\omega^2\right]^{1/2}\right\} \tag{1.2.19}$$

Therefore, the exact diffusion for a local interface is consistent of the unperturbed term in Eq. (1.2.8) and the perturbed term in Eq. (1.2.19) as

$$\begin{aligned}C&=C(z)+C_r(y,z)\\&=C_0+\Delta C_0\exp\left(-\frac{V}{D}z\right)+a\varepsilon\sin(\omega\,y)\exp(-b\,z)\end{aligned} \tag{1.2.20}$$

where

$$\Delta C_0=\frac{C_0}{k}-C_0\quad\omega=\frac{2\pi}{\lambda}\quad b=\frac{V}{2D}+\left[\left(\frac{V}{2D}\right)^2+\omega^2\right]^{1/2}$$

The arbitrary a in Eq. (1.2.20) is obtained by applying the boundary conditions that is similarly illustrated in Eq. (1.2.6) and Eq. (1.2.7)

$$\text{BC1:}\quad C_{z=0}=C_L^* \tag{1.2.21}$$

$$\text{BC2:}\quad -D\left(\frac{\mathrm{d}C}{\mathrm{d}z}\right)_{z=0}=(1-k)\,C_L^*\,V \tag{1.2.22}$$

So,

$$a=\frac{k\,V\,G_c}{(1-k)\,V-D\,b} \tag{1.2.23}$$

On the one hand, under the condition

$$\phi_r=m\left(\frac{\mathrm{d}C}{\mathrm{d}z}\right)_{z=0}-G=m\,G_c\left(1-\frac{k\,V\,b\varepsilon}{(1-k)V-D\,b}\sin(\omega y)\right)-G<0 \tag{1.2.24}$$

[†]The detailed deduction of this analytic solution is illutrated in Appendix C.1.

the perturbed interface remains stable. Even if the fixed λ is initially introduced to the perturbation the local interface along the direction of y at $z = 0$, the subsequent growth along the direction of z tends to increase the scale of λ till its maximum as shown in Fig. 1.2.4. Moreover, when the wavelength of the perturbed morphology $\lambda \to \infty$, Eq. (1.2.24) can be downgraded to Eq. (1.2.11) with no capillarity, indicating the increase in λ raises the difficulty of diffusional mass transfer to suppress interface instability.

On the other hand, the solute diffusion can scale down the tip of a perturbation, leading to the outbreak of dendritic morphology under $\phi_r > 0$, the tip of which will be introduced in Section 1.2.3.

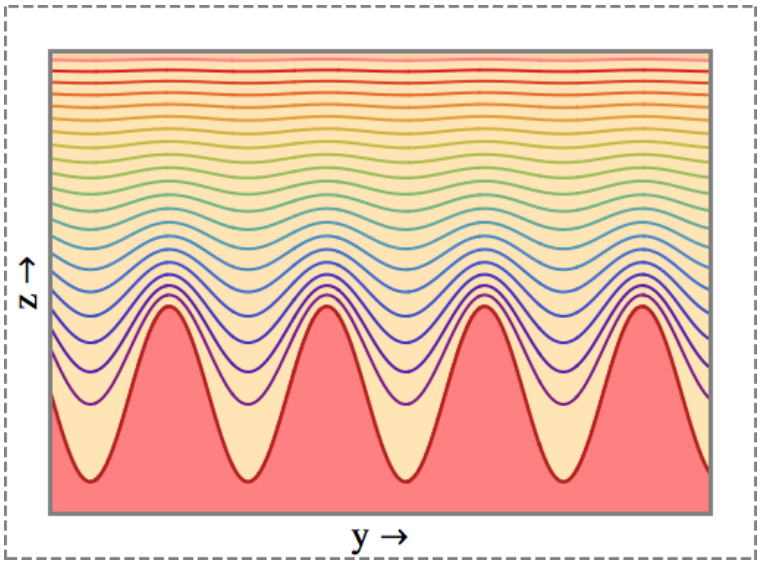

Figure 1.2.4: distribution of iso-concentrates ahead of perturbed solid/liquid interface and liquid

1.2.2 EUTECTIC

Eutectic morphology is characteristic of the simultaneous growth in two solid phases as shown in Fig. 1.2.5, where lamellar α and β are solidified cooperatively from the melt.

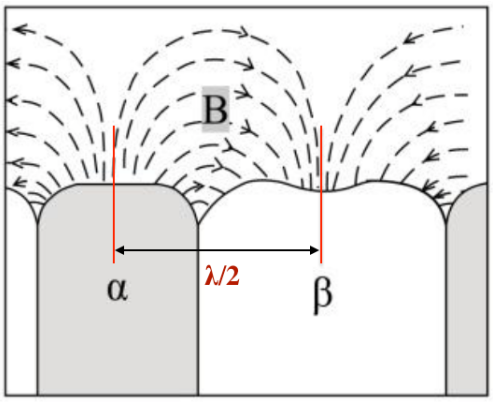

Figure 1.2.5: Diffusion paths of component B ahead of eutectic interface [3]

For $Ag-Cu$ binary system, both elements possessing the entropy of fusion less than 2 give rise to a negligible kinetics of atomic attachment in the preferred direction due to Eq. (1.2.1). So the isotropic solidification takes place in $Ag-Cu$ system to exhibit a regular (non-faceted/non-faceted) eutectic morphology. Both fibrous structure and lamellar structures are the form of a regular growth but is discriminated by volume fraction, that is, $0 \sim 0.28\%Cu$ for fibrous and $0.28 \sim 0.5\%Cu$ for lamellar. Thus, the preferred growth form of $Ag-28wt.\%Cu$ alloy tends to form lamellar structures.

To analyse the growth performance of lamellar eutectic, one half of lamellae between α and β of each phase within wavelength $\lambda/2$ is selected in the following explanation due to periodic diffusion field along the solid/liquid interface as shown in Fig. 1.2.5. In other word, $\lambda/2$ is the characteristic diffusion distance between the constant concentration gradient $C_\alpha^B - C_\beta^B$ of component B in melt.

DIFFUSION-COUPLED GROWTH

In the direction of growth, lamellar α rejects component B into the melt, while lamellar β accepts component B from the melt. The situation that one component rejected by one phase is in favour of the growth of the other phase is to believe the diffusive mass transport of eutectic growth prefers lateral diffusion along the solid/liquid interface to a long-range diffusion ahead of both phases. Thus, the use of Eq. (1.2.14) to express the solute distribution of lamellar α and β is still valid.

Firstly, the general solution of Eq. (1.2.14) to the distribution field of component B can consist of Eq. (1.2.5) characterized by the solute distribution of either lamellae for the unperturbed interface,

and Eq. (1.2.18) by the one for the perturbed interface, as

$$C(y,z) = B_0 + B_1 \exp\left(-\frac{V}{D}z\right) + \left(B_2 \cos(A^{1/2}y) + B_3 \sin(A^{1/2}y)\right) \exp\left\{-z\frac{V}{2D} - z\left[\left(\frac{V}{2D}\right)^2 + A\right]^{1/2}\right\} \tag{1.2.25}$$

In the steady-state growth, the mean composition of the alternative lamellae, α and β, must equal to the composition of the melt, which is the eutectic composition C_e for Ag – 28wt.%Cu alloy. So the two exponential terms in RHS of Eq. (1.2.25) at $z \to \infty$ becomes zero to obtain

$$C(y,z)\Big|_{z\to\infty} = B_0 = C_e \tag{1.2.26}$$

Provided there would be no concentration gradient at the mid-point of each lamellar which is located at $y = 0$ for lamellar α and at $y = \lambda/2$ for lamellar β in the y direction in Fig. 1.2.5, the derivative of Eq. (1.2.25) with respect to y at $y = \lambda/2$

$$\left(\frac{\partial C}{\partial y}\right)_{y=\lambda/2} = 0$$

leads to

$$B_3 = 0 \tag{1.2.27}$$

Because of the symmetry of circular function in the third RHS term in Eq. (1.2.25),

$$A^{1/2} = \frac{2\pi}{\lambda} \Rightarrow A = \left(\frac{2\pi}{\lambda}\right)^2 \tag{1.2.28}$$

When the eutectic interface advances slowly, the value of λ is much smaller than that of the concentration boundary layer δ_c in Eq. (1.2.10), giving rise to

$$\frac{V}{2D} \ll \frac{2\pi}{\lambda} \tag{1.2.29}$$

Thus the power of the second exponential function in Eq. (1.2.25) can be simplified to

$$-z\frac{V}{2D} - z\left[\left(\frac{V}{2D}\right)^2 + A\right]^{1/2} \approx -z\frac{2\pi}{\lambda} \tag{1.2.30}$$

By inserting Eq. (1.2.26), Eq. (1.2.27), Eq. (1.2.28) and Eq. (1.2.30), then Eq. (1.2.25) is simplified as

$$C(y,z) = C_e + B_1 \exp\left(-\frac{V}{D}z\right) + B_2 \cos\left(\frac{2\pi}{\lambda}y\right) \exp\left(-\frac{2\pi}{\lambda}z\right) \tag{1.2.31}$$

Considering the quantity of solute rejected from the local interface concentration kC_L^* to the local melt concentration C_L^* per unit time is balanced by the creation of a concentration gradient in the melt, the flux boundary condition in Eq. (1.2.22) is applied, in which $C_L^* \approx C_e$ due to only a slight deviation from the eutectic composition as

$$\text{lamellar } \alpha\text{:} \quad V\left(k_\alpha - 1\right)C_e = D\left(\frac{\partial C}{\partial z}\right)_{z=0} \tag{1.2.32a}$$

$$\text{lamellar } \beta\text{:} \quad V\left(1 - k_\beta\right)\left(1 - C_e\right) = D\left(\frac{\partial C}{\partial z}\right)_{z=0} \tag{1.2.32b}$$

Thus, the variant of solute removal at the same growth rate (V) via diffusion along the y direction is approximated by the method of *weighted residuals* [3], since only the volume fraction f of lamellar α is in the range of 0 and $\lambda/2$.

For lamellar α,

$$\int_0^{\frac{\lambda}{2}f} V\left(k_\alpha - 1\right) C_e \, \mathrm{d}y = \int_0^{\frac{\lambda}{2}f} D\left(\frac{\partial C}{\partial z}\right)_{z=0} \mathrm{d}y$$

$$\therefore \qquad C_e f\left(1-k_\alpha\right) V\lambda = f V \lambda B_1 + 2D\sin(f\pi) B_2 \tag{1.2.33}$$

For lamellar β,

$$\int_{\frac{\lambda}{2}f}^{\frac{\lambda}{2}} V\left(1-k_\beta\right)\left(1-C_e\right) = \int_{\frac{\lambda}{2}f}^{\frac{\lambda}{2}} D\left(\frac{\partial C}{\partial z}\right)_{z=0} \mathrm{d}y$$

$$\therefore \qquad \left(1-C_e\right)\left(1-f\right)\left(k_\beta - 1\right) V\lambda = \left(1-f\right) V\lambda B_1 - 2D\sin(f\pi) B_2 \tag{1.2.34}$$

The unknown constant B_1 and B_2 in a system of linear Eq. (1.2.33) and Eq. (1.2.34) can be solved by simply using the linear combination method as

$$B_1 = \left(1 - C_\alpha - C_\beta\right) f - \left(1 - C_e - C_\beta\right) \tag{1.2.35}$$

$$B_2 = \frac{f\left(1-f\right)}{2D} \frac{V\lambda}{\sin(f\pi)} \left(1 - C_\alpha - C_\beta\right) \tag{1.2.36}$$

Therefore, the exact solution of solute distribution ahead of solid/liquid interface is obtained by substituting B_1 and B_2 in Eq. (1.2.31) with Eq. (1.2.35) and Eq. (1.2.36) respectively.

$$\begin{aligned} C(y,z) = C_e &+ \left[\left(1 - C_\alpha - C_\beta\right) f - \left(1 - C_e - C_\beta\right)\right] \exp\left(-\frac{V}{D} z\right) \\ &+ \frac{f\left(1-f\right)}{2D} \frac{V\lambda}{\sin(f\pi)} \left(1 - C_\alpha - C_\beta\right) \cos\left(\frac{2\pi}{\lambda} y\right) \exp\left(-\frac{2\pi}{\lambda} z\right) \end{aligned} \tag{1.2.37}$$

UNDERCOOLING

For metals, the temperature of local undercooled eutectic interface T_q^* due to high thermal conductivity κ can be constant at any instant of time. As a result, the temperature difference between the eutectic temperature T_e and T_q^* (undercooling ΔT) is also constant.

In general, the total undercooling gives rise to three contributions, heat flow ΔT_q, solute diffusion ΔT_c, and curvature ΔT_r as

$$\Delta T = \Delta T_q + \Delta T_c + \Delta T_r = T_e - T_q^* = \text{constant} \tag{1.2.38}$$

where ΔT_q is safely neglected under the directional growth of lamellar eutectic.

The solute undercooling ΔT_c is obtained by multiplying the liquidus slope m by the concentration difference ΔC based on the binary phase diagram.

$$\Delta T_c = m\Delta C \tag{1.2.39}$$

The curvature undercooling ΔT_r is attributed to the increase in the free enthalpy due to its curved surface.

$$\Delta T_r = \frac{\sigma}{\Delta S_F} K \tag{1.2.40}$$

where $\sigma/\Delta S_F$ is of order of 10^{-7} K·m for most metals, such as $177\times10^{-3}/1.2\times10^{6} = 1.475\times10^{-7}$ K·m for copper, and the curvature K between two discrete points with a distance L is expressed

$$K = \frac{1}{L}\int_0^L \frac{z''}{\left(1+z'^2\right)^{3/2}}\,\mathrm{d}y = \frac{1}{L}\sin(\arctan(z'))\Big|_0^L \tag{1.2.41}$$

Solute Undercooling

In binary alloys, the liquidus slope m_α and m_β can be obtained from the phase diagram. The concentration difference of the melt ahead of eutectic interface is the average one $\Delta C = \overline{C-C_e}$ within its volume fraction. As shown in Fig. 1.2.5, lamellar α extends between $0 \sim f\lambda/2$, lamellar β between $f\lambda/2 \sim \lambda/2$.

With the aid of Eq. (1.2.37), the solute undercooling ΔT_c^α for lamellar α and ΔT_c^β for lamellar β is

$$\begin{aligned}
\Delta T_c^\alpha &= |m_\alpha|\frac{2}{f\lambda}\int_0^{\frac{\lambda}{2}f}(\overline{C-C_e})_{z=0}\,\mathrm{d}y \\
&= |m_\alpha|\frac{2}{f\lambda}\int_0^{\frac{\lambda}{2}f}\left\{\left[\left(1-C_\alpha-C_\beta\right)f-\left(1-C_e-C_\beta\right)\right]+\frac{f\left(1-f\right)}{2D}\frac{V\lambda}{\sin(f\pi)}\left(1-C_\alpha-C_\beta\right)\cos\left(\frac{2\pi}{\lambda}y\right)\right\}\mathrm{d}y \\
&= |m_\alpha|\left\{\left[\left(1-C_\alpha-C_\beta\right)f-\left(1-C_e-C_\beta\right)\right]+\frac{f\left(1-f\right)}{2D}\frac{V\lambda}{\sin(f\pi)}\left(1-C_\alpha-C_\beta\right)\frac{\sin(f\pi)}{f\pi}\right\} \\
&= |m_\alpha|\left\{\left[\left(1-C_\alpha-C_\beta\right)f-\left(1-C_e-C_\beta\right)\right]+\frac{1-f}{2D\pi}\left(1-C_\alpha-C_\beta\right)V\lambda\right\}
\end{aligned} \tag{1.2.42}$$

$$\begin{aligned}
\Delta T_c^\beta &= -|m_\beta|\frac{2}{(1-f)\lambda}\int_{\frac{\lambda}{2}f}^{\frac{\lambda}{2}}(\overline{C-C_e})_{z=0}\,\mathrm{d}y \\
&= -|m_\beta|\left\{\left[\left(1-C_\alpha-C_\beta\right)f-\left(1-C_e-C_\beta\right)\right]-\frac{f}{2D\pi}\left(1-C_\alpha-C_\beta\right)V\lambda\right\}
\end{aligned} \tag{1.2.43}$$

Curvature Undercooling

According to the formula of curvature in Eq. (1.2.41), the curvature undercoolings of lamellar α with $L_\alpha = f\lambda/2$ and lamellar β with $L_\beta = \lambda/2 - f\lambda/2$ is

$$\Delta T_r^\alpha = \left(\frac{\sigma}{\Delta S_F}\right)_\alpha K_\alpha = \left(\frac{\sigma}{\Delta S_F}\right)_\alpha \frac{1}{L_\alpha}\sin(\arctan(z'))\Big|_0^{L_\alpha} = \frac{2}{f\lambda}\left(\frac{\sigma}{\Delta S_F}\right)_\alpha \sin(\theta_\alpha) \tag{1.2.44}$$

$$\Delta T_r^\beta = \left(\frac{\sigma}{\Delta S_F}\right)_\beta K_\beta = \left(\frac{\sigma}{\Delta S_F}\right)_\alpha \frac{1}{L_\beta}\sin(\arctan(z'))\Big|_0^{L_\beta} = \frac{2}{(1-f)\lambda}\left(\frac{\sigma}{\Delta S_F}\right)_\beta \sin(\theta_\beta) \tag{1.2.45}$$

where $z' = \tan\theta$ and $\theta_\alpha + \theta_\beta \approx 90\,°$.

Combining Eq. (1.2.42) or Eq. (1.2.43) with Eq. (1.2.44) or Eq. (1.2.45) gives

$$\begin{aligned}\Delta T_\alpha &= \Delta T_c^\alpha + \Delta T_r^\alpha \\ &= |m_\alpha|\left\{\left[\left(1-C_\alpha-C_\beta\right)f-\left(1-C_e-C_\beta\right)\right]+\frac{1-f}{2D\pi}\left(1-C_\alpha-C_\beta\right)V\lambda\right\}+\frac{2}{f\lambda}\left(\frac{\sigma}{\Delta S_F}\right)_\alpha\sin(\theta_\alpha)\end{aligned} \tag{1.2.46a}$$

$$\begin{aligned}\Delta T_\beta &= \Delta T_c^\beta + \Delta T_r^\beta \\ &= -|m_\beta|\left\{\left[\left(1-C_\alpha-C_\beta\right)f-\left(1-C_e-C_\beta\right)\right]-\frac{f}{2D\pi}\left(1-C_\alpha-C_\beta\right)V\lambda\right\}+\frac{2}{(1-f)\lambda}\left(\frac{\sigma}{\Delta S_F}\right)_\beta\sin(\theta_\beta)\end{aligned} \tag{1.2.46b}$$

Because $\Delta T = \Delta T_\alpha = \Delta T_\beta =$ constant due to Eq. (1.2.38) in the eutectic growth and the first term in the RHS of Eq. (1.2.46a) and Eq. (1.2.46b) can be efficiently eliminated by

$$|m_\beta|\Delta T_\alpha + |m_\alpha|\Delta T_\beta = \left(|m_\alpha|+|m_\beta|\right)\Delta T \Rightarrow \Delta T = \frac{|m_\beta|\Delta T_\alpha + |m_\alpha|\Delta T_\beta}{|m_\alpha|+|m_\beta|}$$

Thus, the relationship of ΔT with V and λ is

$$\Delta T = \underbrace{\frac{|m_\alpha|\cdot|m_\beta|}{|m_\alpha|+|m_\beta|}\frac{1-C_\alpha-C_\beta}{2D\pi}}_{K_c}\cdot V\lambda + \underbrace{\frac{1}{|m_\alpha|+|m_\beta|}\left\{\frac{2|m_\beta|}{f}\left(\frac{\sigma}{\Delta S_F}\right)_\alpha\sin(\theta_\alpha)+\frac{2|m_\alpha|}{(1-f)}\left(\frac{\sigma}{\Delta S_F}\right)_\beta\sin(\theta_\beta)\right\}}_{K_r}\cdot\frac{1}{\lambda} \tag{1.2.47}$$

where K_c and K_r are alloy-dependent physical constants.

The schematic graphs in Fig. 1.2.6 shows the relationship of the solute undercooling ΔT_c in Eq. (1.2.42) or Eq. (1.2.43), the curvature undercooling ΔT_r in Eq. (1.2.44) or Eq. (1.2.45), and the total undercooling ΔT in Eq. (1.2.46a) or Eq. (1.2.46b), with respect to λ. It can be seen that ΔT is controlled by ΔT_r (capillarity effect) at $\lambda < \lambda_e$ and by ΔT_c (solute diffusion) at $\lambda > \lambda_e$. Although the eutectic lamellar can have a range of wavelengths, it is more likely that the lamellar with λ_e in Fig. 1.2.6 appears in the eutectic solidification due to the minimum undercooling ΔT required.

For regular lamellar eutectic, the extremum criterion of eutectic growth is

$$\frac{\mathrm{d}}{\mathrm{d}\lambda}\left(\Delta T\right) = 0 \tag{1.2.48}$$

Inserting Eq. (1.2.47) into Eq. (1.2.48),

$$\frac{\mathrm{d}}{\mathrm{d}\lambda}\left(K_c V\lambda + \frac{K_r}{\lambda}\right) = K_c V - \frac{K_r}{\lambda^2} = 0 \Rightarrow \lambda^2 V = \frac{K_r}{K_c} \tag{1.2.49}$$

Multiplying Eq. (1.2.47) by λ and combining with Eq. (1.2.49),

$$\lambda\Delta T = K_c\lambda^2 V + K_r \Rightarrow \lambda^2 V = \frac{\lambda\Delta T - K_r}{K_c} = \frac{K_r}{K_c} \Rightarrow \lambda\Delta T = 2K_r \tag{1.2.50}$$

Since $\lambda = 2K_r/\Delta T$ due to Eq. (1.2.50), Eq. (1.2.49) can be modified to

$$\left(\frac{2K_r}{\Delta T}\right)^2 V = \frac{K_r}{K_c} \Rightarrow \frac{\Delta T}{V^{1/2}} = 2\left(K_r K_c\right)^{1/2} \tag{1.2.51}$$

Jackson and Hunt [5] (HJ) are firstly analysed the growth of regular eutectic and derived the relationship of undercooling ΔT with growth rate V and wavelength λ shown in Eq. (1.2.47). Later experimental study of directional eutectic solidification in a model transparent organic system is verified that $\lambda^2 V$ remains constant [6, 7], despite the stable range of eutectic spacings is much smaller than that discussed by Jackson and Hunt.

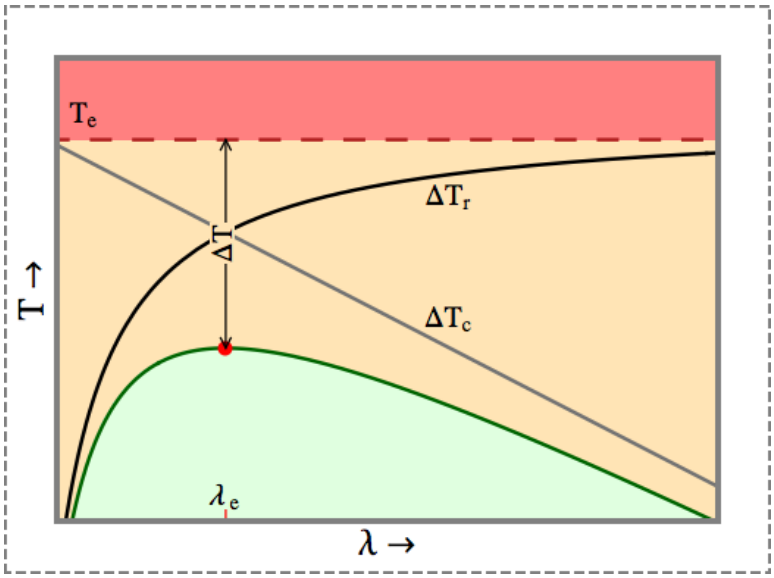

Figure 1.2.6: Eutectic growth temperature with respect to λ at constant growth rate V

1.2.3 DENDRITES

Under non-equilibrium thermodynamic condition, the morphology growth (introduced in Section 1.2.1) might reach or surpass its limitation of stability ($\phi \geq 0$) to enhance the effect of perturbation along solid/liquid interface and consequently to form the tips of dendrites. Depending on the direction of heat flow, these undercooled tips can develop either directional dendrites or equiaxed dendrites.

In the directional solidification, the heat transfers from the melt into the solid, parallel and opposite to the growth direction. These tips are undercooled by constitutional undercooling due to solute diffusion (see in Fig. 1.2.1), and are controlled by the rate of advance of the isotherms.

In the equiaxed solidification, the heat transfers from the solid into the melt has the same direction of the growth. Without the isothermal constraint ahead, the undercooled tips of dendrite are driven by higher gradients and lead to an increased heat and solute flux, and a resultant increase in the growth rate on those tips until they impinge upon other dendrites.

The growth of both types of dendrites adopts an orientation as close as possible to (or opposite to) the heat flow direction, but still follows the preferred crystal growth axe. For example, the cubic crystal system, like Ag and Cu, has the six axes related to [100] which are preferred in the crystal orientation of dendrites. Once trucks are develop in dendrite, the primary spacing between two trucks allows branches to form in another four [100] directions which are perpendicular to the trunk until these tips of secondary branches encounter the diffusion field of neighbouring dendrites. Although tertiary or even higher-order arms might be formed further by consuming the remaining inter-liquid between secondary branches, these highly-branched arms might change with the solidification time into coarser, less branched and more widely-spaced ones in the ripening process.

DENDRITE TIP

A dendrite tip can be regarded as an isolated crystal in solidification. By analyzing the performance of the tip with its heat and mass diffusion field ahead, the morphological parameters, such as the growth rate V, supersaturation Ω, and undercooling ΔT, can be estimated in order of magnitude.

Although the tip shape can be successfully characteristic with a paraboloid of revolution in diffusion problem, the hemispherical cap along the growth axis is a simple approximation, yet giving a clear insight into the physical factors of dendrite.

The general solution of diffusion field around a growing sphere in steady-state condition[‡]

$$C(r) = A + \frac{B}{r}$$

[‡]The mathematical deduction of this diffusion problem shall refer Eq. (1.3.7) in Section 1.3.2, in which variable heat $T(r)$ should be substituted by mass $C(r)$.

with subject to the boundary conditions

$$\begin{aligned} &\text{BC1:} \quad C = C_l^* \qquad r = \delta \\ &\text{BC2:} \quad C = C_0 \qquad r = \infty \end{aligned}$$

gives

$$C(r) = C_0 + \frac{\delta}{r}\left(C_l^* - C_0\right) \tag{1.2.52}$$

The concentration gradient at the tip with radius $r = \delta$ can then be approximated to

$$\left(\frac{\mathrm{d}C}{\mathrm{d}r}\right)_{r=\delta} = \left(-\frac{\delta}{r^2}\left(C_l^* - C_0\right)\right)_{r=\delta} = -\frac{C_l^* - C_0}{\delta} \tag{1.2.53}$$

Considering a hemispherical tip has a cylinder body with a cross-section $A = \pi\delta^2$, then the rejection of solute to form a new cylinder volume is assumed to be identical with the amount of radial solute diffusion through the hemispherical cap with surface area $A_h = 2\pi\delta^2$ to the melt ahead of the tip in any given time step $\mathrm{d}t$ and the corresponding growth rate V as

$$A\,V\left(C_l^* - C_S^*\right) = -D\,A_h\left(\frac{\mathrm{d}C}{\mathrm{d}r}\right)_{r=\delta} \Rightarrow V\,C_l^*\left(1-k\right) = -2D\left(\frac{\mathrm{d}C}{\mathrm{d}r}\right)_{\delta} \tag{1.2.54}$$

Combining Eq. (1.2.53) and Eq. (1.2.54) gives

$$V\,C_l^*\left(1-k\right) = 2D\,\frac{C_l^* - C_0}{\delta} \Rightarrow \underbrace{\frac{V\,\delta}{2\,D}}_{P_c} = \underbrace{\frac{C_l^* - C_0}{C_l^*\left(1-k\right)}}_{\Omega} \tag{1.2.55}$$

where the solute Péclet number P_c stands for the ratio of a characteristic length δ to the concentration boundary layer $\delta_c = 2D/V$ in Eq. (1.2.10) and Ω for the supersaturation.

For small Ω in Eq. (1.2.55) and with aid of $-m\,C_0\,(1-k) = \Delta T_0\,k$, the supersaturation also can be

$$\Omega = \frac{C_l^* - C_0}{C_l^*\left(1-k\right)} \Rightarrow C_l^* = \frac{C_0}{1-\Omega\,(1-k)} \tag{1.2.56}$$

$$\Delta T_c = m\left(C_0 - C_l^*\right) = m\,C_0\left(1 - \frac{1}{1-\Omega\,(1-k)}\right) \approx -m\,C_0\,\Omega\,(1-k) \Rightarrow \Delta T_0\,k\,\Omega$$

$$\therefore \qquad \Omega = \frac{\Delta T_c}{\Delta T_0\,k} \tag{1.2.57}$$

For a given Ω to Eq. (1.2.55), $V\,\delta$ remains constant and has a relationship as shown in the green dashed diagonal line in Fig. 1.2.7. However the smaller tip radius δ might be unlikely to prevail in the dendrite growth since the minimum radius r^* (critical nucleation radius in Eq. (1.1.10)) must be at least satisfied, as the grey dashed vertical line in Fig. 1.2.7 to cut off the diffusion limit.

In order to better define the relationship of the tip radius upon the the growth condition, both solute diffusion and capillarity effects should be considered in the supersaturation formula $\Omega(V,\delta)$ in Eq. (1.2.55).

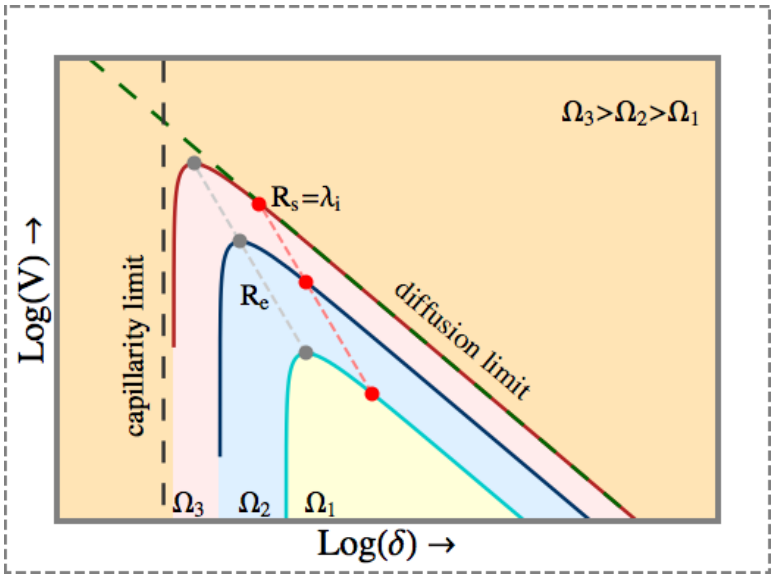

Figure 1.2.7: Growth rate as a function of tip radius

Since Ω tends to be ∞ at

$$\delta = r^* = 2\frac{\sigma}{\Delta S_F \Delta T_c} \approx 0 \tag{1.2.58}$$

as the vertical dashed line in Fig. 1.2.7, the capillarity term in $\Omega(V,\delta)$ should be related to $\propto 1/\delta$.

Assumed the capillarity term is expressed as s/δ and Eq. (1.2.57) is applied in Ω at sufficient small δ,

$$(\Omega)_{\delta \to r^*} = \frac{\Delta T_c}{\Delta T_0 k} = \frac{s}{r^*} = s\frac{\Delta S_F \Delta T_c}{2\sigma} \Rightarrow s = \frac{2\sigma}{\Delta S_F \Delta T_c}\frac{\Delta T_c}{\Delta T_0 k} = \frac{2}{\Delta T_0 k}\frac{\sigma}{\Delta S_F} \tag{1.2.59}$$

Together with the diffusion term in Eq. (1.2.55) and the capillarity term in Eq. (1.2.59),

$$\Omega = \frac{V}{2D}\delta + \frac{2}{\Delta T_0 k}\frac{\sigma}{\Delta S_F}\frac{1}{\delta} \tag{1.2.60}$$

In Fig. 1.2.7, curves with different constant supersaturation ($\Omega_3 > \Omega_2 > \Omega_1$) are displayed by using Eq. (1.2.60). The greater supersaturation Ω, the smaller extreme radius R_e (marked as a grey point) and the higher corresponding growth rate. The reason of these changes gives rise to the concentration gradient inversely related to δ in Eq. (1.2.53), since a greater supersaturation permits a sharper tip, which lead to rejecting solute more efficiently in a steeper gradient.

Under experimental observation [8] and later theoretical development of rapid solidification [9], the radius of tip proves to be much closer to the least wavelength perturbation which is the limit of stability for the outbreak of dendrite from the planar interface as red points shown in Fig. 1.2.7.

1.3 Convection Heat transfer in Flow

The forced convection heat transfer is complicated since fluid motion and heat conduction are under consideration. The fluid motion enhances heat transfer though a fluid and effectively warms the fluid temperature surrounding the hot solid. Then the warmer fluid rises the buoyancy effect on the fluid motion and further changes the heat transfer around the solid.

Section 1.3.1 introduces the basic mechanism of heat transfer, including

(a) Conduction **(b)** Convection **(c)** Radiation

Section 1.3.2 explains the *heat transfer coefficient* and *Nusselt number* of fuild attached to the solid surface. Also, the common solutions of average convection heat transfer coefficient past a sphere surface are further explained.

1.3.1 Mechanisms

For a given superheated melt in the process of solidification, heat is initially conducted through a surface of every unit area normal to the direction of flow. Then, the loss of heat from the melt is delivered to the surrounding gas by convection and radiation. Without external heat source to heat up the melt, the temperature difference between the melt and the gas is reduced until none during cooling solidification.

Conduction

Heat Conduction is defined as a diffusion of thermal energy occurs through intervening matter without bulk motion of the matter, i.e., the movement of thermal energy from a high temperature region to a lower region via molecular vibrations.

In isotropic matter, the heat flux $\dot{q}$ locally related to the temperature gradient ∇T is

$$\dot{q}_{cond} = \frac{\dot{Q}_{cond}}{A} = -\kappa \nabla T \tag{1.3.1}$$

When the interest of *Fourier's law of heat conduction* in 1.3.1 is one-dimensional, the extent of change in heat is analyzed by the thermal conductivity κ under the direction of the interest, normal to the cross-sectional area A.

Convection

Convection is defined as heat transfer of the fluid motion when the heated fluid carrying thermal energy is caused to move away from the heat source. By using *Newton's law of cooling*, the govern-

ing rate for convection heat transfer is

$$\dot{q}_{conv} = \frac{\dot{Q}_{conv}}{A} = -h\left(T_s - T_f\right) \tag{1.3.2}$$

where T_f is the fluid temperature far from the sphere surface and the *heat transfer coefficient* h strongly depends on the fluid properties, the roughness of the solid surface and the type of fluid flow. Since the fluid-motion related h enhances heat transfer, the higher the velocity the higher the heat flux of convection.

RADIATION

Radiation is defined as transmission of thermal energy between two objects through electromagnetic wave, with no necessary presence of matter involved.

It is characteristic with the form of photons moving in a random direction, with random phase and frequency. The behaviour of radiation incident impinging on a surface can be described by absorptance, reflectance, and transmittance.

A basic fact of radiation is that heat flux by radiative heat transfer is proportional to the fourth power of temperature of its source T_∞, as shown in Eq. (1.3.3).

$$\dot{q}_{rad} = \frac{\dot{Q}_{rad}}{A} = \epsilon\,\sigma\left(T_s^4 - T_\infty^4\right) \tag{1.3.3}$$

where the Stefan-Boltzmann constant $\sigma = 5.670 \times 10^{-8}\ \mathrm{W/m^2\,K^4}$ and the emissivity ϵ ideally equals to 1.

Nevertheless, the contribution of heat radiation can be safely neglected in consideration of heat flux though the boundary surface, not only to simplify the heat transfer calculation, but also for the fact that convection is dominant over radiation in cooling process of metallic solid [4, 10].

1.3.2 NUSSELT NUMBER AND HEAT TRANSFER COEFFICIENT

In Section 1.3.1, the heat transfer coefficient is characteristic with the efficiency of heat transfer by the convection. In the common practice, the variables of the governing equations group together into dimensionless numbers. The measure of heat transfer coefficient h in Eq. (1.3.4) is therefore replaced with the corresponding non-dimensional number, *Nusselt number* (Nu).

Assumed there is the temperature difference between T_s and T_f within the characteristic length δ

$$\frac{\mathrm{d}T}{\mathrm{d}x} = \frac{T_s - T_f}{\delta}$$

then Nu is defined as

$$\mathrm{Nu} = \frac{\dot{q}_{conv}}{\dot{q}_{cond}} = \frac{h\left(T_s - T_f\right)}{\kappa\,\dfrac{T_s - T_f}{\delta}} = \frac{h\delta}{\kappa} \tag{1.3.4}$$

which represents the ratio of convective to conductive heat transfer through a fluid layer δ.

When the distance is away from the solid surface, greater than the thermal boundary layer δ, the temperature remains unchanged as the constant fluid temperature T_f.

MOTIONLESS FLOW

When the solid is placed in the steady static fluid, the fluid-motion dependent convection is absent from the heat transfer. In other word, the velocity of the fluid is zero at the wall (no-slip condition), which leads to pure conduction from the solid surface to the fluid layer adjacent to the surface when radiation is neglected. Thus, the heat flux at $\xi+\delta$ around spherical area ($4\pi r^2$) should be equal to that at ξ

$$\dot{Q}_{cond}\Big|_{r+\delta} - \dot{Q}_{cond}\Big|_{r} = 0 \tag{1.3.5}$$

Inserting Eq. (1.3.1), Eq. (1.3.5) becomes

$$4\pi r^2\,\dot{q}_{cond}\Big|_{r+\delta} - 4\pi r^2\,\dot{q}_{cond}\Big|_{r} = 0 \Rightarrow \frac{4\pi r^2\,\dot{q}_{cond}\Big|_{r+\delta} - 4\pi r^2\,\dot{q}_{cond}\Big|_{r}}{\delta} = 0 \Rightarrow \frac{\mathrm{d}}{\mathrm{d}r}\left(r^2\,\frac{\mathrm{d}T}{\mathrm{d}r}\right) = 0 \tag{1.3.6}$$

The general solution of Eq. (1.3.6) should be expressed as

$$T(r) = -\frac{A}{r} + B \tag{1.3.7}$$

Applying the boundary conditions,

$$\begin{aligned} &\text{BC1:} \quad T = T_s \quad r = \delta \\ &\text{BC2:} \quad T = T_f \quad r = \infty \end{aligned}$$

the temperature distribution with respect to r is

$$T(r) = \delta\,\frac{T_s - T_f}{r} + T_f \tag{1.3.8}$$

Combining with Eq. (1.3.8), the heat conduction in Eq. (1.3.1) at the characteristic length δ is

$$\dot{q}_{cond} = -\kappa\,\frac{\mathrm{d}T(r)}{\mathrm{d}r}\Big|_{r=\delta} = \kappa\,\delta\,\frac{T_s - T_f}{r^2}\Big|_{\delta} = \kappa\,\frac{T_s - T_f}{\delta} \tag{1.3.9}$$

Equating the conduction in Eq. (1.3.9) to the convection in Eq. (1.3.4) gives

$$\dot{q}_{cond} = \dot{q}_{conv} \Rightarrow \kappa\,\frac{T_s - T_f}{\delta} = h\left(T_s - T_f\right)$$

$$\therefore \quad \frac{h\delta}{\kappa} = 1 = \mathrm{Nu} \tag{1.3.10}$$

When the characteristic length δ stands for a diameter of sphere,

$$\mathrm{Nu} = 2 \tag{1.3.11}$$

LAMINAR FLOW

When a hot sphere of radius R is immersed in stream of fluid, advective cooling of the surface of the sphere to the cold air involves conduction and convection along the normal to the surface. According to boundary layer theory, the rate of transfer is maximum on the front side of the drop facing the oncoming air stream, gradually decrease to a minimum value near the separation point, and then increase to another, but yet lower maximum rate on the trailing face which experiences velocities in the reverse direction as shown in Fig. 1.3.1(a).

For a dimensionless steady incompressible inviscid fluid[§], the convection-diffusion equation is balanced between the advective term on the LHS of Eq. (1.3.12) which heat moves along with the flow of matter and the RHS which heat streams down temperature gradient as for a fluid at rest.

$$\mathrm{Pe}\left(\vec{v}\cdot\nabla\right)Z = \nabla^2 Z \tag{1.3.12}$$

where[¶]

$$Z = \frac{T - T_\infty}{T_0 - T_\infty} \qquad \xi = \frac{r}{R} \qquad \mathrm{Pe} = \frac{w\,R}{\alpha}$$

Under the low Re Stokes flow (creeping flow), a falling sphere is subject to the velocity component in Eq. (B.1.10a) and Eq. (B.1.10b) and the resulting boundary conditions as

$$Z = 1 \qquad \text{at } \xi = 1 \tag{1.3.13a}$$

$$Z = 0 \qquad \text{at } \xi \to \infty \tag{1.3.13b}$$

In limit of small *Péclet number* Pe, the expansion of an asymptotic series with regards to Pe is

$$Z = Z_0 + \mathrm{Pe}\,Z_1 + \mathrm{Pe}^2\,Z_2 + \ldots \tag{1.3.14}$$

which leads to the leading order of temperature distribution Z_0 in the absence of convective effect in Eq. (1.3.12) and the first-order correction to the temperature distribution Z_1 due to convection as below.

$$\nabla^2 Z_0 = 0 \tag{1.3.15}$$

$$v_\xi \frac{\partial Z_0}{\partial \xi} + \frac{v_\theta}{\xi}\frac{\partial Z_0}{\partial \theta} = \nabla^2 Z_1 \tag{1.3.16}$$

Also, the boundary conditions in Eq. (1.3.13a) and Eq. (1.3.13b) according to Eq. (1.3.14) are ad-

[§]The mathematical introduction of an incompressible forced-convective heat transfer is in Eq. (A.2.3) in Appendix A.2.

[¶]The deduction of dimensionless numbers and the definition of symbols in each dimensionless number for Eq. (1.3.12) shall refer Eq. (3.2.3) in Section 3.2.1.

justed for Eq. (1.3.15) and Eq. (1.3.16).

$$Z_0 = 1 \qquad \text{at } \xi = 1 \tag{1.3.17a}$$

$$Z_0 = 0 \qquad \text{at } \xi \to \infty \tag{1.3.17b}$$

$$Z_1 = 0 \qquad \text{at } \xi = 1 \tag{1.3.17c}$$

$$Z_1 = 0 \qquad \text{at } \xi \to \infty \tag{1.3.17d}$$

The leading order in Eq. (1.3.15) can be simplified to the problem in Eq. (1.3.6) since the spherically symmetric heat transfer without fluid flow, which results in the general solution as Eq. (1.3.7). With assistant of boundary conditions in Eq. (1.3.17a) and Eq. (1.3.17b), the approximation of Eq. (1.3.7) to the temperature field Z_0 is

$$Z_0 = \frac{1}{\xi} \tag{1.3.18}$$

Consequently, Nu should remain 2 as Eq. (1.3.11).

Inserting the solution of Z_0 in Eq. (1.3.18) into the first-order correction in Eq. (1.3.16),

$$\begin{aligned} v_\xi\left(-\frac{1}{\xi^2}\right) + \frac{v_\theta}{\xi}0 = \frac{1}{\xi^2}\frac{\mathrm{d}}{\mathrm{d}\xi}\left(\xi^2\frac{\mathrm{d}Z_1}{\mathrm{d}\xi}\right) + \frac{1}{\xi^2\sin\theta}\frac{\mathrm{d}}{\mathrm{d}\theta}\left(\sin\theta\frac{\mathrm{d}Z_1}{\mathrm{d}\theta}\right) \\ -\left[1-\frac{3}{2}\frac{1}{\xi}+\frac{1}{2}\left(\frac{1}{\xi}\right)^3\right]\cos\theta\left(\frac{1}{\xi^2}\right) = \frac{1}{\xi^2}\frac{\mathrm{d}}{\mathrm{d}\xi}\left(\xi^2\frac{\mathrm{d}Z_1}{\mathrm{d}\xi}\right) + \frac{1}{\xi^2\sin\theta}\frac{\mathrm{d}}{\mathrm{d}\theta}\left(\sin\theta\frac{\mathrm{d}Z_1}{\mathrm{d}\theta}\right) \end{aligned} \tag{1.3.19}$$

Considering Eq. (1.3.19) is an inhomogenous linear differential equation with the inhomogenous term on the LHS which is related to $\cos\theta$, the particular solution should be in the form of $F(\xi)\cos\theta$ which gives

$$Z_1 = \underbrace{\left(A_0 + \frac{B_0}{\xi}\right) + \left(A_1\,\xi + \frac{B_1}{\xi^2}\right)\cos\theta}_{\textit{general solution}} + \underbrace{\left(\frac{1}{2} - \frac{3}{4\xi} - \frac{1}{8\xi^3}\right)\cos\theta}_{\textit{particular solution}} \tag{1.3.20}$$

where the first term of the general solution on the RHS of Eq. (1.3.20) is actually the general solution of Eq. (1.3.15) instead of Eq. (1.3.19). The reason to include $A_0 + B_0/\xi$ in the general solution of Eq. (1.3.19) is that $A_0 + B_0/\xi$ is sufficient to satisfy the Laplace's equation of Z_1.

Because of the boundary conditions Eq. (1.3.17c) and Eq. (1.3.17d), the constants in Eq. (1.3.20) are determined as

$$Z_1\Big|_{\xi=1} = (A_0 + B_0) + \left(A_1 + B_1 + \frac{1}{2} - \frac{3}{4} - \frac{1}{8}\right)\cos\theta = 0 \Rightarrow \begin{cases} A_0 + B_0 = 0 \\ A_1 + B_1 = \dfrac{3}{8} \end{cases} \tag{1.3.21}$$

$$\lim_{\xi\to\infty} Z_1 = A_1 = 0 \tag{1.3.22}$$

Thus, the temperature field of different domains ξ is obtained by Eq. (1.3.14) which is combined with the solution of Z_0 in Eq. (1.3.18) and Z_1 in Eq. (1.3.20).

$$Z = Z_0 + Z_1 = \frac{1}{\xi} + \mathrm{Pe}\left[B_0\left(\frac{1}{\xi} - 1\right) + \left(\frac{1}{2} - \frac{3}{4\xi} + \frac{3}{8\xi^2} - \frac{1}{8\xi^3}\right)\cos\theta\right] \tag{1.3.23}$$

At last, B_0 remains unknown in Eq. (1.3.23). In order to determine it, the diffusion problem of Z_0 in Eq. (1.3.15) needs to be re-considered, since Eq. (1.3.15) is only valid at $\xi \leq 1$. For $\xi \gg 1$ such as $\xi \to \infty$, the convective term in Eq. (1.3.12) can be no longer neglected in consideration of heat transfer. The conservation equation in Eq. (1.3.12) for Z_0 at $\xi \to \infty$ is more likely to be

$$\mathrm{Pe}\left(\cos\theta \frac{\partial Z_0}{\partial \xi} - \frac{\sin\theta}{\xi}\frac{\partial Z_0}{\partial \theta}\right) = \nabla^2 Z_0 \tag{1.3.24}$$

as

$$\lim_{\xi\to\infty} v_\xi = \lim_{\xi\to\infty}\left(1 - \frac{3}{2\xi} + \frac{1}{2\xi^3}\right)\cos\theta \approx \cos\theta$$

$$\lim_{\xi\to\infty} v_\theta = \lim_{\xi\to\infty} -\left(1 - \frac{3}{4\xi} + \frac{1}{4\xi^3}\right)\sin\theta \approx -\sin\theta$$

Although the domain of Eq. (1.3.24) is mainly considered in $\xi \gg 1$, consistency requires that the spherical symmetry in Eq. (1.3.15) remains in Eq. (1.3.24), which is with regards to variable ξ. As a result, a transformation form $\exp\left(Pe\xi\frac{\cos\theta}{2}\right)\Phi(Pe\xi)$ is introduced into Eq. (1.3.24) and gives the solution as

$$Z_0 = \frac{C}{\mathrm{Pe}\,\xi}\exp\left[\frac{\mathrm{Pe}\,\xi}{2}\left(\cos\theta - 1\right)\right] \approx \frac{C}{\mathrm{Pe}\,\xi} + \frac{C}{2}\left(\cos\theta - 1\right) \tag{1.3.25}$$

Again, due to consistency for the same temperature field, Eq. (1.3.25) should be equivalent to Eq. (1.3.23) at $\xi \to \infty$ as

$$\begin{aligned} Z\Big|_{\xi\to\infty} = Z_0 + \lim_{\xi\to\infty} Z_1 = & \frac{1}{\xi} + \frac{\mathrm{Pe}}{2}\left(\cos\theta - 2B_0\right) \\ & \Downarrow \qquad\quad \Downarrow \\ & \frac{C}{\mathrm{Pe}}\frac{1}{\xi} \qquad \frac{C}{2}\left(\cos\theta - 1\right) \end{aligned} \tag{1.3.26}$$

Based on Eq. (1.3.26), $C = \mathrm{Pe}$ and more importantly $B_0 = 1/2$, which results in the exact solution of temperature field as

$$Z = \frac{1}{\xi} + \mathrm{Pe}\left[\frac{1}{2}\left(\frac{1}{\xi} - 1\right) + \left(\frac{1}{2} - \frac{3}{4\xi} + \frac{3}{8\xi^2} - \frac{1}{8\xi^3}\right)\cos\theta\right] \tag{1.3.27}$$

The average Nusselt number $\overline{\mathrm{Nu}}$ due to temperature field in Eq. (1.3.27) can be obtained by using the definition of Nu in Eq. (1.3.10).

$$\overline{\mathrm{Nu}} = 2\xi\frac{h}{\kappa}\Big|_{\xi=1} = 2\xi\left.\frac{\frac{1}{\pi\xi}\frac{\partial}{\partial\xi}\int_0^\pi Z\,\mathrm{d}\theta}{Z_0 - Z_\infty}\right|_{\xi=1} = 2\left(1 + \frac{\mathrm{Pe}}{2}\right) = 2 + \mathrm{Re}\cdot\mathrm{Pr} \tag{1.3.28}$$

where *Preandtl number* Pr is characteristic with the property of the flow and the *Reynolds number*

Re is with the property of the fluid.

$$\mathrm{Re} = \frac{\text{inertial forces}}{\text{viscous forces}} = \frac{\rho_f w_f}{\mu}\delta \tag{1.3.29}$$

$$\mathrm{Pr} = \frac{\nu}{\alpha} = \frac{\frac{\mu}{\rho_f}}{\frac{\kappa}{c_f \rho_f}} = \frac{c_f \mu}{\kappa} \tag{1.3.30}$$

TURBULENCE FLOW

When a stream of higher velocity fluid is introduced on a spherical surface, a transition or turbulent flow might be developed as shown in Fig. 1.3.1(b). Unlike the constant laminar flow, the interrupted flow changes the separation line further to the rear of the sphere, reducing the size of the wake.

Although a set of dimensionless partial differential equations in the incompressible interrupted flow for the sphere can be described by

$$\begin{aligned}
&\text{Heat balance} && (\vec{v}\cdot\nabla)\,Z = \frac{1}{Re\,Pr}\nabla^2 Z \\
&\text{Navier-Stokes equation} && \vec{v}\cdot\nabla\vec{v} = \nabla p + \frac{1}{Re}\nabla^2\vec{v} \\
&\text{Equation of continuity} && \nabla\cdot\vec{v} = 0
\end{aligned} \tag{1.3.31}$$

a general analytical solution of Nu is impossible [11]. Therefore, various semi-empirical correlations related to a sphere immersed in an infinite media are established in the form [10, 11, 12, 13]

$$\overline{\mathrm{Nu}} = 2 + F\big(\mathrm{Re},\mathrm{Pr}\big) \tag{1.3.32}$$

which is Eq. (1.3.28) alike, but has different expressions in $F\big(\mathrm{Re},\mathrm{Pr}\big)$ due to the fluid chosen and the flow geometry as

$$\begin{aligned}
&\textit{Ranz and Marshall}\ [11] && \mathrm{Nu} = 2 + 0.6\,Re^{1/2}\,Pr^{1/3} \\
&\textit{Whitaker}\ [13] && \mathrm{Nu} = 2 + \left(0.4\,Re^{1/2} + 0.06\,Re^{2/3}\right) Pr^{0.4}\left(\frac{\mu_f}{\mu_s}\right)^{1/4}
\end{aligned}$$

In Eq. (1.3.32), the constant 2 in Eq. (1.3.11) represents the motionless term and $F\big(\mathrm{Re},\mathrm{Pr}\big)$ represents the fluid motion term, in which Re is used to predict the flow pattern such as low Re for the laminar flow and high Re for the turbulent flow. When $\mathrm{Re}\to 0$ in Eq. (1.3.32), $F\big(\mathrm{Re},\mathrm{Pr}\big)\to 0$ and $\overline{\mathrm{Nu}}\to 2$ again, indicating the theoretical minimum of the steady Nusselt number for a sphere in Eq. (1.3.11).

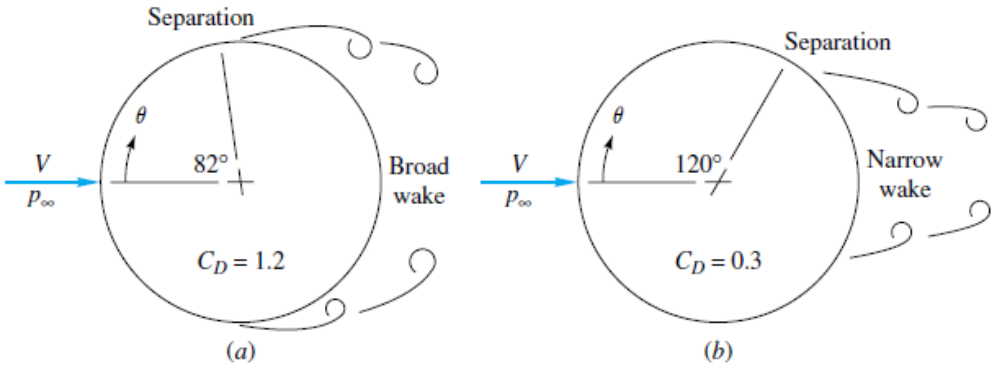

Figure 1.3.1: Schematic diagram of the transition flow from laminar with broad wake (flow separation ~ 80 °) at small *Re* (a) to turbulent flow with narrow wake (flow separation ~ 120 °) at large *Re* (b)[‖]

[‖]Available at https://i.stack.imgur.com/FKoR9.png

CHAPTER 2

LITERATURE REVIEW

2.1 AG-CU SYSTEM

In binary system, the equilibrium phases are present at a given temperature and composition when the phase transformations occur at a fixed pressure of 1atm. To find this equilibrium at the fix pressure, the change of Gibbs free energy is calculated with respect to temperature and composition.

At a given temperature T, the composition-dependent Gibbs free energy is given [1]

$$G = X_A G_A + X_B G_B + \underbrace{\Delta H_{mix} - T\Delta S_{mix}}_{\Delta G_{mix}} \tag{2.1.1}$$

where the mole fraction of atom A and B represented by X_A and X_B has the relation $X_A + X_B = 1$.

In regular solution of binary system, ΔH_{mix} and $-T\Delta S_{mix}$ in the change of Gibbs free energy due to the mixing ΔG_{mix} are displayed in Eq. (2.1.2a) and Eq. (2.1.2b).

$$\Delta H_{mix} = \Omega X_A X_B \tag{2.1.2a}$$

$$-T\Delta S_{mix} = RT\left(X_A \ln X_A + X_B \ln X_B\right) \tag{2.1.2b}$$

Both endothermic ($\Delta H_{mix} < 0$) and exothermic ($\Delta H_{mix} > 0$) solution of high and low temperature are shown in Fig. 2.1.1. At low T, the positive enthalpy of mixing ΔH_{mix} with small negative $-T\Delta S_{mix}$ develops a negative curvature of ΔG_{mix} in the middle. Combined with a baseline $X_A G_A + X_B G_B$, G in Eq. (2.1.1) can also show a similar curvature in Fig. 2.1.2, in which there is a stable region (a miscibility gap) for a mixing of two phases α_1 and α_2. For a larger ΔH_{mix}, the miscibility gap can extend into the liquid phase region and forms a eutectic phase diagram.

To define both stable and metastable equilibrium features of the eutectic Ag-Cu system, the central concern is located at the values ΔG_mix for the solid and the liquid in Eq. (2.1.1). In sub-regular

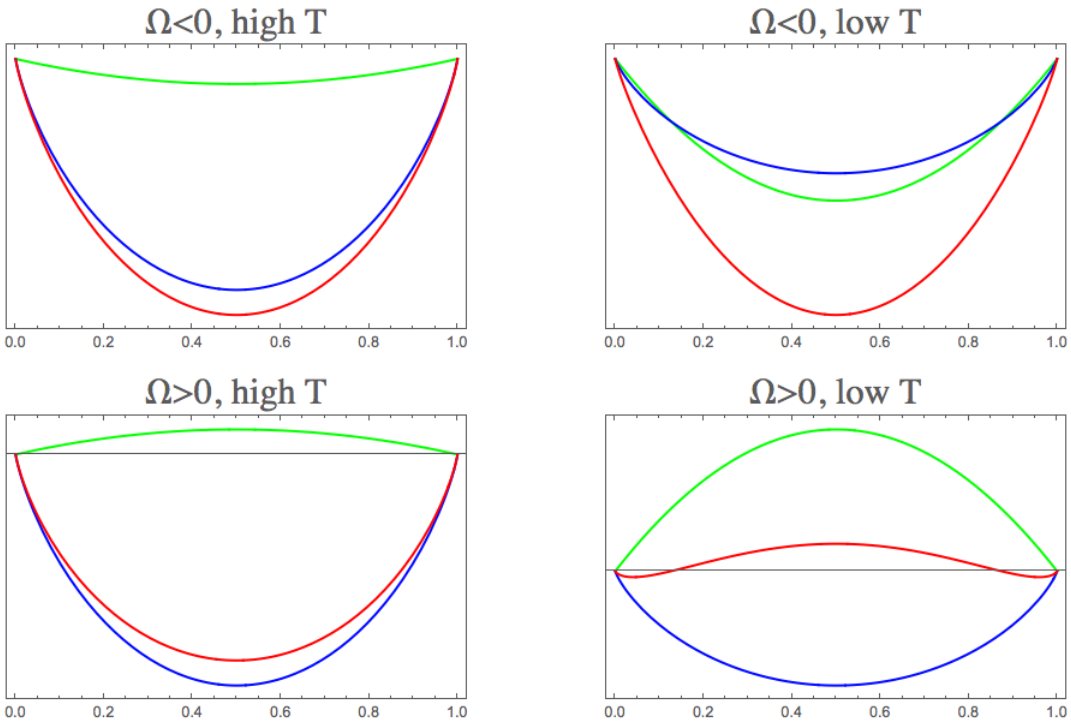

Figure 2.1.1: The effect of Ω and T on ΔH_{mix} (green solid line), $T\,\Delta S_{mix}$ (blue solid line) and ΔG_{mix} (red solid line)

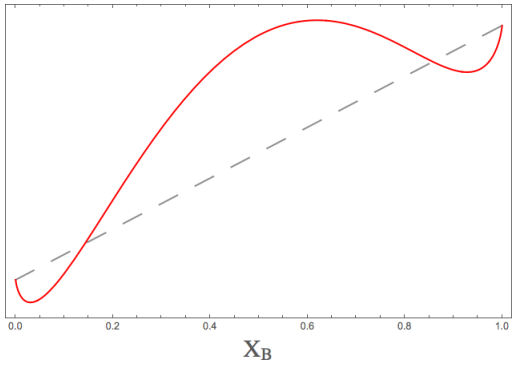

Figure 2.1.2: Molar free energy G in Eq. (2.1.1) at $\Delta H_{mix} > 0$ (red curve) with baseline for $X_A\,G_A + X_B\,G_B$

solution model [14], Eq. (2.1.1) is modified as

$$G = X_A\,G_A + X_B\,G_B + R\,T\left(X_A \ln X_A + X_B \ln X_B\right) + \underbrace{X_A\,X_B \sum_{i=0}^{n} \left(a_i + b_i\,T\right)\left(X_A - X_B\right)^i}_{\Delta G^{ex}} \tag{2.1.3}$$

where the interaction parameter between unlike components for Ag-Cu system is available in [15,

16] and Eq. (2.1.1) equals to Eq. (2.1.3) when only $i = 0$ is considered.

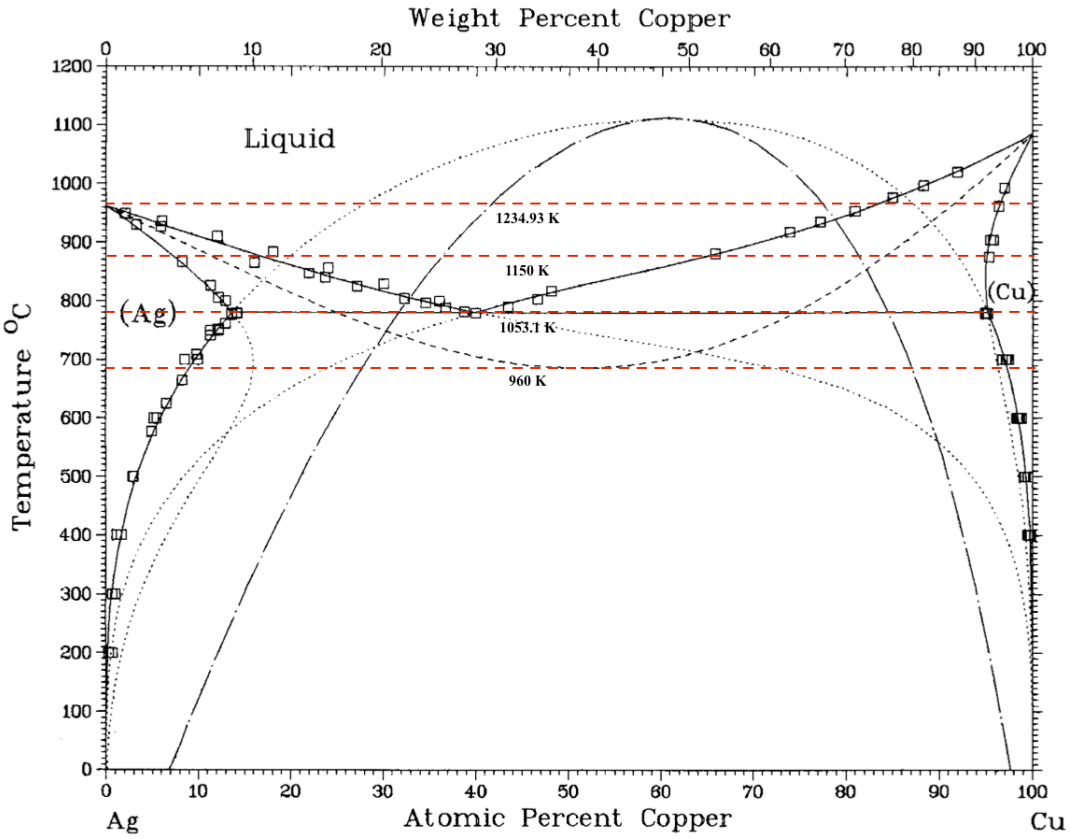

Figure 2.1.3: Calculated metastable equilibria in the Ag-Cu system [16] where the solid lines are the stable equilibria, the dotted lines are the metastable extension of the phase boundaries, and the dashed line is the T_0 curve

The most detail examination of binary Ag-Cu diagram according to Eq. (2.1.3) is performed by Murray [16] as

$$G_l = R\,T\left(X_{Ag}\ln X_{Ag} + X_{Cu}\ln X_{Cu}\right) + \left(15171 - 2.537T\right)X_{Ag}\,X_{Cu} + \left(-2425 + 0.946T\right)X_{Ag}\,X_{Cu}\left(X_{Ag} - X_{Cu}\right) \tag{2.1.4a}$$

$$G_s = \left(-11945 + 9.67T\right)X_{Ag} + \left(-13054 + 9.62T\right)X_{Cu} + R\,T\left(X_{Ag}\ln X_{Ag} + X_{Cu}\ln X_{Cu}\right) + \left(34532 - 9.178T\right)X_{Ag}\,X_{Cu} + \left(-5996 + 1.725T\right)X_{Ag}\,X_{Cu}\left(X_{Ag} - X_{Cu}\right) \tag{2.1.4b}$$

Although the reference in [16] yields rather poor agreement with the measured thermodynamic excess quantities, the optimized Gibbs energy function (Eq. (2.1.4a) and Eq. (2.1.4b)) consist of a least squrares (the *CALPHAD* approach) produces a Ag-Cu diagram with good agreement [17].

Fig. 2.1.3 shows the calculated stable and metastable equilibrium phase boundaries of Ag-Cu system by using Eq. (2.1.4a) and Eq. (2.1.4b). Four selected free energy curves for the liquid G_l (the red

solid line) and solid G_s (the blue solid line) corresponding to temperature 1234.93 K (Ag melting point), 1150 K, 1053.1 K (the eutectic temperature) and 960 K (the minimum T_0 at $X_{cu} \simeq 50\%$) in the Ag-Cu phase diagram Fig. 2.1.3 are also shown in Fig. 2.1.4.

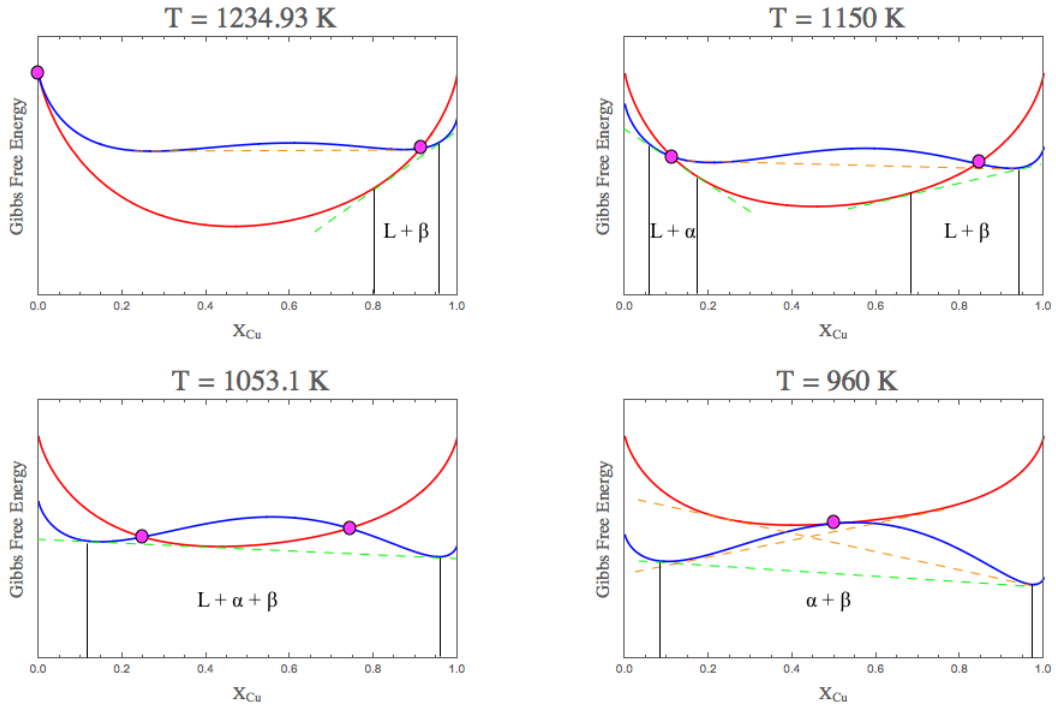

Figure 2.1.4: Gibbs free energy of Ag-Cu alloy system versus atomic concentration at the selected temperature

The equilibrium conditions can be reached when each component has the same chemical potential in the different phases (common tangent rule) as the green dashed line in Fig. 2.1.4 lying on the tangent of G_l and G_s curve at the equilibrium compositions. With the decrease of temperature in a Ag-Cu alloy, the phase changes from L, to $L+\beta$ at 1234.93 K, to $L+\alpha$ and $L+\beta$ at 1150 K, to $L+\alpha+\beta$ at eutectic temperature 1053.1 K, to $\alpha+\beta$. Combining with all those isothermal points of Gibbs free energy curves at the range of temperatures from 300 K to 1400 K, the equilibrium phase diagram can be plotted in the black solid line in Fig. 2.1.3.

2.1.1 Metastable Phase Diagram

In the area of rapid solidification, the metastable extensions of the solidus curves can be evaluated experimentally, such as thermal analysis, X-ray diffraction, TEM, etc. [18, 19]. However, the difficulty in the experimental determination gives way to the extrapolation of the free energy curves as the orange dashed line in Fig. 2.1.4. The metastable extensions of the phase boundaries are characterized by the common tangent construction of metastable solid miscibility gap above the

eutectic temperature 1053.1 K and of a metastable solid solution permitting a supersaturation of the alloying elements below 1053.1 K.

With the use of the X-ray analysis, Fredriksson et al [19] modify the excess free energy of the liquid of [16] and argue the melting temperature of the rapidly solidified Ag-Cu alloy might be neither constant nor near the equilibrium one.

2.1.2 T_0 CURVES

The T_0 curve is the locus of the compositions and temperatures where the free energies of two phases are equals as the pink points in Fig. 2.1.4. The entire T_0 line in Fig. 2.1.3 is extrapolated by a smooth curve extending through the eutectic point and either pure component melting point, in which the minimum T_0 is located at the order of 960 K at 50 at.%Cu and T_0 at the eutectic composition of Ag-Cu system lies just ~ 76 K below the eutectic point.

With the use of the T_0 curve between the liquid and a solid phase, the minimum undercooling of the liquid for the partitionless formation of the solid with the same composition is determined [16, 18, 20]. In the case of Ag-Cu system, T_0 curve provides the minimum undercooling for the formation of the metastable phase γ' [21]. Upon the cooling rate employed in Ag-Cu alloy, several other metastable phase sequences, such as $\alpha' + \beta'$ [22] and γ'' [23], are possible to be detected experimentally by either TEM or XRD evaluation.

Theoretically, Alloy Ag-Cu with slightly depressed T_0 curve system below the stable liquidus in Fig. 2.1.3 is unlikely to depress the solidification temperature towards the glass temperature [20]. By using vapour deposition technique, giving a high cooling rate of the order of ~ 10^{10} K/s, it is possible to obtain an amorphous phase in rapidly quenched alloys of Ag-40at.%Cu [24]. Nevertheless, the glass-forming ability of Ag-40at.%Cu is relative weaker than that of binary alloy with one or two intermetallic compounds, such as Ni-76at.%Zr [25].

2.2 CONTAINERLESS PROCESS

Metastable (non-equilibrium) states, such as metastable crystalline phases, supersaturated solid solutions, and etc, are attained for rapid solidified alloys, when a sufficiently large driving force accumulates at a substantial undercooling. Because of a certain activation energy preventing from a stable-state transformation in the subsequent cooling process (see Fig. 1.1.1), the state of an undercooled melt gives access to solidification into solid states far from equilibrium.

Containerless processing is a way to obtain a deeply undercooled melt, by which a complete avoidance of heterogeneous nucleation on container wall which otherwise dominates the solidification behaviour of a melt [26]. In experimental techniques of containerless processing, the control of nucleation catalysis preventing the establishment of equilibrium is based on two approaches, the one is by a chemical treatment and the other is by a physical separation.

The chemical encasement is to deactivate possible catalytic sites around the sample surface and gives rise to a deep undercooling even at slow cooling of bulk melt prior to nucleation. For example, a melt is embedded in an inactive glass flux, such as B_2O_3, to avoid contact with the container wall nor exposure to the atmosphere in melt fluxing technique [27, 7]. Increasing thermal cycles allows impurities, such as the remaining composition of oxides, to be removed from the sample and hence increasing the potential level of undercooling attainable [28]. In the study of Ag-Cu system by melt-fluxing technique, the highest undercooling is reported in the order of ~ 80 K after 30 thermal cycles [27] before the crucible broke. Although melt-fluxing processed samples are processed under high vacuum with assistance of high thermal cycles to eliminate potential impurities, the heterogeneous nucleation might still be operative for solidification of Ag-Cu alloy as more than one nucleus are found on the surface of sample [27, 7, 29].

The physical separation is to restrict the catalytic effects of active nucleants into a small fraction of the overall sample. By dispersing the liquid into a large number of small droplets within a suitable medium, for example, by drop-tube technique [30], nucleant isolation in droplets becomes possible. Each droplet in flight experiences a high order of cooling rate, giving way to promote high undercoolings by restricting its response time from nucleation.

Unlike the chemical encasement, detailed analysis of thermodynamics and kinetics of rapid solidification with respect to nucleation and crystal growth of alternative and competing phases is different or even impossible in the physical separation approach, since direct investigations of all processes are unable [26].

2.2.1 DROP-TUBE TECHNIQUE

Drop-tube experiments are of two kinds, the one is long drop-tubes (typically greater than 10 m in height) mainly in the study of micro-gravity (*in vacuo*) effect on solidification and only few associated with space research institutions, and the other is short drop-tubes (< 8 m as shown in

Fig. 5.1.2) widely used in the investigation of drop-tube processed materials [26, 31].

A long drop-tube processed single droplet with diameter 3 ~ 10 mm superheated by electromagnetic levitation and solidified at *in vacuo* environment during the free fall loses its heat by purely heat radiation in Eq. (1.3.3). Because of the fourth power of temperature T in Eq. (1.3.3), materials with higher melting point T_m, such as refractory metals and alloys, can be more efficient to cool down below a reduced undercooling $\Delta T / T_m$ of 0.2 in drop-tube of 50 long.

For materials with low entropies of fusion as Ag-Cu alloy, a greatly increased cooling rate by a back-filling inert gas enables short drop-tube to be used to study the effects of undercooling on solidification. Moreover, with the assistance of melt subdivision in a short drop-tube, a spray of fine droplets (having a range of diameters between 25μm and 2mm) isolates nucleants in a fraction of the droplets.

On the one hand, the inert gas introduced in those fine droplets largely increases their external heat extraction rate, at the cost of the detection of thermal emission due to recalescence. On the other hand, those high cooling rates ($10^3 \sim 10^6$K/s) employed on the droplets reduce temperature rise during recalescence, giving way to preserving the initially as-solidified microstructure down to the ambient temperature [32]. For this reason, studies of nucleation temperature or undercooling may emphasize the microstructural information of droplets. Considering there is no other difference of microstructural effect achieved in drop-tube processing from other high undercooling technique, direct comparison of microstructure of these techniques, such as melt fluxing or electromagnetic levitation, which permit measurement of undercooling, gives a good insight of the microstructural characterization of drop-tube processed droplets [31].

2.3 PHASE TRANSFORMATION IN AG-CU ALLOY

Binary Ag-Cu eutectic at equilibrium condition introduced in Section 1.2.2 has the cooperative growth of the same face-centred cubic crystal structure (FCC) in both the Cu-rich (α) and Ag-rich (β) phase. The coupled planar solid-liquid interface can hold stable even with the existence of temperature gradient (undercooling in Eq. (1.2.38)) ahead of it, as long as ϕ_r in Eq. (1.2.24) is less than zero.

Because both Ag and Cu are low entropy, non-faceted, and regular elements having isotropic growth characteristics at undercoolings, it is likely that the instability of both phase α and β is developed simultaneously, leading to the outbreak of either eutectic cells or eutectic dendrites from lamellar eutectic at intermediate undercoolings as shown in Fig. 2.3.1. At the eutectic composition of Ag-Cu system, the formation of a primary single dendrite is unlikely due to the symmetrical coupled zone as the eutectic dendrite would prevail at high undercoolings.

However, the difference of physical properties between Ag and Cu in Ag-Cu system, such as the entropy of Cu relatively greater than that of Ag, may arise the establishment of a slightly skewed zone towards phase β-Cu side as shown in Fig. 2.3.2. Either using Eq. (1.2.51) directly from the HJ model or applying K_c(Pe) in Eq. (2.3.17) from the TMK model into Eq. (1.2.51) is highly suggestive that $\Delta T \propto \sqrt{V}$ and higher ΔT gives higher growth rate V. When the growth rate or undercooling is sufficiently high, highly supersaturated single-phase dendrites can pass the coupled zone and so decouple the growth of two solid phases, during which one phase grows faster than the other. This skewed zone in the Ag-Cu phase diagram results in the primary single α-Ag dendrites at high undercoolings, also experimentally examined and found in [27, 7, 33]. If there would be any liquid in the post-recalescence, the lamellar interdendritic eutectic shall take place to finish the solidification.

2.3.1 $\Delta T = 0 \sim 60$ K

At low growth velocities, lamellar spacing λ is much smaller than the solute diffusion distance δ_c in Eq. (1.2.10), giving rise to the interface composition C_l^* with respect to the equilibrium eutectic composition C_e as shown in Eq. (1.2.32a) and Eq. (1.2.32b). Based on this assumption, JH model [5] establishes the first detailed analytical model for the growth of regular eutectics*, which has the relationship of the undercooling ΔT in Eq. (1.2.47) as

$$\Delta T = K_c \cdot V\lambda + K_r \cdot \frac{1}{\lambda}$$

Using the extremum condition in Eq. (1.2.48), simple relationships, which are of use for obtaining order of magnitude estimates from Eq. (1.2.47), are possible as Eq. (1.2.49), Eq. (1.2.50), and Eq. (1.2.51). In the experimental investigation of directionally solidified Ag-Cu eutectic [35], an

*The detail of HJ model is introduced in Section 1.2.2.

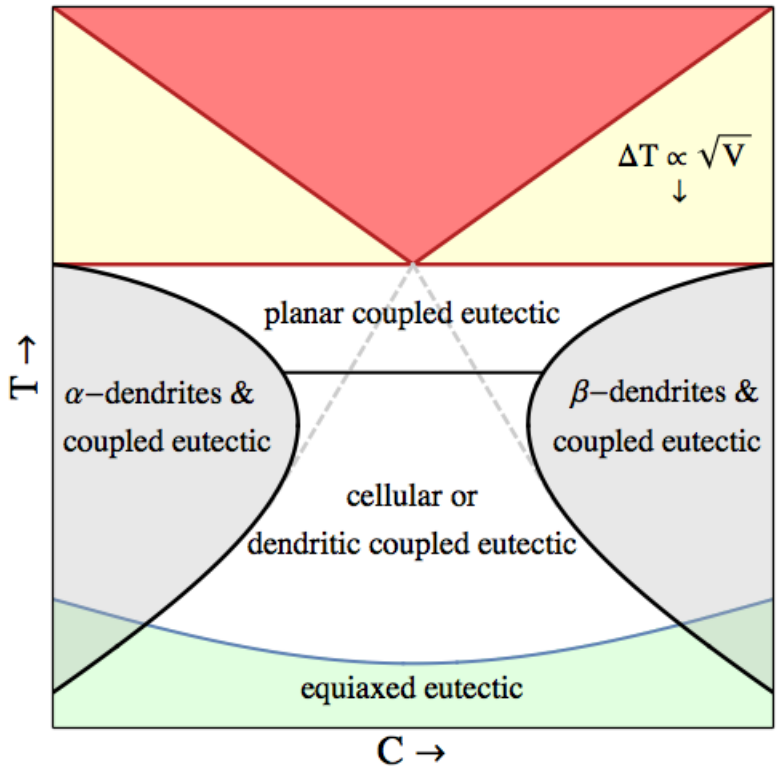

Figure 2.3.1: Sysmmetrical coupled zones of regular eutectic

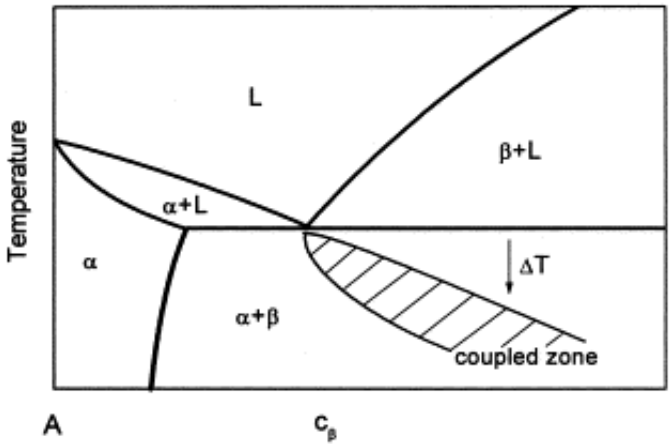

Figure 2.3.2: Skewed coupled zones of regular eutectic [34]

average lamellar spacing of ~ 95 nm for a growth rate upto 0.27 cm/s leads to

$$\lambda^2 V = \frac{K_r}{K_c} = 1.4 \times 10^{-17} \quad [\mathrm{m}^3/\mathrm{s}] \tag{2.3.1}$$

For the eutectic Ag-Cu alloy, Walder and Ryder [27] use the formula $4\sigma T_e/L_F$ to obtain

$$\lambda \Delta T = 2 K_r \simeq \frac{4\sigma T_e}{L_F} = 4.3 \times 10^{-7} \quad [\mathrm{Km}] \tag{2.3.2}$$

Combining with Eq. (2.3.1) and Eq. (2.3.2), $K_r = 2.15 \times 10^{-7}$ and $K_c = 1.5357 \times 10^{10}$ and thus

$$\frac{\Delta T^2}{V} = 4 K_r K_c = 13207.1 \quad [\mathrm{K^2\,s/m}] \tag{2.3.3}$$

The parabolic relation between V and ΔT in Eq. (2.3.3) is only favourable to the near-equilibrium condition, since the liquid diffusion coefficient D_l^e in Eq. (1.2.47) is commonly assumed to be temperature dependent, e.g. 10^{-9} $\mathrm{m^2/s}$ at the eutectic temperature of Ag-Cu alloy.

Boettinger *et al.* [36] use the temperature-dependent diffusion coefficient

$$D_l(T) = 2.4 \times 10^{-7} \exp\left(-\frac{48886.3}{\mathrm{R}\,T}\right) \quad [\mathrm{m^2/s}] \tag{2.3.4}$$

to make the calculated growth velocities of Ag-Cu eutectic well agree with the observed one under the electron beam solidification. Wang *et al.* [37] also apply the temperature-dependent diffusion coefficient in JH model to predict the drop-tube processed microstructure. Since $K_c \propto 1/D$ in Eq. (1.2.47), the modification of Eq. (2.3.3) can be simply obtained as

$$\frac{\Delta T^2}{V} = 4 K_r \left(\frac{D_l^e}{D_l}\right) \cdot K_c = 55.0298 \exp\left(\frac{48886.3}{\mathrm{R}\,T}\right) \quad [\mathrm{K^2\,s/m}] \tag{2.3.5}$$

where R is the gas constant = 8.314 $\mathrm{J/mol \cdot K}$.

Further relaxing the JH assumption of $\lambda \ll \delta_c$, Trivedi, Magnin and Kurz [38] (TMK) extend JH model to the rapid solidification process, in which the metastable extensions of solidus and liquidus lines outward to the metastable region (see dashed lines in Fig. 2.1.3) are considered in the calculation. Because the theoretical *cigar-shape* model is less meaningful to the Ag-Cu solidification on high velocity eutectic growth [38], the review of TMK model mainly concerns with the second model which the distribution coefficient k is an arbitrary constant, but $k_\alpha = k_\beta$ is assumed.

Under steady-state directional solidification conditions, the solute field in liquid governed by

$$\frac{\partial^2 C}{\partial y^2} + \frac{\partial^2 C}{\partial z^2} + \frac{V}{D}\frac{\partial C}{\partial z} = 0 \tag{2.3.6}$$

has a general solution in Eq. (1.2.25) as

$$C(y,z) = C_e + B_1 \exp\left(-\frac{V}{D}z\right) + B_2 \exp(-b\,z) \cos\left(\frac{2\pi y}{\lambda}\right) \tag{2.3.7}$$

where

$$b = \frac{V}{2D} + \sqrt{\left(\frac{V}{2D}\right)^2 + \left(\frac{2\pi}{\lambda}\right)^2} \tag{2.3.8}$$

The flux boundary condition in Eq. (1.2.32a) and Eq. (1.2.32b) which assumes the interface composition in the liquid close to the original eutectic one $C_l^* \approx C_e$ is no longer valid. Two flux conditions

for the eutectic phases α and β established by the method of weighted residuals, which are equivalent to Eq. (1.2.33) and Eq. (1.2.34) are

$$\text{lamellar } \alpha\text{:} \quad \int_0^{\frac{\lambda}{2}f} V\left(k-1\right)C_l^* \ \mathrm{d}y = \int_0^{\frac{\lambda}{2}f} D\left(\frac{\partial C}{\partial z}\right)_{z=0} \mathrm{d}y \tag{2.3.9a}$$

$$\text{lamellar } \beta\text{:} \quad \int_{\frac{\lambda}{2}f}^{\frac{\lambda}{2}} V\left(1-k\right)\left(1-C_l^*\right) \ \mathrm{d}y = \int_{\frac{\lambda}{2}f}^{\frac{\lambda}{2}} D\left(\frac{\partial C}{\partial z}\right)_{z=0} \mathrm{d}y \tag{2.3.9b}$$

where

$$C_l^* = C(y,0) = C_e + B_1 + \cos\left(\frac{2\pi y}{\lambda}\right) B_2 \tag{2.3.10}$$

$$\left(\frac{\partial C}{\partial z}\right)_{z=0} = -\frac{V}{D} B_1 - b\cos\left(\frac{2\pi y}{\lambda}\right) B_2 \tag{2.3.11}$$

The constans B_1 and B_2 can be determined by Eq. (2.3.9a) and Eq. (2.3.9b) as

$$B_1 = \frac{1-k}{k}\left(f\,C_e - (1-f)\,(1-C_e)\right) \tag{2.3.12}$$

$$B_2 = \mathrm{Pe}\,\frac{f\,(1-f)\,(1-k)\left(\dfrac{2\pi}{\mathrm{Pe}}\right)}{\sin(f\,\pi)\left(\sqrt{1+\left(\dfrac{2\pi}{\mathrm{Pe}}\right)^2}+2\,k-1\right)} \tag{2.3.13}$$

where the Péclet number $\mathrm{Pe} = V\,\lambda/2D$.

The average concentration differences ahead of phase α and β are expressed respectively

$$\overline{\Delta C_\alpha} = \frac{2}{f\,\lambda}\int_0^{\frac{\lambda}{2}f} C_l^* - C_e \ \mathrm{d}y = \frac{2}{f\,\lambda}\int_0^{\frac{\lambda}{2}f} B_1 + \cos\left(\frac{2\pi y}{\lambda} B_2\right) \mathrm{d}y = B_1 + B_2\,\frac{\sin(f\,\pi)}{f\,\pi} \tag{2.3.14a}$$

$$\overline{\Delta C_\beta} = \frac{2}{(1-f)\,\lambda}\int_{\frac{\lambda}{2}f}^{\frac{\lambda}{2}} C_l^* - C_e \ \mathrm{d}y = \frac{2}{(1-f)\,\lambda}\int_{\frac{\lambda}{2}f}^{\frac{\lambda}{2}} B_1 + \cos\left(\frac{2\pi y}{\lambda} B_2\right) \mathrm{d}y = B_1 - B_2\,\frac{\sin(f\,\pi)}{(1-f)\,\pi} \tag{2.3.14b}$$

According to Eq. (1.2.38), the contributions to the overall undercooling for eutectic growth as ΔT_c in Eq. (1.2.39) and ΔT_r in Eq. (1.2.40) are

$$\Delta T_\alpha = |m_\alpha|\cdot\overline{\Delta C_\alpha} + \Gamma_\alpha K_\alpha = |m_\alpha|\left(B_1 + B_2\,\frac{\sin(f\,\pi)}{f\,\pi}\right) + \Gamma_\alpha K_\alpha \tag{2.3.15a}$$

$$\Delta T_\beta = -|m_\beta|\cdot\overline{\Delta C_\beta} + \Gamma_\beta K_\beta = -|m_\beta|\left(B_1 - B_2\,\frac{\sin(f\,\pi)}{(1-f)\,\pi}\right) + \Gamma_\beta K_\beta \tag{2.3.15b}$$

where K_α and K_β are shown in Eq. (1.2.38).

Although the rapid solidification results in high growth velocity at the liquid/solid interface, the planar interface of eutectic growth shall remain the relation of $\Delta T = \Delta T_\alpha = \Delta T_\beta =$ constant.

$$|m_\beta|\,\Delta T_\alpha + |m_\alpha|\,\Delta T_\beta = \left(|m_\alpha| + |m_\beta|\right)\Delta T \ \Rightarrow\ \Delta T = \frac{|m_\beta|\,\Delta T_\alpha + |m_\alpha|\,\Delta T_\beta}{|m_\alpha| + |m_\beta|} \tag{2.3.16}$$

Inserting ΔT_α in Eq. (2.3.15a) and ΔT_β in Eq. (2.3.15b) into Eq. (2.3.16) gives

$$\Delta T = \underbrace{\frac{|m_\alpha||m_\beta|}{|m_\alpha|+|m_\beta|}\left(\frac{\frac{2\pi}{\mathrm{Pe}}}{\sqrt{1+\left(\frac{2\pi}{\mathrm{Pe}}\right)^2}+2k-1}\,\frac{1-k}{2D\pi}\right)}_{K_c(\mathrm{Pe})} \cdot V\lambda + \underbrace{\frac{2(1-f)|m_\beta|\Gamma_\alpha\sin(\theta_\alpha)+2f|m_\alpha|\Gamma_\beta\sin(\theta_\beta)}{f(1-f)\left(|m_\alpha|+|m_\beta|\right)}}_{K_r}\cdot\frac{1}{\lambda} \tag{2.3.17}$$

where K_c is no longer constant as Eq. (1.2.47) in JH mode, but is Péclet number dependent.

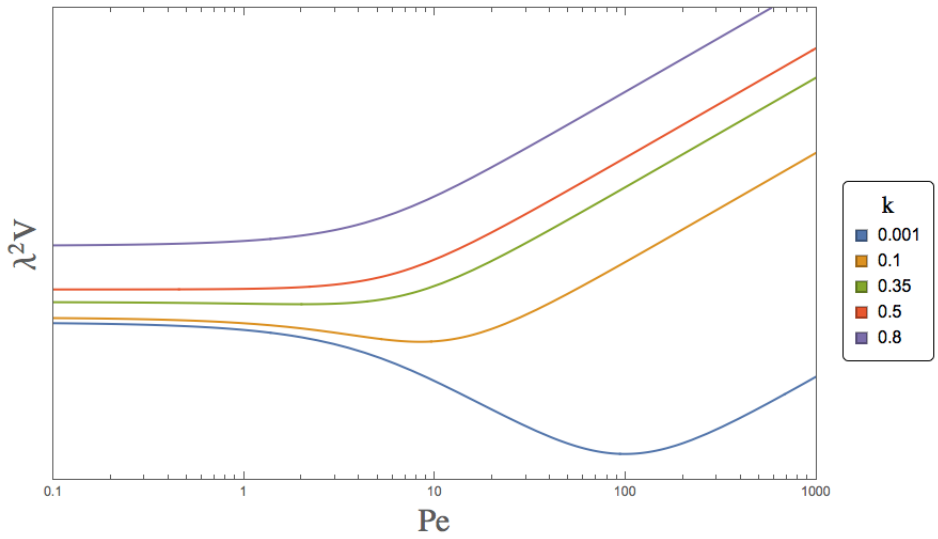

Figure 2.3.3: $\lambda^2 V$ of various equilibrium distribution coefficients deviate from the constant after $\mathrm{Pe} > 1$

Applying $K_c(\mathrm{Pe})$ and K_r from Eq. (2.3.17) into Eq. (1.2.49) gives the relation of $\lambda^2 V$ and Pe in Eq. (2.3.18), in which the value of $\lambda^2 V$ deviates from the constant at large Pe.

$$\lambda^2 V = \frac{(1-f)|m_\beta|\Gamma_\alpha\sin(\theta_\alpha)+f|m_\alpha|\Gamma_\beta\sin(\theta_\beta)}{|m_\alpha||m_\beta|}\,\frac{4\pi}{f(1-f)}\cdot\left(\frac{-1+2k+\sqrt{1+\left(\frac{2\pi}{\mathrm{Pe}}\right)^2}}{\frac{2\pi}{\mathrm{Pe}}}\right)D \tag{2.3.18}$$

Similiarly, the expression of $\lambda\Delta T$ and $\Delta T^2/V$ can also be obtained by substituting K_c and K_r in Eq. (1.2.50) and Eq. (1.2.51) respectively. Fig. 2.3.4 gives an extensive evidence to show the value of the distribution coefficient k affects undercooling ΔT greatly at the same Pe greater than 1. Trivedi [3, 38] suggests that the deep undercooling in eutectic growth in Fig. 2.3.4 gives rise to a glass transition temperature in which two-phase eutectic would be replaced by a single low-k amorphous phase.

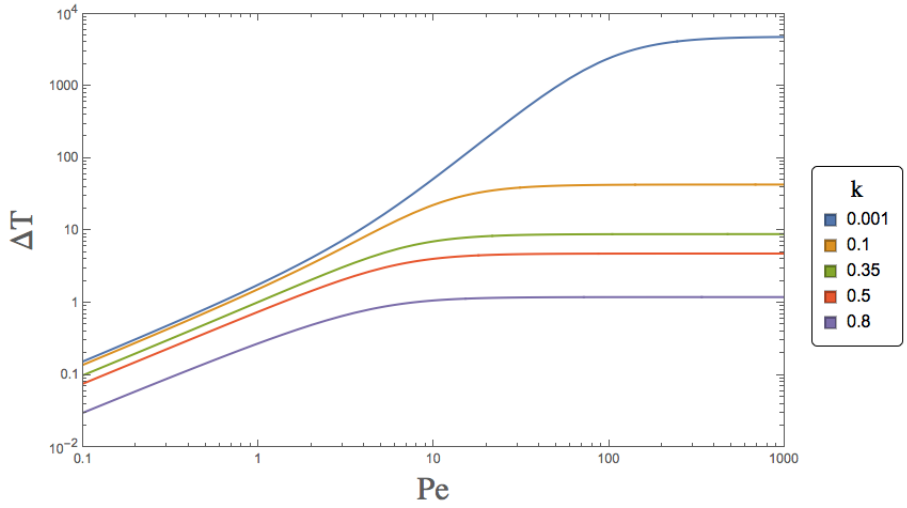

Figure 2.3.4: Interface undercooling ΔT with various distribution coefficients k between 0.001 and 0.8 change differently after Pe > 1

Because of k, the nature of the metastable phase diagram strongly influences the eutectic growth. For Ag-Cu alloys, the amorphous phase due to narrow T_0 curve in Fig. 2.1.3 is unlikely in rapid solidification, but metastable states [36, 39], as an extension of the rather limited solid solubilities observed at equilibrium, and a range of equilibrium and non-equilibrium microstructures, including eutectic [27, 36, 40], dendritic [27, 29], banded [36] and anomalous structures [7, 37, 41, 42], are achieved. At low undercoolings, a mixture of eutectic and anomalous microstructures developed from a single nucleation point, forming radially to zones of microstructure, in which the lamellar eutectic takes the form of cells with anomalous eutectic at the cell boundaries [7, 41, 42].

The similar morphology consisting with anomalous and lamellar eutectic is also observed in drop-tube processed samples [37, 43]. In many cases, a transition from regular lamellar to anomalous eutectic structure is progressive with the volume fraction of anomalous eutectic increasing as the level of undercooling rises. Wang *et al.* [37] suggests the anomalous eutectic is the product of rapid solidification, since the lamellar eutectic preferentially grows from the anomalous eutectic in an epitaxial and radiant way. Clopet *at al.* [7, 41] argue the mechanism of anomalous eutectic at intermediate undercooling (< 60 K) gives rise to remelting of eutectic dendrites in analysis of the brightness-time characteristics of spot regions within the continuous and spasmodic growth zones. In spite of this, the primary eutectic lamellar yielded during recalescence can be disintegrated into anomalous eutectic in the subsequent solidification at high undercoolings, owning to their being supersaturated with solute [44].

The direct observation and measurement of drop-tube formed particles is experimentally impossible, which gives rise to the difficulty to establish the relationship between lamellar spacing and undercooling as well as the relationship between undercooling and cooling rate. Therefore, the theoretical calculations based on JH [5] and TMK [38] eutectic growth model are of practical use to

understand the characteristic of eutectic growth of drop-tube processed Ag-Cu eutectic droplets, *i.e.* [37], and the heat transfer model originally related to gas atomisation [4, 45] is also applied in [43] to understand the thermal behaviour of metallic droplet cooling during the free falling though the tube.

In [37], neither the detailed physical parameters nor the equations applied in theoretical calculations are provided. But it is possible to estimate the relation between eutectic growth velocity V and undercooling ΔT by inserting the physical parameters available in [42] into Eq. (1.2.51) for HJ model, or into Eq. (1.2.51) with Eq. (2.3.4) for HJ model with temperature-dependent diffusion coefficient $D_l(T)$, or into Eq. (1.2.51) with K_c(Pe) and K_r obtained in Eq. (2.3.17) for TMK model. The calculated result of the relation is illustrated in Fig. 2.3.5.

HJ model is known to well predict the lamellar eutectic growth near the equilibrium, whereas TMK model is more capable of eutectic growth during rapid solidification. The deviation of the $\Delta T - V$ relationship appearing at the order of 10 K, which is close to the lower undercooling that the anomalous eutectic is observed in [7], indicates the formation of rapidly solidified eutectic. The dramatic rise of growth velocity V at $\Delta T \simeq 15$ K can be reckoned as the outbreak of dendrites or other non-space filling morphologies. In the case of Ag-Cu alloy, the two-phase (eutectic) cells or dendrites is believed to be responsible for this sudden increase of V in Fig. 2.3.5.

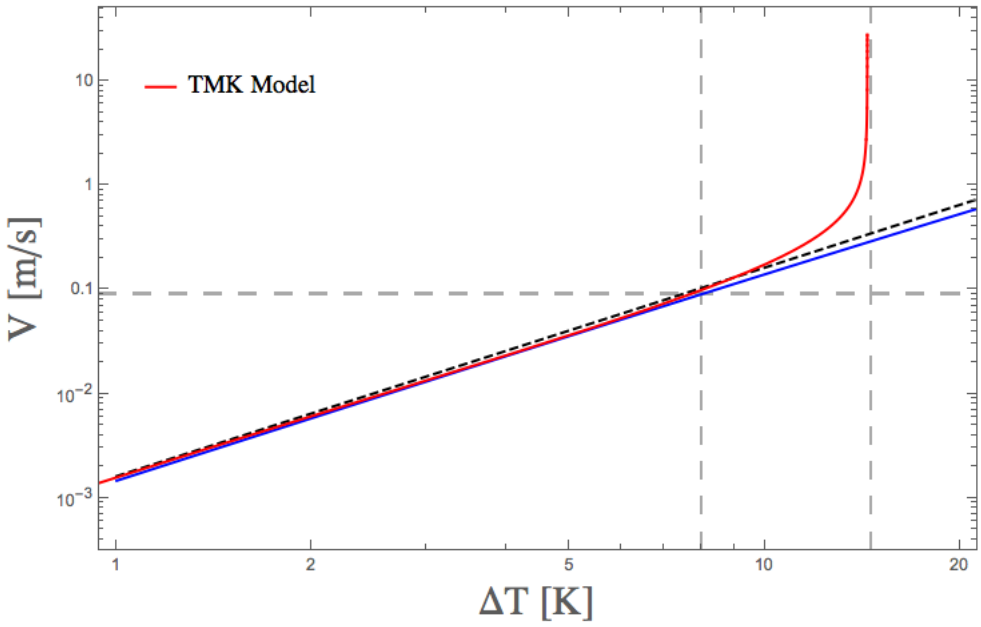

Figure 2.3.5: Eutectic growth velocity versus undercooling of Ag-40at.%Cu alloy, where the dashed black line, the solid blue line and the solid red line represent the result of JH model, JH model with diffusion coefficient $D_l(T)$ in Eq. (2.3.4), and TMK model respectively

The drop-tube formed production of a fine spray of free falling droplets is believed to receive a

sufficient cooling velocity to freeze the partially or fully formed anomalous microstructure into ambient temperature [31]. The cooling rate at the range of 10^3 and 10^6 K/s is reported in [43] by using a simple heat transfer model, similar to the one introduced in Section 3.1. The *Ranz and Marshall* correlation [11] used in the heat extraction past a small sphere [43], however, might overestimate *Nusselt number* and the cooling rate, which will be proved in Section 2.4. Moreover, neither the temperature gradient inside droplet nor the heat transfer circumstance at the wake of flow (see Fig. 1.3.1) is concerned in this calculation.

2.3.2 $\Delta T > 60$ K

At higher undercoolings, the morphology of lamellar eutectic mixed with anomalous eutectic could be dramatically modified into that of lamellar eutectic coupled with single-phase dendrites. The critical undercooling of the morphological change in Ag-40at.%Cu alloy is reported as occurring at 70 K [7, 46], 75 K [27], 76 K [47]. These critical undercoolings are believed to indicate the formation of the supersaturation solid solution, phase γ' in the case of Ag-Cu system, since they are close to the calculated T_0 temperature in Fig. 2.1.3.

Under non-equilibrium conditions, four contributions to the total undercooling ΔT at growth interface are concerned in the classic theory of dendritic growth [3]

$$\Delta T = \Delta T_c + \Delta T_r + \Delta T_t + \Delta T_k \tag{2.3.19}$$

where the undercooling due to solute diffusion ΔT_c, due to curvature ΔT_r, due to heat flow ΔT_t, and due to kinetics ΔT_k.

As introduced in Section 1.2.3, the assumption of a single dendrite tip being an isolated needle in solidification, can be of use in the estimation of radius of curvature, supersaturations, undercoolings. Since the kinetics of metals is negligible (see Section 1.2.1) and the positive temperature gradient of directional solidification has little impact on S/L interface, only the first two undercoolings ($\Delta T_c + \Delta T_r$) in Eq. (2.3.19) are considered in the theoretical model presented in [48].

The simple version of the model can be understood by using a mathematical perturbation interface introduced in Eq. (1.2.13) (see Fig. 1.2.3) and assuming the temperature at tips of the interface T_t is at $y = 3\lambda/4$ and the temperature at depressions of the interface T_d is at $y = \lambda/4$, that is

$$T_t^* = T_f + m\,C_{l,t}^* - \Gamma\,K_t^* \tag{2.3.20a}$$

$$T_d^* = T_f + m\,C_{l,d}^* - \Gamma\,K_d^* \tag{2.3.20b}$$

The total undercooling due to Eq. (2.3.20a) and Eq. (2.3.20b) is

$$\Delta T = T_t^* - T_d^* = \underbrace{m\left(C_{l,t}^* - C_{l,d}^*\right)}_{\Delta T_c} - \underbrace{\Gamma\left(K_t^* - K_d^*\right)}_{\Delta T_r} \tag{2.3.21}$$

where the liquid composition at tips of the interface $C^*_{l,t}$ and at depressions of the interface $C^*_{l,d}$ can be obtained by Eq. (1.2.20) at $z=0$ and $\lambda\to\infty$,

$$C(0,y)\Big|_{\lambda\to\infty}=\frac{C_0}{k}+\varepsilon\sin\left(\frac{2\pi}{\lambda}y\right)\left.\frac{k\,V\,G_c}{(1-k)\,V-D\left(\frac{V}{2D}+\sqrt{\left(\frac{V}{2D}\right)^2+\omega^2}\right)}\right|_{\lambda\to\infty}\approx\frac{C_0}{k}-G_c\,\varepsilon\sin\left(\frac{2\pi}{\lambda}y\right) \tag{2.3.22}$$

Because the concentration of the interface perturbation describes $C^*_{l,t}$ at $y=3\lambda/4$ and $C^*_{l,d}$ at $y=\lambda/4$ in Eq. (2.3.22),

$$C^*_{l,t}-C^*_{l,d}=C\left(0,\frac{3\lambda}{4}\right)-C\left(0,\frac{\lambda}{4}\right)=\left(\frac{C_0}{k}+\varepsilon\,G_c\right)-\left(\frac{C_0}{k}-\varepsilon\,G_c\right)=2\,\varepsilon\,G_c \tag{2.3.23}$$

Due to $\lambda\to\infty$ giving the first derivative of Eq. (1.2.13), $z'\propto\cos(2\pi\,y/\lambda)\to 0$,

$$K=\frac{z''}{\left(1+z'^2\right)^{3/2}}\approx z''=-\frac{4\pi^2}{\lambda^2}\,\varepsilon\sin\left(\frac{2\pi}{\lambda}y\right)$$

$$K^*_t-K^*_d=-\frac{4\pi^2}{\lambda^2}\,\varepsilon\sin\left(\frac{2\pi}{\lambda}\frac{3\lambda}{4}\right)+\frac{4\pi^2}{\lambda^2}\,\varepsilon\sin\left(\frac{2\pi}{\lambda}\frac{\lambda}{4}\right)=\frac{8\pi^2}{\lambda^2}\,\varepsilon \tag{2.3.24}$$

The temperature difference between the tips and depressions can be found by using the heat conduction in Eq. (1.3.1) as

$$-\frac{\mathrm{d}T}{\mathrm{d}z}=\frac{T^*_t-T^*_d}{\varepsilon\sin\left(\frac{2\pi}{\lambda}\frac{3\lambda}{4}\right)-\varepsilon\sin\left(\frac{2\pi}{\lambda}\frac{\lambda}{4}\right)}=\frac{T^*_t-T^*_d}{-2\,\varepsilon}=-G\Rightarrow T^*_t-T^*_d=2\,\varepsilon\,G \tag{2.3.25}$$

Inserting Eq. (2.3.23), Eq. (2.3.24) and Eq. (2.3.25) into Eq. (2.3.21) gives

$$2\,\varepsilon\,G=2\,m\,\varepsilon\,G_c-\Gamma\frac{8\pi^2}{\lambda^2}\,\varepsilon\Rightarrow G=m\,G_c-\left(\frac{2\pi}{\lambda}\right)^2\Gamma\Rightarrow\lambda=2\pi\left(\frac{\Gamma}{m\,G_c-G}\right)^{1/2} \tag{2.3.26}$$

where the interface concentration gradient in liquid G_c is considered the steady-state one introduced in Eq. (1.2.12),

$$G_c=-\Delta C_0\,\frac{V}{D}=-C^*_l\,\underbrace{(1-k)}_{p}\,\frac{V}{D}=-C^*_l\,p\,\frac{V}{D} \tag{2.3.27}$$

The only unknown variable in Eq. (2.3.26) is C^*_l in Eq. (2.3.27), which shall refer the definition of the supersaturation Ω in Eq. (1.2.56) and $\Omega=\mathrm{I}(P_c)$,

$$C^*_l=\frac{C_0}{1-\Omega\,(1-k)}=C_0\,\underbrace{\frac{1}{1-p\,\mathrm{I}(P_c)}}_{\mathrm{A}(P_c)} \tag{2.3.28}$$

Langer and Müller-Krumbhaar [49] proved that dendrite tips R do grow closely to the minimum wavelength of the perturbation interface as Eq. (2.3.26) shown. Thus, combining with Eq. (2.3.26),

Eq. (2.3.27) and Eq. (2.3.28), and also with the definition of solute Pelect number $P_c = R\,V/2\,D$,

$$R = \frac{2\,D\,P_c}{V} = \lambda = 2\pi \left(\frac{\Gamma}{-m\,C_0\,\mathrm{A}(P_c)\,p\,\dfrac{V}{D} - G} \right)^{1/2} \Rightarrow \underbrace{\left(\Gamma\,\frac{\pi^2}{P_c^2\,D^2} \right)}_{A'} V^2 + \underbrace{\left(m\,C_0\,p\,\frac{\mathrm{A}(P_c)}{D} \right)}_{B'} V + G = 0 \tag{2.3.29}$$

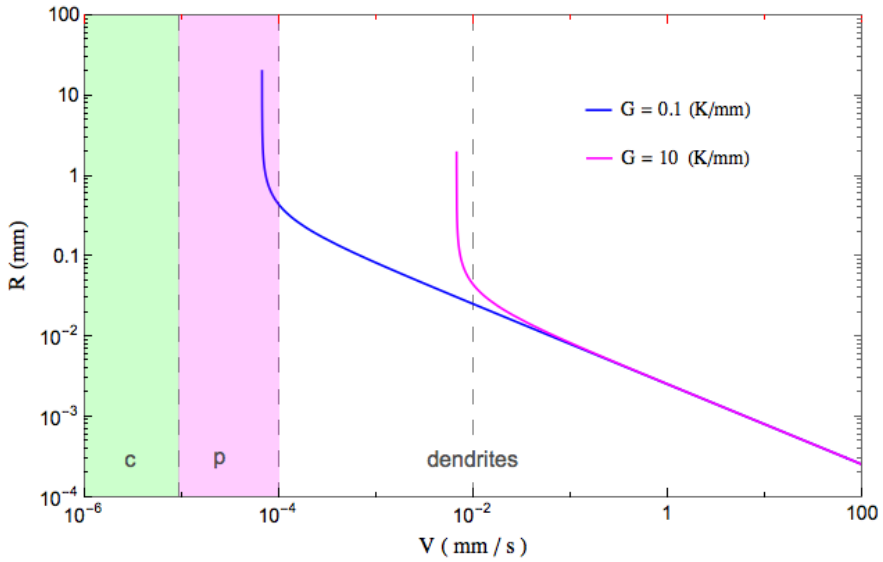

Figure 2.3.6: Tip radius R as a function of growth velocity V at directional growth of S/L interface

By using Eq. (2.3.29) with pre-setting the imposed temperature gradient G, such as 0, 0.1 and 10 K/mm, the approximated relationship of either tip radius R, or liquid concentration C_l^*, or tip temperature T^* as a function of the growth rate V in directional growth for low P_c is shown in Fig. 2.3.6, Fig. 2.3.7 and Fig. 2.3.8 respectively. Because of these relationships, the morphology change from planar (p), to cellular (c) and to dendrites for either a given tip radius or a given liquid concentration or a given tip temperature T^* with respect to a given growth rate becomes possible.

More importantly, the planar front is dominant to the S/L interface again at high growth rates, leading to an homogeneous solidification with the composition C_0, as shown in Fig. 2.3.7 and Fig. 2.3.8. And also the imposed temperature gradient G can be safely neglected at high growth rates, since the divergence between Eq. (2.3.29) with $G = 0$ and Eq. (2.3.29) with $G = 10$ K/mm at high growth rates reduces down to the order of 10^{-7} or even less.

To obtain the approximated relationship of the morphology change as a function of growth rate for high P_c, ΔT_c is no longer equal to $m\,G_c$ applied in Eq. (2.3.26). The solute stability parameter ξ_c in Eq. (2.3.30) [48] is necessary in consideration of solute-dependent undercooling as $\Delta T_c = m\,G_c\,\xi_c$, by which a reasonable agreement of determining the morphological transition between

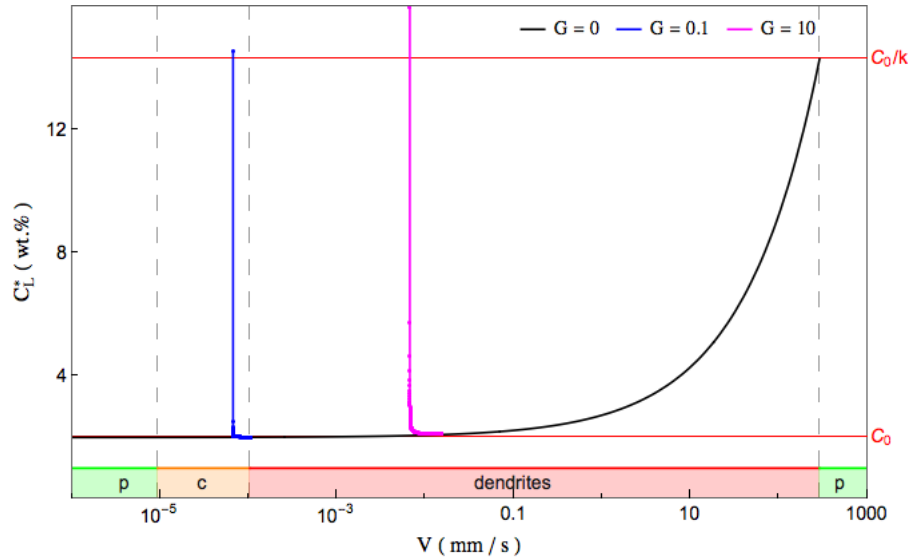

Figure 2.3.7: Liquid concentration C_l^* as a function of growth velocity V at directional growth

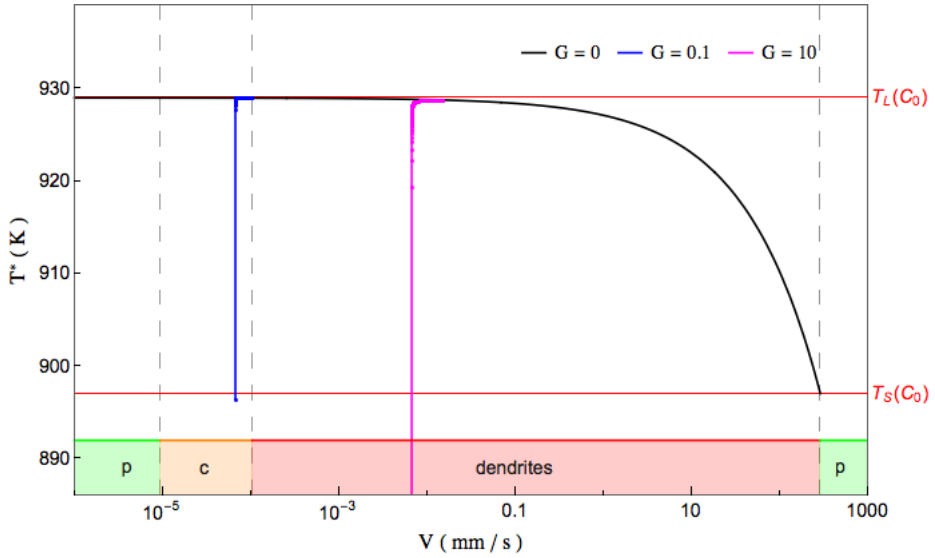

Figure 2.3.8: Temperature of S/L interface T^* as a function of the growth velocity V in directional growth

this theoretical model and the experimental data of Ag-Cu system from [36].

$$\xi_c = 1 - \frac{2k}{\sqrt{1+\left(\frac{4\pi D}{\lambda V}\right)^2} - 1 + 2k} = 1 - \frac{2k}{\sqrt{1+\left(\frac{2\pi}{P_c}\right)^2} - 1 + 2k} \tag{2.3.30}$$

In fact, the solute stability parameter ξ_c is necessary in calculation of ΔT_c at both low and high P_c. When P_c is small, ξ_c in Eq. (2.3.30) can be approximated to unity and leads to $\Delta T_c \approx m G_c$.

Later, Lipton, Kurz, and Trivedi (LKT) [50] extend the theory in [48] to further investigate the microsegregation-free structure in rapid solidification, in which four contributions to ΔT in Eq. (2.3.19), that are due to solute diffusion ΔT_c, due to curvature ΔT_r, due to heat flow ΔT_t, and due to kinetics ΔT_k respectively, are all taken in consideration in Eq. (2.3.31).

$$\Delta T_t = \mathrm{I}(P_t) \qquad \Delta T_r = \frac{2}{\overline{R}} \qquad \Delta T_k = \frac{\overline{V}}{\overline{\mu_0}} \qquad \Delta T_c = \frac{\left(1-k_0\right)\mathrm{I}(P_c)}{1-\left(1-k_0\right)\mathrm{I}(P_c)}\,\overline{C_0} \tag{2.3.31}$$

where the dimensionless variable

$$\overline{V} = \underbrace{\left(\frac{\Gamma\, c_p}{\Delta H_f}\right)}_{d_0}\frac{V}{2\,\alpha_l} \qquad \overline{R} = \underbrace{\left(\frac{\Delta H_f}{\Gamma\, c_p}\right)}_{1/d_0} R \qquad \Delta\overline{T} = \frac{c_p}{\Delta H_f}\,\Delta T \tag{2.3.32}$$

$$P_t = \frac{V\,R}{2\,\alpha_l} = \overline{V}\,\overline{R} \qquad P_c = \frac{V\,R}{2\,D_l} = \underbrace{\left(\frac{\alpha_l}{D_l}\right)}_{\eta} P_t \tag{2.3.33}$$

$$\overline{\mu_0} = \frac{\Gamma}{2\,\alpha_l}\,\mu_0 = \frac{\Gamma}{2\,\alpha_l}\left(\frac{V_0\,\Delta H_f\,M}{R_g\,T_m^2}\right) \qquad \overline{C_0} = C_0\,|m|\,\frac{c_p}{\Delta H_f} \tag{2.3.34}$$

To determine dendrite growth velocity V explicitly in a given undercooling in Eq. (2.3.19), the marginal stability criterion [3] is extended to large Péclet number in the LKT theory, giving

$$\overline{V}\,\overline{R}^2 = P_t\,\overline{R} = \frac{1}{\sigma^*\,\xi_t + 2\sigma^*\eta\,\xi_c\left(\dfrac{(1-k_0)}{1-(1-k_0)\,\mathrm{I}(P_c)}\right)} \tag{2.3.35}$$

where $\sigma^* = 1/4\pi^2$ and

$$\xi_t = 1 - \frac{1}{\sqrt{1+\dfrac{1}{\sigma^*\,P_t^2}}} \tag{2.3.36a}$$

$$\xi_c = 1 + \frac{2\,k_0}{1-2\,k_0\sqrt{1+\dfrac{1}{\sigma^*\,P_c^2}}} \tag{2.3.36b}$$

When Eq. (2.3.19) is applied in the undercooling of pure element, the equilibrium partition coefficient k_0 is equal to 1, leading to no undercooling due to solute diffusion as $\Delta T_c = 0$ and $\mathrm{Pe_t}\,\overline{R} = 1/\sigma^*\,\xi_t$ at marginal stability in Eq. (2.3.35). Combining with Eq. (2.3.19) and Eq. (2.3.35), the relationship of $\Delta\overline{T}$ and $\overline{V}$ of pure Ag and Cu at $k_0 = 1$, and Ag-87.5at.%Cu at $k_0 = 0.25$ [29, 38] are shown as the blue line, the red line and the pink line respectively in Fig. 2.3.9.

Considering the partition coefficient k_0 is dependent on the growth rate as suggested by [51], LKT model is further extended in [52] by replacing k_0 with

$$k(\overline{V}) = \frac{k_0 + 2\eta\epsilon\,\overline{V}}{1+2\eta\epsilon\,\overline{V}} \tag{2.3.37}$$

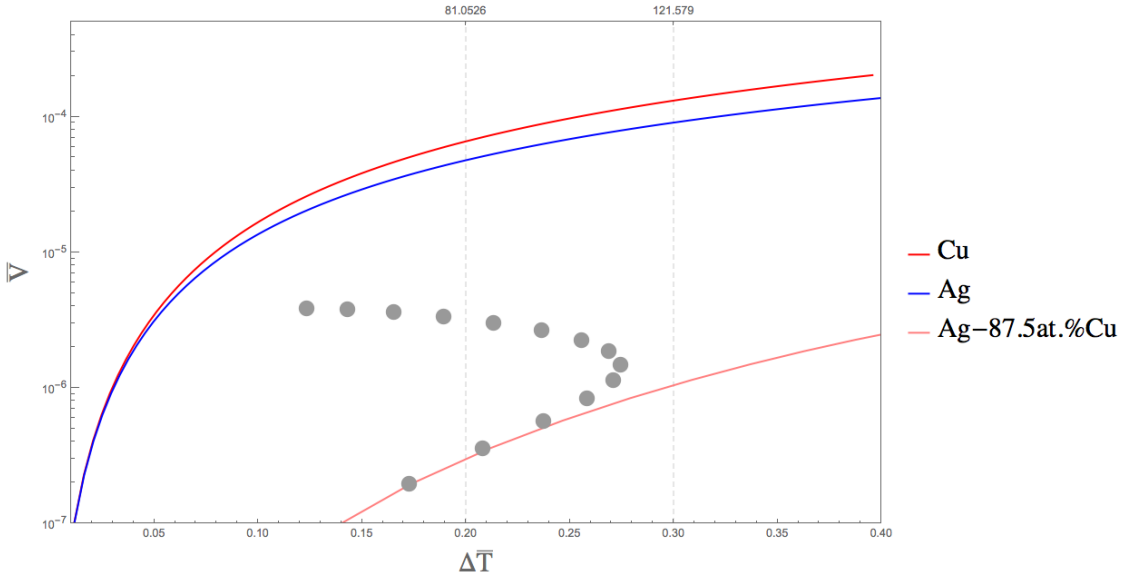

Figure 2.3.9: Theoretically calculated results of dimensionless growth rate $\overline{V}$ with respect to dimensionless undercooling $\Delta\overline{T}$, where $\Delta\overline{T} = 0.2$ and 0.3 correspond to the order of dimensional undercooling 81 and 121 K

where $\epsilon = a_0/d_0$ and the characteristic length a_0 of Ag-87.5at.%Cu equals to 0.6 nm [29].

By using the dependence of the partition coefficient on the growth rate as Eq. (2.3.37) into Eq. (2.3.35), a dramatic change of $\overline{V}$ with respect to $\Delta\overline{T}$ can be obtained as the grey points in Fig. 2.3.9. With the increase of $\overline{V}$ in Eq. (2.3.37), it is likely that $k(\overline{V})$ transfers from the original partition coefficient k_0 to ~ 1 (when $2\eta\epsilon\overline{V} \gg k_0$). This transition of $k(\overline{V})$ gives way to little or no partitioning of the components, since the growth process initiates from the constant k_0 dendrite growth by both solute and heat diffusion, and eventually approaches to the dendrite growth of pure element by only heat conduction in Fig. 2.3.9.

The relevant relationships of $\overline{V}$ with respect to k and $\Delta\overline{T}$ with respect to k are both shown in Fig. 2.3.10. When $\overline{V}$ increases upto a certain large quantity, the value of $2\eta\epsilon\overline{V}$ is dominant in Eq. (2.3.37), giving rise to ~ 1 as the blue line suggested in Fig. 2.3.10. Although the undercooling range between 81 and 121 in Fig. 2.3.9 is in agreement with the critical undercooling related to T_0, resulting in the growth of the supersaturated solid solution, γ', in undercooled Ag-Cu alloy, Walder *et al* [27, 29] fail to detect the lattice parameters of γ' by x-ray diffraction. They believe that the temperature of the dendrite tip must fall below the T_0 temperature in order that metastable γ' may grow, but the following crystallization rises up the temperature of undercooled liquid which makes metastable γ' impossible to retain. Other studies [53, 54] also demonstrate that metastable γ' cannot be remained at room temperature following rapid liquid quenching without a transformation reaction resulting in a partial decomposition. Moreover, the calculated $\Delta\overline{T}$ with regards to $k(\overline{V})$ shown in Fig. 2.3.10 agrees with those experimental investigation of metastable γ' since the $\Delta\overline{T}$

cannot hold the high extent (no less than 0.2) with the increment of k after 0.52.

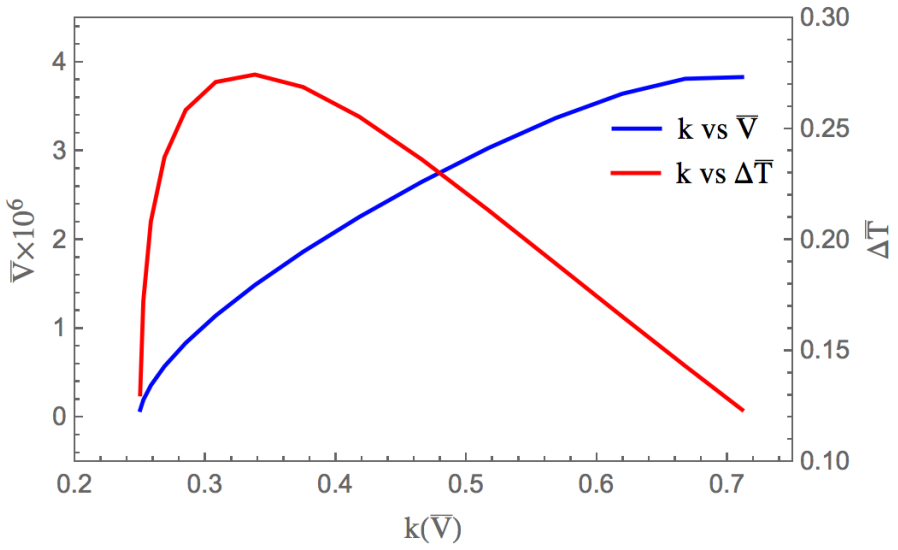

Figure 2.3.10: Calculated result of $\Delta\overline{T}$ with regards to $k(\overline{V})$ (red line) and $\overline{V}$ with regards to $k(\overline{V})$ (blue line) corresponding to Fig. 2.3.9

Besides Ag-87.5at.%Cu, metastable γ' can be produced in a wide range of compositions of Ag-Cu system under optimum cooling condition [55]. Walder *et al* [29] also investigate a range of compositions of undercooled Ag-Cu alloy and find that the critical undercooling (metastable γ') is impossible to attain within the composition range 45 ~ 66 at.%Cu due to the temperature of heterogeneous nucleation higher than the T_0 temperature. In other word, the heterogeneous nucleation prevails before achieving the critical undercooling (metastable γ') in this range of compositions.

2.4 HEAT TRANSFER PAST A SMALL SPHERE

To simplify the complexity of heat transfer past a sphere during its free falling, the cooling rate of a sphere surrounding a flow is often obtained based on the quasi-steady approach [11, 10, 56], by which the *Nusselt number* Nu is assumed to be independent of time and thus equal to the steady-state value at a fixed sphere and at time-averaged hydrodynamical conditions.

Due to this assumption, the minimum value of Nu at the steady-state heat transfer can only be reduced by 2 as proved in Eq. (1.3.11), thereby various semi-empirical correlations for the force-convective heat transfer include the motionless term Nu = 2 such as Eq. (1.3.32). The qualitative imagination on this kind of heat transfer can be referred from Fig. 2.4.1 as the temperature profile (red) at time τ becomes the one (green) at $\tau+\Delta\tau$ when the heat source (sphere) is suddenly turned off. However, such an efficient transfer is unlikely to take place in the realistic cooling process. So the real temperature distribution can be safely replaced with the blue one at $\tau+\Delta\tau$, the propagation of which is coincident with that at τ along the radial direction due to the thermal disturbance. As a result, the region filled in the blue color in Fig. 2.4.1 is the reason that the heat transfer through the fluid is less efficient than that at the quasi-steady situation, resulting in the time-dependent $\mathrm{Nu}(\tau) < 2$.

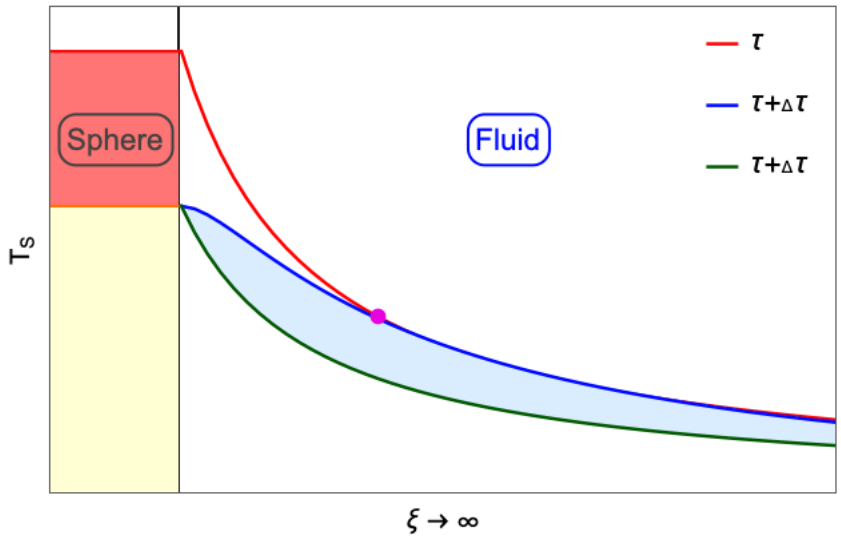

Figure 2.4.1: Schematic diagram of quasi-steady thermal distribution from the surface of hot sphere to the cold fluid at time τ (red) and $(\tau+\Delta\tau)$ (green), and the actual distribution at $(\tau+\Delta\tau)$ (blue)

Another method to prove the possibility of $\mathrm{Nu}(\tau) < 2$ is given by Konopliv and Sparrow [56] who presented an analytical solution for unsteady heat transfer of a highly conductive sphere at Pe = 0,

$$Z(r,\tau) = \frac{2\gamma}{\pi r}\int_0^\infty \xi \exp(-\xi^2\tau)\frac{\xi\cos[(1-r)\xi] - (1-\gamma\xi^2)\sin[(1-r)\xi]}{\left(1-\gamma\xi^2\right)^2+\xi^2}\,\mathrm{d}\xi \tag{2.4.1}$$

where $\gamma = 1/3\,(c\,\rho)_{fs}$ and the ratio of volume heat capacity of the fluid to that of sphere represents $(c\,\rho)_{fs}$.

According to Eq. (3.2.15), the instantaneous *Nusselt number* is obtained by

$$\mathrm{Nu}_\theta = -\frac{2}{Z_s}\left(\frac{\partial Z}{\partial \xi}\right)_{\xi=1}$$

In comparison with the calculated *Nusselt number* with selected $(c\,\rho)_{fs}$ from 0.1 to 10 by using Eq. (2.4.1) with Eq. (3.2.15), the well-known dimensionless expression of *Nusselt number* with respect to dimensionless time τ in Eq. (2.4.2) [57] is used and all results are generated in Fig. 2.4.2.

$$\mathrm{Nu} = 2\left(1 + \frac{1}{\sqrt{\pi\tau}}\right) \tag{2.4.2}$$

Except for the profile using Eq. (2.4.2), the classical minimal value of Nu = 2 which is proved in Eq. (1.3.11) (motionless flow), Eq. (1.3.10) (laminar flow), and Eq. (1.3.32) (turbulence flow) under the steady-state heat transfer is no longer valid in Fig. 2.4.2. In addition, the higher the ratio $(c\,\rho)_{fs}$ is, the quicker the *Nusselt number* drops with the increment of dimensionless time τ.

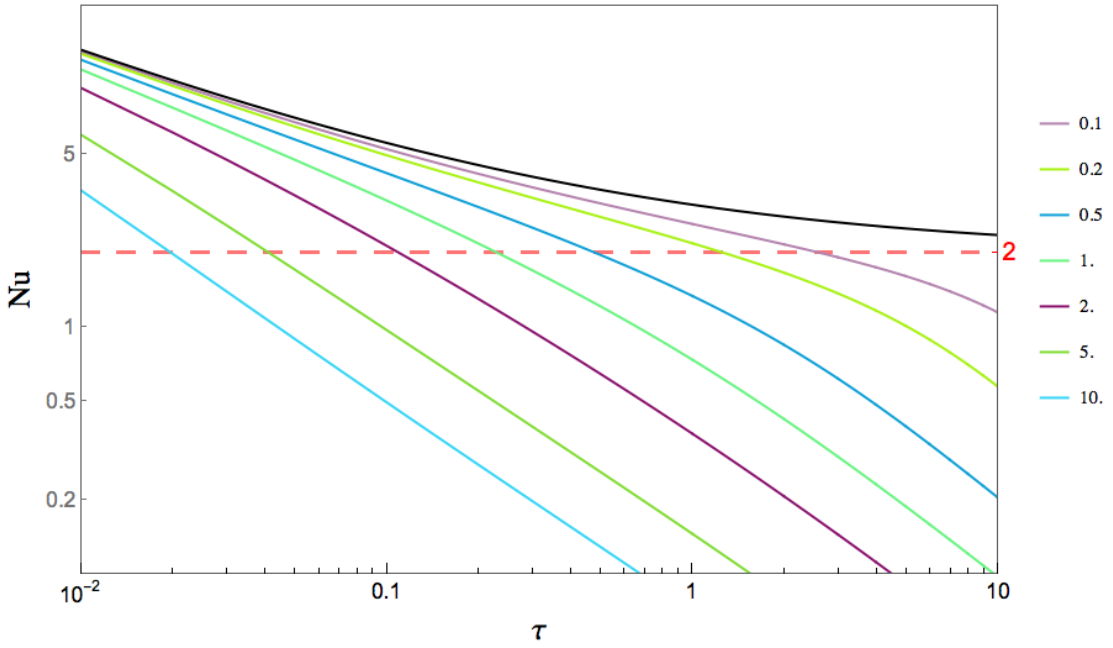

Figure 2.4.2: Time-variation of the instantaneous *Nusselt number* by using Eq. (2.4.1) and Eq. (3.2.15) when a sphere with different ratios of volume heat capacity to that of the fluid is introduced into stagnant fluid

To explain the variation of Nu below 2 in Fig. 2.4.2, considering there would be a physical situation that the heating source of sphere is suddenly turned off and the temperature of static fluid remains unchanged in a sufficiently long period, e.g. $\xi = \infty$ at time τ, the quasi-steady thermal profile at τ

and $\tau + \Delta\tau$ can be attained by Eq. (1.3.8)

$$T(r) = \delta \frac{T_s - T_f}{r} + T_f$$

as shown by the red line and the green line respectively in Fig. 2.4.1. The minimum Nu of sphere in motionless flow which is characteristic with 2 in Eq. (1.3.11) is assumed that the heat transfer in fluid takes place at an infinite quasi-steady state at each time step $\Delta\tau$.

Based on this, a sphere under laminar or even turbulence flow experiences more coefficient force-convective heat transfer surrounding its surface, leading to Nu greater than 2 as the semi-empirical correlations (Eq. (1.3.32)) sum up the minimum value 2 and the additional function with respect to *Reynolds number* and *Preandtl number* together. Provided the sphere is suddenly introduced in the moving flow at τ, then the thermal profile at $\tau + \Delta\tau$ should be within the green region in Fig. 2.4.1.

However, the minimum value of Nu is argued in [10] since the changed sphere temperature penetrates into the static fluid by the radial direction $\Delta\xi \simeq \sqrt{(\alpha_f \Delta\tau)}$ during the time interval $\Delta\tau$. Depending on the thermal diffusivity of fluid α_f, the thermal distribution at $\tau + \Delta\tau$ is more likely to perform as the blue line in Fig. 2.4.1 by using Eq. (C.2.11), which is coincident with the thermal distribution at τ at some point (magenta node). According to the definition of Nu in Section 1.3.2, the value of Nu is affected by the efficiency of heat transfer through a fluid and consequently the cooling rate from an object. Thus, by comparing the quasi-steady distribution (green line) with the more realistic one (blue line), the less coefficient force-convective heat transfer might results in Nu less than 2, which results in lower cooling rate of a sphere in flight.

As introduced in Section 1.3.2, Nu = 2 in Eq. (1.3.11) is the limiting condition for a sphere in still fluid ($v = 0$), of which the velocity boundary layer should be identical with the schematic diagram in Fig. 2.4.3 (left). When the sphere is in flight, the fluid motion should enhance heat transfer and consequently increase Nu greater than 2, giving rise to 2 as the base value in both Eq. (1.3.28) for laminar flow and Eq. (1.3.32) for turbulence flow past through a single sphere. If there would be a case of Nu < 2 by using the unsteady heat transfer formula in Eq. (2.4.1) (see Fig. 2.4.2), the direction of fluid velocity v at the wall is more likely to be the same as that of sphere flight, rather than opposite to that of sphere flight, as shown in the velocity boundary layer (orange) in Fig. 2.4.3 (right). Brauer [58] firstly found that the direction of mass transfer in some cases was reversed in the vicinity of the rear stagnation point when he presented numerical results for the unsteady mass transfer problem from a spherical particle in creeping flow. Later, Abramzon [10] examined transient heat transfer problems for a sphere suddenly inserted in a uniform velocity field numerically and found that the asymptotic Nu appears to be considerably less than the corresponding steady-state values or even 2 for the case of constant sphere temperature. The reason of this divergence might be attributed to negative local Nu in the vicinity of the rear stagnation point of the sphere, which is believed that a major portion of the heat transferred from the leading part of the sphere is returned to the rear part as the schematic diagram shown in Fig. 2.4.3 (right).

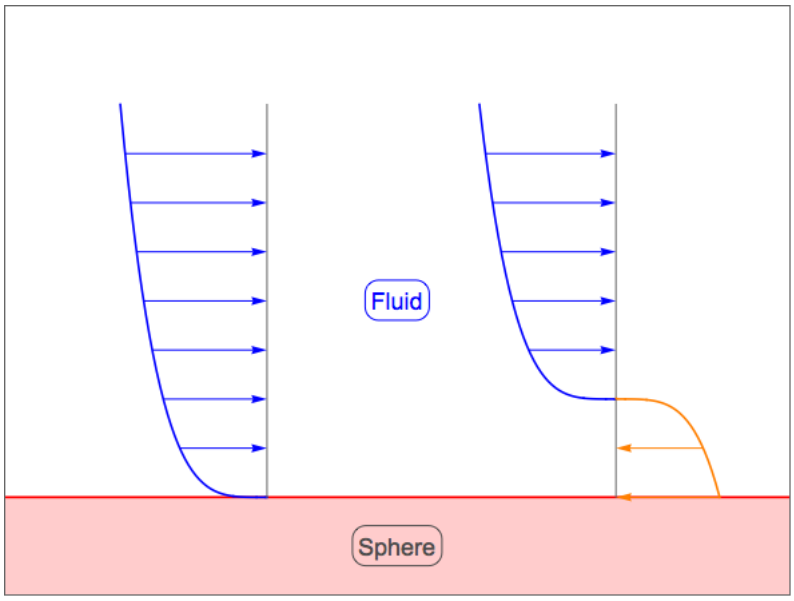

Figure 2.4.3: Force convection under different velocity boundary layers, where the fluid layer on the left has zero velocity at the wall (no-slip condition) and the fluid layer on the right has negative velocity at the wall.

Because the local Nu varies considerably from 0 to 180 ° in polar angle of spherical coordinates and makes the sphere in flow experience the rate of heat transfer differently [10, 58], the assumption that the temperature field inside the sphere remains spatially uniform at any instant of time due to the high thermal conductance of metallic particles is unlikely to be valid.

The experimental investigation of this fact by using a gas-filled drop tube or a close-coupled gas atomizer is impossible, mainly because the direct and accurate measurement of the solidification temperature is impossible [26, 31]. In order to understand the thermal behaviour of spherical droplet, i.e. the cooling rate, the solution is generally on the basis of theoretical models [4, 45] or by examination of various as-solidified microstructures [40, 42, 59, 60].

Mullis [59] estimates cooling rates of various gas-atomized particles by using secondary dendrite arm spacing measurement. Because these secondary arms appear as a sinusoidal perturbation of the paraboloid, grow perpendicularly to the primary trunk, and then ripen into coarser, less branched, and more widely-spaced arms, the secondary spacing λ_2 is believed to be proportional to the solidification time t_f, that is $\lambda_2 \propto t_f$ [3]. Since the cooling rate $\dot{T}$ is reversely proportional to t_f, the relationship of the secondary arm spacing λ_2 and $\dot{T}$ thus can be expressed as [61]

$$\lambda_2 = A\left(\frac{1}{\dot{T}}\right)^n \tag{2.4.3}$$

where both A and n are material-dependent constant, due to the different driving forces for the ripening process. The unknown $\dot{T}$ in Eq. (2.4.3) can then be easily obtained by using λ_2 that is measured from the SE imaging, by which $\dot{T}$ is towards the low end of cooling rate that is made

directly on the basis of theoretical model as[†]

$$\underbrace{\frac{\mathrm{d}T}{\mathrm{d}t}}_{\dot{T}}\left[c_l\,(1-f_s)+c_s\,f_s-L\,\frac{\mathrm{d}f_s}{\mathrm{d}T}\right]=\frac{6\,h}{\rho\,d}\big(T-T_g\big)+\frac{6\,\varepsilon\,\sigma}{\rho\,d}\big(T^4-T_R^4\big) \tag{2.4.4}$$

where the heat transfer coefficient h is with respect to Nu in Eq. (1.3.4) and Nu [11] is

$$\mathrm{Nu}=2.0+0.6\left(\frac{\rho_g\,d}{\mu}\,|v-v_g|\right)^{1/2}\left(\frac{c_g\,\mu}{\kappa_g}\right)^{1/3} \tag{2.4.5}$$

The central argument in [59] is related to the definition of gas temperature T_g and T_R in Eq. (2.4.4). In most of numerical rate models [4, 43, 45], T_g is often assumed as being close to T_R, which is unlikely to be correct. Moreover, the biggest uncertainties by using Eq. (2.4.5) is attributed to the relative velocity between the particle and the gas $|v-v_g|$ that is often calculated by Newton's second law and the decay axial gas velocity [62]. Since the secondary dendrite arm spacing gives some indication of the local solidification condition and also be helpful when cooling curves are unavailable, the cooling rate $\mathrm{d}T/\,\mathrm{d}t=\dot{T}$ in Eq. (2.4.4) can be safely replaced by the results obtained from Eq. (2.4.3). To simplify the difficulty of this calculation arising from the external heat source term, $L\cdot\,\mathrm{d}f_s/\,\mathrm{d}t$, the solid fraction f_s is linear with temperature between the liquidus temperature T_l and the solidus temperature T_s. By this approach, the relative velocity to match the measured cooling rate by Eq. (2.4.3) as a function of particle diameter can be obtained as shown in Fig. 2.4.4. The relatively flat profile of the differential velocity $|v-v_g|$ with respect to particle diameter in Fig. 2.4.4 might suggest the particles do co-move with more likely the much higher gas temperature than the ambient one surrounding particles of a wide range of diameters, which could also explain the reason of the low end of estimated cooling rates by using Eq. (2.4.3).

Although this 1D theoretical model is impossible to consider the variation of local Nu around the spherical surface, the fact of higher gas temperature around particles of all diameters can highly indicate that the application of semi-empirical correlation of Nu in Eq. (2.4.5) might only provide an overestimated rate of the heat transfer for spherical materials in flight, which is in agreement with $\mathrm{Nu}<2$ as shown in Fig. 2.4.2.

Later, Mullis, and *et al.* [63] investigate the density distribution of different phases in an as-solidified $150\sim212\ \mu$m droplets through electron backscatter images. The distinct grey-scale values due to density variation of each phase in these images make the *ImageJ* contour plotting plug-in possible to extract information on the location of the different phases within the particle, by which the amount of phase composition is exposed as a function of dimensionless radial coordinate r/R_0 from the surface at 1 to the origin at 0 in Fig. 2.4.5 (red for high ΔT particle and blue for low ΔT particle). Because the relationship of the thickness of one phase β layer Δ and the time τ in the

[†]The theoretical explanation of 2.4.4 shall refer from Eq. (3.1.1) to Eq. (3.1.6) in Section 3.1.1

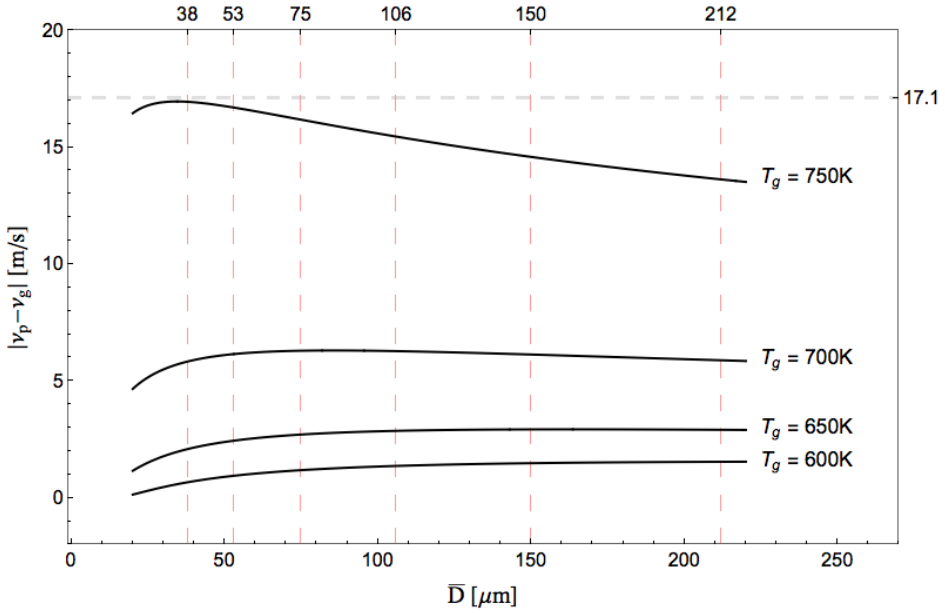

Figure 2.4.4: Calculated differential velocity between the particles and the gas required, as a function of particle diameter, to achieve the measured cooling rates [59]

peritectic transformation is [64],

$$\Delta^2 = \underbrace{2\,D_\beta \frac{\left(C_\beta^l - C_\beta^\alpha\right)\left(C_l^\beta - C_\alpha^\beta\right)}{\left(C_l^\beta - C_\beta\right)\left(C_\beta - C_\alpha^\beta\right)}}_{\text{constant}} \cdot \tau \tag{2.4.6}$$

it is possible to compare the amount of transformed phase composition with the time taken at the peritectic temperature as $\Delta \propto \sqrt{\tau}$. To avoid consideration of the inter-diffusion coefficient, etc. in Eq. (2.4.6), both the dimensionless amount of transformed phase and the dimensionless time taken to reach the peritectic temperature are used to set up the relationship of $\Delta = \sqrt{\tau/\tau_0}$ as a function of the dimensionless radial coordinate r/R_0. The cooling rate with respect to the radial distance shown as the solid line in Fig. 2.4.5 can be obtained by modifying the right-hand side of Eq. (2.4.4) as

$$\underbrace{\frac{\mathrm{d}T}{\mathrm{d}t}}_{\dot{T}}\left[c_l\,(1-f_s) + c_s\,f_s - L\frac{\mathrm{d}f_s}{\mathrm{d}T}\right] = \frac{1}{r^2}\frac{\partial}{\partial r}\left(\kappa\, r^2 \frac{\partial T}{\partial r}\right) \tag{2.4.7}$$

where the solid fraction f_s with regard to T is given by [3, 4]

$$f_s = 1 - (1 - f_r)\left(\frac{T_s - T_r}{T_s - T}\right)^{1/1-k_e} \tag{2.4.8}$$

The transformation profile in Fig. 2.4.5 shows the transformation rate stays almost constant near the centre of the particle (at $r/R_0 < 0.6$) and declines sharply near the surface of the particle (at

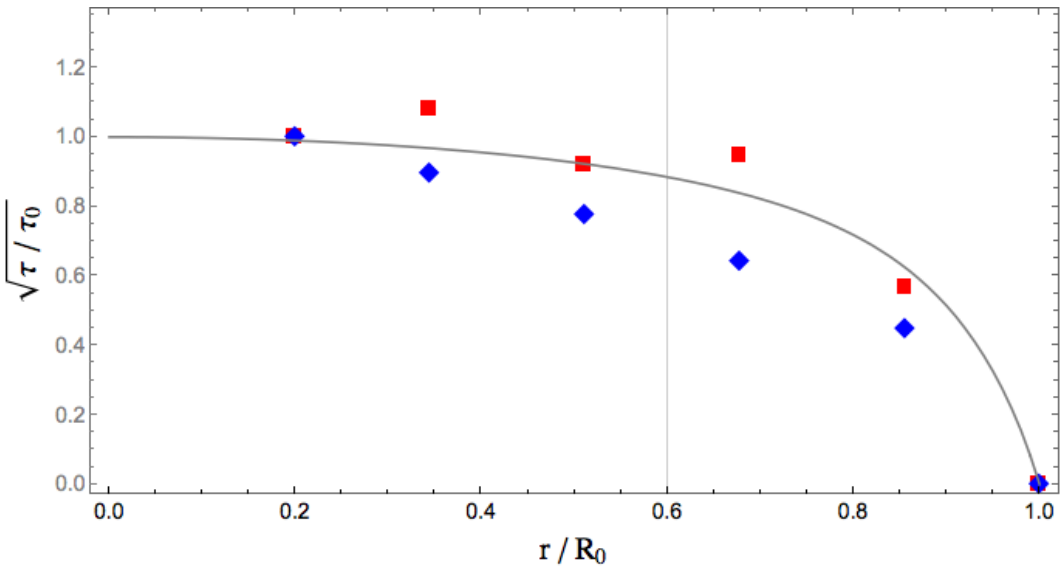

Figure 2.4.5: Calculated cooling rate (solid line) shows the relative difference in time available for the phase transformation and the amount of transformed phase composition as a function of the radial coordinate r [63]

$r/R_0 > 0.6$). The spherical particle experiencing unsteady heat transfer during flight that is believed the cooling rate is so high that there is no temperature gradient during the solidification at any instant of time [4, 43, 45], is unlikely to be true. Although the high cooling rate $\dot{T}$ surrounding the surface of one spherical metallic material with the high thermal conduction can certainly reduce the total amount of solidification time, it is still more likely that high $\dot{T}$ due to high Nu only affects some extent of distance inside this particle. The nearly constant $\dot{T}$ near the centre of this particle can give rise to similar heat extraction against the heat addition due to latent heat during the solidification. Hence, the radial variation in phase composition observed in Fig. 2.4.5 within one particle is highly suggestive of the variation in cooling rate with the radial coordinate r and consequently the existence of temperature gradient in the local region.

Another experimental evidence in agreement with the heat transfer situation inside the particle in Fig. 2.4.5 is found in the rapid solidification of undercooled Ni-Sn eutectic melt in [60], in which the transient microstructures from the surface to the centre of the particle are formed as shown in Fig. 2.4.6. There is a significant difference of cross-sectional microstructures from the surface (fine anomalous eutectics with lamellar eutectic in between) to the centre (coarse anomalous eutectic). Comparing with (a) in Fig. 2.4.6, the average size of anomalous eutectic increases slowly as the distance away from the surface to the centre increases further, *i.e.*, (c) and (d) in Fig. 2.4.6. Moreover, the primary α-Ni dendrites on the particle surface in (e) in Fig. 2.4.6 distinct from the morphology of the cross-sectional microstructure highly indicates that the primary single dendrites are formed initially and grow inward, followed by the rapid release of the heat of fusion due to heterogeneous nucleations around the surface to warm up the undercooled melt and to melt back the arms of

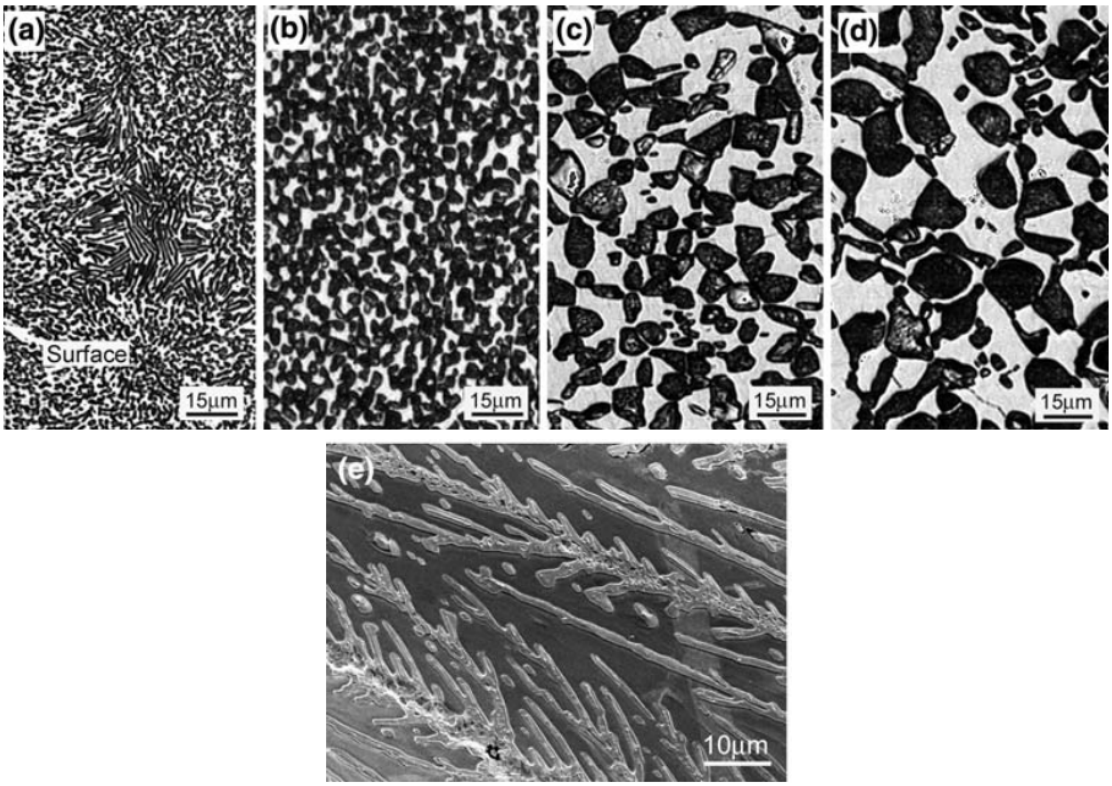

Figure 2.4.6: Transient microstructures of an undercooled Ni-Su eutectic particle section [60] are taken from the region near the surface (a) to the one near the centre (d) and (e) is the surface structure.

these directional dendrites which gives the potential sites for the formation of anomalous eutectic from dendrite fragments left in the melt. During this process, the latent heat due to the phase formation is constantly transferred from the centre to the surface. The efficient heat extraction near the particle surface can lead to the average size of anomalous eutectic less dependent of later latent heat as (a) and (b) in Fig. 2.4.6. The dramatic coarsened anomalous eutectic near the centre however suggests that the heat extraction at this region fails to retain as high as that near the surface. Because of this, the temperature gradient should prevail inside metallic materials with high conduction.

Provided there would be a moving fluid of similar streamlines surrounding a rigid sphere as shown in Fig. 2.4.7, the local temperature of fluid in the vicinity of the sphere surface should increase gradually from t_0 to t_4. At t_0, the local region has the largest heat transfer and the highest Nu since the fresh fluid just encounters the hot sphere. Then the fluid past along the sphere surface receives the heat from the hot sphere to warm up the local temperature of fluid, T_f, with which the rate of local heat loss becomes increasingly weaker and local Nu has the lower value but yet greater than 2. Depending on the roughness of the sphere surface and the properties of fluid flow, the separation

point of fluid in characteristic with Nu = 2 as shown in Fig. 2.4.3 (left) might take place at the region between t_1 and t_4. At the remaining sphere surface, the local Nu still reduces and at some instant of time, the local Nu might drop down close to 0 as Fig. 2.4.2 or even become negative at the region around t_4 as Fig. 2.4.3 (right) [10, 56].

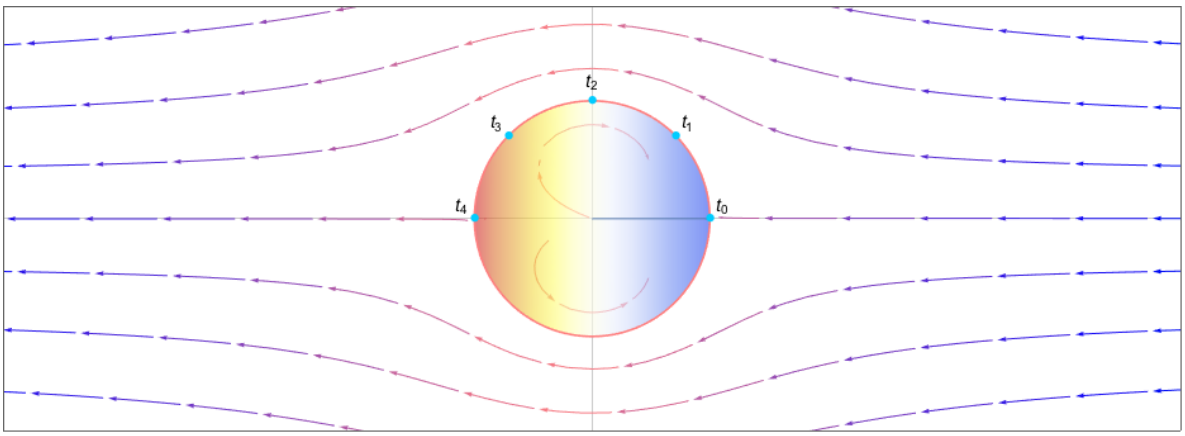

Figure 2.4.7: Schematic diagram of motion field of fluid past the sphere surface

As a result, the variation of local Nu in the vicinity of the sphere surface not only enables the higher gas temperature than the ambient temperature possible as [59] but also enhances the temperature difference inside the hot sphere as [63]. More importantly, the heat transfer inside the sphere is more likely to cause a temperature gradient, as Fig. 2.4.7 shows that the heat from the region t_4 transfers reversely back to the region t_0. In [59], the widely used 1D theoretical model illustrated in Eq. (2.4.4) is proved to overestimate the cooling rate that the particles are experienced. When a transient heat transfer from a spherical particle is considered, the overestimated cooling rate is yet overestimated (the details shall refer Section 3.2).

CHAPTER 3

HEAT TRANSFER MODELLING

3.1 MACROSCOPIC HEAT TRANSFER MODELLING

3.1.1 FORMULATION OF THE PROBLEM

Consider a spherical rigid melt heated over the melting point is subject to a space-variable surface heat flux and a constant initial condition. When a sufficient small sphere, such as $r_0 < 500\ \mu$m, is a solid of high thermal conductivity κ_s, heat conduction within the droplet can be ignored at any instant of time during the entire cooling process[4].

With the definition of enthalpy,

$$H(T) = \int_0^T c(\theta)\ \mathrm{d}\theta + L_s\,(1 - f_s)$$

and

$$\frac{\mathrm{d}H}{\mathrm{d}t} = \nabla \cdot (\kappa \nabla T)$$

the cooling and solidification behaviour of undercooled sphere, as shown in Eq. (3.2.8) in Section 3.2.3, can be described by the change of sphere enthalpy H_s with respect to time t.

$$\frac{dH_s}{dt} = c_s \frac{dT_s}{dt} - L_s \frac{df_s}{dt} \tag{3.1.1}$$

The heat capacity of sphere c_s is consist of the heat capacity of solid c_S and liquid c_L of interest material and the latent heat of sphere L_s is generated by using Eq. (1.1.2a)

$$c_s = c_L - (c_L - c_S)\, f_s \tag{3.1.2a}$$

$$L_s = L_F - \int_{T_S}^{T_L} \Delta c\ \mathrm{d}T = L_F - (c_L - c_S)(T_L - T_s) \tag{3.1.2b}$$

Further expansion of Eq. (3.2.8) gives

$$\rho_s V_s \left(c_s \frac{dT_s}{dt} - L_s \frac{df_s}{dt} \right) = A_s \cdot \dot{q}_f$$

$$c_s \frac{dT_s}{dt} - L_s \frac{df_s}{dt} = \frac{A_s}{V_s} \frac{\dot{q}_f}{\rho_s} = -\frac{3}{r_0} \frac{h(T_s - T_f)}{\rho_s}$$

$$\therefore \qquad c_s \frac{dT_s}{dt} = -\frac{3}{r_0} \frac{h(T_s - T_f)}{\rho_s} + L_s \frac{df_s}{dt} \tag{3.1.3}$$

To calculate the actual temperature of sphere T_s at any instant of time during continuous cooling, the heat transfer coefficient h must be determined at first by the well-known *Ranz and Marshall correlation*[65]

$$h = \frac{\kappa_f}{2r_0} \left(2.0 + 0.6\, Re^{1/2}\, Pr^{1/3} \right) \tag{3.1.4}$$

Re in Eq. (1.3.29) and Pr in Eq. (1.3.30) are used

$$Re = 2r_0 \frac{w' \rho_f}{\mu_f} \tag{3.1.5a}$$

$$Pr = \frac{c_f \mu_f}{\kappa_f} \tag{3.1.5b}$$

where η_f is the dynamic viscosity of fluid and w' the relative velocity between sphere w_s and fluid w_f.

$$w' = \left| w_s - w_f \right| \tag{3.1.6}$$

Initial and Boundary Condition

Both initial and boundary condition illustrated in Eq. (3.2.12) and Eq. (3.2.13) are satisfied in this modelling. However, the reversed transformation from dimensionless conditions to dimensional ones shall be made initially before applying Eq. (3.1.3) in calculation of cooling process of all times ($t > 0$).

$$T_s(0) = T_0 \tag{3.1.7a}$$

$$T_s(t) = T_f(t, r, \theta) \tag{3.1.7b}$$

3.1.2 Nucleation and Recalesence

The nucleation event in the continuous cooling is

$$I(T_s) = \frac{V_s \cdot J_v(T_s)}{\dot{T}_s} \quad \text{at} \quad \dot{T}_s = -\frac{\mathrm{d}T_s}{\mathrm{d}t} \tag{3.1.8}$$

where the nucleation rate J_v in units of $\mathrm{m}^{-3}\,\mathrm{s}^{-1}$ is referred from Eq. (1.1.22) with Eq. (1.1.7)

$$J_v = K_v \exp\left(-\frac{16\pi}{3\,k_B\,T_s}\cdot\frac{T_L^2\,\sigma_{SL}^3\,f_\theta}{\rho_s^2\,L_F^2\,(T_L-T_s)^2}\right) \tag{3.1.9}$$

The initialization of nucleation event might be considered under condition

$$\int_{T_n}^{T_L} I(T_s)\ \mathrm{d}T_s \approx 1 \tag{3.1.10}$$

When the droplet temperature reaches the nucleation temperature T_n to meet with Eq. (3.1.10) in continuous cooling, the recalesence giving rise to the subsequent release of latent heat is assumed to instantly respond after the formation of one single nucleus of the undercooled droplet. Because the nucleation rate J_v is extremely sensitive with temperature T_s, the small increase of T_s can greatly decrease the value of J_v from the extent of 10^{12} to that of 10^{-11}. The possibility of the formation of external nucleus becomes very low during rapid heating of the undercooled droplet. Therefore, it is safely to assume there would be only one nucleus to proceed the rest of solidification.

Considering the nucleation event initiates at the droplet surface in the form of a twinned spherical segment and also remains the same curvature in growth during recalescence,

$$f_s = \frac{3}{2}\left(\frac{x}{D}\right)^2 - \frac{1}{2}\left(\frac{x}{D}\right)^3 \tag{3.1.11}$$

The growth speed of interface between liquid and solid is approximated by

$$\frac{\mathrm{d}x}{\mathrm{d}t} = M_{SL}\,(T_L - T_s) \tag{3.1.12}$$

where x in Eq. (3.1.11) and Eq. (3.1.12) is the proceeding distance of solid in droplet.

The temperature change during recalesence is obtained by

$$\begin{aligned} c_s\frac{\mathrm{d}T_s}{\mathrm{d}t} + \frac{6\,h}{D\,\rho_s}\,(T_s - T_\infty) &= L_s\frac{\mathrm{d}f_s}{\mathrm{d}x}\frac{\mathrm{d}x}{\mathrm{d}t} \\ &= L_s\,M_{SL}\,(T_L - T_s)\frac{\mathrm{d}f_s}{\mathrm{d}x} \end{aligned} \tag{3.1.13}$$

where M_{SL} is the liquid/solid interface mobility and the derivative of Eq. (3.1.11) against x is expressed by

$$\frac{\mathrm{d}f_s}{\mathrm{d}x} = \frac{3}{D}\left\{\left(\frac{x}{D}\right) - \frac{1}{2}\left(\frac{x}{D}\right)^2\right\} \tag{3.1.14}$$

Inserted Eq. (3.1.14) into Eq. (3.1.13), the formula is modified

$$c_s\frac{\mathrm{d}T_s}{\mathrm{d}t} = -\frac{6\,h}{D\,\rho_s}\,(T_s - T_\infty) + \frac{3}{D}\left\{\left(\frac{x}{D}\right) - \frac{1}{2}\left(\frac{x}{D}\right)^2\right\} L_s\,M_{SL}\,(T_L - T_s) \tag{3.1.15}$$

When the heat extraction rate through gas and the release rate of latent heat,

$$\frac{\mathrm{d}T_s}{\mathrm{d}t} = 0 \Rightarrow L_s\frac{\mathrm{d}f_s}{\mathrm{d}t} = \frac{6\,h}{D\,\rho_s}\,(T_s - T_\infty) \tag{3.1.16}$$

the recalesence approaches to the end and the subsequent eutectic solidification is ready to take over the remaining solidification until the melt is fully solid.

3.1.3 SEGREGATED SOILIFICATION AND EUTECTIC SOLIDIFICATION

When the segregated solidification takes place during the decrease in droplet temperature T_s, the heat extraction equation in Eq. (3.1.3) has an unknown variable f_s which is usually described by *Scheil's* equation [3, 4, 66] as

$$f_s = 1 - (1 - f_r)\left(\frac{T_s - T_r}{T_s - T}\right)^{1/1-k_E} \tag{3.1.17}$$

where f_r is the solid fraction after recalescence and so

$$\frac{\partial f_s}{\partial T} = -\frac{1 - f_r}{(1 - k_E)(T_s - T_r)}\left(\frac{T_s - T_r}{T_s - T}\right)^{\frac{2-k_E}{1-k_E}} \tag{3.1.18}$$

Combining Eq. (3.1.3) with Eq. (3.1.18) gives

$$\begin{aligned}
-\frac{3}{r_0}\frac{h(T_s - T_f)}{\rho_s} + L_s\frac{df_s}{dT}\frac{dT}{dt} &= c_s\frac{dT_s}{dt} \\
-\frac{3}{r_0}\frac{h(T_s - T_f)}{\rho_s} &= \left(c_s - L_s\frac{df_s}{dT}\right)\frac{dT_s}{dt} \\
-\frac{3}{r_0}\frac{h(T_s - T_f)}{\rho_s} &= \left(c_s + L_s\frac{1 - f_r}{(1 - k_E)(T_s - T_r)}\left(\frac{T_s - T_r}{T_s - T}\right)^{\frac{2-k_E}{1-k_E}}\right)\frac{dT_s}{dt}
\end{aligned} \tag{3.1.19}$$

When the droplet temperature is cooled down to the eutectic temperature T_E, the coupled eutectic growth takes place. The isothermal local interface proceeds to the remaining liquid phase until the droplet is fully solidifed.

Considering the eutectic solidification grows slowly at constant equilibrium T_E, Eq. (3.1.3) is modified

$$\begin{aligned}
c_s\frac{dT_s}{dt} = -\frac{3}{r_0}\frac{h(T_s - T_f)}{\rho_s} + L_s\frac{df_s}{dt} = 0 \\
\therefore \qquad L_s\frac{df_s}{dt} = \frac{3}{r_0}\frac{h(T_s - T_f)}{\rho_s}
\end{aligned} \tag{3.1.20}$$

After the melt is fully solid, substitution of $f_s = 1$ into Eq. (3.1.3) should give the heat transfer of the pure solid phase cooling with no extra heat source involved as

$$c_S\frac{\mathrm{d}T_s}{\mathrm{d}t} = -\frac{6h}{D\rho_s}(T_s - T_\infty) \tag{3.1.21}$$

When the segregation solidification is also considered to take place prior to the eutectic solidification, the thermal variation of different flight-in droplet size should be similar with Fig. 3.1.1, in which liquid cooling, recalescence, segregated solidification, eutectic solidfication and lastly solid cooling are calculated.

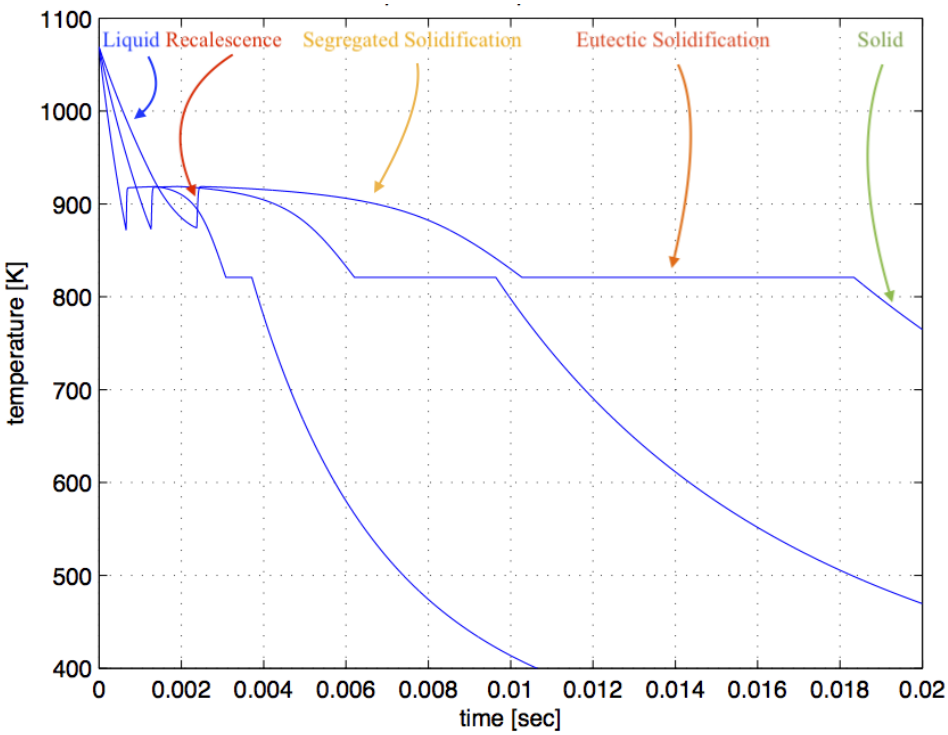

Figure 3.1.1: Schematic illustration showing cooling and solidification behaviour of a droplet in flight which is assumed to undergo five different thermal regions

3.2 UNSTEADY CONVECTION HEAT TRANSFER MODELLING

3.2.1 FORMULATION OF THE PROBLEM

Consider a solid spherical body having an initially uniform temperature T_0 at time $t = 0$ encounters a fluid with an initially uniform temperature T_∞. The fluid free-stream temperature for all subsequent times at $r \to \infty$ is also T_∞.

The surface temperature is assumed to be identical to the spherical inner temperature T_i at any instant of time when a metallic sphere of high thermal conductivity is selected.

$$\frac{\partial T_f}{\partial t} + u_r \frac{\partial T_f}{\partial r} + \frac{u_\theta}{r}\frac{\partial T_f}{\partial \theta} = \alpha_f \left[\frac{1}{r^2}\frac{\partial}{\partial r}\left(r^2 \frac{\partial T_f}{\partial r}\right) + \frac{1}{r^2 \sin\theta}\frac{\partial}{\partial \theta}\left(\sin\theta \frac{\partial T_f}{\partial \theta}\right)\right] \tag{3.2.1}$$

where $T_f(t, r, \theta)$ denotes the fluid temperature.

Provided the characteristic time of stabilization of velocity field near a sphere is sufficient small to be neglected in the convection term in Eq. (3.2.1), the flow field $u(r, \theta)$ is time independent and uniform far away from this sphere.

For such stokes flow around a sphere [67], the velocity components of u_r and u_θ (Appendix B.1) are expressed as

$$u_r = \frac{w_f}{2}\left(-2 + 3\frac{r_0}{r} - \frac{r_0^3}{r^3}\right)\cos\theta \tag{3.2.2a}$$

$$u_\theta = \frac{w_f}{4}\left(4 - 3\frac{r_0}{r} - \frac{r_0^3}{r^3}\right)\sin\theta \tag{3.2.2b}$$

where w_f is a uniform free-stream fluid velocity along z-axis.

Upon introducing dimensionless variables and parameters

$$Z_f = \frac{T_f - T_\infty}{T_0 - T_\infty} \qquad \xi = \frac{r}{r_0} \qquad \tau = \frac{\alpha_f t}{r_0^2} \qquad Pe = \frac{r_0 w_f}{\alpha_f} \tag{3.2.3}$$

Non-dimensional forms of the variation term, the convection term and the diffusion term in Eq. (3.2.1) become

$$\begin{aligned}
\frac{\partial T_f}{\partial t} &= (T_0 - T_\infty)\frac{\alpha_f}{r_0^2}\frac{\partial Z_f}{\partial \tau} \\
u_r \frac{\partial T_f}{\partial r} &= (T_0 - T_\infty)\frac{v_\xi w_f}{r_0}\frac{\partial Z_f}{\partial \xi} \\
\frac{u_\theta}{r}\frac{\partial T_f}{\partial \theta} &= (T_0 - T_\infty)\frac{v_\theta w_f}{r_0 \xi}\frac{\partial Z_f}{\partial \theta} \\
\frac{\alpha_f}{r^2}\frac{\partial}{\partial r}\left(r^2 \frac{\partial T_f}{\partial r}\right) &= (T_0 - T_\infty)\frac{\alpha_f}{r_0^2 \xi^2}\frac{\partial}{\partial \xi}\left(\xi^2 \frac{\partial Z_f}{\partial \xi}\right) \\
\frac{\alpha_f}{r^2 \sin\theta}\frac{\partial}{\partial \theta}\left(\sin\theta \frac{\partial T_f}{\partial \theta}\right) &= (T_0 - T_\infty)\frac{\alpha_f}{r_0^2 \xi^2 \sin\theta}\frac{\partial}{\partial \theta}\left(\sin\theta \frac{\partial Z_f}{\partial \theta}\right)
\end{aligned} \tag{3.2.4}$$

Combined with Eq. (3.2.1) and Eq. (3.2.4), the dimensionless energy equation for the unsteady convection flow is expressed by

$$\frac{\partial Z_f}{\partial \tau} + Pe\left[v_\xi \frac{\partial Z_f}{\partial \xi} + v_\theta \frac{1}{\xi}\frac{\partial Z_f}{\partial \theta}\right] = \frac{1}{\xi^2}\frac{\partial}{\partial \xi}\left(\xi^2 \frac{\partial Z_f}{\partial \xi}\right) + \frac{1}{\xi^2 \sin\theta}\frac{\partial}{\partial \theta}\left(\sin\theta \frac{\partial Z_f}{\partial \theta}\right) \tag{3.2.5}$$

where the non-dimensional velocity components are

$$v_\xi = \frac{1}{2}\left(-2 + \frac{3}{\xi} - \frac{1}{\xi^3}\right)\cos\theta \tag{3.2.6a}$$

$$v_\theta = \frac{1}{4}\left(4 - \frac{3}{\xi} - \frac{1}{\xi^3}\right)\sin\theta \tag{3.2.6b}$$

3.2.2 Initial and Boundary Condition

Considering the dimensionless fluid temperature distribution Z_f at $\tau = 0$ is uniform as zero before a hot sphere is suddenly introduced into this steady, axisymmetric fluid flow,

$$Z_f(\tau, \xi, \theta)\big|_{\tau=0} = 0 \tag{3.2.7a}$$

$$Z_f(\tau, \xi, \theta)\big|_{\xi=\xi_\infty} = 0 \tag{3.2.7b}$$

$$\left.\frac{\partial Z_f(\tau, \xi, \theta)}{\partial \theta}\right|_{\theta=0} = 0 \tag{3.2.7c}$$

$$\left.\frac{\partial Z_f(\tau, \xi, \theta)}{\partial \theta}\right|_{\theta=\pi} = 0 \tag{3.2.7d}$$

Eq. (3.2.7a) indicates the initial condition which the local fluid temperature is uniform at $\tau = 0$. Eq. (3.2.7b) shows the fluid temperature far from the hot sphere is not disturbed. Eq. (3.2.7c) and Eq. (3.2.7d) is developed due to θ axisymmetric temperature field of fluid along the stagnation lines at 0 and π.

3.2.3 Time-Dependent Sphere Temperature

Provided a sphere of radius r_0 has a sufficiently high thermal conductivity κ_s, resulting in a spatially uniform sphere temperature at any instant of time, time-piecewise variations of sphere temperature T_s are governed by the balance between the surface heat transfer to the surrounding fluid and the change of internal energy within the solid

$$\rho_s V_s \frac{\mathrm{d}H_s}{\mathrm{d}t} = A_s \cdot \dot{q}_f \tag{3.2.8}$$

To simplify the problem of heat transfer through unsteady fluid flow, there would be only heat convection happening on the sphere surface, at which the fluid velocity is assumed to remain zero

at all times. In consequence, the overall heat transfer from the sphere surface to the nearest fluid layer adjacent to the surface is by pure conduction instead (explained in Section 1.3.1).

$$\rho_s c_s \left(\frac{4}{3}\pi r_0^3\right) \frac{\mathrm{d}T_s}{\mathrm{d}t} = 2\pi r_0^2 \kappa_f \int_0^\pi \sin\theta \left(\frac{\partial T_f}{\partial r}\right)_{r_0} \mathrm{d}\theta \tag{3.2.9}$$

Because of unsteady fluid flow, the heat flux of fluid $\dot{q}_f$ varies with the location of θ and thus the overall heat transfer is calculated by the integral of multiplication of unit sphere area to θ dependent conduction at radius r_0 in the right-hand side of Eq. (3.2.9).

Referring to the dimensionless variables illustrated in Eq. (3.2.3), the dimensionless counterpart of Eq. (3.2.9) is

$$\rho_s c_s \left(\frac{4}{3}\pi r_0^3\right) \frac{\alpha_f}{r_0^2} \frac{\mathrm{d}Z_s}{\mathrm{d}\tau} = 2\pi r_0^2 \int_0^\pi \kappa_f \frac{\sin\theta}{r_0} \left(\frac{\partial Z_f}{\partial \xi}\right)_{\xi=1} \mathrm{d}\theta$$

$$\therefore \quad \frac{\mathrm{d}Z_s}{\mathrm{d}\tau} = \frac{3}{2} \frac{\rho_f c_f}{\rho_s c_s} \int_0^\pi \left(\frac{\partial Z_f}{\partial \xi}\right)_{\xi=1} \sin\theta \ \mathrm{d}\theta \tag{3.2.10}$$

where

$$Z_s(\tau) = \frac{T_s - T_\infty}{T_0 - T_\infty} \tag{3.2.11}$$

3.2.4 Initial and Boundary Condition

The initial dimensionless temperature of sphere Z_s is

$$Z_s(\tau)|_{\tau=0} = 1 \tag{3.2.12}$$

For particles with sufficient high conductivity, there might be less temperature gradient within the sphere at each instant of time and consequently the temperature of sphere $Z_s(\tau)$ is identical to that of fluid at sphere wall ($\xi = 1$).

$$Z_s(\tau) = Z_f(\tau, \xi, \theta)\big|_{\xi=1} \tag{3.2.13}$$

which is also the boundary condition of sphere temperature at all times $\tau > 0$.

3.2.5 Nusselt Number

Nusselt number Nu is characteristic with the ratio of convection (in Section 1.3.1) to conduction (in Section 1.3.1) in heat transfer across a boundary.

According to Eq. (1.3.1) and Eq. (1.3.4),

$$h_f A(T_s - T_\infty) = -\kappa_f A \frac{\partial}{\partial r}\left(T_f - T_s\right)$$

$$\therefore \quad Nu = \frac{h_f L}{\kappa_f} = -\frac{L}{T_s - T_\infty} \frac{\partial}{\partial r}\left(T_f - T_s\right) \tag{3.2.14}$$

where L is the characteristic length from T_s to the local point of interest T_f and the expression of heat transfer coefficient in Eq. (1.3.5) is also proved in Eq. (3.2.14).

For a sphere with radius r_0, $2\,r_0$ is selected as L and the local instantaneous Nu_θ is

$$Nu_\theta = -\frac{2\,r_0}{T_s - T_\infty}\frac{\partial}{\partial r}\left(T_f - T_s\right)$$

In substitution of dimensionless variables from Eq. (3.2.3) and Eq. (3.2.11), Nu_θ becomes

$$Nu_\theta = -\frac{2r_0}{Z_s\,(T_0 - T_\infty)}\ \frac{\partial}{r_0\,\partial\xi}(Z_f - Z_s)\,(T_0 - T_\infty)\Big|_{\xi=1} = -\frac{2}{Z_s}\left(\frac{\partial Z_f}{\partial\xi}\right)_{\xi=1} \tag{3.2.15}$$

where

$$\frac{\partial Z_s}{\partial\xi} = 0$$

since Z_s is only time dependent.

By integrating Nu_θ over sphere surface, the average Nusselt number $\overline{Nu}$

$$\overline{Nu} = \frac{1}{A}\int_0^\pi 2\pi\,\xi^2\,\sin\theta\,Nu_\theta\ \mathrm{d}\theta\Big|_{\xi=1} = -\frac{1}{Z_s}\int_0^\pi\left(\frac{\partial Z_f}{\partial\xi}\right)_{\xi=1}\sin\theta\ \mathrm{d}\theta \tag{3.2.16}$$

in combination with Eq. (3.2.10) gives

$$\overline{Nu} = -\frac{2}{3}\frac{\rho_s\,c_s}{\rho_f\,c_f}\frac{1}{Z_s}\frac{\mathrm{d}Z_s}{\mathrm{d}\tau} = -\frac{2}{3}\frac{\rho_s\,c_s}{\rho_f\,c_f}\frac{\mathrm{d}}{\mathrm{d}\tau}\ln Z_s \tag{3.2.17}$$

CHAPTER 4

NUMERICAL ESTIMATION

When a differential equation can not be solved analytically or the analytic solution is so involved with non-linear parameters, numerical approximations, such as finite difference method and finite volume method, are alternative approaches to the solution of the differential equation.

In finite difference method, the approximation is that the derivative at a given point is represente by a derivative taken over a finite interval across the point. The values oof the unknown dependent variable over the problem domain are considered at a finite number of nodal points instead. For example, at a finite number of nodal points N, N algebraic equations were established by discretizing the governing differential equation subjected with the boundary conditions for its problem. This set of algebraic equations transformed from the partial differential equation are then solved by a suitable algorithm and generate numerical results afterwards.

Section 4.1 introduces the first and the second central difference approximation as the fundamental contributions in *Finite Difference Method*. Also the first non-central finite difference approximation of high-order accuracy is introduced to achieve the same accuracy of grids on the boundary numerically as that in the interior grids. Based on the finite difference schemes introduced in Section 4.1, the numerical schemes for heat conduction equation is then illustrated in Section 4.2.

In this work, the physical problem involves solving parabolic-type equation on spherical domains. Both the two-dimensional heat transfer of solid sphere for spherical polar coordinates system and the treatment of the geometrical singularity happening on the origin ($r = 0$) and the north and south poles ($\theta = 0, \pi$) of the spherical domain are explained in development of the *Alternating Direction Implicit* (ADI) method in Section 4.2.2.

Nevertheless, considering the ADI scheme of hollow sphere is identical with that of solid sphere, the application of ADI scheme in spherical polar coordinates for hollow sphere is presented in Appendix D.2.

4.1 DISCRETIZATION

The derivation of the finite difference approximations for the derivatives of a function $f(x)$ are based on forward and backward Taylor series expansions of $f(x)$ about x.

$$f(x+\delta) = f(x) + \delta f'(x) + \frac{\delta^2}{2!} f''(x) + \frac{\delta^3}{3!} f'''(x) + \cdots \tag{4.1.1a}$$

$$f(x-\delta) = f(x) - \delta f'(x) + \frac{\delta^2}{2!} f''(x) - \frac{\delta^3}{3!} f'''(x) + \cdots \tag{4.1.1b}$$

For first central difference approximations,

$$f(x+\delta) - f(x+\delta) = 2\delta f'(x) + \frac{\delta^3}{3} f'''(x) + \cdots$$

$$\therefore \qquad f'(x) = \frac{f(x+\delta) - f(x-\delta)}{2\delta} - \frac{\delta^2}{6} f'''(x) - \cdots \tag{4.1.2}$$

where $\mathcal{O}(\delta^2)$ is the truncation error in Eq. (4.1.2)

$$\mathcal{O}(\delta^2) = \frac{\delta^2}{6} f'''(x) \tag{4.1.3}$$

For second central difference approximations,

$$f''(x) = \frac{f(x+\delta) - 2f(x) + f(x-\delta)}{\delta^2} + \frac{\delta^2}{12} f^{(4)}(x) + \cdots \tag{4.1.4}$$

where the truncation error

$$\mathcal{O}(\delta^2) = \frac{\delta^2}{12} f^{(4)}(x) \tag{4.1.5}$$

Besides central difference approximations, non-central finite approximations are widely used to compute the derivatives at a node on the boundary.

The forward finite difference approximations are shown in Eq. (4.1.6a) for two-point formulae, Eq. (4.1.6b) for three-point formulae.

$$f'(x) = \frac{f(x+\delta) - f(x)}{\delta} + \mathcal{O}(\delta) \tag{4.1.6a}$$

$$f'(x) = \frac{-f(x+2\delta) + 4f(x+\delta) - 3f(x)}{2\delta} + \mathcal{O}(\delta^2) \tag{4.1.6b}$$

The backward finite difference approximations are

$$f'(x) = \frac{f(x) - f(x-\delta)}{\delta} + \mathcal{O}(\delta) \tag{4.1.7a}$$

$$f'(x) = \frac{3f(x) - 4f(x-\delta) + 3f(x-2\delta)}{2\delta} + \mathcal{O}(\delta^2) \tag{4.1.7b}$$

When there are more than two grid points on one side of the boundary, the accuracy of approximations can be improved, for example, Eq. (4.1.6b) and Eq. (4.1.7b) from first-order to second-order accuracy [68].

4.2 HEAT CONDUCTION EQUATION

The form of partial differential equation is widely used to describe a family of problems, such as heat, mass, momentum transport with a time variable.

A simplest one-dimensional problem governed by the linear parabolic differential equation

$$\frac{\partial T(x,t)}{\partial t} = \alpha \frac{\partial^2 T(x,t)}{\partial x^2} \tag{4.2.1}$$

subjected to appropriate boundary condition will be demonstrated in Section 4.2.1 by the combined method.

Then the multidimensional parabolic system illustrated in Eq. (A.2.4) (see Appendix A.2)

$$\frac{\partial T(x,t)}{\partial t} = \alpha \nabla^2 T \tag{4.2.2}$$

will be further discussed by the *Alternating Direct Implicit* (ADI) method in Section 4.2.2, which is also the fundamental algorithm applied in the modelling in Section 3.2.1.

The computational advantage of the parabolic system lies in the fact that significant reduction in computer time and computer storage can be realized. In the case of finite-difference solution of heat diffusion in Eq. (4.2.1), the temperature field at any time is only related with that at the previous times. Once the initial temperature field is set up, the afterwards temperature field is computered at successive time step.

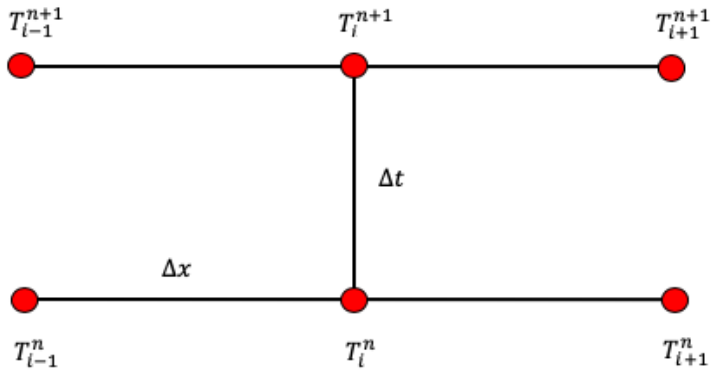

Figure 4.2.1: The finite-difference molecules for the combined scheme

4.2.1 COMBINED SCHEME

The differential equation in Eq. (4.2.1) can be discretized directly by using the second-order accurate finite-difference formula in Eq. (4.1.2) and Eq. (4.1.4) as

$$\frac{T_i^{n+1}-T_i^n}{\Delta t}=\alpha\left[\theta\,\frac{T_{i-1}^{n+1}-2\,T_i^{n+1}+T_{i+1}^{n+1}}{\Delta x^2}+(1-\theta)\,\frac{T_{i-1}^{n}-2\,T_i^{n}+T_{i+1}^{n}}{\Delta x^2}\right]$$

$$\therefore$$

$$-r\,\theta\,T_{i-1}^{n+1}+(1+2\,r\,\theta)\,T_i^{n+1}-r\,\theta\,T_{i+1}^{n+1}=r\,(1-\theta)\,T_{i-1}^{n}+[1-2r\,(1-\theta)]\,T_i^{n}+r\,(1-\theta)\,T_{i+1}^{n} \tag{4.2.3}$$

where the constant θ is the weight factor between 0 and 1 and

$$r=\frac{\alpha\,\Delta t}{\Delta x^2}$$

Also, Fig. 4.2.1 schematically illustrates the combined scheme of finite-difference approximation of Eq. (4.2.3). In general, $\frac{1}{2}\le\theta\le 1$ makes Eq. (4.2.3) unconditionally stable for all values of r, whereas $0\le\theta<\frac{1}{2}$ is conditionally stable if and only if

$$0\le r\le\frac{1}{2-4\theta}$$

For certain specific values of θ, the discretization of Eq. (4.2.3) reduces to one of three well-known schemes for parabolic differential equations.

- $\theta=0.0$ leads to *the explicit scheme*
- $\theta=0.5$ leads to *the Crank-Nicolson scheme*
- $\theta=1.0$ leads to *the fully implicit scheme*

Finite difference methods shown above can be efficiently extended to handle derivative terms in more than one dimension. The detail of both the explicit method and the fully implicit method in two-dimensional stencils is displayed in Appendix D.1.1 and Appendix D.1.2.

4.2.2 ALTERNATING DIRECTION IMPLICIT SCHEME

Although the fully implicit method (Eq. (4.2.3) at $\theta=1.0$) introduced in Section 4.2.1 is unconditionally stable at all values of r, the computation problems become enormous for multi-dimensional situation*.

In brief, a two-dimensional problem with N interior nodes in each direction contains N^2 nodes. There would be $N^2\times N^2$ nodes in matrix to be solved at each time step by using fully implicit scheme, which certainly becomes impractical for large node setting in calculation.

*The tri-diagonal matrix algorithm (TDMA) of 2D finite-difference implicit scheme is illustrated in Appendix D.1.2.

To minimize the number of calculation without loosing accuracy, convergence and stability, the alternating direction implicit (ADI[†]) method is invented to split the finite difference equation into two, the one with the implicit scheme (Eq. (4.2.3) at $\theta = 1.0$) in the x-direction and the explicit scheme in the y-direction (Eq. (4.2.3) at $\theta = 0.0$) at the first half time step, and the other with the implicit scheme in the y-direction and the explicit scheme in x-direction at the second half-time step [68].

In the following subsection, the ADI scheme for spherical polar coordinates system in the application of heat conduction equation is emphasized.

SPHERICAL POLAR COORDINATES

The general heat conduction equation assumed with constant physical properties and no external source term in Eq. (4.2.2) for spherical polar coordinates system is expressed by using the chain rule

$$\frac{1}{\alpha}\frac{\partial T}{\partial t} = \frac{\partial^2 T}{\partial r^2} + \frac{2}{r}\frac{\partial T}{\partial r} + \frac{1}{r^2}\frac{\partial^2 T}{\partial \theta^2} + \frac{\cos\theta}{r^2 \sin\theta}\frac{\partial T}{\partial \theta} \tag{4.2.4}$$

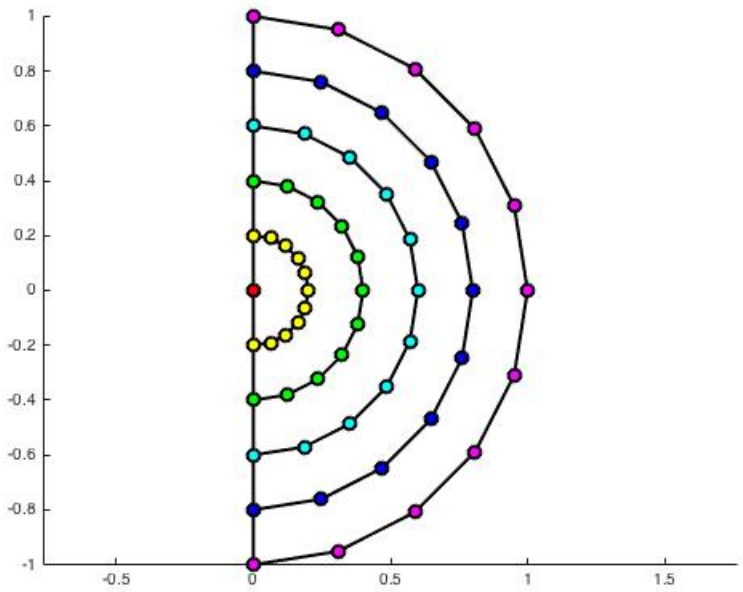

Figure 4.2.2: The mapping of the spherical region for computational calculation

Fig. 4.2.2 shows the grid arrangement for numerical calculation of heat transfer in the polar spherical coordinates. The singularities at $r = 0$, $\theta = 0$ and π need the extra care which is carefully deduced below.

[†]The details of grid construction and ADI stencils involved with Dirichlet boundary and Neumann boundary in Cartesian coordinates system shall refer to Appendix D.1.3.

SINGULARITIES

In the radial direction term of Eq. (4.2.4), the origin of sphere ($r = 0$) is singular. The problem at r approaching to zero is easily reduced by using L'Hôpital's rule when there is neither latitudinal variation θ nor longitudinal variation ϕ in heat flux around the singular node [69].

$$\begin{aligned}\frac{1}{\alpha}\frac{\partial T}{\partial t} &= \lim_{r\to 0}\left(\frac{\partial^2 T}{\partial r^2}+\frac{2}{r}\frac{\partial T}{\partial r}+\frac{1}{r^2}\frac{\partial^2 T}{\partial \theta^2}+\frac{\cos\theta}{r^2\sin\theta}\frac{\partial T}{\partial \theta}\right)\\ &= \lim_{r\to 0}\left(\frac{\partial^2 T}{\partial r^2}+\frac{2}{r}\frac{\partial T}{\partial r}\right)=\frac{\partial^2 T}{\partial r^2}+2\frac{\partial^2 T}{\partial r^2}=3\frac{\partial^2 T}{\partial r^2}\end{aligned} \tag{4.2.5}$$

If this symmetry conditions do not prevail in the heat flux around the the singular node, the simplest numerical approximation is to replace the spherical polar coordinate form of $\nabla^2 T(r,\theta,\phi,t)$ with its Cartesian equivalent counterpart $\nabla^2 T(x,y,z,t)$.

$$\begin{aligned}\frac{1}{\alpha}\frac{\partial T}{\partial t} &= \lim_{r\to 0}\left(\frac{\partial^2 T}{\partial r^2}+\frac{2}{r}\frac{\partial T}{\partial r}+\frac{1}{r^2}\frac{\partial^2 T}{\partial \theta^2}+\frac{\cos\theta}{r^2\sin\theta}\frac{\partial T}{\partial \theta}\right)=\lim_{(x,y,z)\to 0}\left(\frac{\partial^2 T}{\partial x^2}+\frac{\partial^2 T}{\partial y^2}+\frac{\partial^2 T}{\partial z^2}\right)\\ &\approx \frac{T_1+T_2+T_3+T_4+T_5+T_6-6T_0}{\Delta r^2}+\mathcal{O}\{\Delta r^2\}=6\frac{\overline{T}-T_0}{\Delta r^2}\end{aligned} \tag{4.2.6}$$

where $\overline{T}$ is a mean value of nearest Ts around T_0 at $r = 0$.

The latitudinal direction term in the right-hand side of Eq. (4.2.4) at $\theta = 0$ and π is also singular. If the symmetry prevails at $\theta = 0$ and π due to the zero heat flux between each side of stagnant lines, the Singularities can be resolved again by uisng L'Hôpital's rule.

$$\begin{aligned}\frac{1}{\alpha}\frac{\partial T}{\partial t} &= \lim_{\theta\to 0,\pi}\left(\frac{\partial^2 T}{\partial r^2}+\frac{2}{r}\frac{\partial T}{\partial r}+\frac{1}{r^2}\frac{\partial^2 T}{\partial \theta^2}+\frac{\cos\theta}{r^2\sin\theta}\frac{\partial T}{\partial \theta}\right)\\ &= \frac{\partial^2 T}{\partial r^2}+\frac{2}{r}\frac{\partial T}{\partial r}+\frac{1}{r^2}\frac{\partial^2 T}{\partial \theta^2}+\frac{\cos\theta}{r^2}\lim_{\theta\to 0,\pi}\left(\frac{1}{\sin\theta}\frac{\partial T}{\partial \theta}\right)\\ &= \frac{\partial^2 T}{\partial r^2}+\frac{2}{r}\frac{\partial T}{\partial r}+\frac{2}{r^2}\frac{\partial^2 T}{\partial \theta^2}\end{aligned} \tag{4.2.7}$$

ADI STENCILS

The ADI algorithms of interior mesh in Eq. (4.2.4) are given by

$$\begin{aligned}\frac{T_{i,j}^{n+0.5}-T_{i,j}^{n}}{0.5\alpha\Delta t} &= \frac{T_{i+1,j}^{n+0.5}-2T_{i,j}^{n+0.5}+T_{i-1,j}^{n+0.5}}{\Delta r^2}+\frac{2}{(i-1)\Delta r}\frac{T_{i+1,j}^{n+0.5}-T_{i-1,j}^{n+0.5}}{2\Delta r}\\ &+\frac{1}{[(i-1)\Delta r]^2}\frac{T_{i,j+1}^{n}-2T_{i,j}^{n}+T_{i,j-1}^{n}}{\Delta\theta^2}+\frac{\cos((j-1)\Delta\theta)}{\sin((j-1)\Delta\theta)}\frac{1}{[(i-1)\Delta r]^2}\frac{T_{i,j+1}^{n}-T_{i,j-1}^{n}}{2\Delta\theta}\end{aligned} \tag{4.2.8a}$$

$$\begin{aligned}\frac{T_{i,j}^{n+1}-T_{i,j}^{n+0.5}}{0.5\alpha\Delta t} &= \frac{T_{i+1,j}^{n+0.5}-2T_{i,j}^{n+0.5}+T_{i-1,j}^{n+0.5}}{\Delta r^2}+\frac{2}{(i-1)\Delta r}\frac{T_{i+1,j}^{n+0.5}-T_{i-1,j}^{n+0.5}}{2\Delta r}\\ &+\frac{1}{[(i-1)\Delta r]^2}\frac{T_{i,j+1}^{n+1}-2T_{i,j}^{n+1}+T_{i,j-1}^{n+1}}{\Delta\theta^2}+\frac{\cos((j-1)\Delta\theta)}{\sin((j-1)\Delta\theta)}\frac{1}{[(i-1)\Delta r]^2}\frac{T_{i,j+1}^{n+1}-T_{i,j-1}^{n+1}}{2\Delta\theta}\end{aligned} \tag{4.2.8b}$$

Both the explicit terms of θ-direction in Eq. (4.2.8a) and those of r-direction in Eq. (4.2.8b) are known such that the solution follows a simple TDMA matrix at each half time step $0.5\,\Delta t$. Hence ADI method offers an alternative solution in deal with $N \times N$ for N times at each half time level $0.5\,\Delta t$, rather than calculating $N^2 \times N^2$ for each time level by the fully implicit scheme.

Further rearranging Eq. (4.2.8a) and Eq. (4.2.8b) for computational purpose gives

$$-\frac{s_r}{2}\frac{i}{i-1}T^{n+0.5}_{i+1,j}+(1+s_r)\,T^{n+0.5}_{i,j}-\frac{s_r}{2}\frac{i-2}{i-1}T^{n+0.5}_{i-1,j}$$
$$=\frac{s_\theta}{2(i-1)^2}\left(1+\cot((j-1)\Delta\theta)\frac{\Delta\theta}{2}\right)T^{n}_{i,j+1}+\left(1-\frac{s_\theta}{(i-1)^2}\right)T^{n}_{i,j}+\frac{s_\theta}{2(i-1)^2}\left(1-\cot((j-1)\Delta\theta)\frac{\Delta\theta}{2}\right)T^{n}_{i,j-1} \tag{4.2.9a}$$

$$-\frac{s_\theta}{2(i-1)^2}\left(1+\cot((j-1)\Delta\theta)\frac{\Delta\theta}{2}\right)T^{n+1}_{i,j+1}+\left(1+\frac{s_\theta}{(i-1)^2}\right)T^{n+1}_{i,j}-\frac{s_\theta}{2(i-1)^2}\left(1-\cot((j-1)\Delta\theta)\frac{\Delta\theta}{2}\right)T^{n+1}_{i,j-1}$$
$$=\frac{s_r}{2}\frac{i}{i-1}T^{n+0.5}_{i+1,j}+(1-s_r)\,T^{n+0.5}_{i,j}+\frac{s_r}{2}\frac{i-2}{i-1}T^{n+0.5}_{i-1,j} \tag{4.2.9b}$$

where Eq. (4.2.9a) and Eq. (4.2.9b) are applied only for interior mesh points ($2 \le i \le N_r - 1 \quad 2 \le j \le N_\theta - 1$) and

$$s_r = \frac{\alpha\,\Delta t}{\Delta r^2} \qquad s_\theta = \frac{\alpha\,\Delta t}{\Delta r^2\,\Delta\theta^2}$$

For stagnant lines along $\theta = 0$ and π, the ADI arrangement of Eq. (4.2.7) is

$$-\frac{s_r}{2}\frac{i}{i-1}T^{n+0.5}_{i+1,j}+(1+s_r)\,T^{n+0.5}_{i,j}-\frac{s_r}{2}\frac{i-2}{i-1}T^{n+0.5}_{i-1,j}=\frac{s_\theta}{(i-1)^2}T^{n}_{i,j+1}+\left(1-\frac{2s_\theta}{(i-1)^2}\right)T^{n}_{i,j}+\frac{s_\theta}{(i-1)^2}T^{n}_{i,j-1} \tag{4.2.10a}$$

$$-\frac{s_\theta}{(i-1)^2}T^{n+1}_{i,j+1}+\left(1+\frac{2s_\theta}{(i-1)^2}\right)T^{n+1}_{i,j}-\frac{s_\theta}{(i-1)^2}T^{n+1}_{i,j-1}=\frac{s_r}{2}\frac{i}{i-1}T^{n+0.5}_{i+1,j}+(1-s_r)\,T^{n+0.5}_{i,j}+\frac{s_r}{2}\frac{i-2}{i-1}T^{n+0.5}_{i-1,j} \tag{4.2.10b}$$

Because the symmetry conditions of Eq. (4.2.7) do not include the singular node at $r = 0$ along the stagnant lines, Eq. (4.2.10a) and Eq. (4.2.10b) are to exclude latitudinal contributions along the radius position $r = 0$ by introducing a heat conduction in a hollow sphere which is one unit step Δr away from the origin, followed by applying Eq. (4.2.6) to obtain the grids at $r = 0$.

4.3 STABILITY, ACCURACY, CONVERGENCE AND EFFICIENCY

4.3.1 STABILITY

The schemes of the explicit, implicit and Crank-Nicolson method have different stability properties as shown in Section 4.2.1. For the ADI method, the intermediate time point $n+0.5$ is introduced to reduce two-dimensional problems to a succession of many one-dimensional problems (see Section 4.2.2 for spherical polar coordinate system and Appendix D.1.3 for Cartesian coordinate system). Because the ADI method in both coordinates shares the same stability. For simplicity, the ADI scheme in Cartesian coordinates is selected in stability analysis and also assumes $\Delta x = \Delta y = h$ in both Eq. (D.1.11a) and Eq. (D.1.11b) as

$$U_{i,j}^{n+0.5} = U_{i,j}^{n} + \frac{\alpha \Delta t}{2h^2}\left(U_{i-1,j}^{n+0.5} - 2U_{i,j}^{n+0.5} + U_{i+1,j}^{n+0.5} + U_{i,j-1}^{n} - 2U_{i,j}^{n} + U_{i,j+1}^{n}\right) \tag{4.3.1a}$$

$$U_{i,j}^{n+1} = U_{i,j}^{n+0.5} + \frac{\alpha \Delta t}{2h^2}\left(U_{i-1,j}^{n+0.5} - 2U_{i,j}^{n+0.5} + U_{i+1,j}^{n+0.5} + U_{i,j-1}^{n+1} - 2U_{i,j}^{n+1} + U_{i,j+1}^{n+1}\right) \tag{4.3.1b}$$

Replacing $U_{i,j}^{n}$ by $\varepsilon^n \exp(ikx)\exp(imy)$, Eq. (4.3.1a) becomes

$$\begin{aligned}
&\varepsilon^{n+0.5}\exp(ik\cdot i\Delta x)\exp(im\cdot j\Delta y) - \varepsilon^{n}\exp(ik\cdot i\Delta x)\exp(im\cdot j\Delta y)\\
&= \frac{\alpha\Delta t}{2h^2}\varepsilon^{n+0.5}\exp(im\cdot j\Delta y)\left(\exp(ik\cdot(i-1)\Delta x) - 2\exp(ik\cdot i\Delta x) + \exp(ik\cdot(i+1)\Delta x)\right)\\
&\quad + \frac{\alpha\Delta t}{2h^2}\varepsilon^{n}\exp(ik\cdot i\Delta x)\left(\exp(im\cdot(j-1)\Delta y) - 2\exp(im\cdot j\Delta y) + \exp(im\cdot(j+1)\Delta y)\right)
\end{aligned}$$

$$\therefore\quad \varepsilon^{n+0.5} = \varepsilon^{n} + \frac{\alpha\Delta t}{2h^2}\varepsilon^{n+0.5}\left(\exp(-ikh) - 2 + \exp(ikh)\right) + \frac{\alpha\Delta t}{2h^2}\varepsilon^{n}\left(\exp(-imh) - 2 + \exp(imh)\right) \tag{4.3.2}$$

According to Euler's formula between analysis and trigonometry

$$\cos x = \frac{\exp(ix) + \exp(-ix)}{2}$$

and the trigonometric identities of the double-angle formulae

$$\cos x = 1 - 2\sin^2\frac{x}{2}$$

Eq. (4.3.2) can be simplified as

$$\begin{aligned}
\varepsilon^{n+0.5} &= \varepsilon^{n} + \frac{\alpha\Delta t}{2h^2}\varepsilon^{n+0.5}\left(2\cos kh - 2\right) + \frac{\alpha\Delta t}{2h^2}\varepsilon^{n}\left(2\cos mh - 2\right)\\
&= \varepsilon^{n} - 2\frac{\alpha\Delta t}{h^2}\varepsilon^{n+0.5}\sin^2\frac{kh}{2} - 2\frac{\alpha\Delta t}{h^2}\varepsilon^{n}\sin^2\frac{mh}{2}
\end{aligned}$$

$$\therefore\quad \frac{\varepsilon^{n+0.5}}{\varepsilon^{n}} = \frac{1 - 2\dfrac{\alpha\Delta t}{h^2}\sin^2\dfrac{kh}{2}}{1 + 2\dfrac{\alpha\Delta t}{h^2}\sin^2\dfrac{mh}{2}} \tag{4.3.3}$$

Similarly, Eq. (4.3.1b) becomes

$$\frac{\varepsilon^{n+1}}{\varepsilon^{n+0.5}} = \frac{1-2\dfrac{\alpha\Delta t}{h^2}\sin^2\dfrac{mh}{2}}{1+2\dfrac{\alpha\Delta t}{h^2}\sin^2\dfrac{kh}{2}} \tag{4.3.4}$$

Combining Eq. (4.3.3) and Eq. (4.3.4),

$$\frac{\varepsilon^{n+1}}{\varepsilon^{n}} = \left(\frac{1-2\dfrac{\alpha\Delta t}{h^2}\sin^2\dfrac{kh}{2}}{1+2\dfrac{\alpha\Delta t}{h^2}\sin^2\dfrac{mh}{2}}\right)\left(\frac{1-2\dfrac{\alpha\Delta t}{h^2}\sin^2\dfrac{mh}{2}}{1+2\dfrac{\alpha\Delta t}{h^2}\sin^2\dfrac{kh}{2}}\right) \tag{4.3.5}$$

For arbitrary Δt, Eq. (4.3.5) satisfies

$$\max\left|\frac{\varepsilon^{n+1}}{\varepsilon^{n}}\right| < 1 \tag{4.3.6}$$

Therefore, the ADI scheme is unconditionally stable.

4.3.2 ACCURACY

The accuracy of the ADI schemes is determined to the accuracy of approximation of each partial derivative in

$$\frac{\partial U}{\partial t} = \alpha\nabla^2 U$$

The local truncation error of $\alpha\nabla^2 U$ for the second central difference approximation as shown in Eq. (4.1.5) has the order of $\mathcal{O}(\Delta x^2)$ and $\mathcal{O}(\Delta y^2)$. The accuracy of the time derivative can also be obtained with the help of a Taylor expansion (Eq. (4.1.1a) and Eq. (4.1.1b)).

Considering Taylor series around $U_{i,j}^{n+0.5}$ on both forward and backward direction,

$$U_{i,j}^{n+1} = U_{i,j}^{n+0.5} + \frac{\partial U}{\partial t}\left(\frac{\Delta t}{2}\right) + \frac{1}{2!}\frac{\partial^2 U}{\partial t^2}\left(\frac{\Delta t}{2}\right)^2 + \frac{1}{3!}\frac{\partial^3 U}{\partial t^3}\left(\frac{\Delta t}{2}\right)^3 + \cdots \tag{4.3.7}$$

$$U_{i,j}^{n} = U_{i,j}^{n+0.5} - \frac{\partial U}{\partial t}\left(\frac{\Delta t}{2}\right) + \frac{1}{2!}\frac{\partial^2 U}{\partial t^2}\left(\frac{\Delta t}{2}\right)^2 - \frac{1}{3!}\frac{\partial^3 U}{\partial t^3}\left(\frac{\Delta t}{2}\right)^3 + \cdots \tag{4.3.8}$$

Subtracting Eq. (4.3.8) from Eq. (4.3.7),

$$U_{i,j}^{n+1} - U_{i,j}^{n} = 2\frac{\partial U}{\partial t}\left(\frac{\Delta t}{2}\right) + \frac{2}{3!}\frac{\partial^3 U}{\partial t^3}\left(\frac{\Delta t}{2}\right)^3 + \cdots$$

$$\frac{\partial U}{\partial t} = \frac{U_{i,j}^{n+1} - U_{i,j}^{n}}{\Delta t} - \frac{1}{3!}\frac{\partial^3 U}{\partial t^3}\left(\frac{\Delta t}{2}\right)^3 + \cdots \tag{4.3.9}$$

Therefore the ADI method has second order accuracy with a truncation error of $\mathcal{O}\left(\Delta t^2, \Delta x^2, \Delta y^2\right)$

4.3.3 CONVERGENCE AND EFFICIENCY

Even though the ADI scheme is theoretically unconditionally stable (see Section 4.3.1) and second-order accurate in both time and space derivative (see Section 4.3.2) regardless of the choice of the size of time step and space step, ensuring those properties in PDE subjected with various boundary conditions tends to an increase in iterations for producing more accurate numerical results in a finer discretization. This approach however significantly decreases the computational performance in convergence with exact analytic solutions (Eq. (C.1.14) for solid sphere and Eq. (C.2.11) for hollow sphere) shown below

$$U(r,t) = U_1 - (U_0 - U_1)\,\frac{2b}{\pi r}\sum_{n=1}^{\infty}\frac{(-1)^n}{n}\sin\left(\frac{n\pi}{b}\,r\right)\exp\left\{-\kappa\left(\frac{n\pi}{b}\right)^2 t\right\} \tag{4.3.10}$$

$$\begin{aligned} U(r,t) = {} & \frac{1}{r}\left(a\,U_1 + \frac{b\,U_2 - a\,U_1}{b-a}(r-a)\right) \\ & + \frac{2}{\pi r}\sum_{n=1}^{\infty}\left(\frac{a\,(U_0-U_1) - b\,(U_0-U_2)\cos(n\pi)}{n}\right)\sin\left(n\pi\,\frac{r-a}{b-a}\right)\exp\left\{-\kappa\left(\frac{n\pi}{b-a}\right)^2 t\right\} \end{aligned} \tag{4.3.11}$$

The reason to make use of 1D analytic solutions in Eq. (4.3.10) and Eq. (4.3.11) to test 2D numerical solutions is that Eq. (4.2.4) with a constant initial and fixed Dirichlet boundary condition reduces its numerical results to a function of the radial coordinate alone [70].

In order to find the fast convergence but yet very little change in each local value of $U(t,r,\theta)$ in a selected region, the space size 51×26, 101×51, 201×101, 1001×1001 with time step (Δt) 0.0001, 0.01, 0.1 are tested.

HOLLOW SPHERE

The reason to separate the test of convergence between Eq. (4.3.11) and the ADI solution of Eq. (3.2.5) (see Appendix D.2.2) in hollow sphere from that in solid sphere is due to the natural bound to the domain (refer Dirichlet boundary condition in Eq. (3.2.7b)) at any change of time. The narrow space domain might generate an incorrect estimation in Eq. (4.3.11) at large elapsed time, whereas the wider domain might significantly increase unnecessary numerical calculation. Thus, restraining the domain without influencing the quality of numerical estimation at reasonable elapsed time for droplet flight through the drop tube is required.

CHAPTER 5

METHODOLOGY

5.1 EXPERIMENTAL METHOD

In this project, the undercooled droplet of various sizes are generated by the drop tube equipment. The further investigation of non-equilibrium morphologies of those undercooled droplets is by means of *Scanning Electron Microscopy* (SEM) and *Differential Thermal Analysis* (DTA). The detail of sample preparation and the introduction of characterization techniques (SEM and DTA) are described below.

5.1.1 CHOICE AND PREPARATION OF ALLOY

Ag-Cu binary system is widely investigated under the equilibrium and non-equilibrium condition by various means in years. Because both element Ag and Cu have the same face-centered cubic (FCC) crystal structure and share similar physical properties, such as low entropy and high conductivity, the liquidus, solidus, and solid solubilities as well as the extensive curves characteristic with metastable phase boundary and having identical Gibbs free energies between two phases in the binary phase diagram in Fig. 2.1.3, are all accurately determined. Those extensions give a theoretical insight in the estimation of other physical properties, including possible minimum undercoolings in the range of binary composition at non-equilibrium condition.

More importantly, the physical parameters of different weight percentages (wt.%) from liquid temperature to ambient temperature can be well measured in Ag-Cu system, and the empirical formulas with respect to temperature to estimate those parameters are also available else where [14, 16, 47], which is of use in later calculation of heat transfer when those parameters are required.

All starting materials are purchased from Alfa Aesar and are of 99.9999% purity metallic (silver and copper) shot. The eutectic composition (Ag-28wt.%Cu) ingot was weighed and sealed in quartz tubing before being arc-melted under a protective argon atmosphere. The ingot after the

arc-melting process were weighed again to ensure no weight loss throughout the preparation process. During the arc-melting process, melting below the solidus temperature is repeated several times with aim of improving the composition distribution and alleviating potential significant resident stress inside ingot.

Although the whole homogenization is under the noble gas atmosphere, it is unlikely that the ingot surface is oxide free. Once those high temperature-resistant oxides ($T_m > 2000$ K) are generated, the elimination of them through superheating up to ~ 850 K is impossible. Therefore the heterogeneous nucleation can take place on those sites.

5.1.2 DROP TUBE

The 6.5 m drop tube technique (see Fig. 5.1.2) is chosen to study the free-falling rapid solidification. With lack of potential container wall along 6.5 m stainless steel tube to hinder new heterogeneous nucleations, the rapid in-flight cooling largely can constrain the nucleation solidification in response, so as to attain high undercooling [31]. Those metal oxides obtained during the ingot preparation, however, are more likely to be isolated in a fraction of small droplets in the in-flight dispersion of the melt, as shown in Fig. 5.1.1. Thus this subdivision increases the possibility of homogeneous nucleation in individual sphere and potentially further enlarges the amount of undercooling.

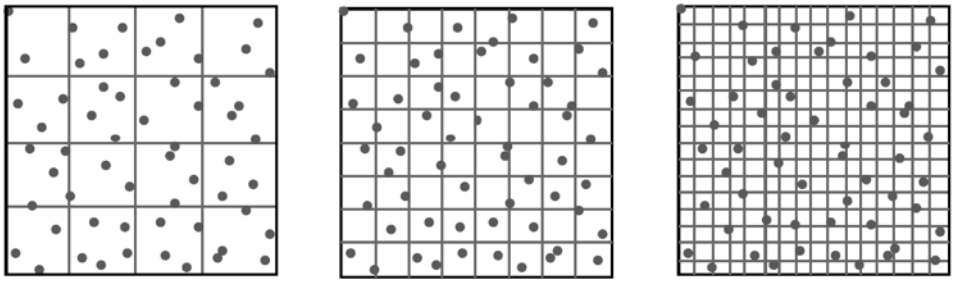

Figure 5.1.1: Principle of isolation of heterogeneous nucleation motes in the volume of a macroscopic melt and formed by different sizes of subdivision into many small particles [71]

Besides this 6.5 m tube, there are three main built-in systems in drop tube, which is

(a) Heating system **(b)** Vacuum and gas supply system **(c)** Water-cooling system

HEATING SYSTEM

The prepared Ag-28wt.%Cu ingot placed in an alumina crucible with 3 laser drilled holes (300 μm) in the base is located inside the graphite susceptor. The *radio-frequency* (RF) coil surround the graphite susceptor on the top of drop tube in Fig. 5.1.2 superheats the ingot up to ~ 1095 K (higher

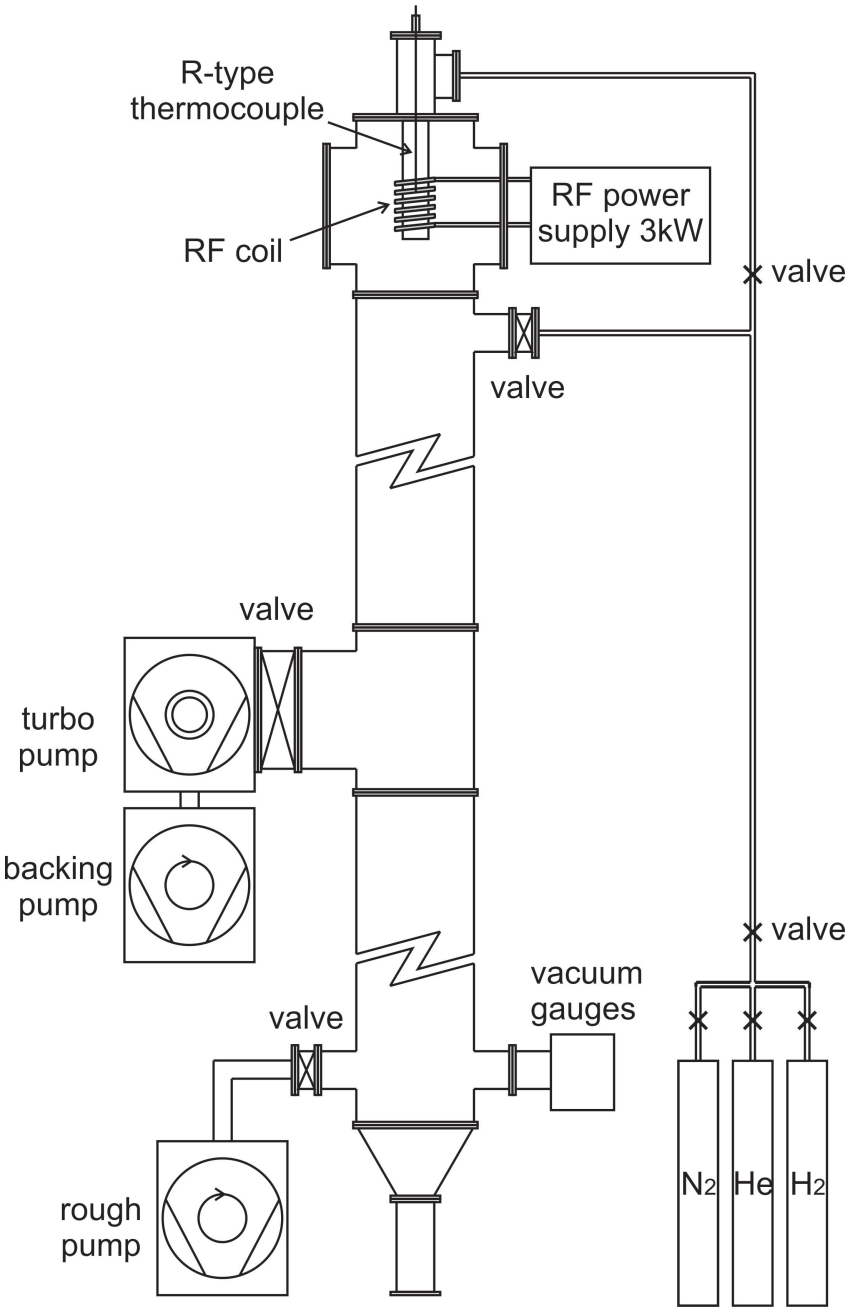

Figure 5.1.2: Schematic view of the 6.5 m drop tube

than Ag-28wt.%Cu melting point 1052.25 K) by means of no-contact electromagnetic induction to ensure the fully molten ingot in the crucible. The R-type thermocouple is set on the top steel lid of drop tube and penetrated inside the crucible to detect the local temperature change of ingot. The digital detector connecting with the other side of thermocouple on the lid accepts the signal from the thermocouple and transfers it into the temperature output on the monitor.

WATER-COOLING SYSTEM

The RF induction furnace on the top of drop tube consists of a 5 mm diameter tube of water-cooled cooper rings surrounding a container of refractory material (the graphite susceptor).

On the one hand, a radio-frequency alternating current generated by 3 kW RF power supply is passed through the copper coil of wires to transfer energy from electromagnetic induction to the conducting object (Ag-28wt.%Cu ingot). On the other hand, the induction takes control of the intensity in heating action. Although the energy transfer efficiency is largely dependent on the operating frequency acted on the working coil, the chilled water supply running through the coil continually removes waste heat and so guarantees a consistent heating cycle.

VACUUM AND GAS SUPPLY SYSTEM

The vacuum and gas system is equipped to avoid oxidization in the process of induction heating and consequently for a catalytic free atmosphere.

The experimental procedure to obtain such a clean environment is complex, which requires a few steps as following. The presence of air pressure inside drop tube needs to be vacuumed down $\sim 10^{-4}$ Pa by the mechanical rotaryvane pump and further down $\sim 10^{-7}$ Pa by the turbo-molecular pump. Then the subsequent backfilling of 40 kPa nitrogen gas (N_2) keep the drop-tube environment clean and insert.

EXPERIMENTAL PROCEDURE

Firstly, the ingot is loaded in the RF induction system before the top lid was sealed and then the extended thermocouple was connected with the digital detector by an electrical wire. Subsequently, the inner air pressure wa pumped down $\sim 10^{-7}$ Pa with the assistance of the oil-sealed rotaryvane and turbo-molecular pump, followed by backfilling 40 kPa protective N_2 gas. When the clean environment is ready, the ingot located in RF induction furnace starts to be heated continuously and slowly till $\sim$ 1095 K is reached. Then the external 3×10^5 Pa N_2 gas is filled in the crucible to force the molten liquid to spray throughout 3 laser drilled holes. After the solidified droplets cool down the ambient temperature, they are collected from the bottom of drop tube.

5.1.3 DIFFERENTIAL THERMAL ANALYSIS

Differential thermal analysis (DTA) is a thermo-analytic technique in determination of sample properties. As shown in Fig. 5.1.3, the sample under study and an inert reference are symmetrically placed in the separate pan in DTA, to ensure each is subjected to identical thermal conditions. The thermocouple beneath each pan is made to track the temperature calibration between the sample

and the reference. The temperature change $\Delta T = T_s - T_r$ at a fixed time step is recorded to generate thermogram which is the differential temperature against temperature, either exothermic or endothermic. In Fig. 5.1.4, the endothermic reaction is shown downwards as a function of temper-

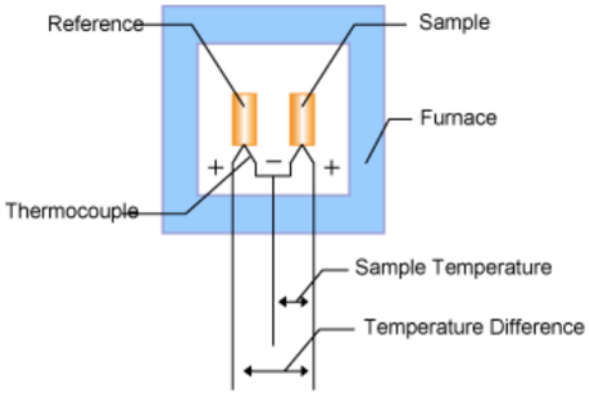

Figure 5.1.3: Schematic diagram of a DTA cell

ature on the abscissa. Firstly, there is only baseline between point A and B, denoting no reaction in between. At point B, the curve starts to deviate from the baseline (the dash line BD) and the conjectural point G by interpretation of the curve AB and CG represents the onset temperature of the endothermic reaction. The temperature difference arises greatly up to the maximum rate of heat evolution at point C, indicating either phase or melting transition take place. Once the temperature past point C, the endothermic change reduces down to point D and turns back the baseline DE. The baseline of pre- and post-reaction is extrapolated under the BCD peak, giving two separate baselines AB and DE due to distinct heat capacity of the sample relative to the reference. Also, it should be noted that one of temperatures at a range between point G and D can be the onset one of phase change or the first-order transition, depending on the pre-defined thermal program in run. For no or a small temperature gradient in the first-order transition, it is more like to the extrapolated onset (G) which is intersected with a tangent line through the greatest sharp slop of the leading edge of the peak (CG) and the extrapolated baseline (AB), whereas the peak (C) is more favorable for a broad melting range or a large temperature gradient [72].

In the case of drop-tube processed Ag-40at.%Cu droplet, the cooling process shall pass the eutectic point where three phases exist in equilibrium so that only small temperature gradient exists in this transformation. Thus the onset temperature (G) can be regarded as the eutectic temperature. Because the main theory behind phase diagrams is based around the latent heat that is evolved when a mixture is cooled, changes caused by exothermic reactions are more useful in examination of an onset temperature of transformation than that by endothermic ones.

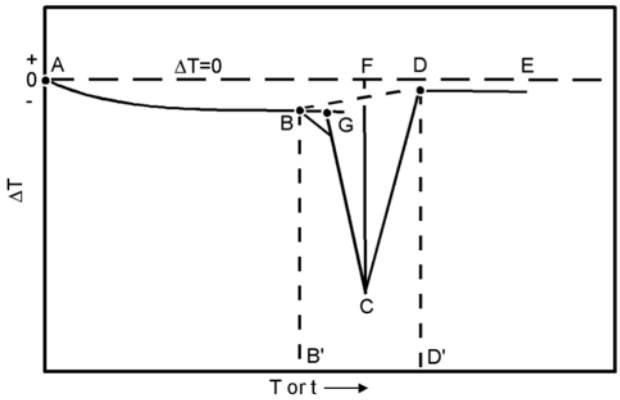

Figure 5.1.4: Thermogram of endothermic change in the sample relative to the inert reference

EXPERIMENTAL PROCEDURE

The undercooled Ag-Cu droplet and the reference were embraced by Al_2O_3 in each pan to avoid the potential contamination from the molten liquid during heating process, followed by moving into each holder in DTA cell. The reason to choose Al_2O_3 as the experimental reference is that Al_2O_3 has similar physical properties such as conductivity and heat capacity to the specimen Ag-40at.%Cu but yet no thermal event nor reaction in the operating temperature range. Moreover, the sharp peak of exothermic reaction in thermogram is highly sensitive to the cooling rate, since the temperature range under this peak might be too small to be detected at the large thermal rate. Therefore, each pan was then subjected to the identical pre-set thermal cycles (from 950 to 1100 K with the rate of 5 K/min) in desired constant Nitrogen atmosphere (0.4 MPa). The output of the detected temperature difference was transferred into the signal form of a thermal analysis curve (DTA curve) against temperature as shown in Fig. 5.1.5.

The interpretation of the onset temperature in exothermic reactions is similar with that in endothermic reactions. So the extrapolated onset of melting G in Fig. 5.1.5 is likely to occur the eutectic reaction. The temperature at G close to but not exactly at T_E can be attributed to many issues, including thermal rate, sample size and thermocouple position by using the SAT-8000 simultaneous thermal analyser. Under the endothermic reaction, however, there are two peaks instead of only one for the specimen at the exact eutectic composition. The possible interpretation of this change might give rise to the Ag-rich lamella with lower melting point starting to melt prior to the Cu-rich one. As a result, a larger amount of Ag-rich phases is molten to generate higher negative peak due to the lever rule, followed by smaller negative peak in response to melting of Cu-rich phases.

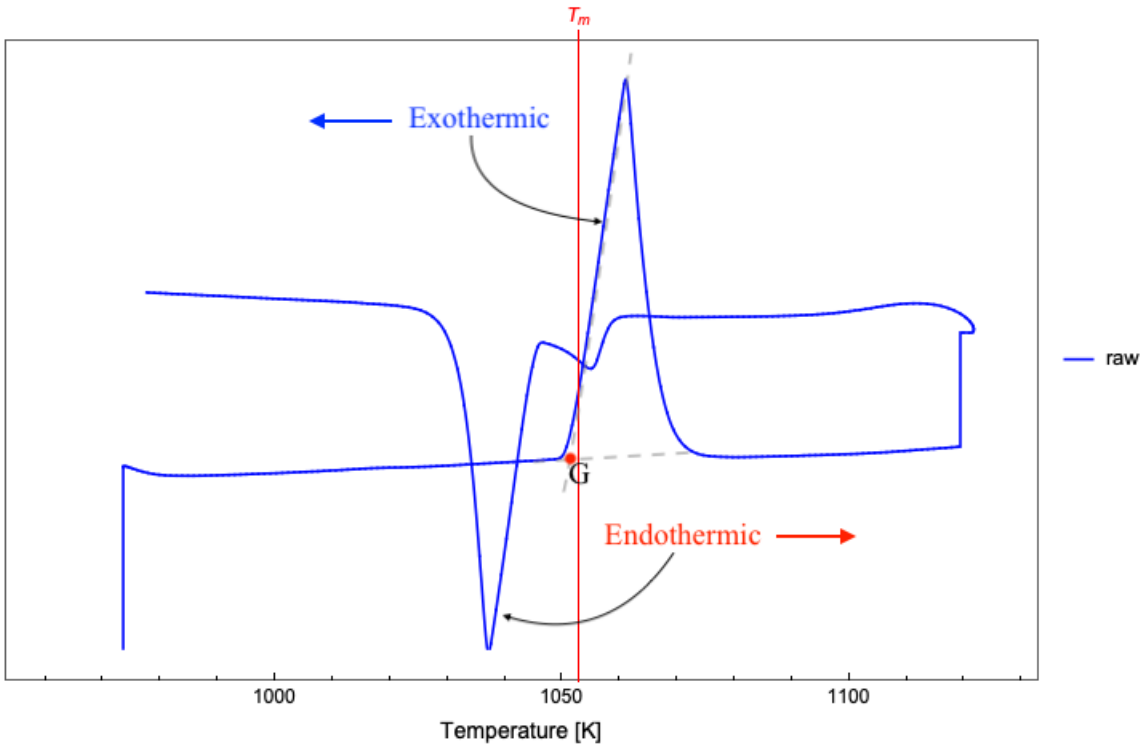

Figure 5.1.5: Thermogram of Ag-40at.%Cu droplet ingot

5.1.4 SCANNING ELECTRON MICROSCOPE

A scanning electron microscope (SEM) schematically shown in Fig. 5.1.6 employs a beam of electrons directed at a specimen, with which produces and magnifies images by the surface, or near surface structure of the specimen. The accelerated electrons supplied by the electron gun interact with atoms of specimen and encourage various secondary emissions backscattered out of sample to form the interaction volume as shown in Fig. 5.1.7. Those selected portions of electrons, such as secondary electron (SE), backscattered electron (BSE), characteristic X-ray (EDX) are collected by various detectors and transformed into the resulting signals that contain information of surface feature and composition. Depending on the type of detectors selected in SEM, those amplified signals combined with the position of electron beam produce an SEM image.

IMAGE FORMATION

The electron gun shown in Fig. 5.1.6 initially generates free electrons and accelerates them up to energies ranging from 1 ~ 40 keV. The electron beam of a current I_0 passes through two electro-

*Available at https://en.wikipedia.org/wiki/Scanning_electron_microscope
†Available at https://myscope.training/images/SEM-module/figure_26.gif

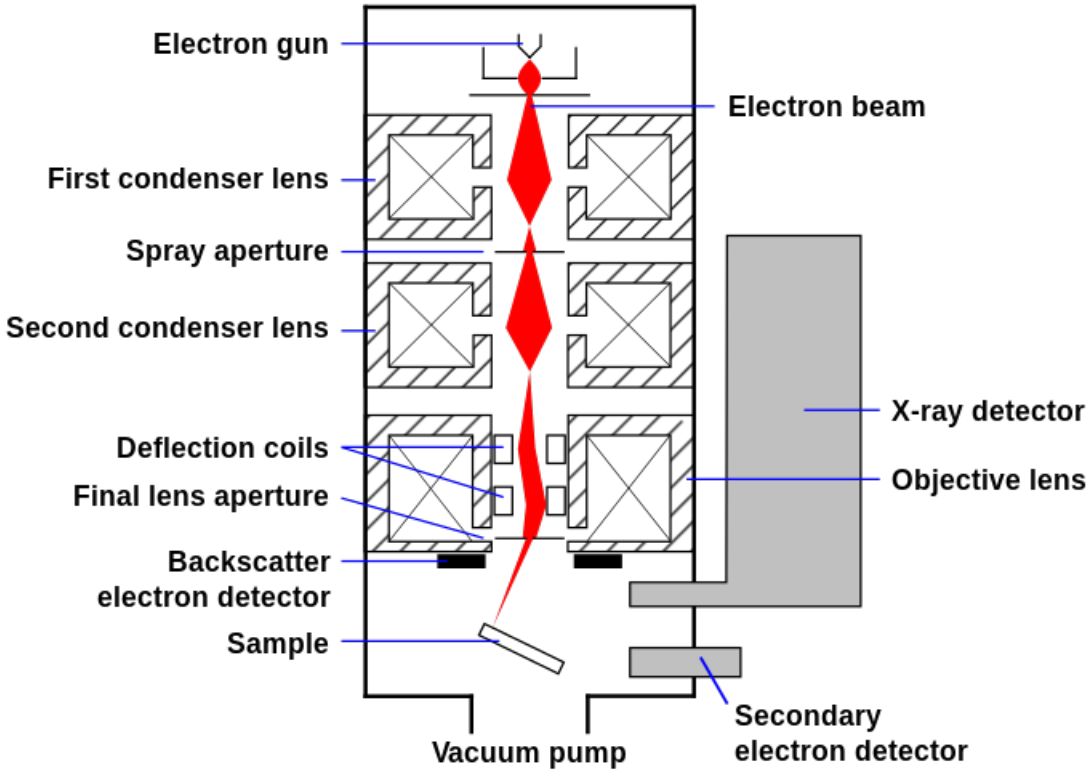

Figure 5.1.6: Schematic diagram of scanning electron microscope (SEM)*

magnetic condenser lenses and corresponding lens apertures to de-magnify the electron-beam crossover diameter, and then through pairs of scanning coils to deflect the beam in $x-$ and $y-$ axis for scanning a raster pattern on the specimen surface, followed by through the final lens aperture to minimize spherical aberration and control the current before entering the specimen [73]. The vacuum environment better than $\sim 10^{-5}$ Pa is necessary for all the optical paths in the specimen chamber of SEM to avoid scattering of the electron beam before reaching the specimen and so a reduction in image resolution by a larger probe size. And the liquid nitrogen filled in SEM operation chamber guarantees that the additional amount of heat generated during the demagnification of high current through multiple lenses can be cooled down.

When the primary electron beam penetrates the specimen, the interaction between accelerated primary electrons and the atoms of the specimen elastically and inelastically, generates the interaction volume in a form of hemisphere (Fig. 5.1.7) for intermediate and high atomic number Z, from which various radiations including SE, BSE, EDX and light or heat are generated. An analogue signal intensity from each radiation is measured by specialized detectors and amplified by electronic amplifiers before being digitally saved in response to the position of the beam scanning on the specimen surface.

Fig. 5.1.8 is one of SEM images that is obtained by detecting elastically BSE that remains unchanged

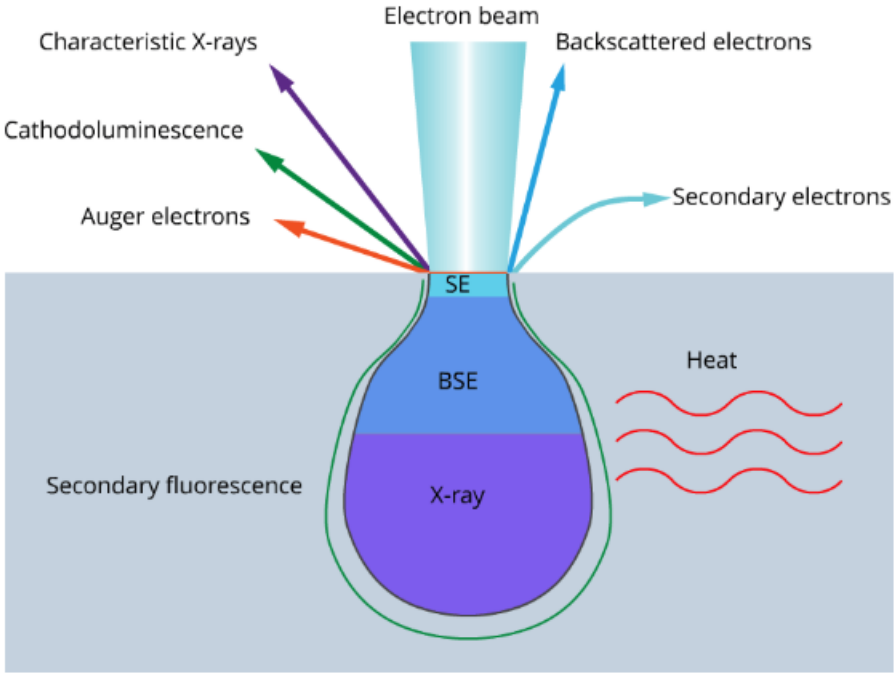

Figure 5.1.7: Signals emitted from different parts of the interaction volume, where secondary electron stands for SE, backscattered electron for BSE, and X-ray consists of both Bremsstrahlung and Characteristic X-ray[†]

kinetic energy and velocity of primary electron but come back out of the sample after the primary trajectory circle around the positive nucleus due to its attraction.

Resolution

Technically, SEM magnification can surpass $\sim 100,000\times$ in a scanning mode, but such high magnification in practical SEM examination only makes the detail bigger and more obscure. Because there is a limitation of SEM to distinguish two closest entities apart, which is also known as the resolution.

In SEM, the spatial resolution r depends on the electron probe size d ($\approx 2r$) and the theoretical minimum probe size is calculated by only considering diffraction at the aperture as

$$d_d = \frac{1.22\,\lambda}{\mu \sin\alpha} \approx 1.22\,\frac{\lambda}{\mu\,\alpha} \tag{5.1.1}$$

where the refractive index μ is assumed to be unity and the semi-angle of the beam is sufficiently small to have $\sin\alpha = \tan\alpha = \alpha$. When using reasonable values of $\lambda = 0.0037$ nm and $\alpha = 0.1$ radians, the SEM resolution is about $1.22 \times 0.0037/0.1 \approx 0.046$ nm. Such small size of probe is impossible to

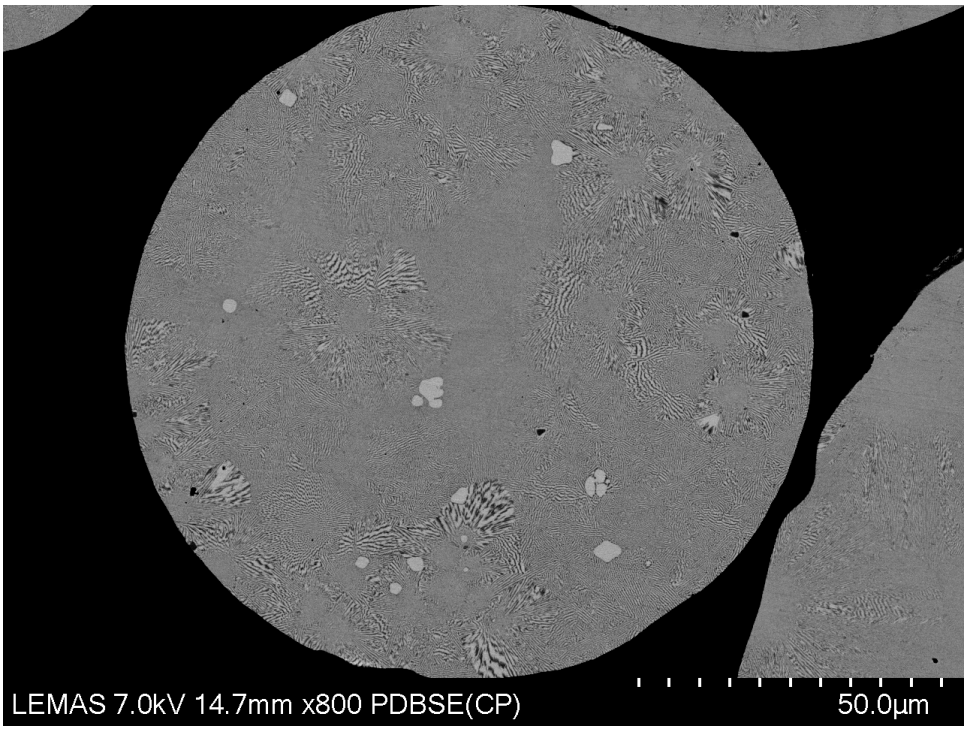

Figure 5.1.8: Cross-section SEM image generated by backscattered electron (BSE) in which the silver (Ag) rich region is characteristic with light grey, the copper (Cu) rich region is with dark grey and the eutectic region is with the greyscale in between

achieve, because the spherical aberration (monochromatic aberration) due to the different path lengths of different beams restricts the probe size from disc of least confusion by

$$d_s = 2\,C_s\,\alpha^3 \tag{5.1.2}$$

where C_s is the coefficient of spherical aberration of the lens.

It seems that decrease of the aperture size α can reduce the impact of spherical aberration on d_s. In fact, the SEM resolution becomes worse since d_d increase greatly in the range of $\alpha \in [0, 0.1]$ radians (Eq. (5.1.1)) and the beam current might decrease too low to generate a usable signal from the interaction volume (**??**).

Without considering the de-magnified diameter of the beam (d_1), the real value of probe size may be expressed as

$$d = \sqrt{d_s^2 + d_d^2} = \sqrt{\left(\frac{1.22\,\lambda}{\alpha}\right)^2 + \left(2\,C_s\,\alpha^3\right)^2} \tag{5.1.3}$$

Guessing the optimum size of aperture value α_{opt} for the minimum probe size might be expressed as

$$\alpha_{opt} = A\,\lambda^{1/4}\,C_s^{-1/4} \tag{5.1.4}$$

then

$$d = \left(\frac{1.4884}{A^2} + 4\,A^6 \right)^{1/2} \lambda^{3/4}\, C_s^{1/4} \tag{5.1.5}$$

When the electrons are accelerated to a velocity which is a significant fraction of the velocity of light at the accelerating voltages λ, the approximation of electron wavelength is [73]

$$\lambda = \left(\frac{1.5}{V + 10^{-6} V^2} \right)^{1/2} \text{[nm]} \tag{5.1.6}$$

As Fig. 5.1.9 shows, the probe size approaches the minimum value at $A = 0.77$ as

$$d_{opt} = 1.83\,\lambda^{3/4}\, C_s^{1/4} \quad \text{[nm]} \tag{5.1.7}$$

$$\alpha_{opt} = 0.77\,\lambda^{1/4}\, C_s^{-1/4} \quad \text{[radian]} \tag{5.1.8}$$

In SEM operated with an objective lens of $C_s = 20$ mm, change of convergence angle and probe size with respect to energy difference can be obtained by applying sem-mag-08 into both Eq. (5.1.7) and Eq. (5.1.8). The calculated relationships are both shown in Fig. 5.1.10 respectively.

On the one hand, increase of volts applied in SEM electron gun reduces the size of probe and consequently improves the resolution of imaging. On the other hand, the beam current I is sensitive with the change of the convergence angle of beam α. Only a portion of current within 2α can pass through this objective aperture, leading to more noises rather than useful information of surface properties being generated from the detected signals.

In general, the resolution is largely restricted from the size of interaction volume. The greater the kV, the greater the power of penetration by the beam into the sample, the higher the possibility of specimen damage due to the external heat, and the larger the interaction volume, which leads to a reduction in the spatial resolution created from those signals. Although the SEM resolution can ideally achieve the half size of probe diameter $d/2$ as $2 \sim 3$ nm which is in the range of $5 \sim 10$ kV (Fig. 5.1.10), it is impossible for BSE to have the resolution below ~ 0.1 μm [73] due to the limitations of the interaction volume as shown in Fig. 5.1.11.

Depth of Field

The *depth of field* is defined as a range of positions for an object without change in the sharpness of the image. In SEM, the depth of field h is approximated when the minimum size of specimen pixel ($\sim 0.1/\mathrm{M}$ mm) on a cathode ray tube (CRT) is equal to the electron beam diameter as

$$\frac{0.1}{\mathrm{M}} = h\,\alpha \iff h = \frac{0.1}{\alpha\,\mathrm{M}} \tag{5.1.9}$$

The probe convergence angle α after the final lens aperture shown in Fig. 5.1.7 is determined by the diameter of the final lens aperture D and the working distance WD.

$$\alpha = \frac{D}{2\,\mathrm{WD}} \tag{5.1.10}$$

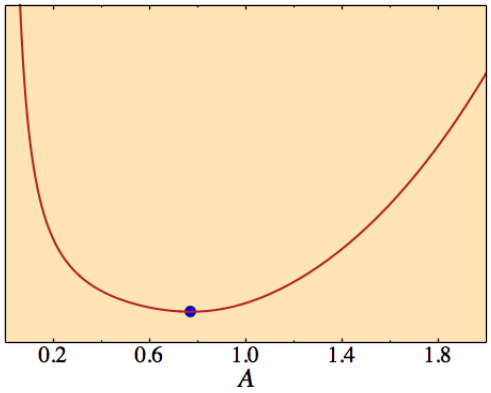

Figure 5.1.9: Relationship between the probe size and the constant A in Eq. (5.1.5)

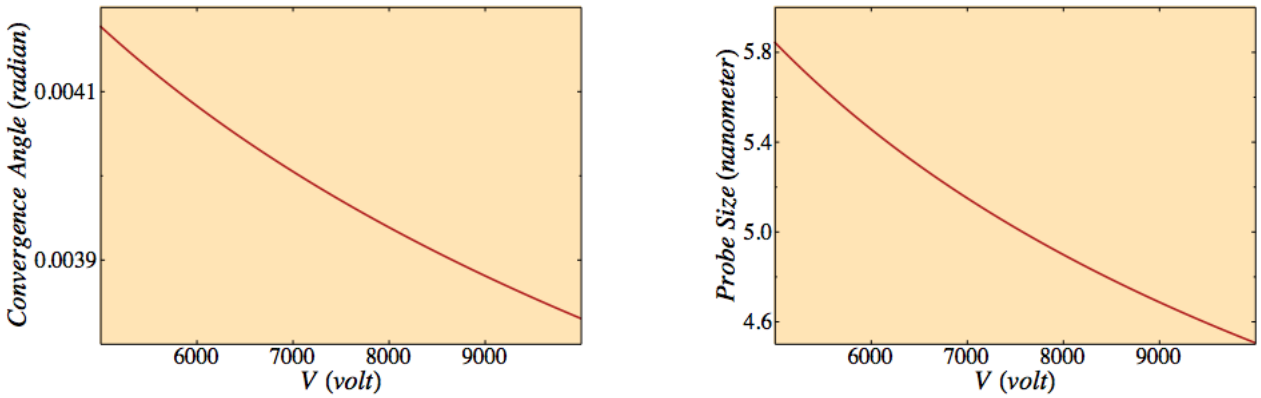

Figure 5.1.10: Curves of convergence angle α_{opt} and probe size d_{opt} against energy difference

Combining with Eq. (5.1.9) with Eq. (5.1.10),

$$h = \frac{0.2}{D\,\mathrm{M}} \cdot \mathrm{WD} \quad [\mathrm{mm}] \tag{5.1.11}$$

Provided for typical value of D = 0.1 mm and WD = 30 mm at magnification 300×, the depth of field should be obtained by Eq. (5.1.11), which is at the order of 200 μm. Because of this, the interpretation of SEM image of three-dimensional (3D) objects at low magnifications is intuitive and no prior knowledge of image formation in this apparatus is required as shown in Fig. 5.1.12.

5.1.5 Microstructural and Compositional Characterization

Sample Preparation

The droplets are initially classified into different size groups by the sieves of sizes among 38 ~ 53, 53 ~ 75, 75 ~ 106, 106 ~ 150, 150 ~ 212, 212 ~ 300, 300 ~ 500, 500 ~ 850, 850 ~ 1000 and > 1000 μm.

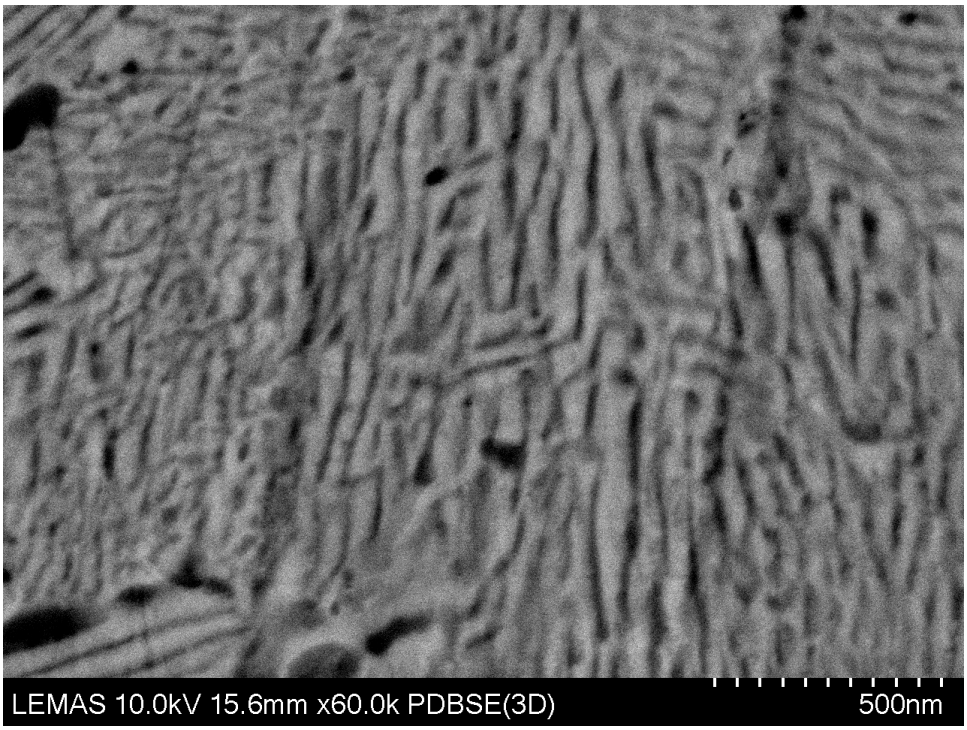

Figure 5.1.11: SEM image of droplet cross-section generated by BSE at magnification ×60.0 K

For examination of topographic image in SEM, each group of droplets only need to be fixed firmly on one conductive specimen holder.

For examination of compositional image and quantitative analysis in SEM, each group of droplets needs to be prepared in one hot mounting resin by the conductive powders with carbon filler. The mounted specimens are then ground down using a series of progressively finer SiC grinding papers from 400, 800 to 1200 grit and are polished with diamond compounds using 3, 1, 0.25 μm polishing cloths on a semi-automatic polishing machine. In process of sample preparation, the additional care is necessary, not only for the surface quality check, but also for the diameter measurement of ground droplets in each resin, by means of optical microscopy. Because an Axiocam MRC5 Zeiss digital camera installed on its top of the selected Nikon Optishot optical microscope is connected with computer and operated by built-in AxioVision software, the scratch check and the grinding size measurement are accomplished together on computer screen with aid of the scale bar function.

Both the mounted specimens and the fine droplets demand external carbon coatings to improve the imaging by using a turbo-pumped thermal evaporator, in which the carbon source is settled between two high-current electrical terminals in a vacuum system and then is heated up to its evaporation temperature to produce a stream of carbon finely deposited on the their surface.

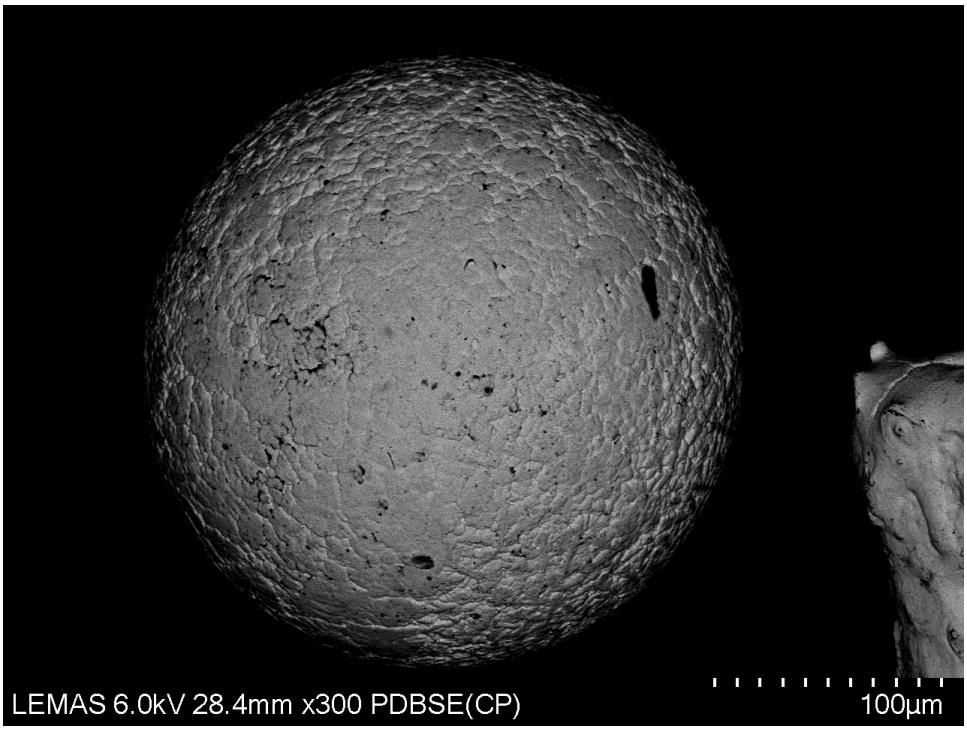

Figure 5.1.12: SEM image of droplet surface (in the range of diameter 212 ~ 300 μm) generated by backscattered electron (BSE) displays 3D semi-sphere macro-structure

COMPOSITIONAL IMAGE

The compositional information from sample surface can be yielded by detecting BSE signals. Fig. 5.1.8 generated by BSE provides information about the distribution of different phases, which can be interpreted following.

First of all, the monochromatically gray-scale SEM image (with no external color) gives rise to electron wavelengths of detected signal having much smaller than the smallest wavelength of visible light. Secondly, the amount and direction of BSE coming out of sample surface is sensitive to the surface condition and electronic structure of the material. According to those, the polished flat specimens are prerequisite under sample preparation prior to SEM examination and the unique physical property of each material such as atomic number Z and density makes the grey-scale value different and forms compositional contrast when multiple materials exist in a specimen. Since heavy atoms with a high atomic number can scatter stronger than those with a low one, the silver-rich region ($Z_{Ag} = 47$) is characteristic with brighter grey scale and the copper-rich region ($Z_{Cu} = 29$) is with dark one. Either anomalous or regular eutectic is assumed as the evenly cooperative growth so its grey scale is in between.

Lastly, those small electrons captured by the detector can have unlimited magnification, but the resolution of SEM degrades the practical range and is limited to ~ 0.1 µm in the area of composi-

tional interest.

TOPOGRAPHIC IMAGE

In SEM, both SE and BSE are widely used to study the surface features of a specimen, *topography*.

SE has very low energies due to the smallest sampling interaction volume on specimen, so its signal provides particularly good detail of the shape and morphology of specimen surface. Although the compositional image is sufficient good for phase identification in this experimental work, the polished surface can be well checked by means of SE topogrphic image as shown in Fig. 5.1.13. At most of cases, the dark region can be easily identified as Cu-rich region whereas others might be suspected as internal imperfections, i.e. shrink holes and porosities, due to isolated pools of liquid during rapid solidification. Then the SE image in Fig. 5.1.13a can be helpful to distingish those internal defects from microstructure. Moreover, the assistance of SE topography can easily determine else imperfection such as dirt and scratch on sample surface which might form unknown phases on BSE images.

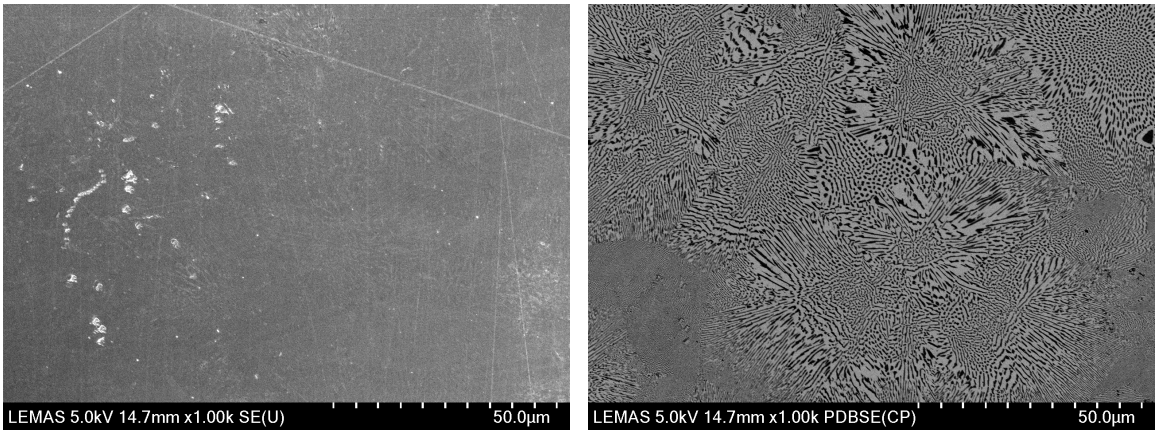

(a) SE image (b) BSE image

Figure 5.1.13: Both SE and BSE image taken at the same selected location

BSE can also provides a good insight to not only compositional identification but also understanding of topography and morphology on examined specimens. As shown in Fig. 5.1.14a and Fig. 5.1.14b, there are two different topographies taking place on the surface of rapid-solidified droplet. The characterization of surface topography shown in Fig. 5.1.14 will be related to the solidification circumstance to further explain in Section 6.1.

EDS X-RAY MICROANALYSIS

When the primary electrons spread out in the sample to form the interaction volume, X-rays are also produced by interaction of the electron beam with the sample (Fig. 5.1.7), which consist

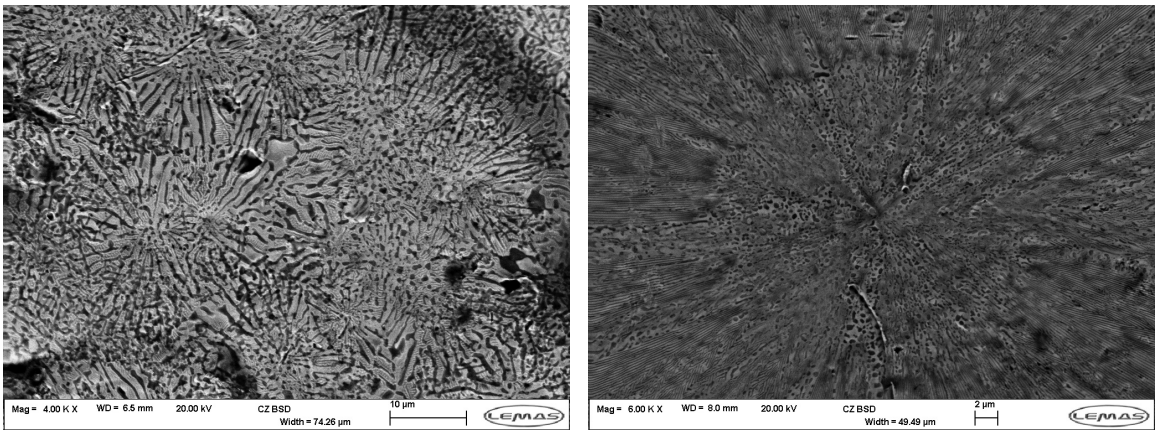

(a) (b)

Figure 5.1.14: Topography of droplet surface obtained by BSE

of both Bremsstrahlung and Characteristic X-ray. The characteristic peak superimposed on the Bremsstrahlung background forms X-ray spectrum shown in Fig. 5.1.15a.

Bremsstrahlung X-rays, known as Bremsstrahlung background, are produced by slowing down of the primary beam electrons due to the electric field surrounding the nuclei of the atoms within the sample. Because of the Duane-Hunt limit, the energy of Bremsstrahlung X-rays cannot be greater than that of the primary electrons (E_0). In the case of Fig. 5.1.15a, X-ray spectra is in the range of energies from 0 to 9 keV. Also, a 'whale-like' shape in the X-Ray spectrum diagram can be explained that the chance to lose all of primary energy in one single interaction between the primary electron and the sample is very rare. It is more likely to have a number of interactions in which small proportions of the initial energy are lost and an equivalent number of low-energy X-rays is produced continuously until no more energy is left in the primary electron. Because of this, the intensity of X-ray increases gradually from E_0 to lower energies. However the fact that the X-ray intensity at energies towards 0 eV reduces to zero gives a reason for a large number of very low-energy Bremsstrahlung X-ray absorbed by either the sample or the X-ray detector before being detected.

Characteristic X-rays, known as characteristic peaks, are produced by electron transitions between the outer electron and inner shell vacancy. The electrons of each shell and sub-shell have specific ionization energies in response to every element. Because of this, the difference between the energies of the two excited states in different shells thus is used to characterize the particular atomic species. In order to excite characteristic X-rays, the primary electron (E_0) controlled by the accelerating voltage must have enough energy to overcome the critical ionization energy so that localized inner-shell electrons can be knocked out of an atom. The simple estimation of those energies can be given by

$$E_n = -13.57 \frac{(Z-1)^2}{n^2} \tag{5.1.12}$$

where Z is the atomic number and n is the principal quantum number such as K-shell for 1 and L-

shell for 2. For the transition of a single electron of Cu from M-shell to K-shell, the potential energy difference can thus be estimated as

$$\Delta E = E_3 - E_1 = -13.57\,\frac{29-1}{3} + 13.57\,\frac{29-1}{1} = -1182.1 + 10638.9 \approx 9\ \text{keV} \tag{5.1.13}$$

In SEM, the keV range of X-ray spectrum is controlled by the accelerating voltage (kV). The maximum keV can not surpass the accelerating voltage applied in SEM, i.e., 9 keV spectrum will range from approximately 0 to 9 keV when 9 kV is applied. Although $K_{b_1} \approx 9$ keV calculated in Eq. (5.1.13) is the critical energy for Cu to excite a characteristic peak, Fig. 5.1.15a fails to show a discrete peak out of Bremsstrahlung background. The reason can be explained that an efficient generation of x-rays in the spectrum diagram not only requires the critical excitation energy inside the range of keV energies but also satisfies the ratio of E_0 to E_n (the over-voltage ratio) under 2.7. For a beam at 9 keV applied in Fig. 5.1.15a, an average x-ray enrgy due to the over-voltage ratio is around 3 keV, which gives a sufficient energy to knock out the L shell of Cu (refer Table 5.1.1) and so generates a discrete peak around 0.9 keV. For Ag, both sub-shell L_a and L_b as listed in Table 5.1.2 are excited and generate two separate overlapping peaks in Fig. 5.1.15a in qualitative EDX microanalysis using SEM.

The advantage of using low energy such as 9 keV to excite L-shell of both Cu and Ag instead of K-shell is that the lower number keV has a narrower peak and so requires the shorter process time to yet achieve a high resolution peak. As a result, the dead time is shorter and potentially the sample is damage free in EDX analysis. Moreover, the short dead time can reduce a fixed counting time of each point during elemental X-ray map and thus largely improve the efficiency of X-ray mapping for the distribution of particular elements.

Elemental X-ray maps are produced by recording a number of X-ray photons over a selected rectangular area as shown in Fig. 5.1.16. When the electron beam is rastered over this area, the X-ray detector collects this number of X-ray photons at each point which is transferred into a grey-scale value ($0 \sim 255$) for a pixel on the screen. Then the built-in software, *AZtec*, can automatically determine the particular element at each pixel and provides a function to assign a selected color to a single grey scale. In Fig. 5.1.16b, Cu and Ag are assigned into red and green respectively and also combined together to form a false colorful image. Combining Fig. 5.1.16a with Fig. 5.1.16b, the EDX map can reveal more information related to variations of composition over the selected area.

Table 5.1.1: K and L shell emission lines (eV) of Cu[‡]

K_{a_1}	K_{a_2}	K_{b_1}	L_{a_1}	L_{a_2}	L_{b_1}
8047,78	8027.83	8905.29	927.7	929.7	949.8

[‡]Available at http://xdb.lbl.gov/Section1/Periodic_Table/Cu_Web_data.htm.
[§]Available at http://xdb.lbl.gov/Section1/Periodic_Table/Ag_Web_data.htm.

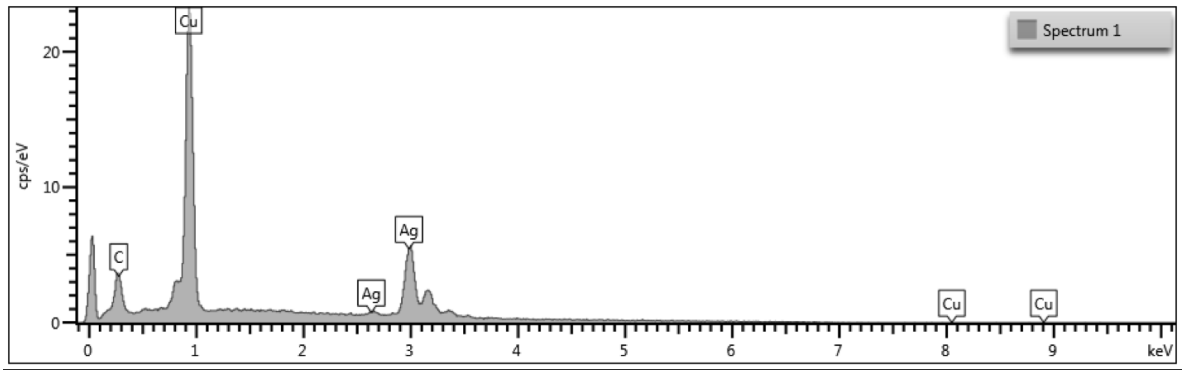

(a)

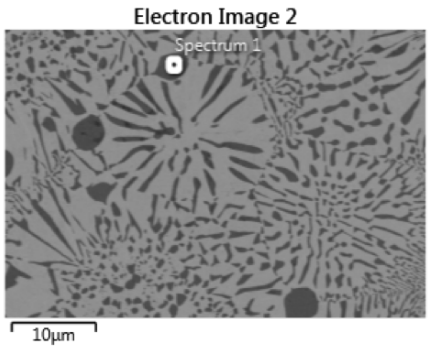

(b)

Figure 5.1.15: (a) X-ray spectrum excited from the interaction volume by a beam of 9 keV and (b) location of EDX point analysis

Table 5.1.2: K and L shell emission lines (eV) of Ag[§]

K_{a_1}	K_{a_2}	K_{b_1}	L_{a_1}	L_{a_2}	L_{b_1}	L_{b_2}
22162.9	21990.3	24942.4	2984.3	2978.2	3150.9	3347.8

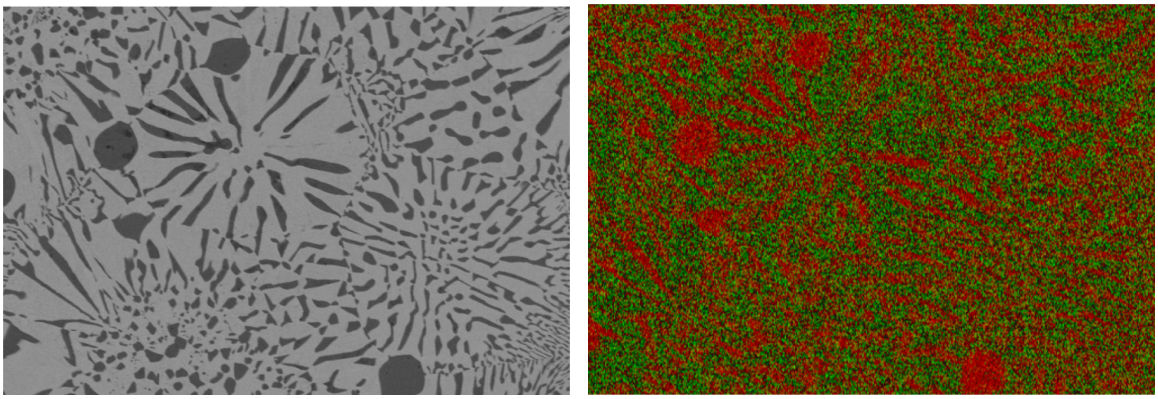

(a) (b)

Figure 5.1.16: BSE image (a) and X-ray distribution map (b) for eutectic Ag-Cu sample where red (Cu) and green (Ag) are combined together

5.2 Quantitative Image Analysis

Although SEM enable a quantitative analysis by taking the Characteristic X-rays in comparison with data measured from standard reference materials to obtain the weight percent of the elements present either at a spot (Fig. 5.1.15b) or over an area (Fig. 5.1.16b), the quantitative measurement of anomalous eutectic (introduced in Section 2.3) over a selected area is impossible to achieve by the EDS micro-analysis. In [63], the *ImageJ* contour plotting is used to identify three distinct phases successfully owning to each phase having a distinct range of grey-scale values. Firstly the threshold for the phase with the middling greyscale values is carefully set to separate it from the other two phases. Then the remaining phases can be identified as the greyscale values either below or above this threshold respectively as shown in Fig. 5.2.1.

For the eutectic morphology, the simultaneous growth of two phases (Fig. 1.2.5) leads to distinct compositions in each phase since one component rejected by one phase is in favour of the growth of the other. As a result, each phase has different average atomic mass and gives rise to different greyscale value in BSE image in Fig. 5.1.16a. Those two separate greyscale values increase the difficulty of *ImageJ* contour plotting to automatically recognize the eutectic region. However, it is interesting to note that the darkest regions in Fig. 5.2.1 are the eutectic phases. Either low magnification applied in SEM or fine eutectic spacing contributes to low resolution over these eutectic regions and consequently density variation inside eutectic resolves as an average density to appear nearly uniform greyscale value in BSE image. Therefore, it is possible to recognize the lamellar eutectic by *ImageJ* when the greyscale values of both phases are merged towards a uniform one.

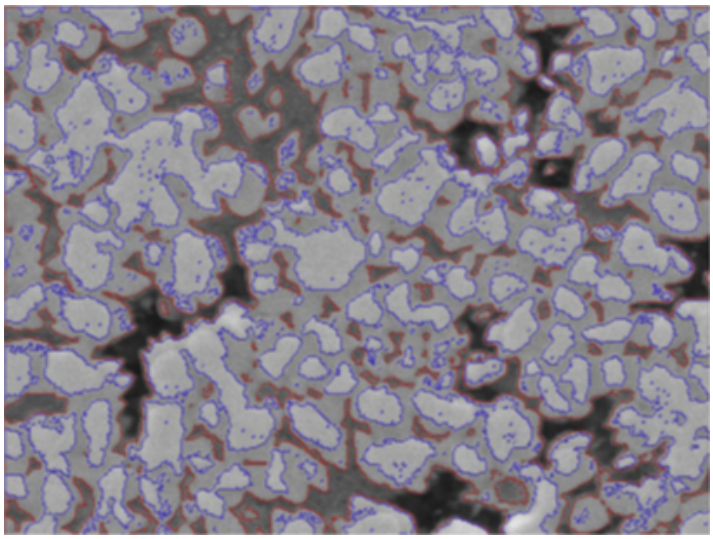

Figure 5.2.1: Use of the *ImageJ* contour plotting add-on to establish density ranges for each phase [63]

When different gaussian blurs are applied in Fig. 5.2.2a, Fig. 5.2.2b and Fig. 5.2.2c, the corresponding change of plot profiles due to the change of greyscale values can be noticed as Fig. 5.2.3a,

Fig. 5.2.3b, and Fig. 5.2.3c respectively. In the original image Fig. 5.2.2a, the anomalous eutectic is located in the left side of image and surrounded by lamellar eutectic, in which the plot profile in Fig. 5.2.3a shows the greyscale value changes from 0 to 255. When the gaussian blur increases from 0 to 1 to 2, the plot profile gradually reveals the lamellar eutectic on the right side of Fig. 5.2.3c (red circle marked).

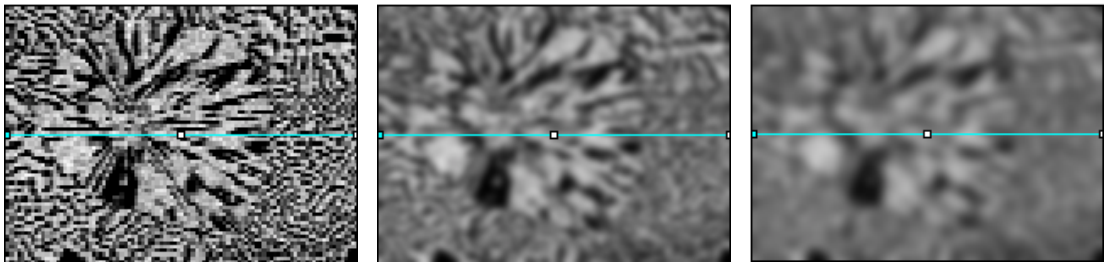

(a) (b) (c)

Figure 5.2.2: BSE image that is applied with gaussian blur = 0 (a), = 1 (b), = 2 (c)

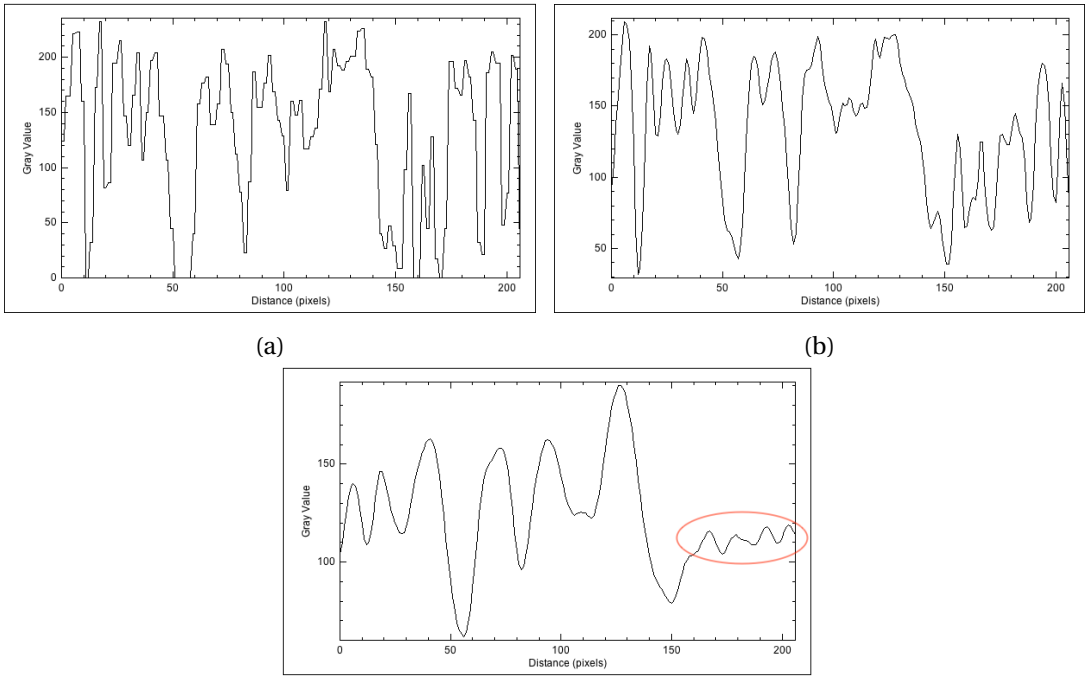

(a) (b)

(c)

Figure 5.2.3: Plot profile measured from BSE image that is applied with gaussian blur = 0 (a), = 1 (b), = 2 (c)

Combining the filter function with the binary function, then anomalous eutectic region can be identified by *ImageJ* as Fig. 5.2.4 shows. At last, a macro program is written within *ImageJ* to extract image density data from a series of ellipses of decreasing size. Through the mask as shown

in Fig. 5.2.5, density data for each ellipse was subtracted from the preceding ellipse in order to produce density data for a series of annuli. The processing result will be illustrated in Section 6.2.1.

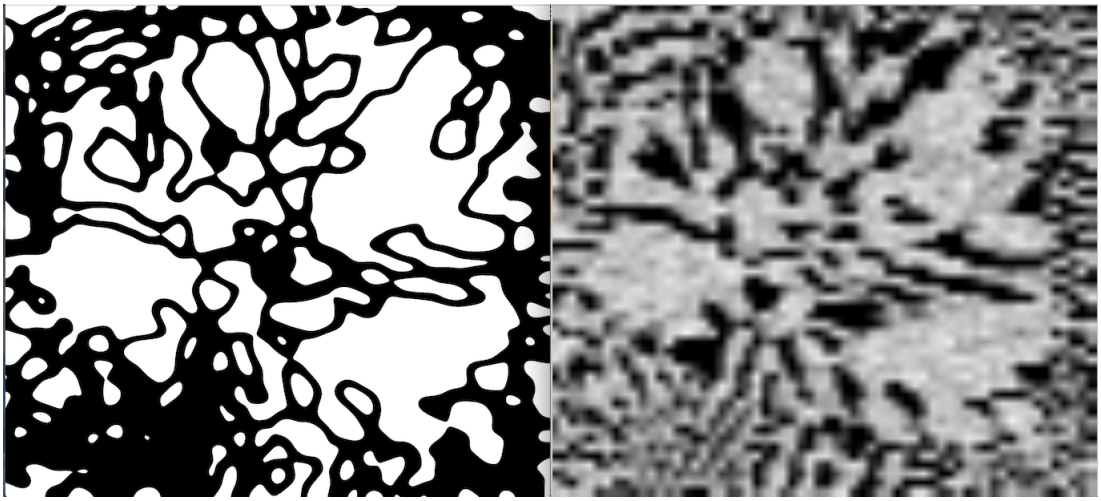

Figure 5.2.4: Comparison of marked anomalous eutectic region with BSE anomalous eutectic region

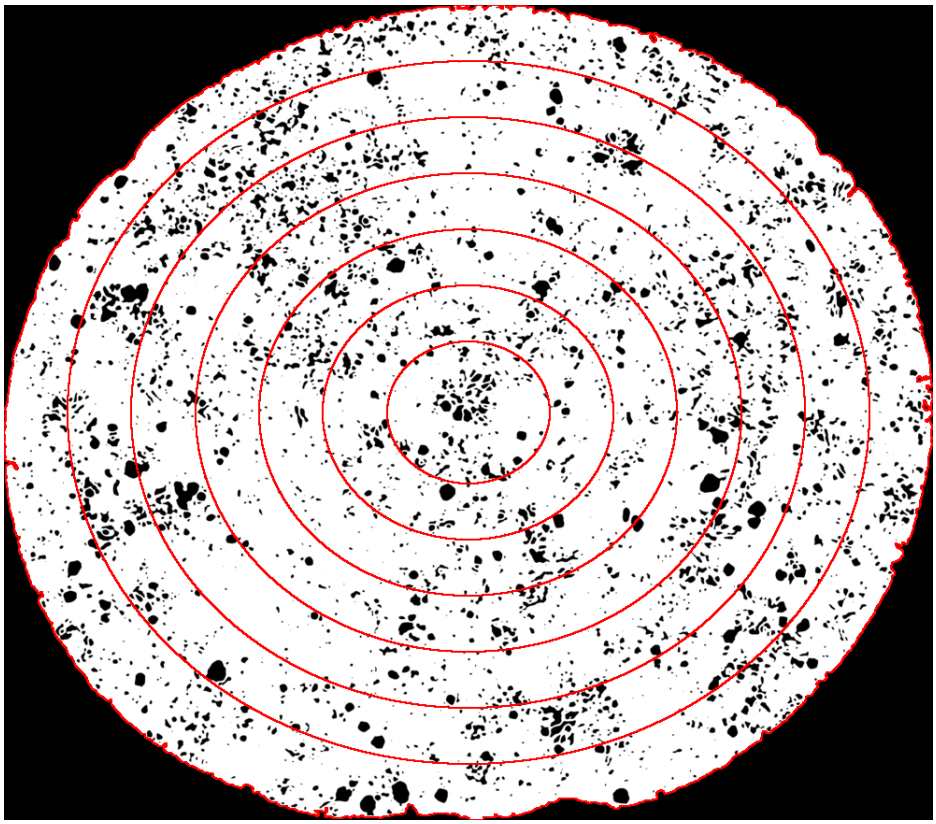

Figure 5.2.5: Positions of the annuli used in the quantitative image analysis

5.3 NUMERICAL METHOD

The objective of the 2D forced convection heat transfer modelling in Section 3.2 is to simulate the local change of fluid temperature surround the spherical solid by Eq. (3.2.1) and the corresponding change of local Nussult number Nu_θ by Eq. (3.2.15).

Although the local heat transfer coefficient Nu_θ can be obtained by refering Eq. (3.2.15) and then applied as the boundary condition in calculation of temperature distribution inside the spherical droplet numerically by ADI scheme (Section 4.2.2), the overall thermal change of solidification might be impossible to achieve by a means of Eq. (4.2.4) with external heat source term. Since neither the estimation of nucleation site nor the prediction of the interface growth between liquid and solid is possible under the rapid heat transfer. The macroscopic heat transfer modelling (see Section 3.1) is then used to analyze the time-dependent temperature change of droplet of different sizes under cooling process before the droplets touch down the bottom of drop-tube.

In the macroscopic heat transfer modelling, the metallic sphere is assumed to have a sufficiently high heat conductivity κ_s for a droplet with sufficiently small size, such that the temperature gradient inside droplet is safely neglected at any instant of time in a liquid or gaseous environment. However, this assumption might only be suitable for droplets at small size range 38 ~ 100 μm. For the droplet size between 100 and 8500 μm, the temperature gradience inside droplet during solidification would be existed to generate different local Nu_θ at any instant of time.

The average temperature of each size of droplets determined by averaging the local temperatures over the entire sphere volume will be compared with that obtained by Eq. (3.1.3) under the constant Stokes flow velocity w_f.

On the other hand, the convection heat transfer coefficient h introduced in Section 1.3.2 strongly depends on the type of the fluid flow, either laminar or turbulent. For a creeping flow, the fluid velocity is expressed by Eq. (3.2.2a) and Eq. (3.2.2b) in Section 3.2.1, in which the flow around the sphere is steady at $r \to \infty$. For a turbulent circular free jet emerging from an orifice into a fluid at rest, the gas velocity decay profile $u_f(z)$ along the centerline of the incompressible free jet with distance (z) is expressed

$$\frac{u_f(z)}{u_0} = \left\{1 + \left(\frac{z}{\lambda}\right)^{20}\right\}^{-0.05} \quad \text{and} \quad \lambda = 10.5\sqrt{A_e} \tag{5.3.1}$$

where the initial velocity of the atomizing gas

$$u_0 = 0.03973 \frac{p_f}{\rho_f \cdot \sqrt{T_0}} \tag{5.3.2}$$

To estimate a realistic forced flow over the sphere surface, both Eq. (3.2.2a) and Eq. (3.2.2b) for the creeping flow and Eq. (5.3.1) for the turbulent flow will be applied in the heat transfer modelling in Section 3.1.

CHAPTER 6

RESULT

6.1 EXPERIMENTAL RESULT

6.1.1 RAW MATERIAL FOR DROP-TUBE PROCESS

A commercial Ag-Cu eutectic ingot was chosen as the experimental material for the drop-tube processing, by which droplets of various sizes were generated in flight (as introduced in Section 5.1.2). The main reason for using this alloy rather than else alloy in the experimental investigation of drop tube processing is its thermo-physical data are comparatively well known and also various containerless processing techniques, such as gas atomisation [4, 45], drop tube processing [33, 43], electromagnetic levitation [19] and melt fluxing [7, 41, 42] have been carried out on it.

In Fig. 6.1.1, lamellar Ag-Cu eutectic is clearly observed from the cross section of this commercial ingot, despite there are a few regions of coarse eutectic isolated from those fine lamellar eutectic. As the response to the distinct difference between the atomic mass of Ag (47) and Cu (29), the location of different phases in the sectioned sample can be clearly revealed by the different greyscale levels in BSE image (introduced in Section 5.1.5). Thus, the Ag-rich phase (β) scatters electrons more strongly than the Cu-rich phase (α) does, so β-phase appears lighter than α-phase in Fig. 6.1.1. Because of greyscale changes via density variation in BSE images, it is possible to use the built-in *ImageJ* function, line profile, to measure the interlamellar space λ of lamellar eutectic. Depending on the response from the backscatter detector, the greyscale values of α phase and β phase along the selected white line in Fig. 6.1.1 are 90 ~ 110 and 160 ~ 190 respectively as shown in Fig. 6.1.2. As a result, the interlamellar space is around 0.1 μm.

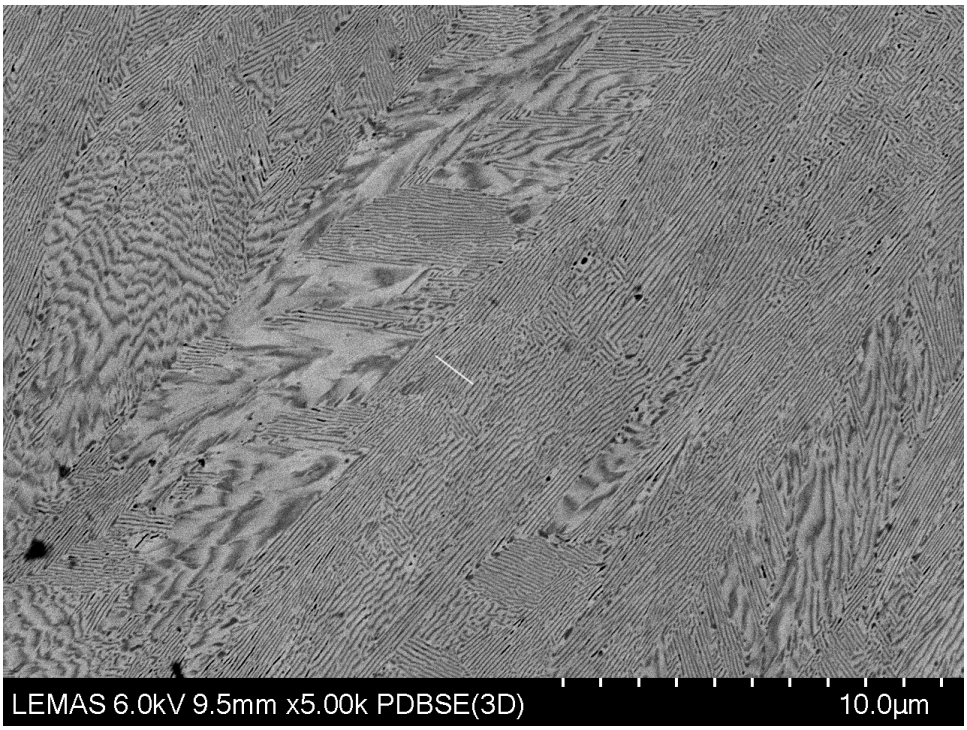

Figure 6.1.1: BSE image showing mircrostructure of Ag-Cu eutectic ingot

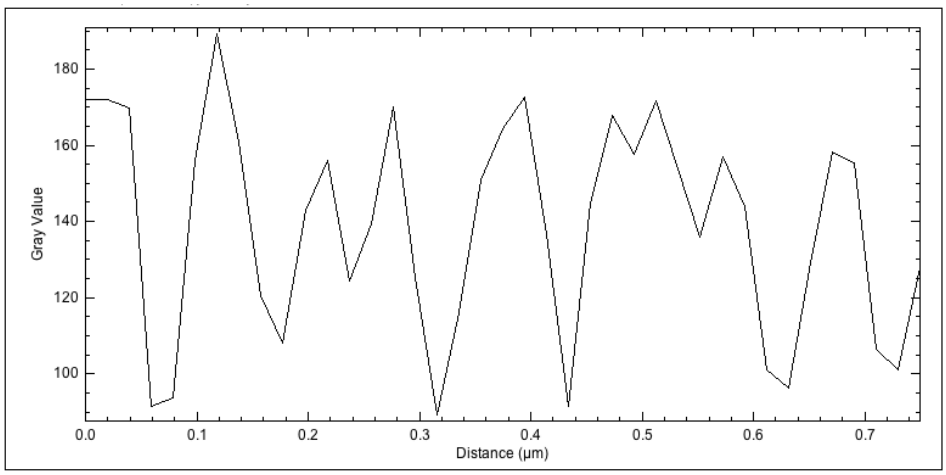

Figure 6.1.2: Line profile characteristic with a selected line across a section of lamellar eutectic in Fig. 6.1.1

6.1.2 SEM / EDS VALIDATION OF PHASES

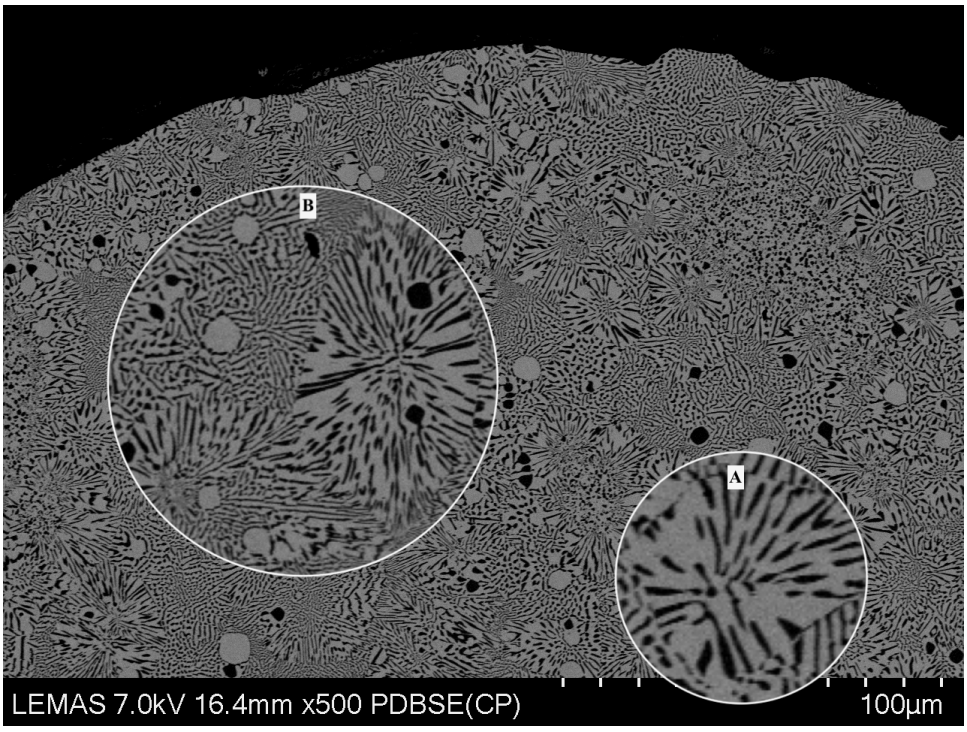

(a) Anomalous eutectic formed inside the droplet

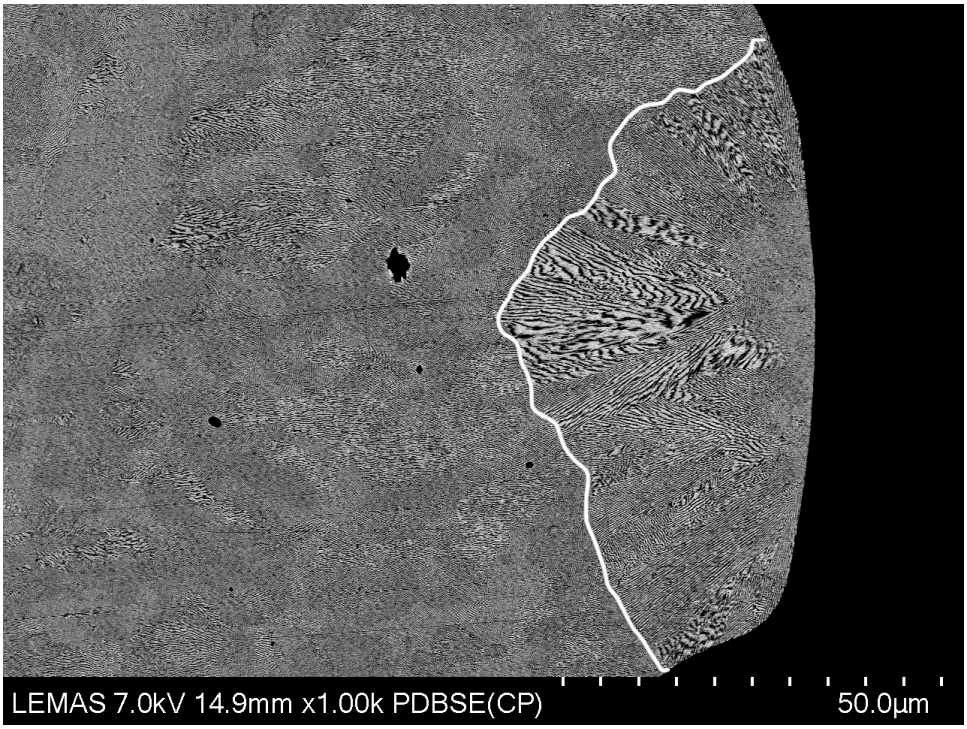

(b) Anomalous eutectic formed from the surface

Figure 6.1.3: Microstructure of anomalous eutectic in the sectioned samples

The selected commercial Ag-Cu ingot (Fig. 6.1.1) was superheating up to ~ 860 K in the crucible before being ejected to form various droplets during the free falling. Depending on the cooling conditions such as undercoolings and cooling rates, subjected to the spray, either anomalous eutectic or single-phase dendrite coming with lamellar eutectic can be observed from the microstructure as BSE images in Fig. 6.1.3 at size range 500 ~ 850 μm and Fig. 6.1.4 at 212 ~ 300 μm respectively.

The contract of BSE images is attributed to the average density of each phase. Thus, Ag-rich phases have a brighter greyscale than Cu-rich ones, which is broadly in agreement with the extensive EDX analysis in Fig. 6.1.7. It is cleary observed that a few anomalous eutectic regions are either isolated among lamellar eutectic in Fig. 6.1.3a or grow radiantly through the heterogeneous nucleation on the outer surface in Fig. 6.1.3b. For some finest lamellar, BES images featuring poor resolutions might fail to show the distinctive contract of these two phases such that only an average greyscale is shown in some regions in Fig. 6.1.3b.

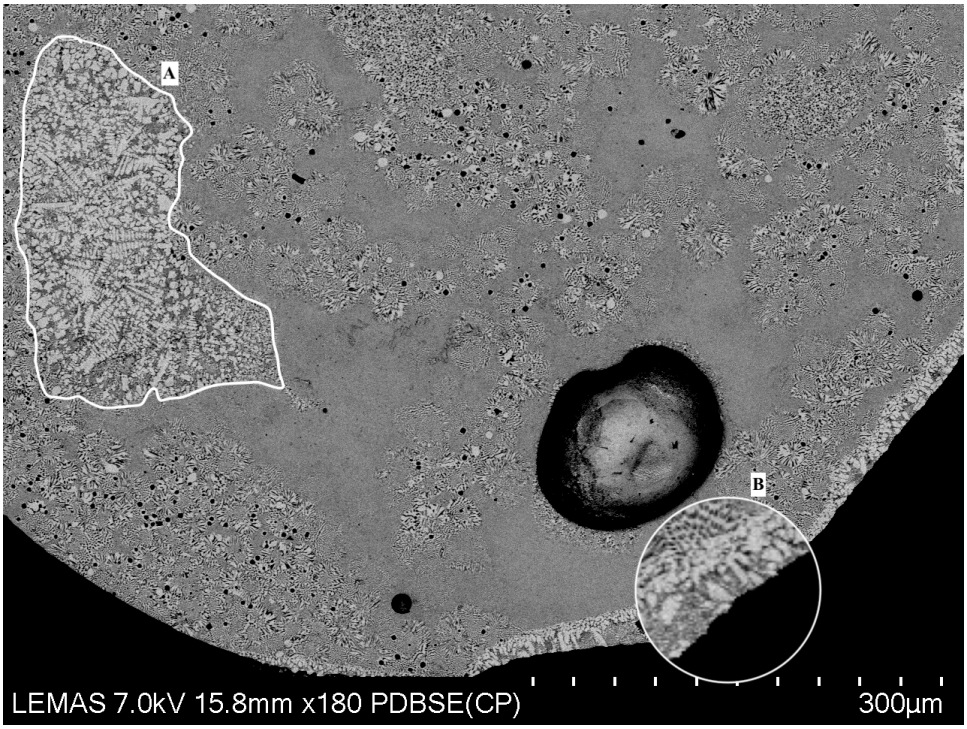

Figure 6.1.4: Microstructure of single phase dendrite in the sectioned samples

Also, there is the drop-tube formed morphologies of the partially melted ingot prior to ejection in Fig. 6.1.8 in comparison with those of the fully melted ingot prior to ejection in Fig. 6.1.3. The dark Cu-rich spot located at the centre of equi-axed grains of anomalous eutectic in Fig. 6.1.8 indicates that Cu-rich inclusions having the higher melting temperature than either the eutectic one or the Ag-rich one are more likely to stay at the molten melt and perform as the origins of anomalous eutectic radiating to the surround undercooled melt. This morphology, however, is not the case

for the fully molten melt prior to ejection, by which the as-solidified microstructure has more Ag-rich inclusions that tend to cluster at colony boundaries of anomalous eutectic in Fig. 6.1.3a and Fig. 6.1.7.

Additionally, there is few regions of single-phase dendrite in presence of sectioned samples in Fig. 6.1.4. By means of other containerless solidification techniques, the morphological transition from lamellar eutectic with anomalous eutectic to that coupled with single-phase dendrites at Ag-Cu eutectic composition gives rise to the molten melt experiencing the critical undercooling which is reported as 70 K [7], 75 K [27], and 76 K [47]. Also, for the reason that the drop-tube processed microstructure is no case unique in the study of rapid solidification and is often similar to those formed in rapid quenching and the emulsion technique [31], the single-phase dendrite in Fig. 6.1.4 is believed as the microstructure of high undercoolings, despite the direct measurement of undercoolings under process of the experiment is impossible. The detailed illustration of morphology of various droplet sizes to show the microstructural evolution will be in Section 6.1.3.

The back-filling inert gas introduced in drop tube process in Section 2.2.1 and Section 5.1.2 increases the cooling rate of a spray of fine Ag-Cu droplets, leading to the destabilisation of initial planar interface between liquid and solid. The low heat extraction rate for Ag-Cu alloy at the eutectic point can stimulate the planar couple eutectic overgrowth simultaneously to form two-phase cells or dendrites (see Fig. 2.3.1). With increasing this rate, the diffusion from the L/S interface becomes inefficient, resulting in the heavily constitutional undercooling along the long-range boundary layer built up ahead of the interface. Thus, the high undercooling is likely to achieve due to solute diffusion, curvature and heat flow (introduced in Section 2.3.2). Because of the effect of the slightly skewed zone towards phase β-Cu side in the Ag-Cu phase diagram, the off-eutectic single α-Ag dendrites is yet possible to form at the eutectic point. Given the significant phase structure at different cooling rates, the mechanisms of anomalous structure must be accordingly different. In the previous studies of rapid solidified Ag-Cu samples, the formation of anomalous Ag-Cu eutectic can be attributed to the remelting of eutectic dendrites during rapid recalescense at low undercoolings (< 60 K) [27, 7, 44], and the decomposition or fragmentation of highly supersaturated single-phase dendrites at high undercoolings (> 60 K) [47]. The schematic illustration of the mechanism by which the anomalous eutectic forms from eutectic dendrites at low undercoolings is shown in Fig. 6.1.5a and that of the mechanism by which the anomalous eutectic forms from single-phase dendrites at high undercoolings is shown in Fig. 6.1.5b. The mechanism by which drop-tube processed anomalous eutectic forms shall refer to Section 6.1.3, in which microstructures of all sizes are illustrated.

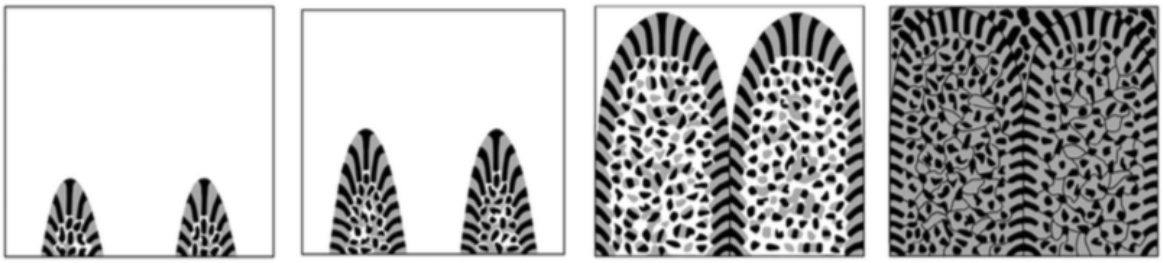

(a) Anomalous eutectic formation from primary eutectic dendrites

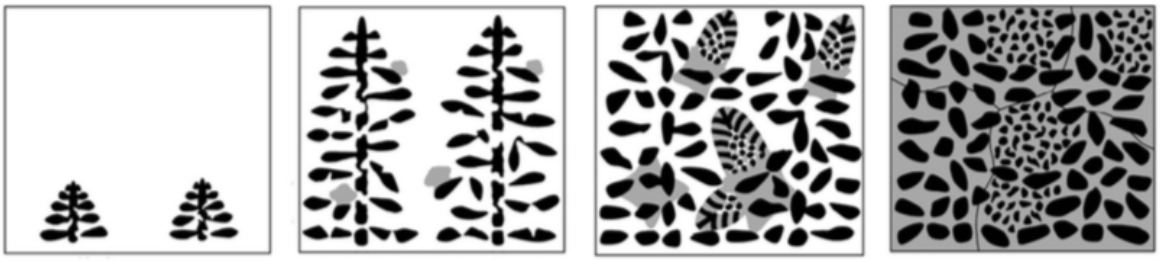

(b) Anomalous eutectic formation from primary single-phase dendrites

Figure 6.1.5: Schematic diagram of the mechanism by which anomalous eutectic forms [74]

The drop-tube processed microstructure in Fig. 6.1.3b appears clearly that the development of the anomalous structure from the outer surface radiantly to the inner droplet is nearly aligned with the direction of heat transfer and takes the form of branched 'fingers'. This anomalous eutectic in dendritic form propagating through the sample is highly suggestive that the initially formed two-phase (eutectic) dendritic is remelted or disintegrated as the origin of anomalous eutectic during the recalescence, followed by the planar front growth of lamellar eutectic filling in the inter-dendritic region.

Likewise, those fine-grained anomalous eutectic located inside the droplet in Fig. 6.1.3a result from the remelting of eutectic dendrite, despite the loss of dendrite shape. Yang *et al.* [75] suggest that the grained anomalous eutectic can also be formed by the small fragmentation of supersaturated single-phase dendrites at high undercoolings. However, this is not the case for Ag-Cu alloy at the eutectic point. Even though the undercooled liquid can be warmed up to more rapidly during recalescence by the formation of single-phase dendrite than that of eutectic dendrite due to the faster growth velocity, the temperature according to Ag-Cu phase diagram in Fig. 2.1.3 can never rise beyond the eutectic temperature and is not high enough to partially remelt the off-eutectic composition of primary single-phase dendrite. In other words, the lowest melting temperature at the eutectic point cannot break down the single-phase dendrite into fragmentations where the heterogeneous nucleation of anomalous eutectic begin. Accordingly, these primary single-phase dendrites remain unchanged as the morphology shown in Fig. 6.1.4 once being solidified, and the

following recalescense re-warms the undercooled liquid ahead of dendrite interface, giving rise to the origin of lamellar eutectic.

Although different microstructures are detected in Fig. 6.1.3 and Fig. 6.1.4, the composition of droplet with 300 ~ 800 μm are further confirmed by DTA analysis. In Fig. 6.1.6, the onset temperatures for droplet of 300 ~ 800 μm in exothermic reaction are nearly equal to the eutectic temperature (the vertical red line). This excess evidence further proves the droplet composition did not occur any departure from the eutectic one during rapid solidification.

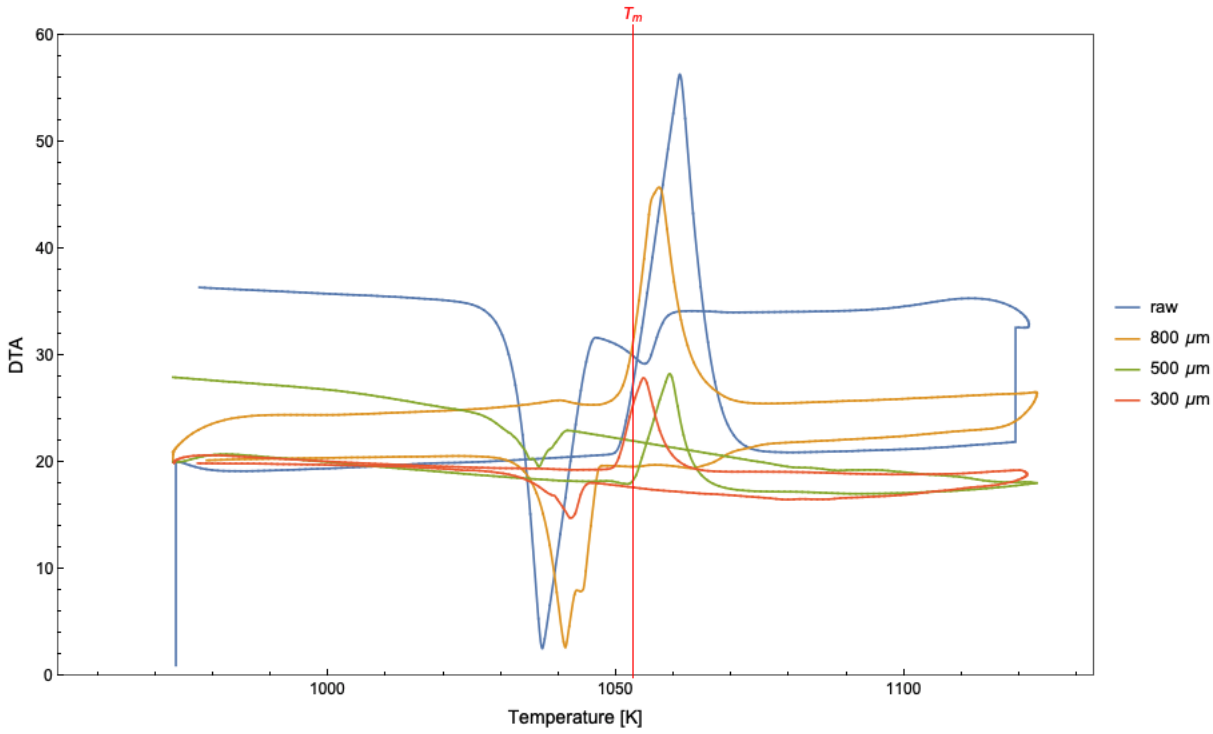

Figure 6.1.6: DTA result in thermal cycle between 950 to 1100 K at the rate of 5 K/min

Moreover, either the metastable phase γ' or the amorphous phase fails to be found in this spray of fine Ag-Cu droplets. As introduced in Section 2.1.2, T_0 temperature that is only 76 K below the eutectic point is not low enough to attain either phase. When those droplets experience high cooling rate in flight along the drop tube, the morphology of either eutectic dendrite or single-phase dendrite under lower undercooling than 76 K would prevail before the sufficient high undercooling is achieved for the partitionless solidification. This is also the reason that the undercooling of Ag-Cu alloy higher than 76 K by means of containerless solidification techniques has not been reported in elsewhere yet.

Fig. 6.1.3a at high magnification shows both Ag-rich and Cu-rich inclusions, besides anomalous eutectic coupled with lamellar eutectic. The EDX map scan in Fig. 5.1.16b and the EDX line scan

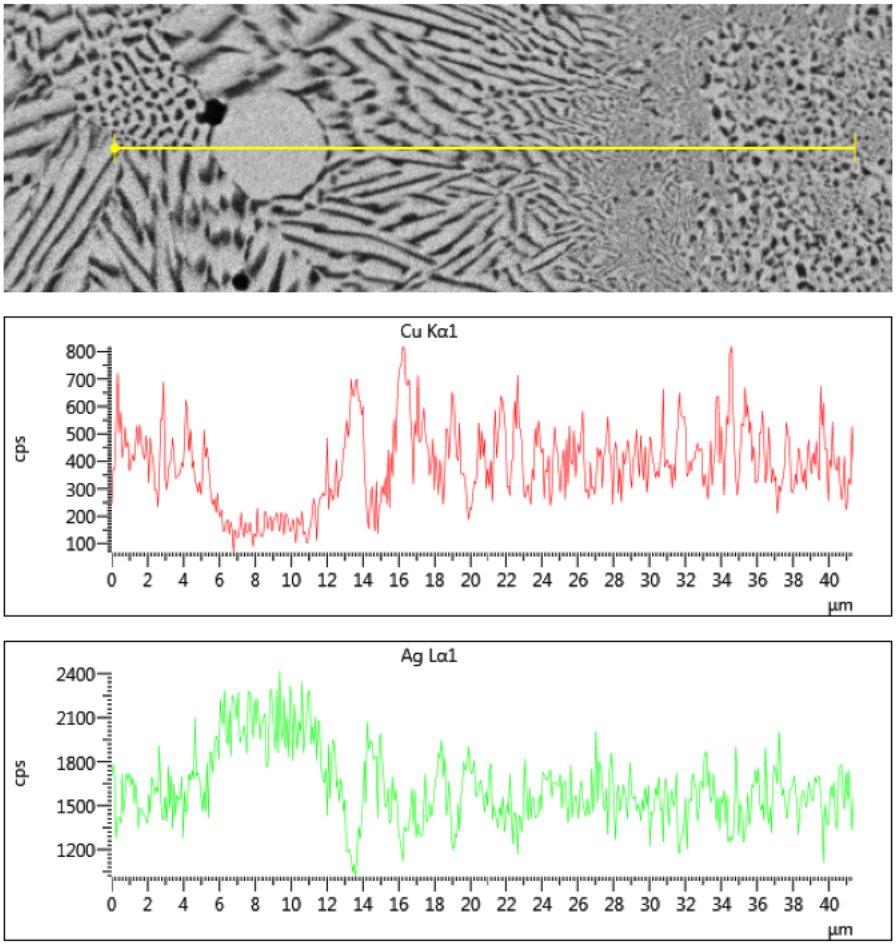

Figure 6.1.7: EDX line scan of anomalous eutectic region

in Fig. 6.1.7 conforms that the inclusion composition is indeed Cu-rich and Ag-rich respectively. Unlike those Cu-rich inclusions in the drop-tube formed microstructure from the partially melted ingot acting as the places for heterogeneous nucleation (see Fig. 6.1.8), both inclusions are located at or near the boundaries of the eutectic colonies. With reference to the Ag-Cu phase diagram in Fig. 2.1.3, the metastable extension (dotted line) of Ag solidus line has the large slope towards the couple zone than that of Cu solidus line in the other side of phase diagram. In consequence, for the lamellar eutectic in dendrite shape formed from the undercooled parent melt initially, the Ag-rich phase is supersaturated in larger atomic percentages of Cu than the Cu-rich phase is in atomic percentages of Ag. In other words, the separation between the metastable solidus and the solvus lines would lead to greater supersaturation of the Ag-rich phase in Cu than of the Cu-rich phase in Ag. With the subsequent formation of lamellar eutectic along the interface of eutectic dendrite, the remaining liquid is Ag-rich in comparison with the eutectic composition, which is plausibly attributed to the Ag-rich inclusions at the grain boundaries of anomalous eutectic. Meanwhile, upon reheating to the eutectic temperature during the recalescence, the supersaturated Ag-rich phase

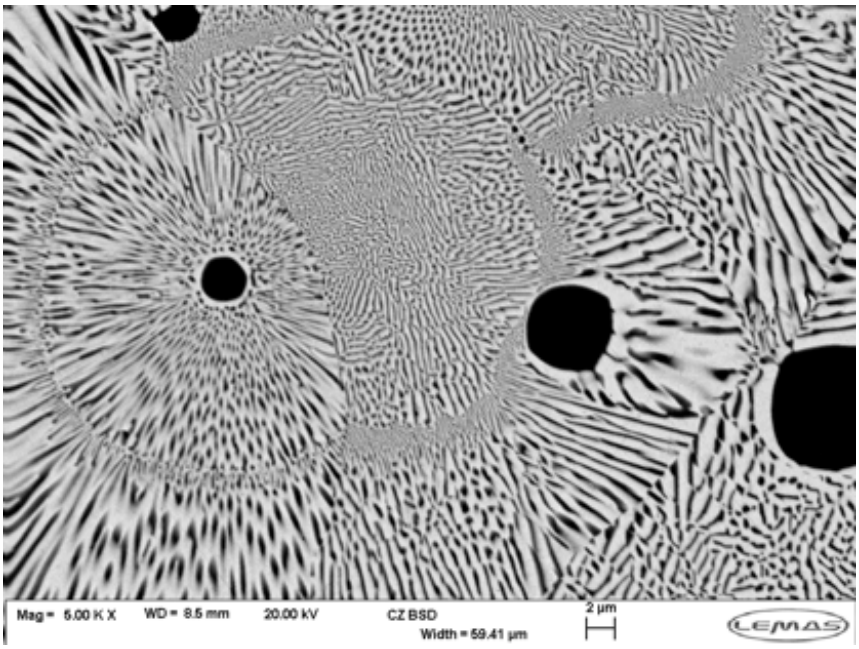

Figure 6.1.8: Microstructure of anomalous eutectic formed through un-melted Cu-rich fragments

would disintegrate or partially remelt. Because of rapid heat extraction rate surround individual droplets, the recalescence has a limited influence on the local regions such that the short-range diffusion would be activated to diffuse Cu out of Ag-rich phases to the nearby residual liquid, giving rise to the observed Cu-rich inclusions embraced by Ag-rich phases rather than lamellar eutectic growing outwards.

Based on the above explanation, the order of drop-tube processed microstructure is from the eutectic dendrite, to anomalous eutectic due to remelting of former phase, to lamellar eutectic by heterogeneous nucleations along the interface of anomalous eutectic, to eventually either Ag- or Cu-rich inclusions relative to the eutectic composition. The extensive evidence to highly support those inclusions were the last solidified microstructure in droplet is by observing the change of the lamellar eutectic spacing. Considering the strong heat extraction gives insufficient time for inter-diffusion to separate two phases clearly in the growth of lamellar eutectic, the fine interlamellar spacing is hardly identified by low-resolution BSE image in Fig. 6.1.3b, whereas the coarser eutectic spacings nearby those inclusions reducing gradually into the nano scale indicate that the inclusions are the last feature to solidify after the formation of both anomalous and lamellar eutectic.

However, the roughly spherical form of the inclusions can imply that the equi-axed spots experienced the restricted growth to the undercooled melts. Otherwise, the last remaining liquid should be solidified into various forms by filling in any spacious gap within the regions of anomalous and lamellar eutectic. The reasonable explanation for this issue can be given that the interaction between the free falling droplets and the back-filling inert gas results in the random rotation through

either azimuth or zenith angle, by which the near spherical Cu-rich inclusions were in contact with the Ag-rich liquid and spherodized due to surface tension.

As a result, the remaining liquid with small radius of curvature plausibly gives way to that with larger radius of curvature.

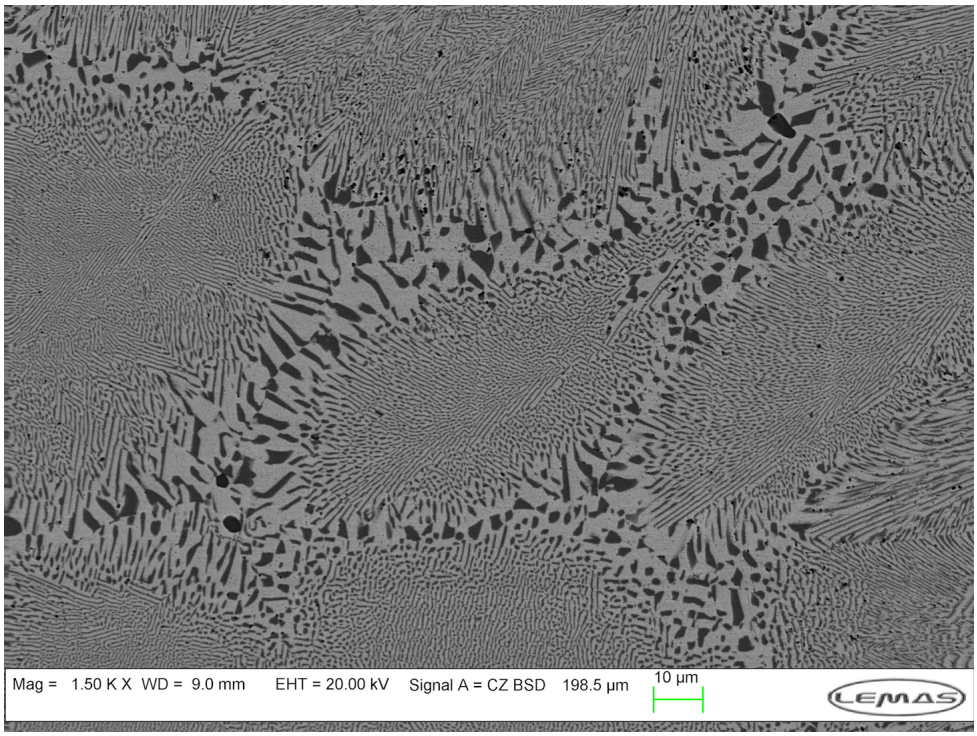

Figure 6.1.9: Morphology of anomalous eutectic processed by melt fluxing [41]

Additionally, the existence of self-rotation in every droplet due to residual electromagnetic stirring from the RF heating field might give rise to the samples processed by drop tube technique forms the microstructure in Fig. 6.1.3 and Fig. 6.1.4 slightly different from those processed by melt fluxing in Fig. 6.1.9. The microstructure of flux undercooled Ag-Cu sample placed at the static crucibles with no external force involved in the entire solidification is generally cellular, with a typical cell consisting of lamellar eutectic in the body of the cell with anomalous eutectic occurring at the cell boundaries [7, 41]. In contrast, the anomalous eutectic formed in drop tube processed samples has a less clear distinction between these morphologies due to the interruption of the inner force. Therefore the cellular microstructure in drop-tube formed sample cannot last in the final formed morphology, since the 'bridges' connected with individual colonies of anomalous eutectic has the small radius of curvature, giving way to isolated colonies of anomalous eutectic that have the average larger radius of curvature around the eutectic boundaries as shown in Fig. 6.1.3a.

6.1.3 DROP-TUBE FORMED PHASE TRANSITION

The investigation of undercooled droplets by using short drop-tube technique gives a good insight in phase transitions of drop-tube processed solidification. The drop-tube technique is featured in melt subdivision and high cooling rate, which give rise to isolation of the exiting nucleants in a faction of one spray and a range of undercoolings prior to nucleation.

Depending on the composition and the growth kinetics of chosen alloy at the given solidification condition, two-phase eutectic structures tend to have different mechanisms to form anomalous eutectic. Based on Section 6.1.2, there are three types of morphologies in drop-tube processed Ag–39.9 at.%Cu droplet, which can be briefly explained as following.

Type I For those droplets experiencing cooling rates that can attain low undercoolings (10 ~ 60 K) in Fig. 6.1.3, the initial supersaturated eutectic grows as branches, to dissipate the latent heat into the undercooled liquid efficiently. The subsequent growth of lamellar eutectic surround the primary eutectic dendrite not only warms up the remaining liquid, but also develops the remelted zones inside eutectic dendrite. The disintegration of the primary phase takes place in those zones, giving way to the formation of anomalous eutectic. After the large volume fraction of phase growing to impinge on each other, the isolated melts are solidified as single phase-rich inclusions at or near the colony boundaries.

Type II For those droplets experiencing cooling rates that can attain high undercoolings (> 60 K) in Fig. 6.1.16b, the primary single phase grows dendritically into the undercooled melt, followed by the rapid recalescence due to the high growth kinetic of primary phases rises the undercooled melts up to or near the eutectic temperature for the growth of lamellar eutectic surround until the last liquid is finished. Those off-eutectic single dendrites featuring higher melting point than the eutectic one is impossible to be remelted into the fragments for the origins of anomalous eutectic as mentioned in Section 6.1.1. But its formation and growth release massive heat into the undercooled liquid up to the eutectic temperature. Thus the microstructure in this type consists of the single-phase dendrite and the lamellar eutectic.

Type III For those droplets consisting of single-phase dendrite, anomalous eutectic and lamellar eutectic as shown in Fig. 6.1.4, it is believed that the droplets should still experience high undercoolings ~ 60 K to initiate the primary single-phase dendrites. Although the latent heat released in the subsequent phase growth can continuously increase the undercooled melt, it is unlikely that the undercooled melt is re-warmed up to the eutectic temperature when the rapid heat extraction is surround the droplet. Moreover, the highest recalescence temperature can be gradually reduced with the increase of undercooling [27]. As a result, the melt in the following phase growth might yet exist a certain extent of undercooling, by which the lamellar eutectic grows in the dendritic form. Those eutectic dendrites would be then remelted as the origin of anomalous eutectic, whereas the heterogeneous nucleations of lamellar eutectic take place around the region boundary of eutectic dendrite.

On the basis of theoretical models [4, 45, 59], which are established by the balance of heat fluxes for a given droplet, the estimate of cooling rates taking place during the in-flight is believed to affect the solidification process in a number of aspects, such as with the decrease in droplet size,

- The increase in the cooling rate to induce larger undercooling
- The decrease in the latent heat of fusion
- The increase in the amount of anomalous eutectic transformed from the primary phase

This hypothesis about the drop-tube processed solidification highly indicates the critical undercooling of Ag-Cu eutectic alloy (70 K [7, 74]) would be achieved at smaller sizes of droplet. Thereby the transitive microstructures from anomalous eutectic embraced with lamellar eutectic, to both anomalous eutectic and single-phase dendrite embraced with lamellar eutectic, to eventually single-phase dendrite embraced with lamellar eutectic is expected in the range of droplet size from 38 to 850 μm.

In the presented experimental result, three types of microstructure are found in SEM. But the microstructural evolution with the variation of droplet diameter is unclear. The microstructures of all ranges are illustrated in the following as 500 ~ 850 μm in Fig. 6.1.10, 300 ~ 500 μm in Fig. 6.1.11, 212 ~ 300 μm in Fig. 6.1.12, 150 ~ 212 μm in Fig. 6.1.13, 106 ~ 150 μm in Fig. 6.1.14, 75 ~ 106 μm in Fig. 6.1.15, 53 ~ 75 μm in Fig. 6.1.16, and 38 ~ 53 μm in Fig. 6.1.17.

500 ~ 850 μm

The overview of structure at the range of 500 ~ 850 μm shows that numerous regions of anomalous eutectic are approximately equiaxed and distributed in the surround lamellar eutectic randomly in Fig. 6.1.10a. It is believed that the *Type I* mechanism takes place inside this as-solidified microstructure, despite lack of its primary eutectic dendrites in the final structure.

Those primary two-phase structures grow rapidly to the undercooled melt to warm up the liquid temperature close to eutectic temperature and then are remelted into fragments for the subsequent formation of anomalous eutectic. At the short period of time, i.e. recalescence, those fragments are free to float in the remelting liquid due to the droplet rotation during in-flight and thereby the distribution of anomalous eutectic regions observed in Fig. 6.1.10a has no particular order. For a spherical droplet, the droplet–gas interaction in the spray, delivering the internal heat contents to the surrounding gas by convection and radiation, can expect that the coolest place appears on the outer layer, at which the primary phase is more likely to attain in the final microstructure. Careful examination of the region near and away from droplet surface can find that the colonies of anomalous eutectic remain roughly unchanged in the approximate size within 15 ~ 30 μm as shown in Fig. 6.1.10b and Fig. 6.1.10c respectively. The microstructure in Fig. 6.1.10b therefore indicates the thermal conduction inside droplet efficiently transfers the external latent heat to the

outer layer and keeps any inner temperature gradient minimal. At a result, the microstructure of corresponding outer structure can only detect re-formed eutectic colonies in Fig. 5.1.14a, since the primary phases formed from the outer layer to the undercooled melt are completely melted back.

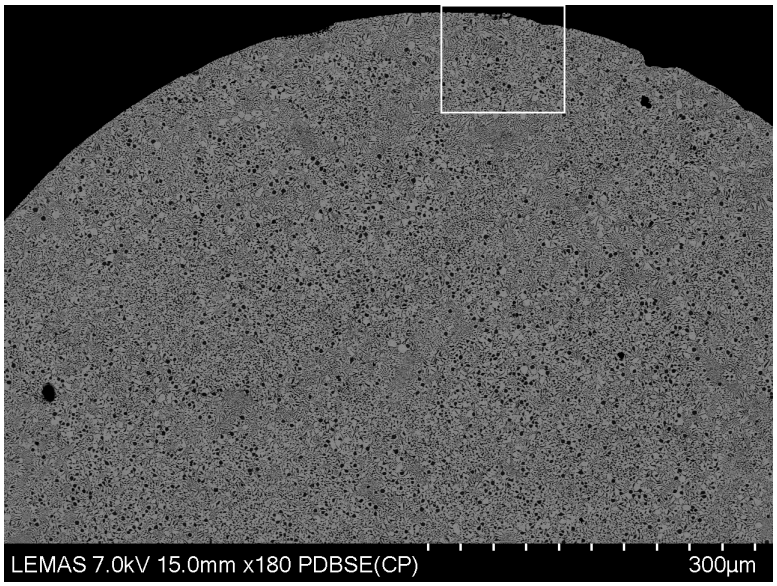

(a)

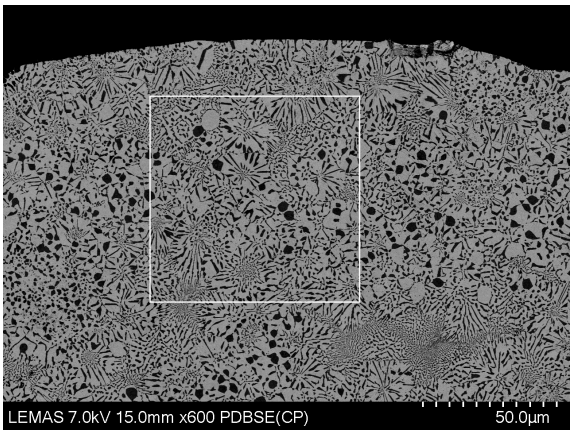

(b)

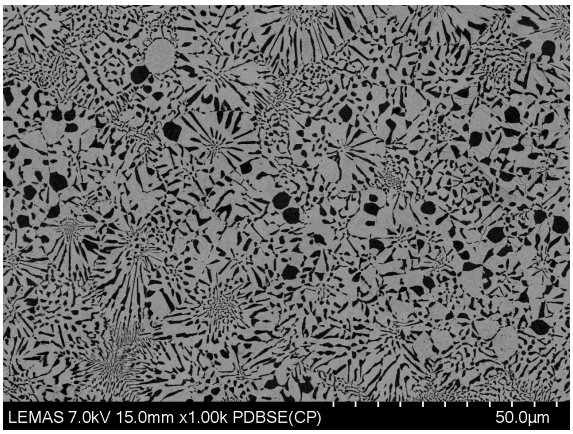

(c)

Figure 6.1.10: (a) Macrostructure of the sample section in the range of 500 ~ 850 μm, (b) Microstructure of the selected region in Fig. 6.1.10a, (c) Microstructure of the selected region in Fig. 6.1.10b

300 ~ 500 μm

The smaller range of droplets due to the balance of heat flux tends to process relatively faster cooling rates and consequently to freeze the molten droplet higher undercooled than the larger range does. With the increase of undercooling, the volume faction of anomalous eutectic in the microstructure should rise.

Comparing Fig. 6.1.11a with Fig. 6.1.10a, the microstructure of droplets at the range of 300 ~ 500 μm has the exactly same morphology as that at the range of 500 ~ 850 μm, giving rise to the *Type I* mechanism for the formation of anomalous eutectic. However the increase in the volume fraction of anomalous eutectic between these two ranges is less clear. Neither the direct counting nor the area measurement of those regions can give a good insight of the variation in the volume of anomalous eutectic. Consequently, the image processing by means of *ImageJ* introduced in Section 5.2, will quantitatively analyse the volume fraction of anomalous eutectic in every range of droplets (see Section 6.2.1).

Careful examination of the region near droplet surface in Fig. 6.1.11b and Fig. 6.1.11c can find that the colonies of anomalous eutectic are more loosely located at or near the droplet surface so that the margins amongst those colonies filled in lamellar eutectic are more obvious than those at the larger range in Fig. 6.1.10b.

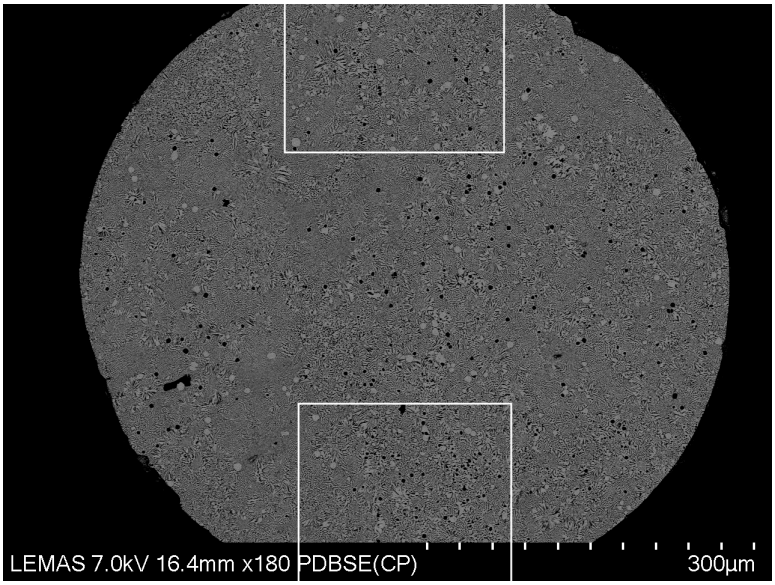

(a)

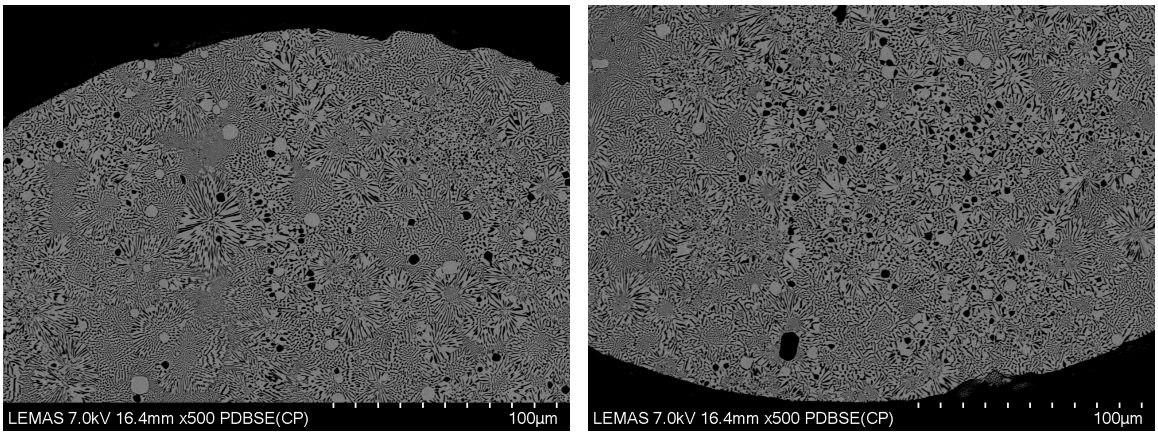

(b) (c)

Figure 6.1.11: (a) Macrostructure of the sample section in the range of 300 ~ 500 μm, (b) and (c) Microstructure of the selected regions in Fig. 6.1.11a

212 ~ 300 μm

With the decrease of droplet range down to 212 ~ 300 μm, the macrostructure in Fig. 6.1.12a shows a greater amount of anomalous eutectic regions crowded together. The high-resolution images indeed shows those regions are crowded and increasingly equiaxed with the diameter around 10 μm in Fig. 6.1.12e.

The high-resolution images indeed shows those regions are crowded and increasingly equiaxed with the rough diameter around 10 μm in Fig. 6.1.12e. Careful examination of microstructure around the outer layer in Fig. 6.1.12b, Fig. 6.1.12c, and Fig. 6.1.12d, also find that the morphology consisting of anomalous eutectic and lamellar one has no difference from elsewhere inside and is independent on the direction of droplet in-flight. Under observation of Fig. 6.1.12, it is highly suggestive that the free-falling droplet is rotated along the gas stream to receive an average cooling rate around the outer layer. And, to some extent, a higher cooling rate can attain not only a higher undercooling, but also a higher average recalescence temperature. The reasonable explanation for this is that the greater volume fraction of eutectic dendrites outbreak initially at this order of undercoolings, which gives more spacious remelted zones for the formation of anomalous eutectic during the recalescence. In other words, higher undercooling has given rise to a finer lamellar structure leading to an easier remelting. Therefore, with the increase of undercooling, the primary phases not only degenerate quickly, but also are continuously refined to more crowded eutectic colonies with the great volume fraction.

In Section 6.1.2, either Ag- or Cu-rich inclusions proves its formation followed by anomalous eutectic since they tend to cluster at boundaries of eutectic colony. Such segregated solidification can be easily found in Fig. 6.1.10c for 500 ~ 850 μm, Fig. 6.1.11c for 300 ~ 500 μm, and Fig. 6.1.12e for

212 ~ 300 μm. This observation then indicates that the solute supersaturation takes place in the primary eutectic dendrite and so the remaining undercooled melt which provides the condition for the formation of those inclusions.

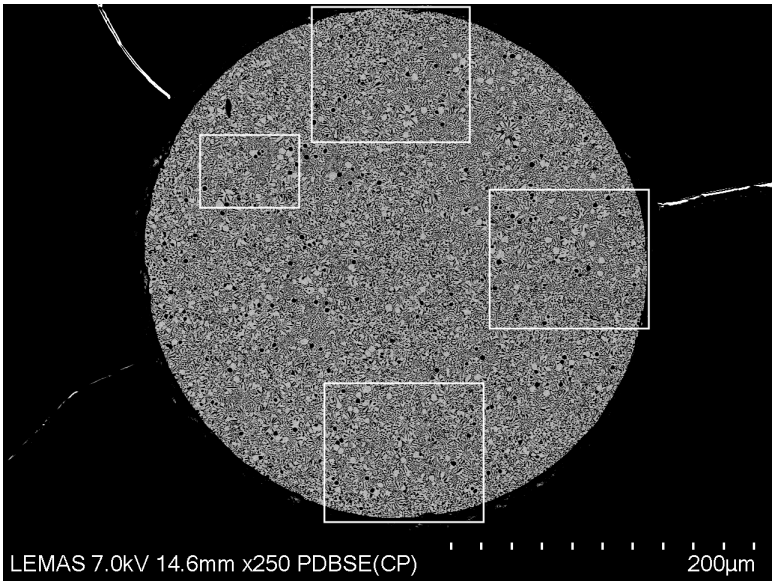

(a)

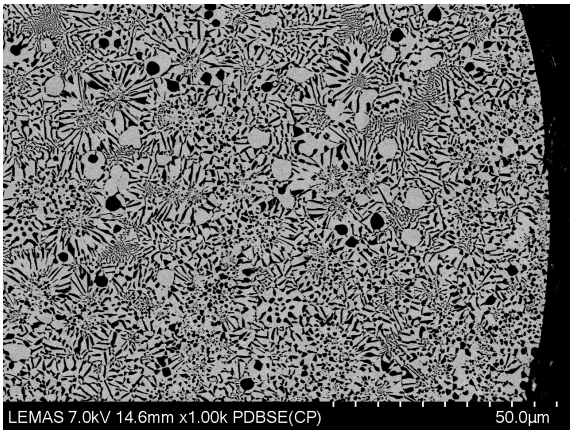

(b)

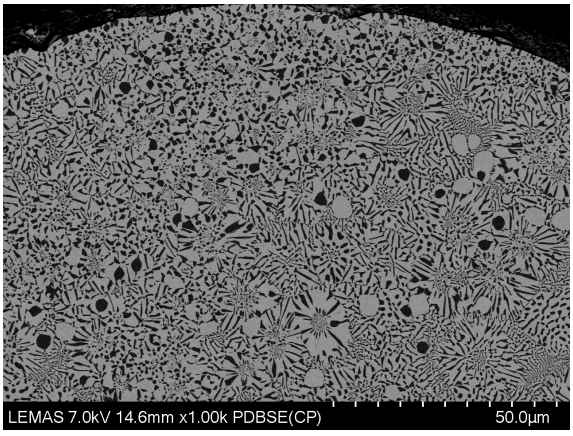

(c)

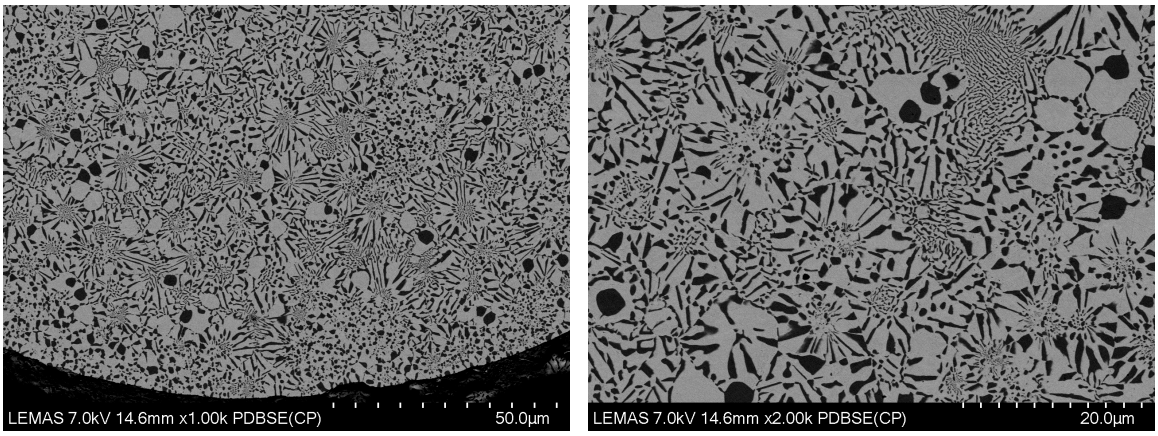

(d) (e)

Figure 6.1.12: (a) Macrostructure of the sample section in the range of 212 ~ 300 μm, (b), (c), (d) and (e) Microstructure of the selected regions in Fig. 6.1.12a

150 ~ 212 μm

The distribution of anomalous eutectic at the range of 150 ~ 212 μm is quite distinct from that at the larger ranges. The colonies of anomalous eutectic shown in Fig. 6.1.13a, tend to form near the outer layer where the local heat extraction rate is high, while those at the larger ranges have no preferred location. Careful examination of microstructure near the outer layer in Fig. 6.1.13b and Fig. 6.1.13c, can find that the morphology of this range is still attributed to the remelting of eutectic dendrites (*Type I* mechanism), since the anomalous eutectic still form in the dendritic skeleton. Moreover, comparing Fig. 6.1.12a with Fig. 6.1.13a, the volume faction of anomalous eutectic with the cooling rate does not increase monotonically. The most likely reason for this is that the cooling rate at this range can efficiently extract the heat that is released from the heat of fusion during the growth of primary phase, so that the undercooled liquid ahead of the growth front takes more heat to partially remelt the primary phase after recalescence. As a result, the small 'remelted zone' cannot allow the re-formed pieces floating freely.

Yu, *et al.,* [33] investigated the rapid solidification of Ag-Cu eutectic alloy processed via melt fluxing and drop-tube techniques and found that the anomalous eutectic in flux-undercooled samples preferentially forms at cell boundaries around the lamellar eutectic in the cell body (see Fig. 6.1.9), whereas in drop-tube processed samples it tends to distribute randomly inside the droplets and at much smaller volume fractions. The conclusion is quite right for the morphology observed at the certain ranges of droplets, *i.e.,* 212 ~ 850 μm. For samples at this range, the anomalous eutectic tends to form more like cell boundaries surrounding the lamellar eutectic as shown in Fig. 6.1.13d and Fig. 6.1.13e. The former figure clearly shows two lamellar eutectic regions are separated by the boundary-like anomalous eutectic region and the latter figure shows there are several long and thin 'hair-like' anomalous eutectic regions around lamellar eutectic.

More importantly, the smaller lamellar spacing in Fig. 6.1.13e than that in Fig. 6.1.12d is highly suggestive that the equilibrium planar growth takes place under the undercooling less than 12 K (introduced in Section 2.3.1). Because of the solidus of Ag and Cu at small undercooling extended inside the couple-growth zone, each phase of lamellar eutectic is supersaturated with solute. Additionally, the small undercooling in assistance with high heat extraction rate, can efficiently trap the solute inside the solidified phase and give less time to diffuse into the left liquid. Therefore, there is few inclusions solidified at last during the segregated solidification.

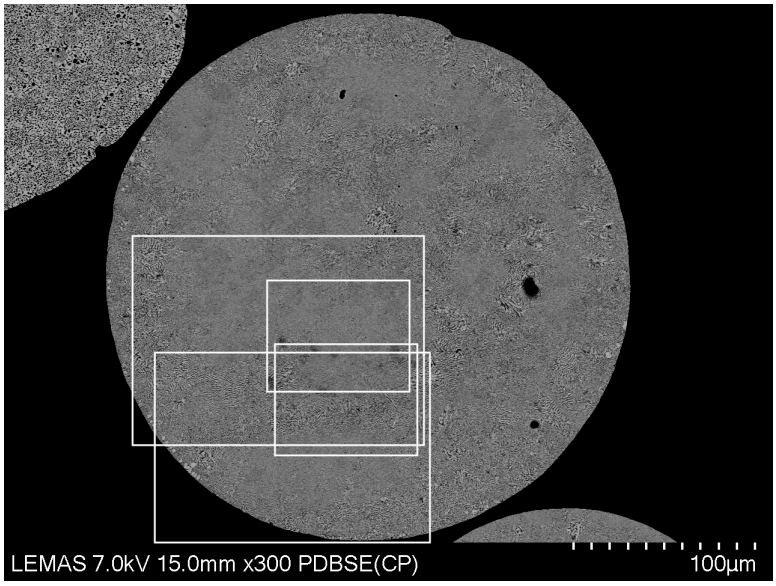

(a)

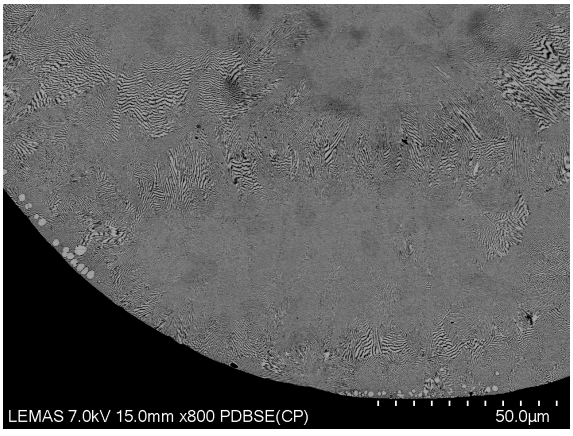

(b)

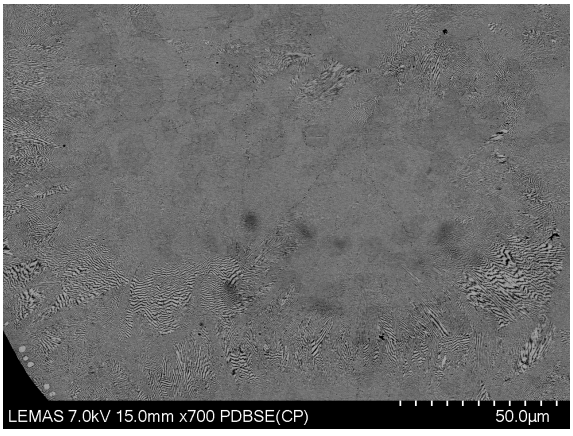

(c)

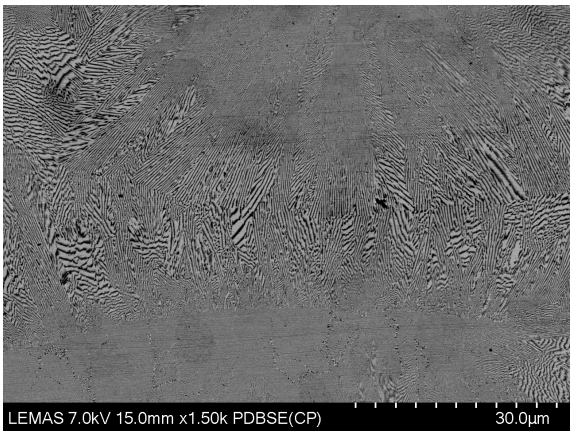

(d)

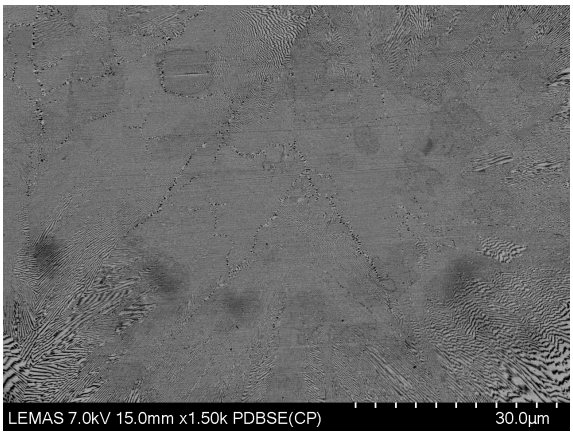

(e)

Figure 6.1.13: (a) Macrostructure of the sample section in the range of 150 ~ 212 μm, (b), (c), (d) and (e) Microstructure of the selected regions in Fig. 6.1.13a

106 ~ 150 μm

The microstructure at the range of 106 ~ 150 μm in Fig. 6.1.14a shows no much difference from that at the range of 150 ~ 212 μm in Fig. 6.1.13a, expect for less heterogeneous nucleation sites around the outer layer.

The initial non-equilibrium solidification at the undercooled melt still leaves a sort of 'footprint' in the final microstructure in Fig. 6.1.14b, in which is the dendritic skeleton filled in anomalous eutectic propagating from the outer layer through the entire sample. Such heterogeneous nucleation in the sectioned sample can be also revealed in the corresponding spherical surface structure in Fig. 5.1.14b. At the other end of outer layer, however, the microstructure in Fig. 6.1.14c shows more lamellar eutectic cooperatively growing towards the droplet surface.

The microstructural distribution thereby suggests that:

- The inner temperature gradient shall exist on the small range of droplets that are yet subjected with high cooling rate due to the outbreak of primary two-phase structure mainly at the outer layer. At a result, the relatively larger volume fraction of lamellar eutectic as the production of either equilibrium solidification or solidification with undercooling lower than 10 K, tends to grow in the inner droplet.

- The heat extraction inside the droplet shall transfer the inner heat in its preferred direction. Clearly, there is the growth direction from the nucleation site in Fig. 6.1.14b towords the other end, in which the volume fraction of anomalous eutectic gradually reduces in favour of lamellar eutectic. Such a structural variation in Fig. 6.1.14 is highly indicative that the nucleation site receives higher cooling rate to have insufficient time for solidification, whereas

the microstructure at the other end receives much lower cooling rate to keep the cooperative lamellar growth. In other words, the nucleation site might be more likely the location of upwind direction during the droplet in-flight, despite the fast rotation coming along.

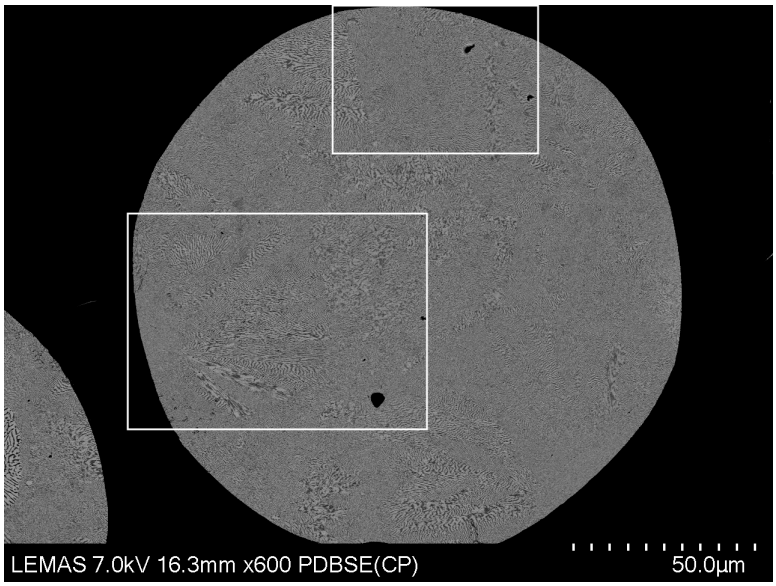

(a)

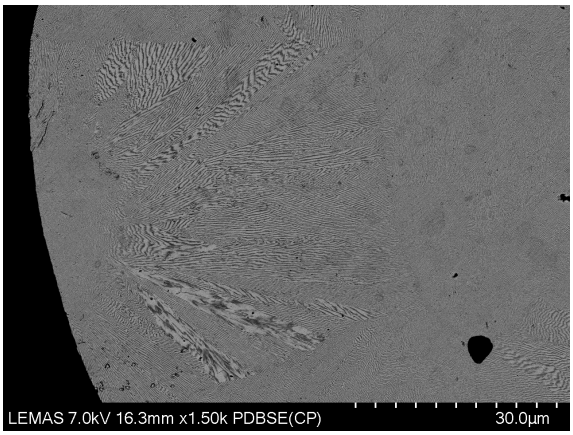

(b)

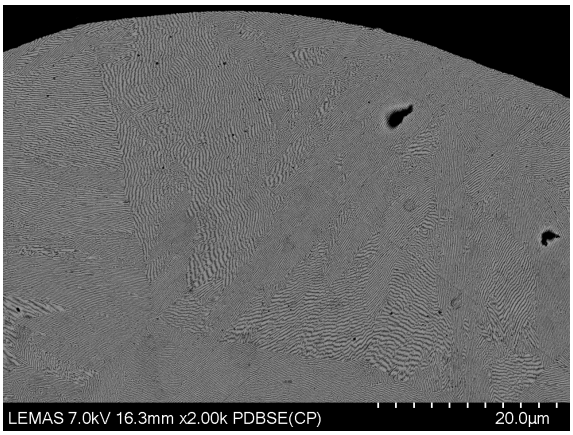

(c)

Figure 6.1.14: (a) Macrostructure of the sample section in the range of 106 ~ 150 μm, (b) and (c) Microstructure of the selected regions in Fig. 6.1.14a

75 ~ 106 μm

With decreasing droplet size it is much more likely that individual droplets will achieve higher undercooling during drop-tube processing due to the melt sub-division effect. Although the mor-

phology at the range of 75 ~ 106 μm in Fig. 6.1.15a is close to that at the range of 212 ~ 300 μm in Fig. 6.1.12a, the segregated solidification might be more likely to occur at the onset of solidification as the primary off-eutectic single phase. Unlike those inclusions clustering near the eutectic colony boundary in the larger ranges (212 ~ 850 μm), these single phases not only have a sort of dendritic structure, but also tend to stay at the centre of lamellar eutectic regions. Therefore, the mechanism should belong to *Type III*.

When the high cooling rate delays the onset of solidification, the critical undercooling (~ 70 K) might achieve to stimulate these single phases. For a planar phase growth, rapid release of the heat of fusion into the undercooled recalescence melt then leads to the increase of liquid temperature and so the decline of primary phase growth. Based on the microstructure shown in Fig. 6.1.15, it is more likely that the eutectic grows first, then becomes unstable and so a single phase dendrite emerges beyond the eutectic front. Because the volume of interdendritic liquid is sufficient to act as a sink for the latent heat, the second or third arms of single phases having the richer solute receive the latent heat greatly and so be partially remelted back to the primary trucks in the final microstructure as shown in Fig. 6.1.15b and Fig. 6.1.15c. The subsequent eutectic solidification can easily initiate the heterogeneous nucleation on those tip fragments.

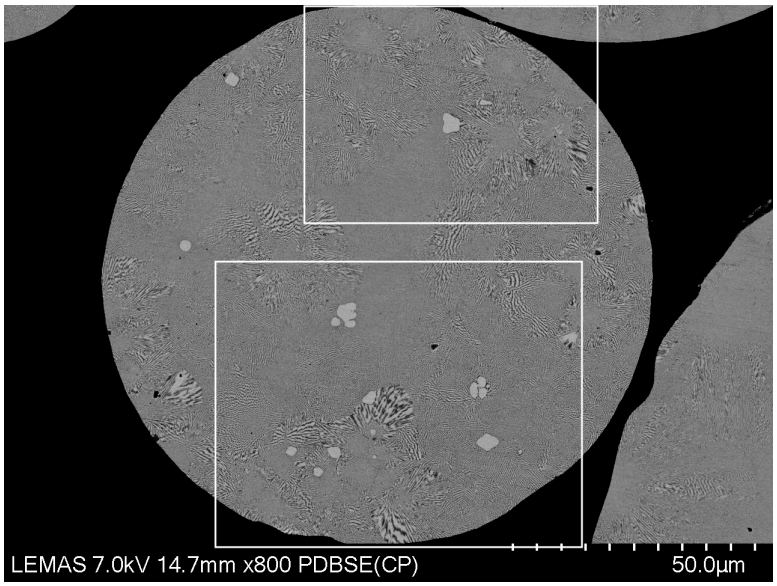

(a)

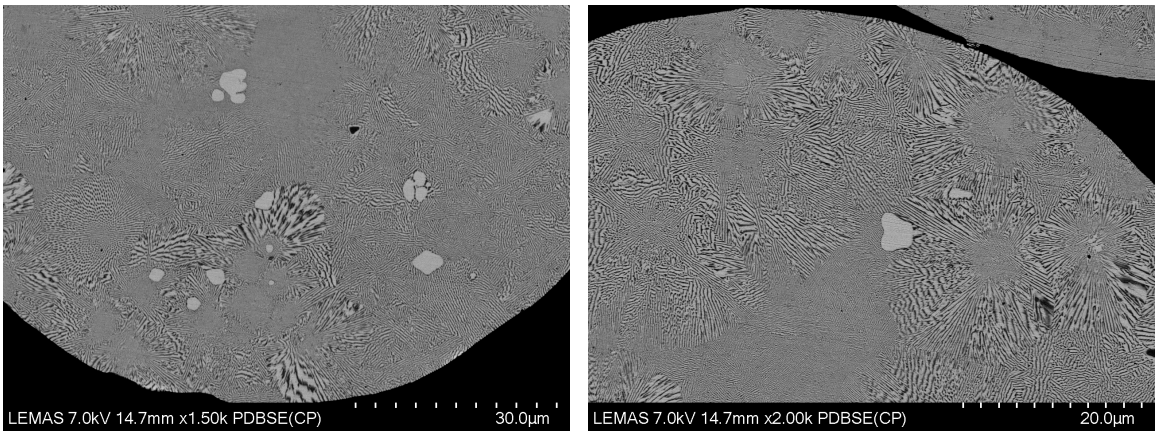

(b) (c)

Figure 6.1.15: (a) Macrostructure of the sample section in the range of 75 ~ 106 μm, (b) and (c) Microstructure of the selected regions in Fig. 6.1.15a

$$53 \sim 75\ \mu\text{m}$$

For droplets at the range of 53 ~ 75 μm, the higher undercooling can be successfully achieved, so that the morphology consisting of single phase dendrite and lamellar eutectic is found in Fig. 6.1.16a. The anomalous eutectic however fails to observe in this final microstructure, which might be attributed to the recalescence rate. Walder, *et al.,* [27] measured the thermal variation of melt-fluxing processed sample by means of a radiation pyrometer and found, when the single phase dendrite is formed, the maximum recalescence rate can reach higher than 10^4 Ks^{-1} for about 0.6 ~ 1.0 s. At such high recalescence rate, the undercooled melt can be warmed up to the eutectic temperature roughly at the onset of recalescence, lasting for 0.6 s. By using Eq. (2.3.3) which is basic on the JH model [5], the growth velocity of lamellar eutectic is

$$V = \frac{1}{4}\frac{\Delta T^2}{K_r K_c} \approx \frac{70^2}{13207} = 0.37 \quad \text{m s}^{-1} \tag{6.1.1}$$

Provided the predicted velocity of lamellar eutectic is 0.37 m s^{-1}, lasting for 0.6 s, then the total proceeded distance is approximately equal to 2 m, which is sufficiently fast to fill in the rest of liquid during the recalescence indeed. Nevertheless, the velocity obtained in Eq. (6.1.1) shall be seriously underestimated since the velocity predicted by TMK model has a clear departure from that predicted by JH model, as shown in Eq. (2.3.4).

However, there is a greater number of droplets with the microstructure in Fig. 6.1.16b than the microstructure in Fig. 6.1.16a. The reason to cause the former microstructure will be further explained in the following sub-section, since at the smallest range only the latter microstructure is found.

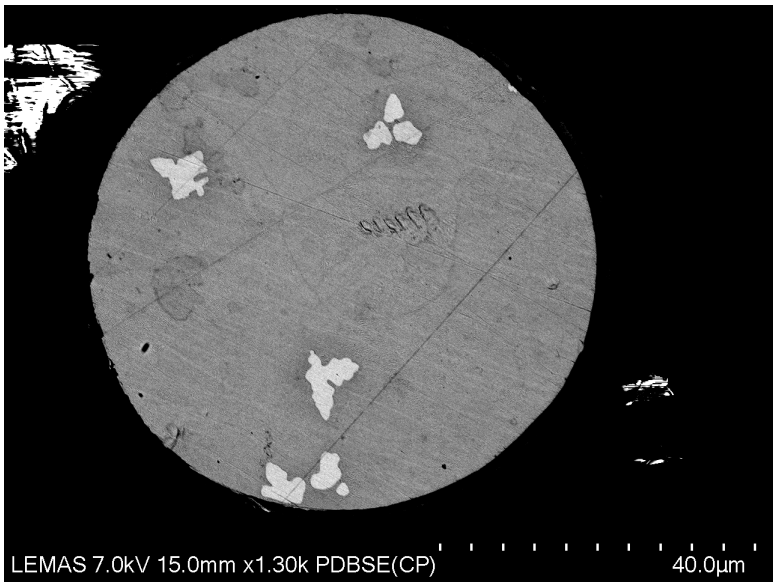

(a)

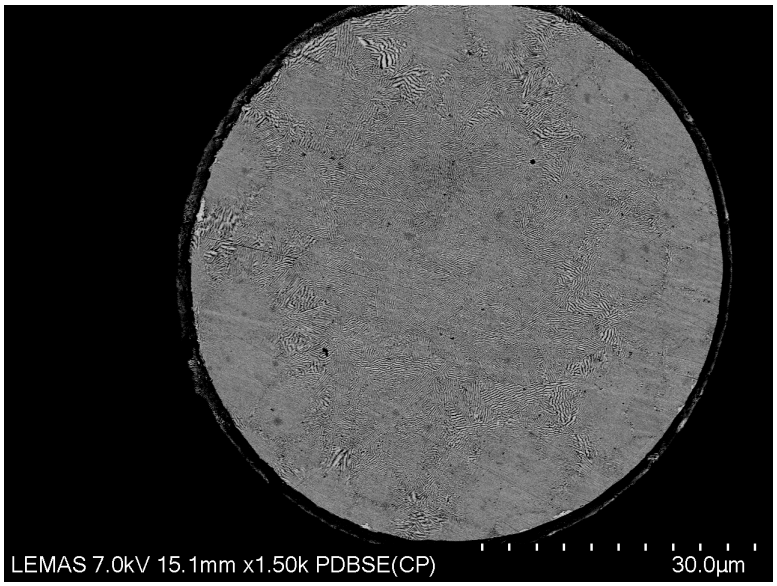

(b)

Figure 6.1.16: (a) and (b) Macrostructure of the sample section in the range of 53 ~ 75 μm,

38 ~ 53 μm

The droplets at the smallest range (38 ~ 53 μm) should experience the highest cooling rate due to the balance of heat flux, to freeze the nucleation down to the lowest temperature. Thereby it should be seen that the formation of single-phase dendrites becomes increasingly intense with decreasing

droplet size. In contrast, both Fig. 6.1.17a and Fig. 6.1.17b reveal the morphology for microstructure formation return to *Type I* mechanism, by which the anomalous eutectic colonies are surrounded with lamellar eutectic. Moreover, the normally accepted tendency that volume fraction of anomalous eutectic is a monotonically increasing function of the undercooling in bulk undercooled alloys, is not the case for drop-tube processed samples either. Comparing with Fig. 6.1.13 at 150 ~ 212 μm, there is a clear reduction on the volume fraction of anomalous eutectic with decreasing droplet size.

The possible reasons to not have a clear transitive microstructures from anomalous eutectic with lamellar eutectic, to single-phase dendrite with lamellar eutectic can be explained as:

- The numerical estimation of the cooling process for a metal droplet in an environment similar to gas atomisation (introduced in Section 3.1) exists many uncertainties, giving rise to using the average thermal properties in calculation and lack of understanding of the momentum transfer between the gas and the free-falling droplets. As a result of those uncertainties, the calculated cooling rate should be towards the high end or even overestimated.

- Even though the low heat input to the system from the molten metal can achieve the cooling rate as high as the order of 10^4 Ks^{-1} and melt sub-division can restrict the catalytic effect of active nuclei from solidification at higher undercoolings in the drop-tube study [59, 33], a potent nucleation site to cause the heterogeneous nucleation can reduce the undercooling significantly. As shown in Fig. 6.1.14, Fig. 6.1.15, Fig. 6.1.16 and Fig. 6.1.17, the initial nucleation begins at the outer layer of spherical droplet, which requires a much smaller barrier towards the phase transition (see Fig. 1.1.1). Before a higher undercooling would be reached at such a high cooling rate, the heterogeneous nucleation already begin to form the eutectic dendrites around the droplet surface towards the undercooled melt, followed by the growth of lamellar eutectic after recalescence.

- There would be a temperature gradient inside the molten metals subjected with high cooling rates. Mullis, *et al.* [63], investigated the peritectic transformation $Ni_2Al_3 + L \rightarrow NiAl_3$ of gas-atomised Al-Ni powders at the range of 150 ~ 212 μm and found that there are more Ni_2Al_3 and less $NiAl_3$ at the surface than in the centre. This observation highly suggest that the high heat extraction of in-flight droplet can only intensively influence the part of region near the droplet surface while the central region remain unchanged as shown in Fig. 2.4.5. Moreover, the propagation of primary eutectic dendrite interface relies upon either continued heat extraction through the solid to the surface or the undercooled liquid ahead of the front acting as a sink for the latent heat, which might keep any gradient minimal in the centre. The less or no undercooled melt in the centre at the onset of recalescence, then prevents the primary phase from branching through the centre of droplet and so provides the limited space for the formation of anomalous eutectic.

Because the images with higher resolution up to (6K) fails to observe the finest lamellar structure

in Fig. 6.1.17, it is possible for these fine 'lamellar' eutectic regions to be truly featureless. As introduced in Section 3.1, the smallest droplet size would reach the highest cooling rate, which could not only leads to high undercooling but also increase the heat extraction rate to possibly neglect the release of latent heat during solidification. As a result of this, the partitionless solidification might take place in these 'lamellar' eutectic regions.

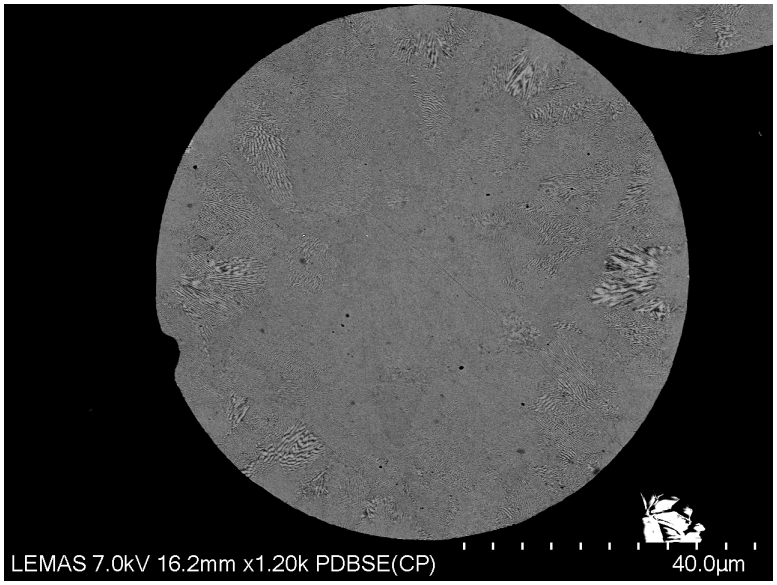

(a)

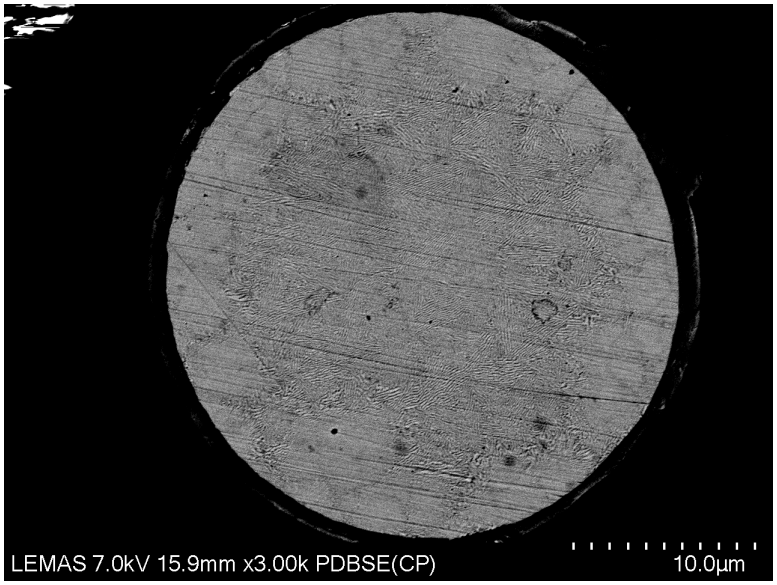

(b)

Figure 6.1.17: (a) and (b) Macrostructure of the sample section in the range of 38 ~ 53 μm,

6.2 IMAGE PROCESSING RESULT

6.2.1 IMAGEJ MASK

The anomalous eutectic within droplets is characterised with reference to the undercooled solidification, wherein the density of anomalous eutectic is the most reliable indicator of the level of undercooling. The distribution of anomalous eutectic can be clearly identified by BSE images in Section 6.1.2, but the quantitative analysis of those regions by X-ray and neutron diffraction is almost impossible. Since both anomalous eutectic and lamellar eutectic share the face centered cubic (FCC) structure and are formed by solid solution and solid solution. Even by means of Electron backscatter diffraction (EBSD) to identify the microstructural feature of both phases, neither of these two eutectic phases shows a strong preferred orientation in such a structure [74]. Therefore, the image processing of BSE images introduced in Section 5.2 might become the most efficient approach to the quantitative analysis of volume fraction of anomalous eutectic as a function of radial co-ordinate.

The mask in Fig. 6.2.1a is well in conjunction with the greyscale macrostructure in Fig. 6.1.17a, making the quantitative analysis of volume fraction for a series of annuli possible. More importantly, *ImageJ* masks not only show the anomalous eutectic in dendritic form in Fig. 6.1.17a, but also reveal the anomalous eutectic in equal-axe form in Fig. 6.1.17b.

In [63], the width of each annulus was fixed at 15 μm and so, with the procedure of reducing the ellipse axes 30 μm at a time being repeated until the centre of the particle was reached. Because the size of particles varies slightly from 150 to 212 μm, the fixed reducing step can only make the central annulus different. For the size range changing from 38 to 850 μm in this study, it is difficult of the fixed step to generate a comparative phase density at each annulus for all ranges.

Owing to this, the width of annulus resulting in six annular regions per droplet can be obtained by

$$\text{Annulus Width} = \frac{\text{Droplet Diameter}}{6} \tag{6.2.1}$$

The positions of the annuli at lower limit of size range and those at the upper limit of size range by using Eq. (6.2.1) are shown in Fig. 6.2.1a and Fig. 6.2.1b respectively. Thereby, except for their outer surfaces that were formed by disrupting the melt stream during the drop-tube process, the inner annuli have similar shapes but comparatively different size scales. The volume fraction of anomalous eutectic in a series of annuli from the origin (Label I) to the surface (Label VI) at one size range becomes comparable with that at counterparts. Also the masks from the selected droplets of other size ranges between 53 and 500 μm are illustrated in Fig. 6.2.2 respectively.

Combining Fig. 6.2.1 with Fig. 6.2.2, the overall volume fraction of anomalous eutectic for all ranges can be categorised into two typical particles, that is, the one at higher ranges (300 ~ 850 μm) has the anomalous eutectic all-over and the other at lower ranges (38 ~ 300 μm) is favourable to clustering around the surface. The quantitative analysis of variation on the volume fraction of

anomalous eutectic as a function of radial co-ordinate will be proceeded in Section 6.2.2.

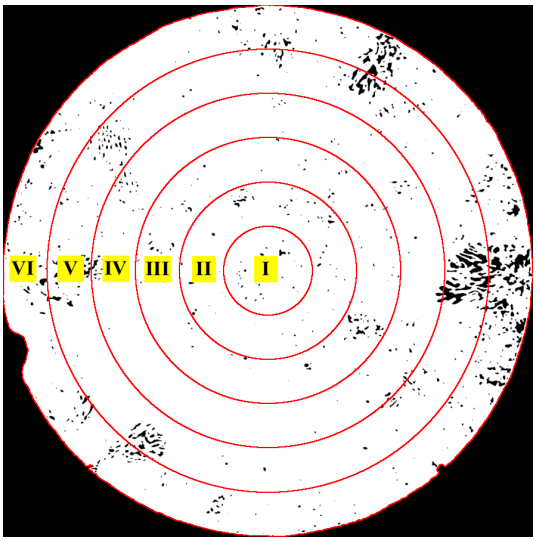

(a) 38 ~ 53 μm

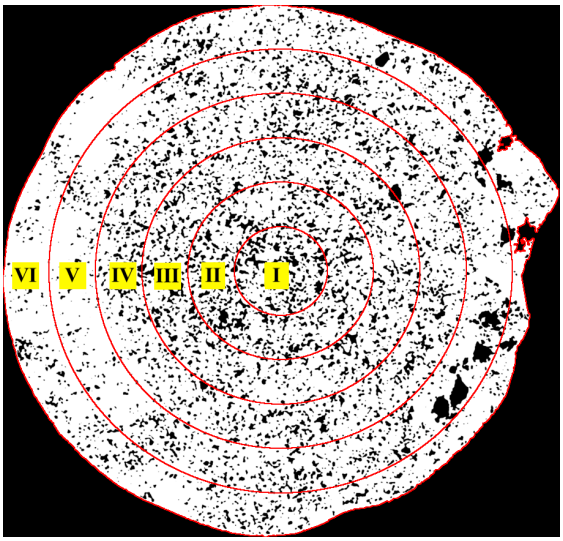

(b) 500 ~ 850 μm

Figure 6.2.1: Comparison of the positions of the annuli of droplet (38 ~ 53 μm) and those of droplet (500 ~ 850 μm) used in the quantitative analysis introduced in Section 5.2

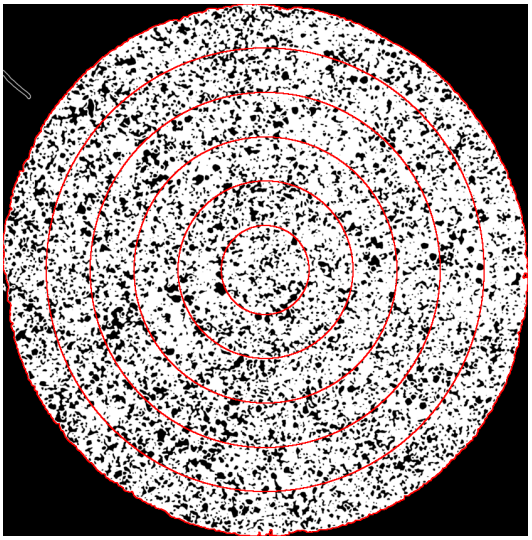

(a) 300 ~ 500 μm

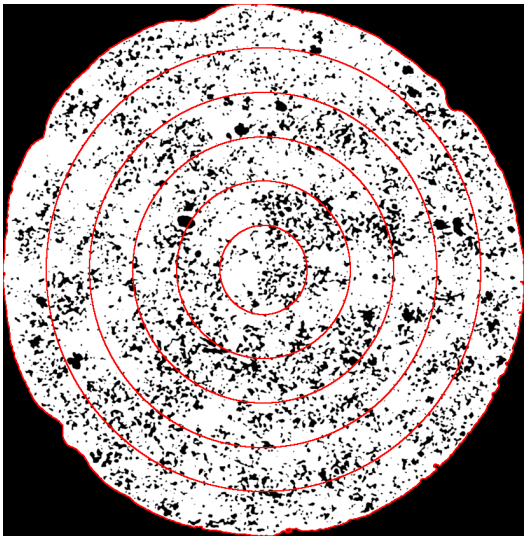

(b) 212 ~ 300 μm

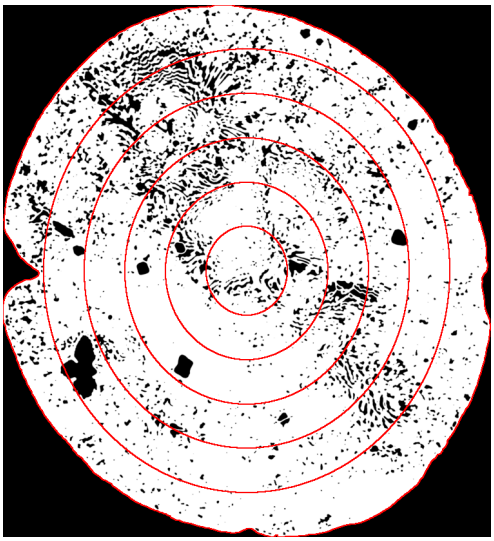

(c) 150 ~ 212 μm

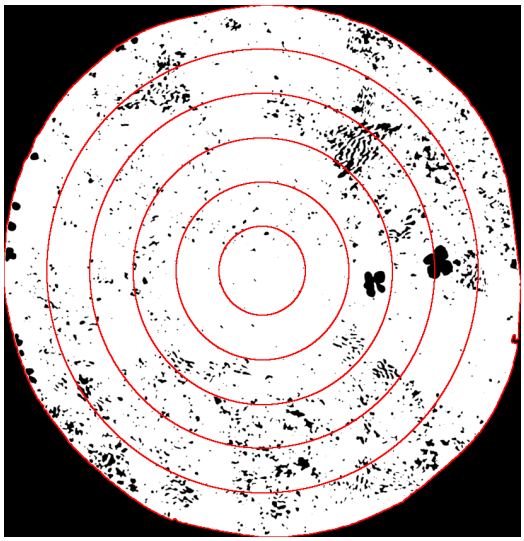

(d) 106 ~ 150 μm

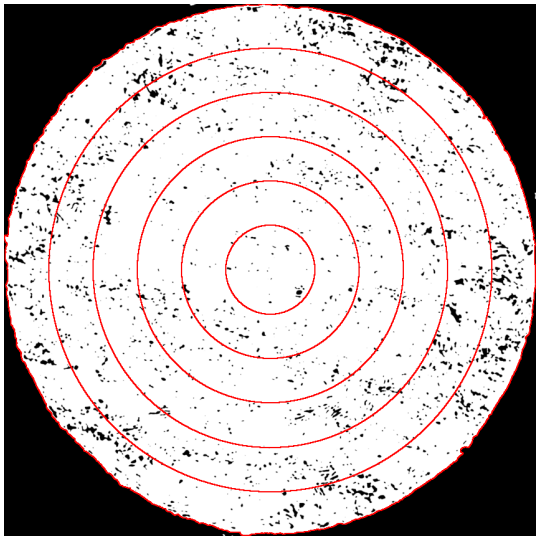

(e) 75 ~ 106 μm

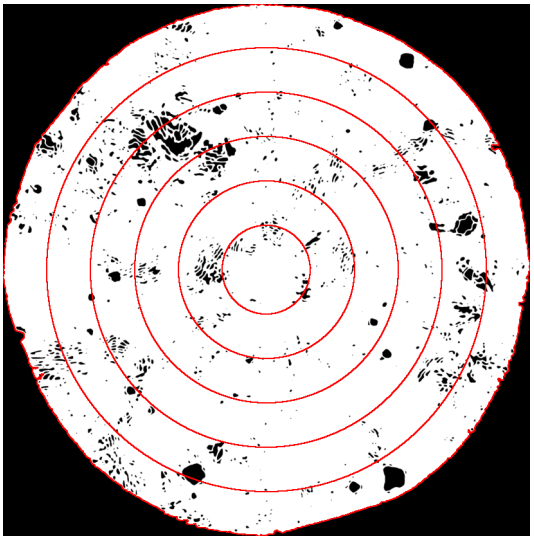

(f) 53 ~ 75 μm

Figure 6.2.2: ImageJ mask of selected droplets in each size range from 53 ~ 500 μm showing the distribution of anomalous eutectic respectively

6.2.2 QUANTITATIVE MICROSTRUCTURAL ANALYSIS

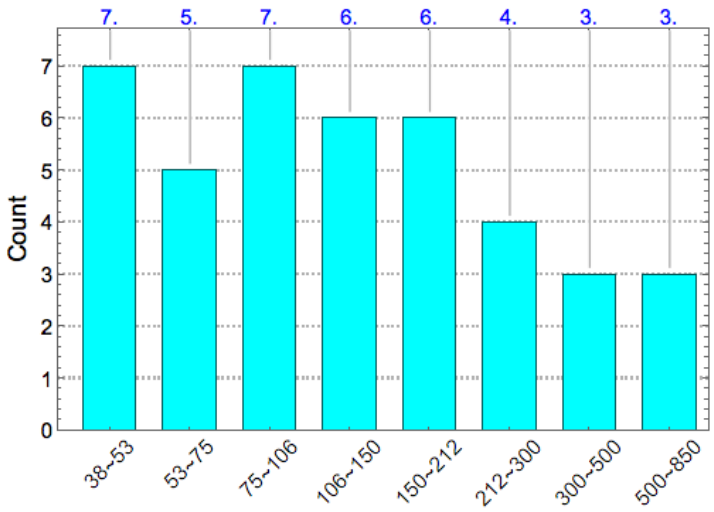

Figure 6.2.3: Apparent size distribution of the droplets investigated (upper and lower limit if size range in μm)

A total of 41 different droplets from 38 to 850 μm were analysed by the image processing method as each cross-section mask of characteristic size range is shown in Fig. 6.2.1 and Fig. 6.2.2. The number and the distribution of the apparent diameters of the droplets under investigation is as shown in Fig. 6.2.3.

Although the volume fraction of anomalous eutectic for each ellipse was subtracted from the preceding ellipse in order to produce volume fraction for a series of annuli, the automatic phase identification by the *ImageJ* macro script is heavily upon the built-in blur feature, which is mainly dependent on the image resolution, the brightness and the greyscale contrast. In consequence, the recorded fraction at one range might not be used to compare with that at another range quantitatively. This is kind of true since one mask would underestimate the area of anomalous eutectic region (see Fig. 6.2.2e) whereas another can overestimate this area (see Fig. 6.2.2a)

To overcome this drawback, the volume fraction obtained by area of anomalous eutectic against area of lamellar eutectic at each annulus, is re-calculated by

$$\text{Volume Fraction} = \left(\frac{\text{Annulus Area of Anomalous Eutectic}}{\text{Annulus Area}}\right)\left(\frac{\text{Droplet Area}}{\text{Droplet Area of Anomalous Eutectic}}\right) \tag{6.2.2}$$

As the macrostructure shown in Fig. 6.1.10, Fig. 6.1.11, Fig. 6.1.12, Fig. 6.1.13, Fig. 6.1.14, Fig. 6.1.15, Fig. 6.1.16, and Fig. 6.1.17, the individual BSE image was taken under the same photographic condition which should result in the detected anomalous region under the relatively same fraction by *ImageJ*. At the cost of real volume fraction of anomalous eutectic, either underestimated or overestimated data should be transferred to the comparable data for all ranges by using Eq. (6.2.2).

The example bar chart representative with the mask in Fig. 6.2.2a is shown in Fig. 6.2.4. Each bar is characteristic with the volume fraction at the corresponding annulus within droplet. Because the anomalous eutectic at the range 300 ~ 500 μm grows through the entire droplet, there is less clear tendency based on the radial variation on volume fraction from the centre (Label I) to the surface (Label VI).

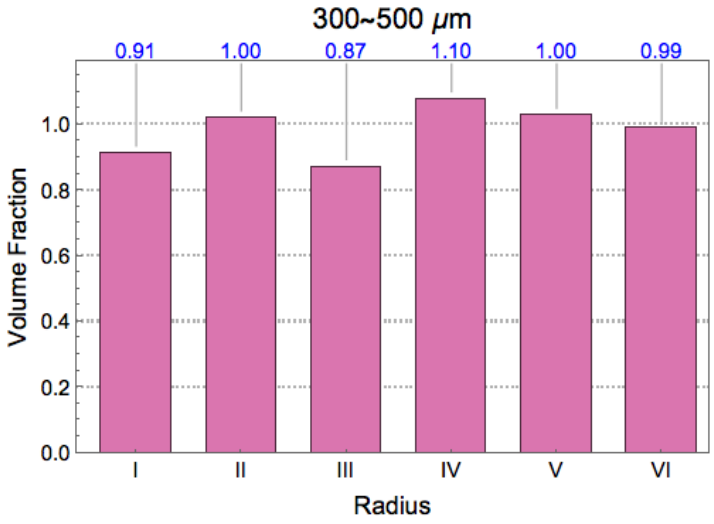

Figure 6.2.4: Volume fraction of anomalous eutectic as a function of radius for a single droplet

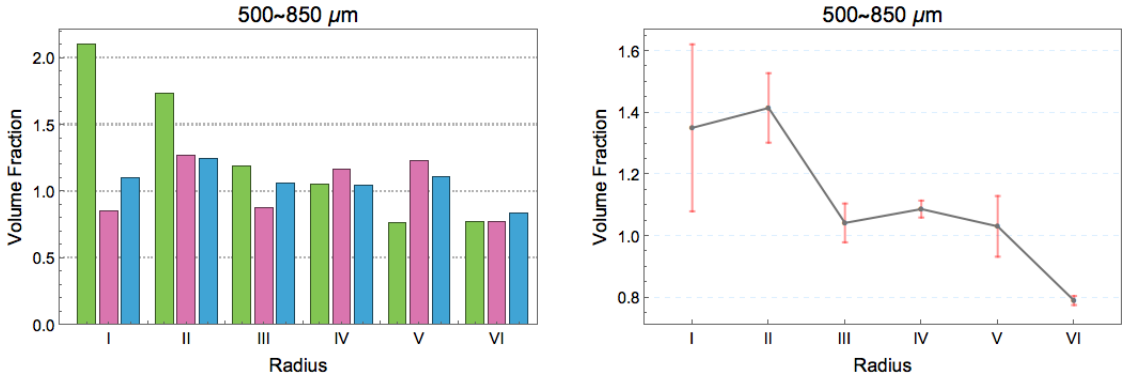

(a) Volume fraction of every chosen droplets

(b) Average volume fraction

Figure 6.2.5: Volume fraction of anomalous eutectic as a function of radius for droplets with 500 ~ 850 μm

The selected droplets illustrated in Fig. 6.2.3 are analysed by the same fashion as shown in Fig. 6.2.4. But the multiple volume fraction of selected droplets at the corresponding size range are combined together in one bar chart, for example, as shown in Fig. 6.2.5a which consists of 3 different colour bar for 3 different selected droplets. In order to have a better overview of volume variation on

anomalous eutectic inside the droplet, the volume fractions illustrated in Fig. 6.2.5a are used to generate the mean and the standard deviation of the mean at each annular region as shown in Fig. 6.2.5b.

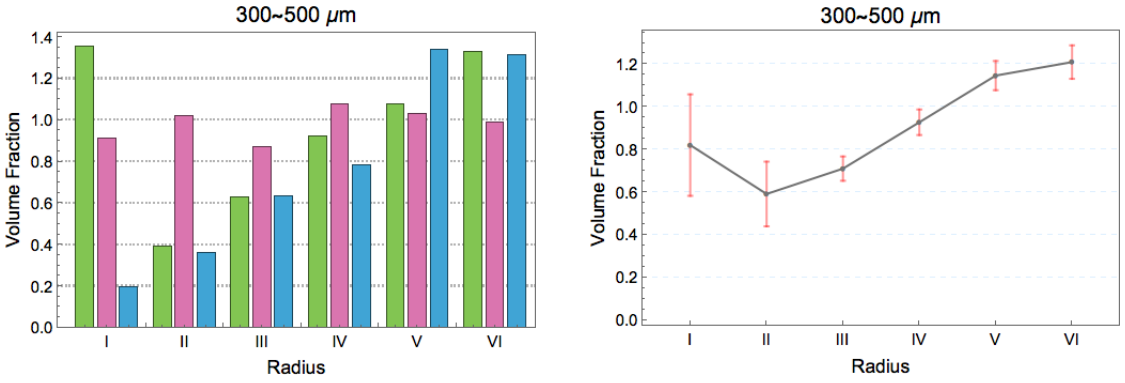

(a) Volume fraction of every chosen droplets (b) Average volume fraction

Figure 6.2.6: Volume fraction of anomalous eutectic as a function of radius for droplets with 300 ~ 500 μm

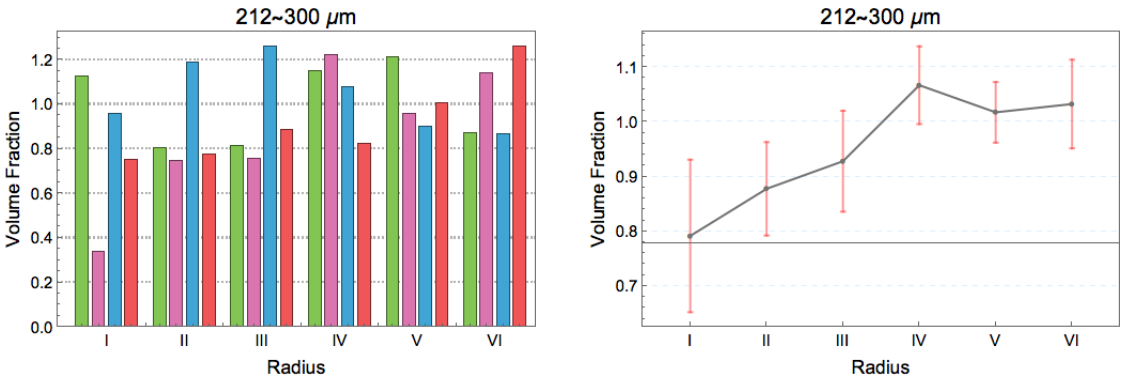

(a) Volume fraction of every chosen droplets (b) Average volume fraction

Figure 6.2.7: Volume fraction of anomalous eutectic as a function of radius for droplets with 212 ~ 300 μm

According to Fig. 6.2.5, Fig. 6.2.6, Fig. 6.2.7, Fig. 6.2.8, Fig. 6.2.9, Fig. 6.2.10, Fig. 6.2.11, and Fig. 6.2.12, the anomalous eutectic formed by *Type I* mechanism at all size ranges can indeed have two different phase distribution as a function of the radial distance from the centre of the droplet, which is consistent with the mask observation in Section 6.2.1. On the one hand, droplets in the higher size range between 150 and 850 μm are subject with average phase transformation on anomalous eutectic from the centre to the surface. The larger the droplet size, the more likely the anoma-

lous eutectic is attained at the inner annular regions. On the other hand, droplets in the lower size range between 38 and 150 μm have more anomalous eutectic in dendritic form growing radiantly towards inside. As a result, there is an obvious positive change of volume fraction with the increase in radical coordinate.

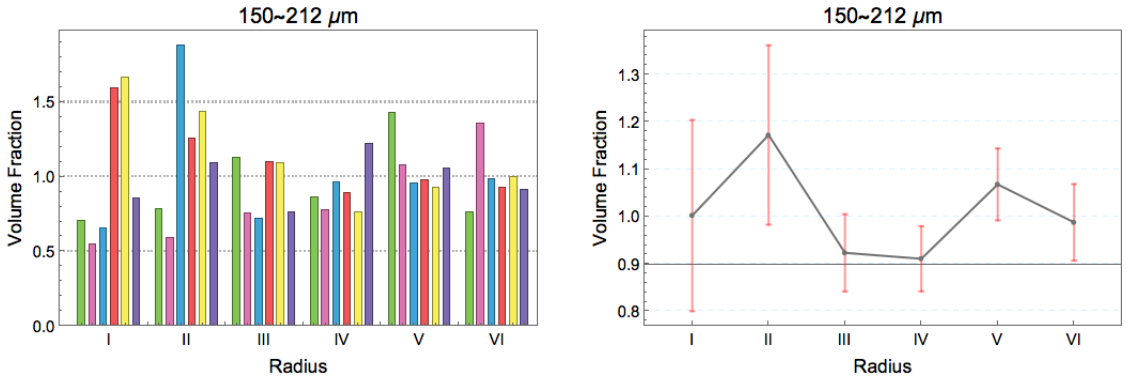

(a) Volume fraction of every chosen droplets (b) Average volume fraction

Figure 6.2.8: Volume fraction of anomalous eutectic as a function of radius for droplets with 150 ~ 212 μm

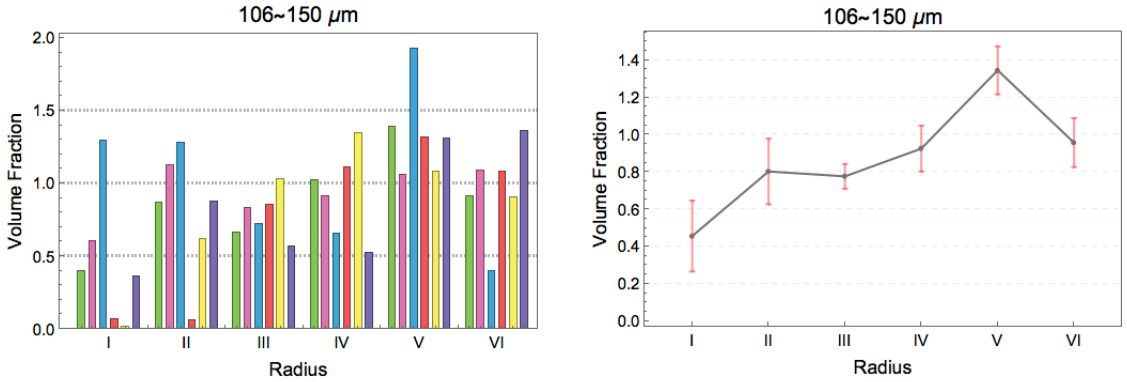

(a) Volume fraction of every chosen droplets (b) Average volume fraction

Figure 6.2.9: Volume fraction of anomalous eutectic as a function of radius for droplets with 106 ~ 150 μm

Also it is interesting to find that the volume fraction between the annulus region V and VI has the negative variation at lower size ranges as shown in Fig. 6.2.9b, Fig. 6.2.11b, and Fig. 6.2.12b, which is consistent with lamellar eutectic in BSE images in Fig. 6.1.14b, Fig. 6.1.16b and Fig. 6.1.17a. This variation might give rise to the recalescence during the growth of primary eutectic dendrite. Although the heat extraction could take place through both the undercooled melt and the solid, the high conductivity of Ag-Cu alloy could minimize the potential temperature gradient within such a

small spacious droplet during the recalescence. Therefore the direction of heat transfer should be eventually towards the outer surface from the centre such that the remaining liquid near the surface should continuously warm up to the temperature < 10 K below the eutectic temperature to form the finer, but yet lamellar eutectic as shown clearly in Fig. 6.1.16b and Fig. 6.1.17a.

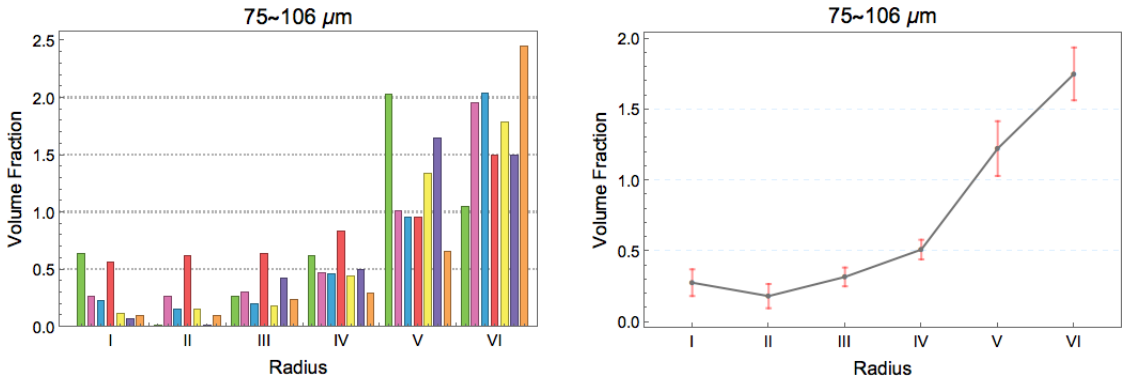

(a) Volume fraction of every chosen droplets

(b) Average volume fraction

Figure 6.2.10: Volume fraction of anomalous eutectic as a function of radius for droplets with 75 ~ 106 μm

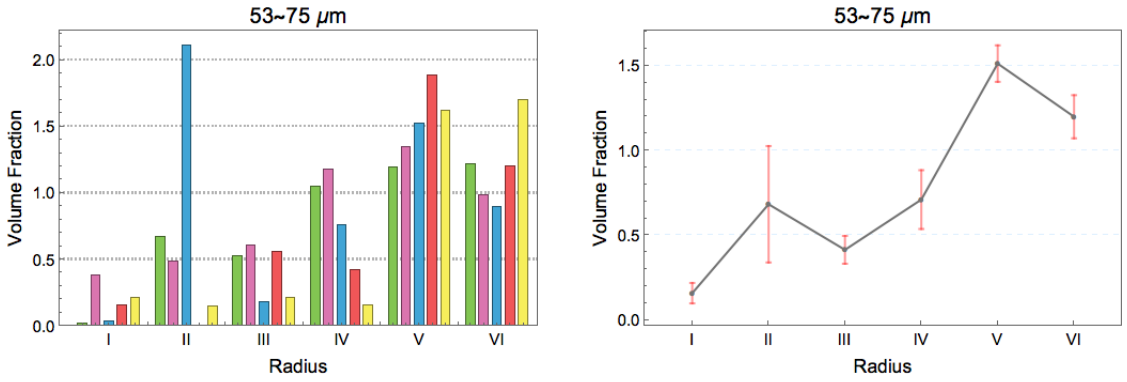

(a) Volume fraction of every chosen droplets

(b) Average volume fraction

Figure 6.2.11: Volume fraction of anomalous eutectic as a function of radius for droplets with 53 ~ 75 μm

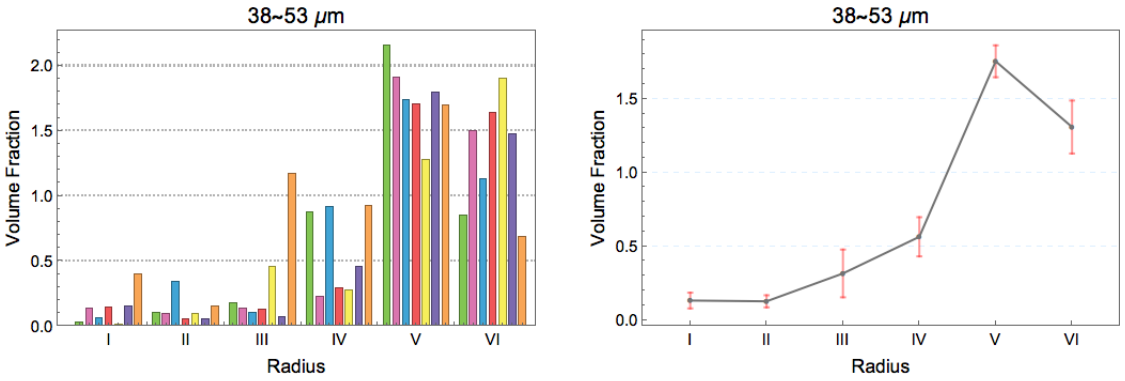

(a) Volume fraction of every chosen droplets

(b) Average volume fraction

Figure 6.2.12: Volume fraction of anomalous eutectic as a function of radius for droplets with $38 \sim 53\ \mu$m

6.2.3 MICROSTRUCTURAL EVOLUTION

The average phase density at every annulus region is shown in Fig. 6.2.13, which is combined with the average volume fraction of anomalous eutectic for all size ranges in Section 6.2.2. It is clearly shown that the distribution of anomalous eutectic neither changes randomly at different annulus position, nor can be well described by a single linear relationship regarding the radial phase variation across the entire droplet for all size ranges. For small size ranges (38 ~ 150 μm, the trend of the population of anomalous eutectic appears to have a relatively sharp rise in the amount of anomalous eutectic near the surface of the droplet, whereas an approximately low constant amount of anomalous eutectic near the centre. In contrast, for larger size range (150 ~ 850 μm), either slightly less or approximately identical amount of anomalous eutectic is presented at the annulus VI, comparing with three annulus nearest the centre (I, II, III).

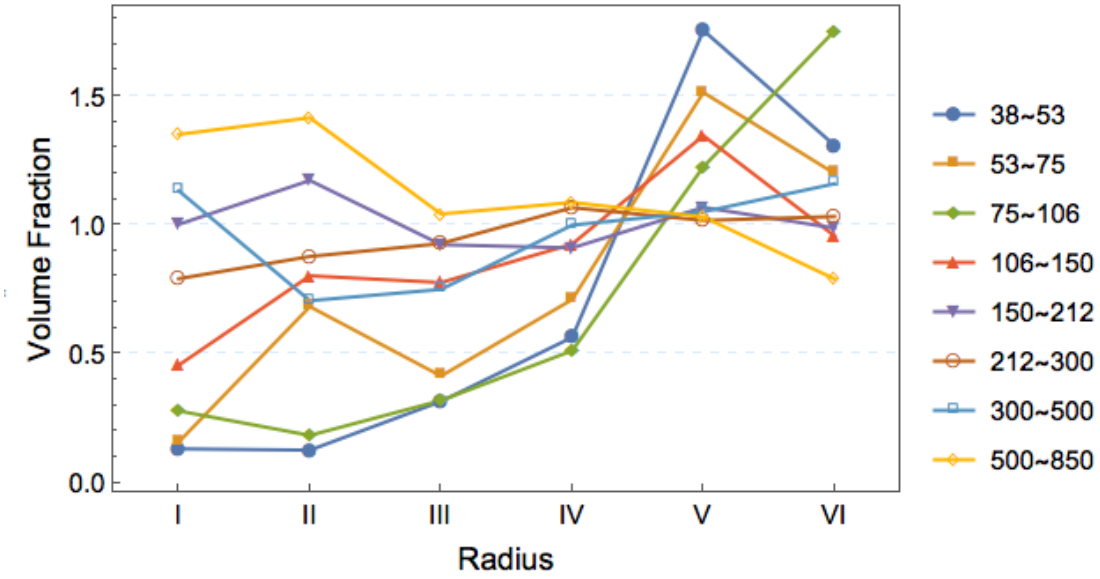

Figure 6.2.13: Variation on anomalous eutectic as a function of radial coordinate for all size ranges

The above observation might be highly suggestive as following:

- The temperature gradient should exist in the entire rapid solidification at any instant of time, due to the phase variation across different annulus positions.
- The morphology of anomalous eutectic is largely determined by the local heat transfer situation.

Based on the experimental BSE images shown in Section 6.1.3 and the phase volume fraction illustrated in Fig. 6.2.13, the overall population of anomalous eutectic at the smaller size ranges of droplets becomes gradually less intensive than that at the higher size ranges, despite such small

droplets potentially subjected with the high cooling rates up to 10^5 K/s. The reason, as mentioned in Section 6.1.3, could be attributed to the rapid recalescence preventing the primary phase from branching and so giving rise to the subsequent equilibrium solidification at the annulus regions near the centre. Moreover, the phase variation profile in Fig. 6.2.13 with a shape rise of volume fraction from the region IV can also suggestive the so-called high cooling rate around an individual droplet could be highly overestimated, since only two of six annulus regions might experience the high heat extraction to prompt the solidification of primary phase. Even for a 150-μm droplet, the region on which the heat extraction has the most influence, is approximately $(2/6) \times 150 = 50$ μm away from the outer surface.

Given the large size of droplets, especially greater than 212 μm, the overall high population with the small extent of the radial variation within droplets becomes increasingly obvious. Such a different trend in Fig. 6.2.13 can indicate that the undercooled melt ahead of the tip of primary phase at larger ranges of droplet, acting as a heat, sink is more spacious than that at smaller ones. As a result, the propagation of primary dendritic phase might be more likely throughout the entire droplet prior to the onset of remelting during the recalescence.

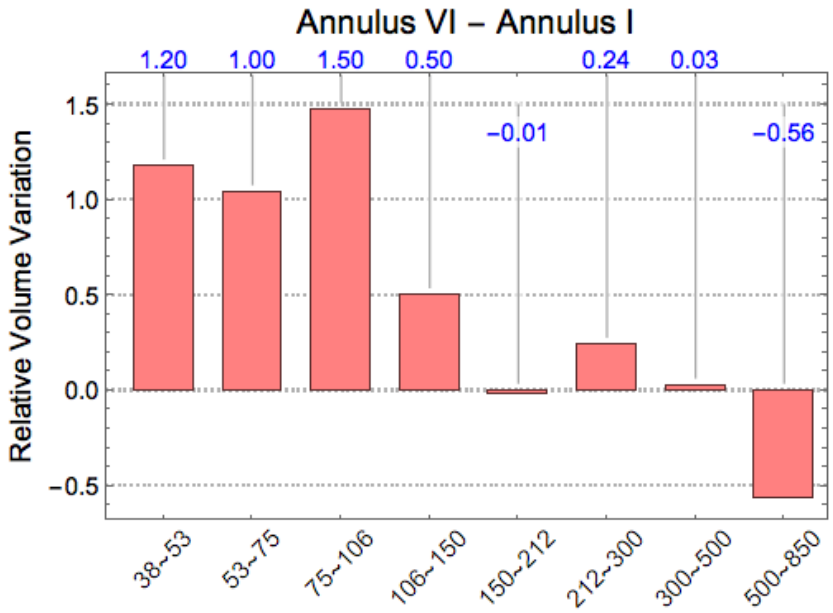

Figure 6.2.14: Difference of anomalous eutectic at annulus region VI and I for all size ranges

To have a better insight of two different distributions of anomalous eutectic within the droplets, the variation is characterised by the difference of anomalous eutectic between the centre and outer most annulus as shown in Fig. 6.2.14. The negative difference in the bar chart indicates more anomalous eutectic retained in the centre of droplet. Also the difference of two typical droplets become more recognisable as the size range (150 ~ 212 μm) is kind of threshold size to transfer one morphology to the other.

6.3 NUMERICAL RESULT

6.3.1 RESULT OF MACROSCOPIC HEAT TRANSFER MODELLING

The macro heat transfer model introduced in Section 3.1, is good to identify quantitatively how the variables, such as, undercooling, cooling rate, solid fraction, and the ratio of gas flow and melt flow, affect dynamic and thermal behaviour of various size ranges. However, the droplet velocity behaviours are far from being well understood and thereby prevents from the essential understanding of the heat transfer between the droplets and the gas stream. Ignored the droplet breakup in the initial stage of drop-tube processing, a turbulent circular free jet emerging from an orifice into a static fluid is used as illustrated in Eq. (5.3.1), in which the initial gas velocity is assumed as 4 m/s due to 0.4 MPa gas pressure used to force the superheated melt out of the crucible base. The gas stream resulting from 0.4 MPa gas pressure should have highest velocity at the onset of ejection and gradually decay down to minimum as shown in Fig. 6.3.1.

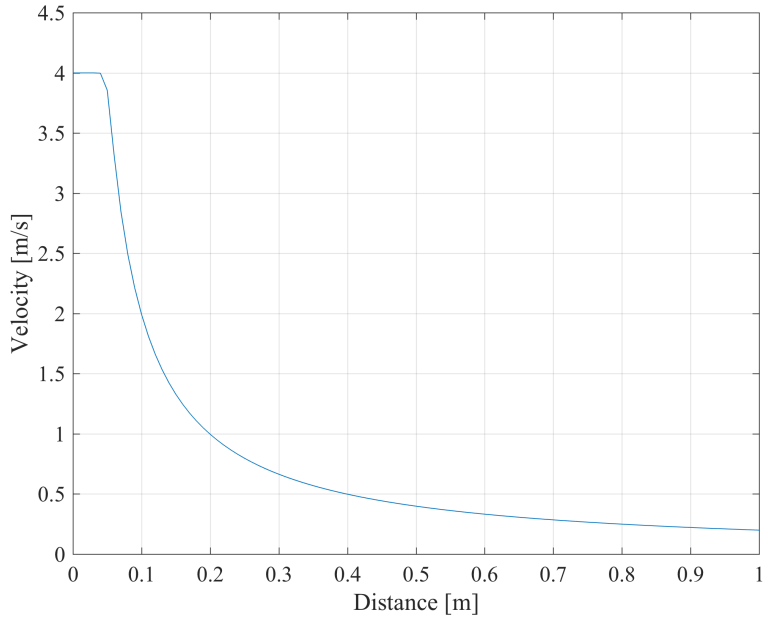

Figure 6.3.1: Fluid stream profile against flight distance

The forces due to drag, gravity, and inertia during the droplet in-flight are balanced by

$$\rho V_s \frac{\mathrm{d}w_s}{\mathrm{d}t} = V_s(\rho_s - \rho_f)g - \frac{1}{2}\rho_f A_s C_D |w_s - w_f|(w_s - w_f) \tag{6.3.1}$$

Combining Eq. (6.3.1) with Eq. (5.3.1), the velocity of various droplets can be obtained as

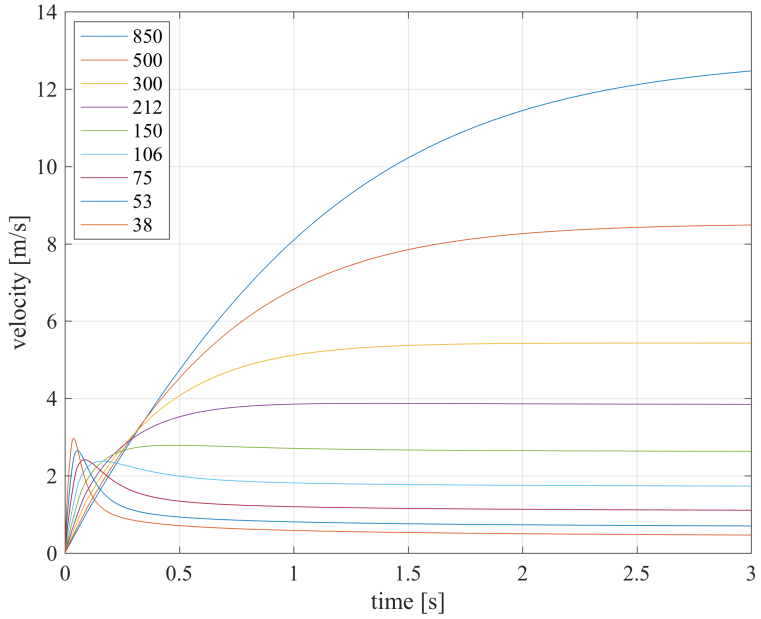

Figure 6.3.2: Droplet velocity profile against time

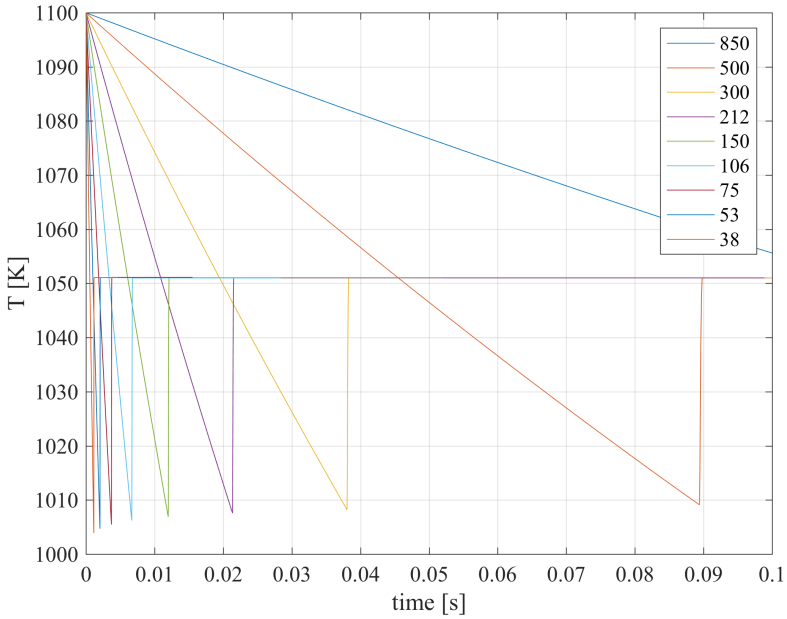

Figure 6.3.3: Thermal profile against time for various droplet sizes

Because the smaller the droplet, the stronger the drag force. After efficiently accelerated by the gas stream up to the maximum velocity, the smaller droplets are affected by the drag fore significantly

and so keep some extent of low flight velocity after decelerating by the drag force as shown in Fig. 6.3.2.

Considering the high conductivity of metallic material can efficiently transfer the inner heat to the environment, a Newtonian heat transfer formulation is used here to predict the variation on droplet temperature during its flight, the formulation of which was well introduced in Section 3.1.1. For eutectic Ag-Cu alloy, the cooling and solidification process should undergo four basic thermal regions, that is, liquid phase cooling, recalescence, eutectic solidification and solid phase cooling as shown in Fig. 6.3.3.

However, droplet subjected with high undercooling can surpass the eutectic point to solidify the primary single phase in the skewed zone of phase diagram as Fig. 2.3.2. Moreover, the solute supersaturation might take place at high undercooled melt during the initial solidification, giving rise to the single rich-element phase solidified from the last remaining liquid. Thus, the segregated solidification might still take place either before or after eutectic solidification at the exact eutectic composition as the experimental result shown in Section 6.1.3. In order to predict the thermal behaviour of drop-tube processed droplet quantitatively, such solidification can be safely neglected.

By using the macroscopic modelling, droplets of different sizes experience similar cooling process as shown in Fig. 6.3.3. Depending on the liquid cooling rate, the heat is efficiently extracted out of droplet to reduce the droplet temperature pass the eutectic point T_E but yet remain at liquid cooling. This process leads to the temperature prior to nucleation T_N far below the eutectic temperature T_E. Thus, the undercooling ΔT of various droplets can be obtained by $T_E - T_N$ as shown in Fig. 6.3.4.

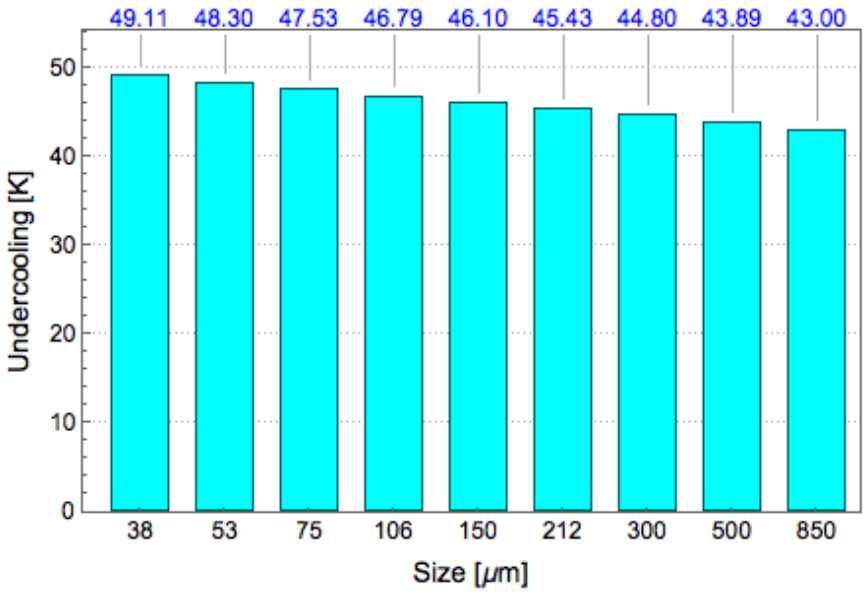

Figure 6.3.4: Undercooling for various droplet sizes

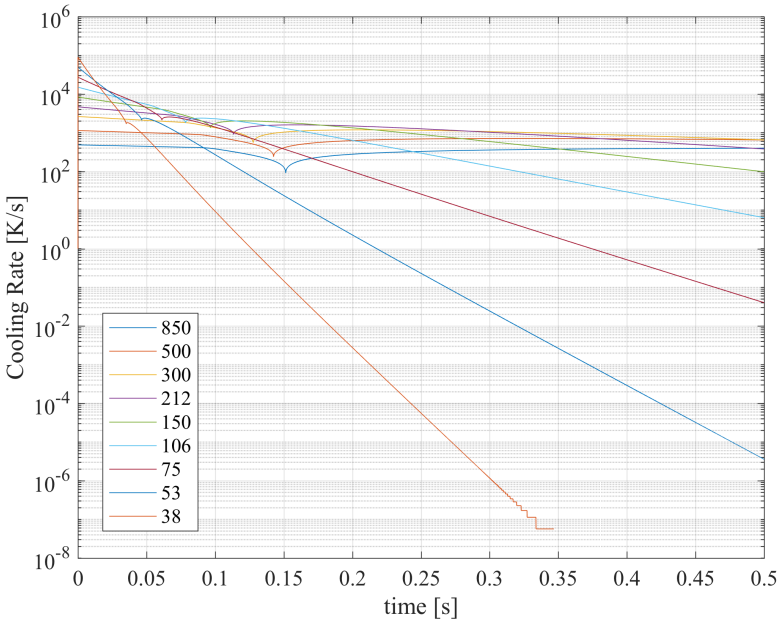

Figure 6.3.5: Cooling rate for various droplet sizes

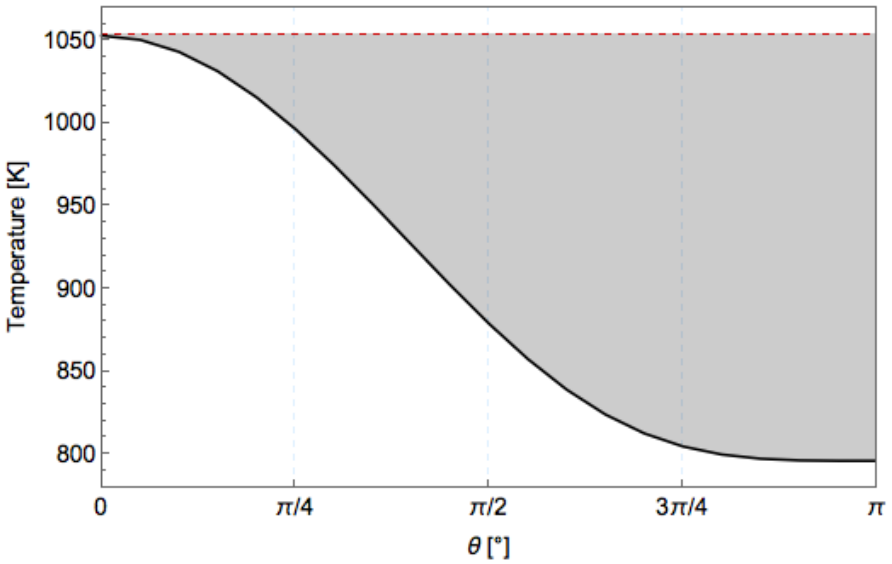

Figure 6.3.6: Nucleation temperature against the contact angle θ

At the recalescence region, the thermal profile rises up rapidly due to the assistance of the external latent heat during the solidification. Subsequently, the eutectic solidification occurs when the melt temperature rise up to the temperature near the eutectic temperature, followed by the solid

cooling. The heat extraction rate in the entire cooling process can be clearly seen in Fig. 6.3.5. The smaller droplet size has the greater range of cooling rates, such as the 38-μm droplet can achieve the cooling rate up to 10^6 K/s in the first thermal region.

Taking a close look at nucleation temperature, there is small variation as the undercooling increase lightly with the decrease of droplet size in Fig. 6.3.4. Although the cooling rates change dramatically from $< 10^3$ K/s at 850 μm up to $\sim 10^6$ K/s at 38 μm in Fig. 6.3.5, the variation on undercooling is highly suggestive that the high cooling rate might not be the key factor to affect on the undercooling. The undercooling that can be attained prior to the nucleation is significantly sensitive with the wetting angle θ as seen in Fig. 6.3.6. With the decrease of the wetting angle, the nucleation temperature would start at the higher possible temperature. When θ becomes 180 ° in calculation of nucleation event, the nucleation should have no contact site and become the homogeneous nucleation, which indeed requires highest undercooling to overcome the energy barrier for phase transformation (see Fig. 1.1.1). However the undercooling surpasses 77 K to have the partitionless solidification is highly unlikely at Ag-Cu system as explained in Section 2.1.2. Hence the wetting angle should be no greater than 60 °. In this study, 40 ° is selected since this value is widely used for the heterogeneous nucleation in else publication [4, 45].

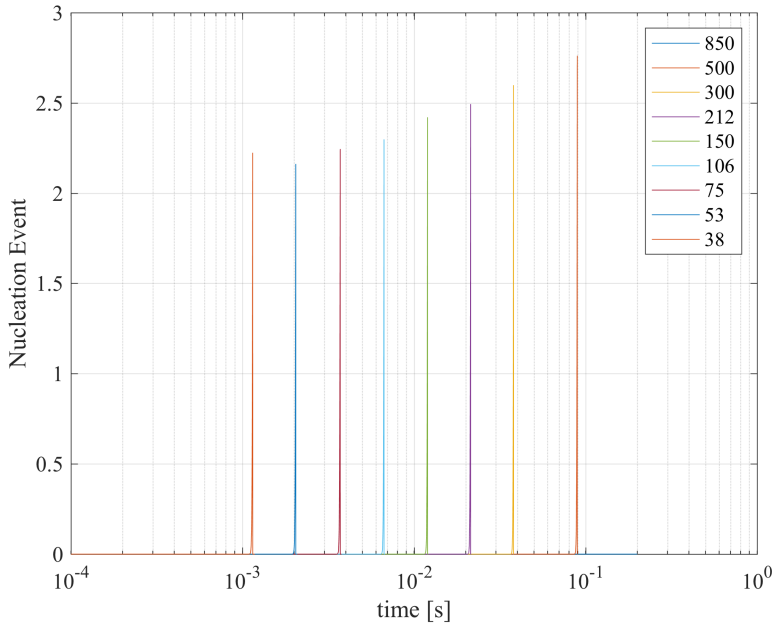

Figure 6.3.7: Nucleation event against time for various droplet sizes

At the fixed contact angle, the nucleation event is highly sensitive with the temperature change. With further cooling, the nucleation Event increase rapidly to a maximum value before the onset of recalescence. Although there would be 2 ~ 3 nucleation events within individual droplets, this calculation is assumed that only a single heterogeneous nucleation takes place at the outer surface

and to grow throughout the entire droplet. The growth of solid / liquid interface during the recalescence is calculated by considering a twinned sphereical segement. Thus, the liquid-solid interface mobility in Eq. (3.1.11) becomes the key variable to affect the recalescence mostly. In order to have a related value of this mobility, the approximated value is obtained by using HJ and TMK model in Fig. 2.3.5, that is $\approx (0.5-0.1)/(16-8) = 0.05$ m/s K.

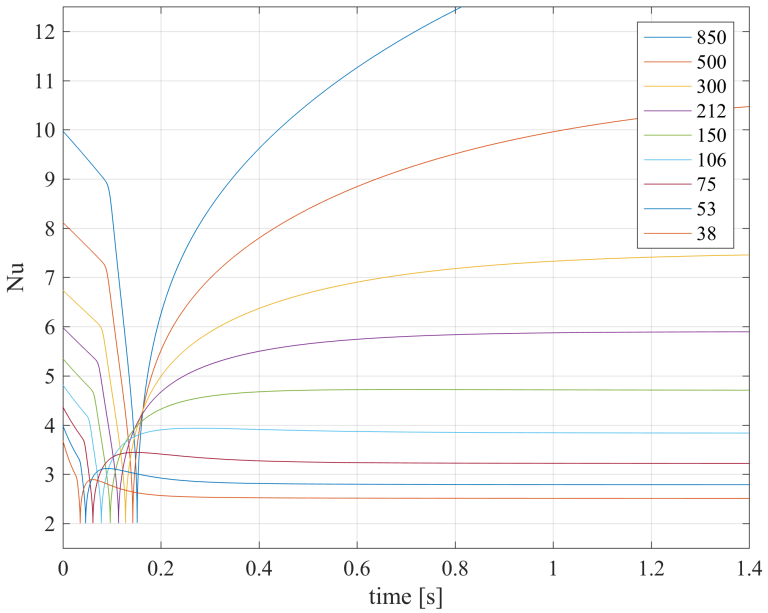

Figure 6.3.8: Nusselt number against time for various droplet sizes

At last, Nusselt number (Nu) which is related to the heat transfer coefficient will be illustrated here, mainly because the efficiency of heat transfer is largely determined by this dimensionless valuable. As shown in Fig. 6.3.8, there is the general tendency that the Nusselt number increase with increasing the droplet size under the low initial gas velocity. This anomalous profile of Nu can be explained that, when the droplets are away from the orifice, the relative velocity between the gas and the droplet is reduced to none, followed by the increasing droplet velocity is gradually dominant in the slip velocity such that the Nu increase with the rest of free falling.

6.3.2 RESULT OF UNSTEADY HEAT TRANSFER MODELLING

In the previous macroscopic heat transfer modelling, the entire cooling process of drop-tube formed droplets is based on quasi-steady approach which assumes the heat transfer coefficients are independent of time. However the quasi-steady approach can be valid when the processes of stabilisation of fluid dynamical and thermal fields near the surface of the sphere are of much shorter duration than the characteristic time of cooling during the solidification. In the drop-tube processing, the interaction between the fluid and the droplets is too complex to simply assume those assumptions are valid in the realistic cooling process*. Consequently, neither the time for stabilisation of thermal field nor that for stabilisation of fluid velocity field near the droplet surface can be safely neglected. The unsteady heat transfer modelling introduced in Section 3.2, therefore, is applied in predicting more realistic heat transfer coefficient and Nusselt number, etc., for this research.

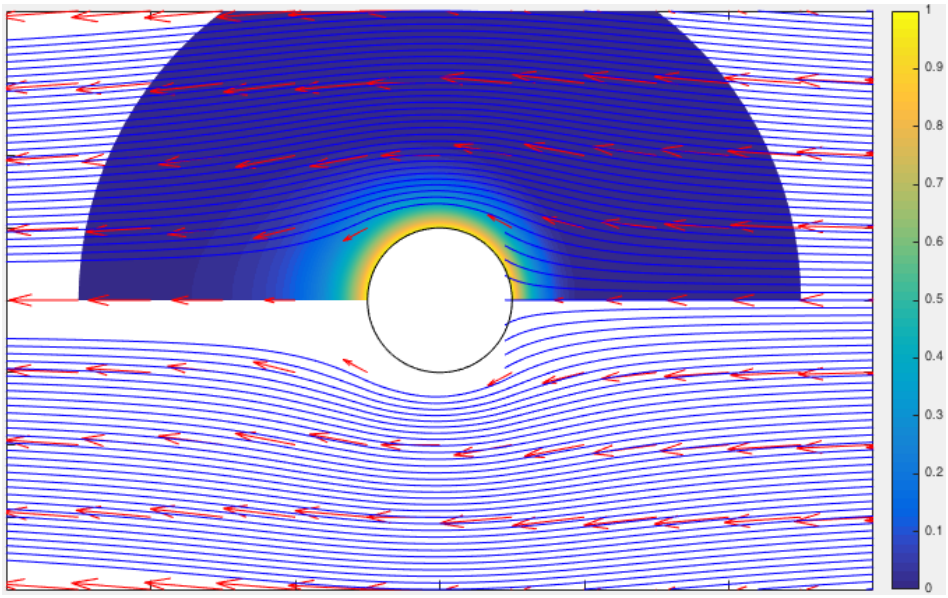

Figure 6.3.9: Overview of fluid temperature distribution with the streamlines of fluid velocity around a spherical droplet

By using the dimensionless energy equation in Eq. (3.2.5), the contour plot of fluid temperature distribution is shown in Fig. 6.3.9. When the droplet passes through the upwind fluid, the fluid would be bended to give way of the droplet as the streamlines show. As a result, the local temperature around the droplet surface should vary with the angle θ based on the direction of droplet velocity. In Fig. 6.3.10, there is an uneven temperature distribution developed in the cold fluid with the elapsed time as different colours represent different temperatures. The normalized temperature at the forward region ($\theta = 0$) is more intensive than that at the rear region ($\theta = \pi$). Also, an attached thermal wake is clearly appeared behind the sphere in the last two elapsed times.

*The potential issue of applying the macroscopic modelling was explained in Section 2.4.

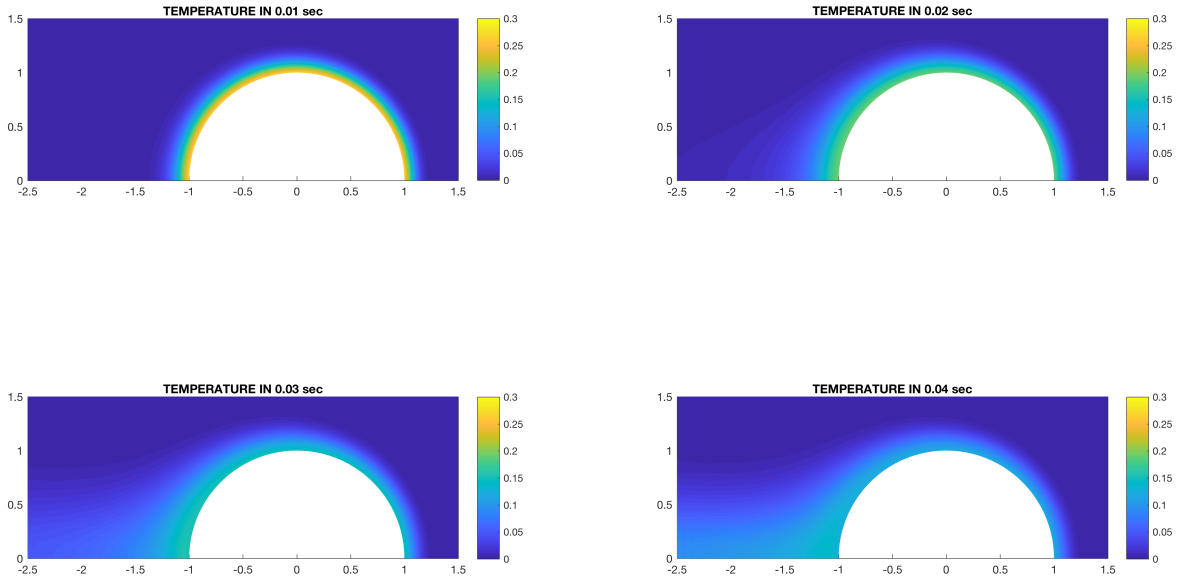

Figure 6.3.10: Variation on the fluid temperature with the elapsed time

The distinction of thermal field between the forward stagnation point and the rear stagnation point in Fig. 6.3.10 can be clearly seen from the thermal profile in Fig. 6.3.11 at $\theta = 0$ and in Fig. 6.3.12 at $\theta = \pi$ along the radial coordinate respectively. In general, the temperature change in Fig. 6.3.11 is more rapid than that in Fig. 6.3.12 at each time step. More importantly, tt dimensionless time $\tau = 0.04$, the temperature profile at $\theta = \pi$ has the maximum value at dimensionless radius $\xi = 1.13$, which is not the nearest position to the droplet surface. Nevertheless, the overall variation on droplet temperature at $\xi = 1$ is also shown in Fig. 6.3.13.

This anomalous change in the thermal profile at $\theta = \pi$ can be attributed to the variation on local Nu in Fig. 6.3.14. Unlike the average $\overline{\text{Nu}}$ applied by *Ranz and Marshall* correction in Eq. (3.1.4) as shown in Fig. 6.3.8, the smallest droplet size ($\sim 38\ \mu$m) subjected with highest heat extraction rate ($\sim 10^6$ K/s) cannot reduce $\overline{\text{Nu}}$ less than 2 with the increase of time. By using the unsteady heat transfer modelling„ the local Nu obtained can indeed be reduced down the negative value at the rear stagnation at $\theta = \pi$ and also be increased up to the highest local Nu at the forward stagnation point at $\theta = 0$ at time ($\tau > 0.03$)[†]. Such a variation on local Nu along the droplet surface gives the extensive evidence of the variation on thermal field in Fig. 6.3.11.

[†]The basic background of force convection due to different velocity boundary layers was introduced in Fig. 2.4.3.

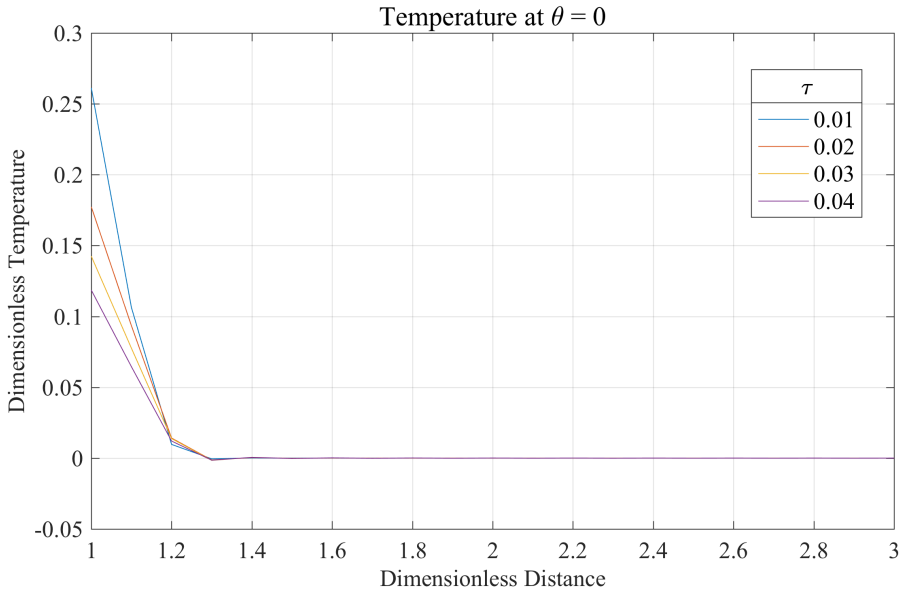

Figure 6.3.11: Variation on temperature along the radius coordinate at $\theta = 0$

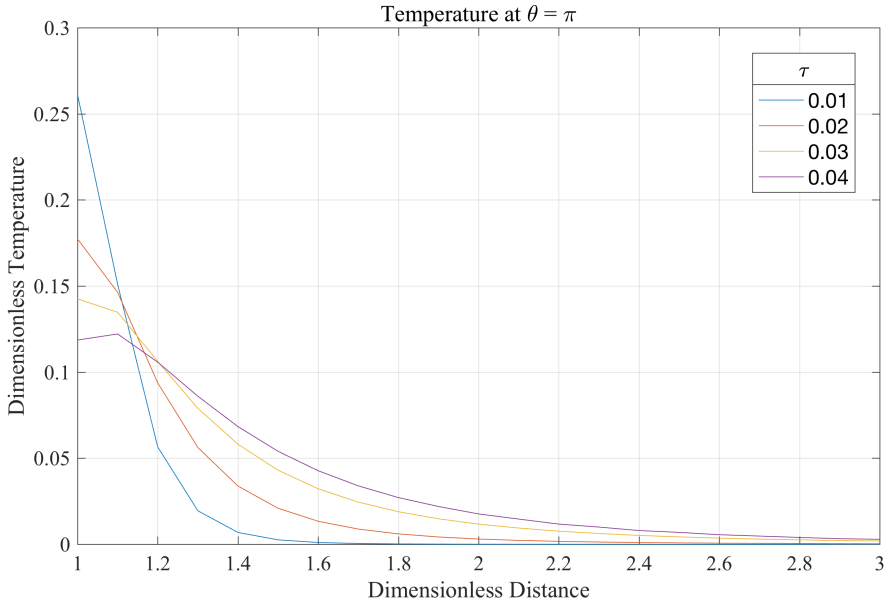

Figure 6.3.12: Variation on temperature along the radius coordinate at $\theta = \pi$

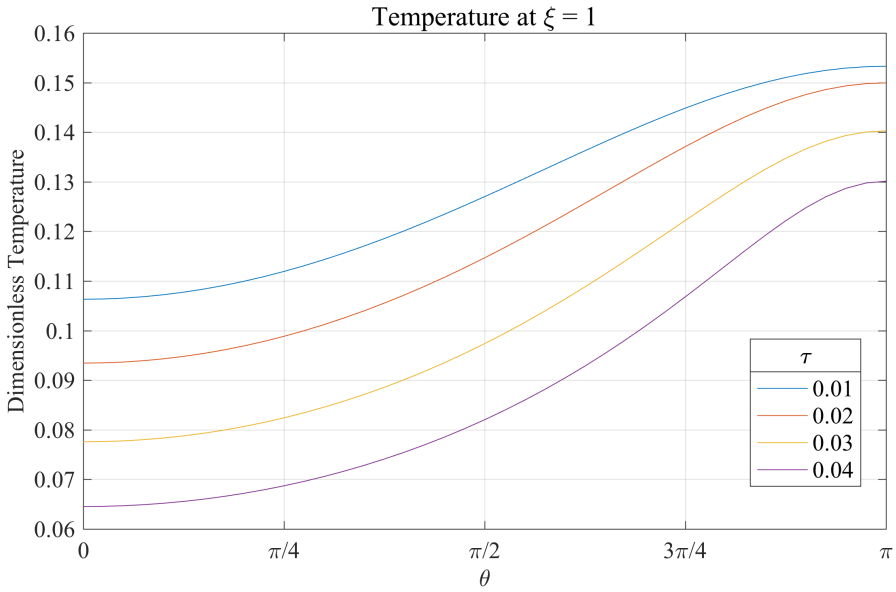

Figure 6.3.13: Variation on droplet temperature along the polor angle θ at $\xi = 1$

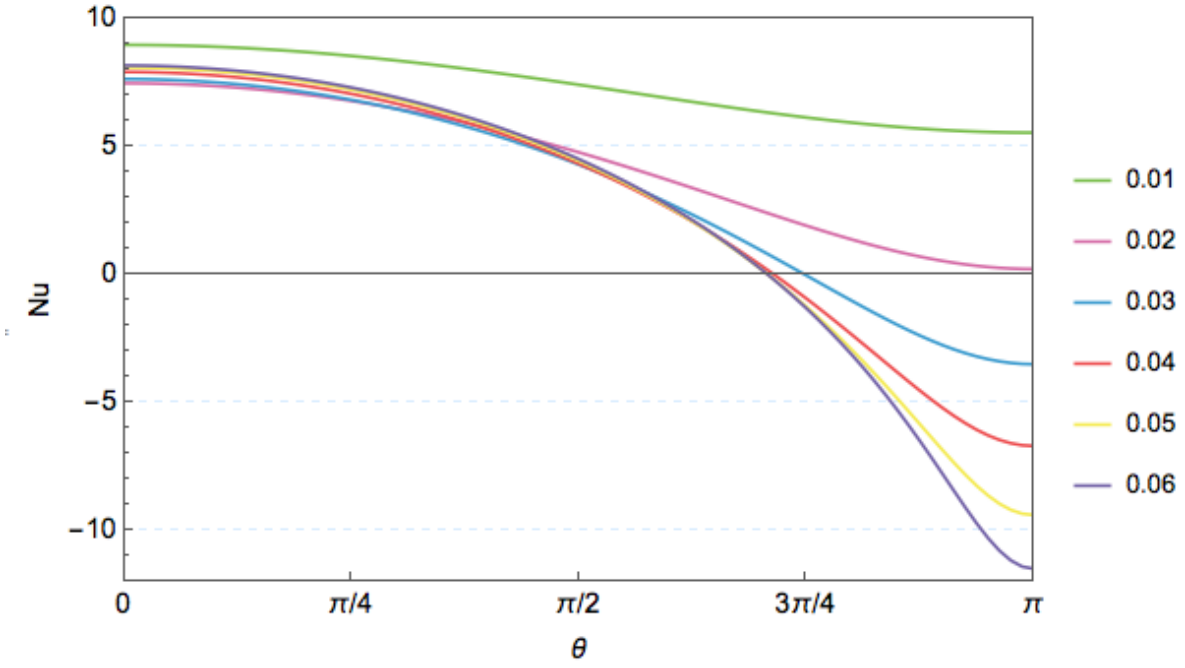

Figure 6.3.14: Variation on local Nu along the polar angle θ at $\xi = 1$

When the cold fluid encounters the superheat spherical melt at the forward stagnation point and so passes around the spherical surface to approach the separation point, the temperature of fluid gradually increases, meanwhile, the temperature of droplet decreases due to certain amount of heat carried by the fluid during the interaction. With the time elapsed, the fluid shifts through the separation point of droplet surface to rise up the temperature of fluid probably higher than that of hot droplet, which is shown in Fig. 6.3.12. As a result, the reversal heat transfer would take place since the local Nu is negative.

With the increase of τ, the asymptotic behaviour of heat transfer is possible as the steady temperature distribution is established in the thermal field of fluid around the droplet. In the case of Fig. 6.3.14, the asymptotic Ni is attained at $\tau \approx 0.06$. Based on the reference in [57], the asymptotic local Nu is approximated by

$$\mathrm{Nu} = \frac{1}{(\rho c)_{fs}\,\tau} \tag{6.3.2}$$

where $(\rho c)_{fs} = (\rho_f c_f)/(\rho_s c_s)$ and the critical time for this asymptotic thermal behaviour is by

$$\tau \approx \frac{1}{\mathrm{Pe}^{2/3}} \tag{6.3.3}$$

Combining Eq. (6.3.2) with eq:ht2d-02, the local Nu at time for stabilisation of thermal field should have the relationship as below:

$$Nu \propto \frac{1}{(\rho c)_{fs}} \propto \mathrm{Pe} \tag{6.3.4}$$

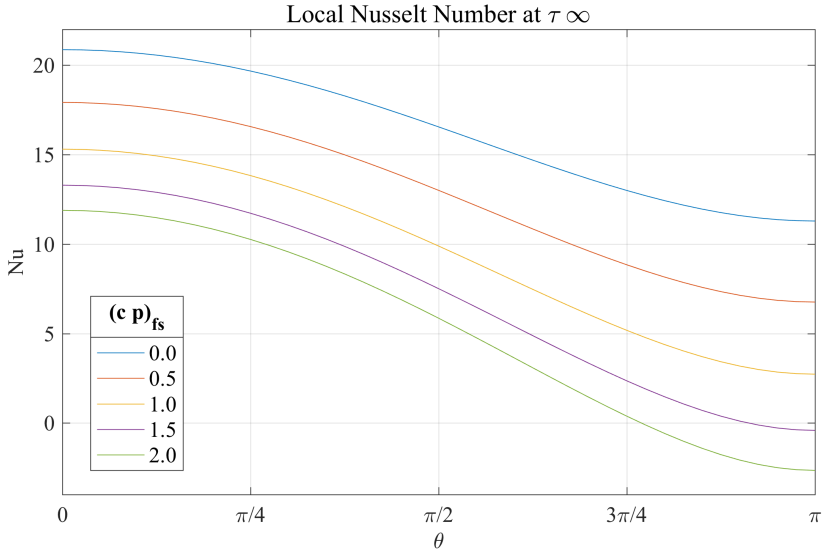

Figure 6.3.15: Variation on local Nu by using different $(\rho c)_{fs}$ along the polar angle θ at $\xi = 1$

In Fig. 6.3.15, the asymptotic local Nu at the fixed Pe = 200 decreases with the increase of $(pc)_{fs}$ and the separation point that the local $Nu = 0$ moves from the point at $\theta \approx \pi$ to that at $\theta \approx 3\pi/4$. In Fig. 6.3.16, the asymptotic local Nu at the fixed $(pc)_{fs} = 2.0$ decreases with the decrease of Pe and so the separation point moves from the point at $\theta \approx \pi$ to that at $\theta \approx 5\pi/8$.

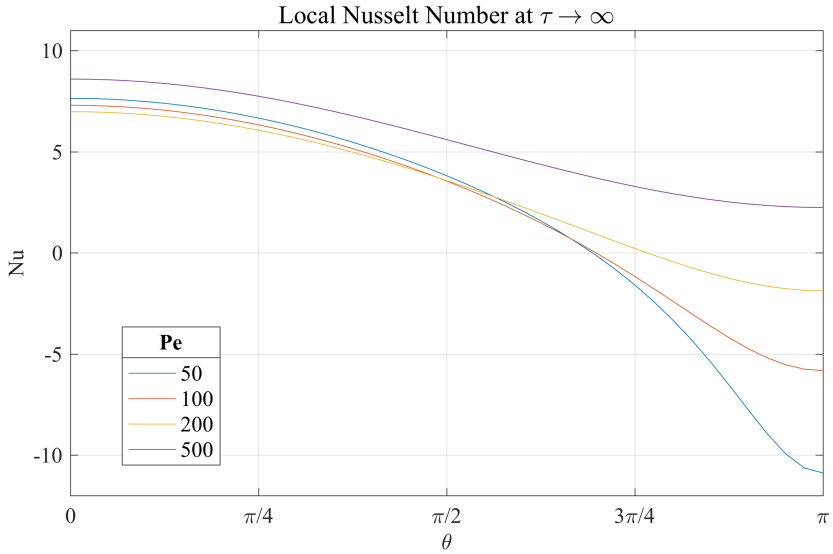

Figure 6.3.16: Variation on local Nu by using different Pe along the polar angle θ at $\xi = 1$

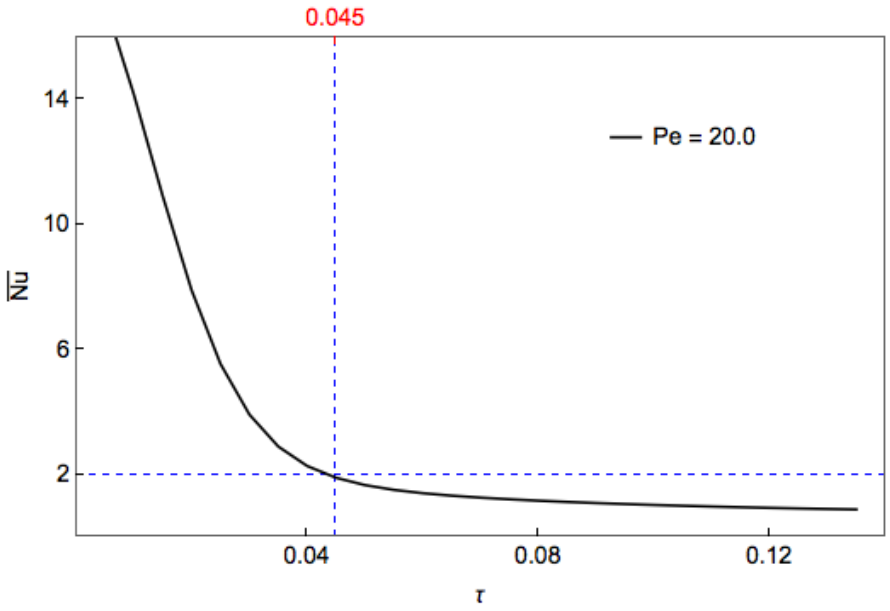

Figure 6.3.17: Variation on local Nu at small Pe and large $(\rho c)_{fs}$ along the polar angle θ at $\xi = 1$

Therefore, the tendency of local Nu along θ in Fig. 6.3.15 and Fig. 6.3.16 is well predicted by the relationship in Eq. (6.3.4) and the most likely situation to have a reversal heat transfer at the rear stagnation points should combine a larger $(\rho c)_{fs}$ with a low limit end of Pe. At Pe = 20.0, not only the local Nu at θ greater than $\pi/2$ is highly possible to be negative, but also the average $\overline{\text{Nu}}$ reduces down below 2[‡]is possible after τ greater than 0.045 as shown in Fig. 6.3.17.

Comparing Fig. 6.3.17 with Fig. 6.3.8, the cooling rate of every droplet size might be highly overestimated. When the time τ increases up to the critical time for the asymptotic thermal behaviour, the fluid temperature might be likely to have the maximum temperature within this wake (see in Fig. 6.3.12), giving rise to a reversal heat transfer in the vicinity of the rear stagnation points of the sphere and so more time for the first thermal region (liquid cooling) prior to the onset of nucleation.

[‡]$\overline{\text{Nu}}$ = 2 is the minimum value for the steady-state heat transfer around a sphere, which was well introduced in Section 1.3.2

CHAPTER 7

DISCUSSION

The experimental result in Section 6.1 and the numerical result in Section 6.3 will be combined together to discuss the thermal change in the drop-tube proceed solidification. In brief, the in-flight Ag-Cu droplet should undergo the following thermal regions as:

- The Ag-Cu melt is superheated in the coil furnace before being ejected through the orifice at the bottom of a quartz tube by Nitrogen overpressure (0.4 mPa).
- The sub-division and the gas atomisation occur on the melt to form various fine droplets.
- Depending on the local cooling rate, the droplets might be undercooled before the nucleation temperature is attained.
- The rapid release of latent heat of fusion due to the kinetics of primary phase might increase the droplet temperature near the eutectic point.
- The formation of lamellar eutectic then takes place at the temperature near the eutectic one.
- The segregated solidification, including inclusions introduced in Section 6.1.3, might yet come for the eutectic Ag-Cu alloy since rapid solidification leads to the composition of primary phase departing from the equilibrium phase diagram.

7.1 SUPERHEAT

First of all, melt superheat plays a crucible role in the quality of final as-solidified droplets in the drop-tube technique. On the one hand, when the superheat is too low, small unmelted inclusions might be attained in the melt before the ejection of the liquid out of crucible. As a result, a high order of undercooling would be impossible to achieve in as-solidified droplets since the heterogeneous nucleation could take place easily on those small amount of undercooling as shown in Fig. 6.1.8. On the other hand, when the superheat is too high, the ejected superheat melt might take more time to release this external heat in the liquid cooling process, resulting in low undercooled droplet too.

Even though the superheat is selected to apply in the drop-tube processing well, the solid fraction within the spherical droplet might be excessive in the initial solidification so that the surface layer is no longer interconnected for lack of liquid to fill pores and voids. As shown in Fig. 7.1.1, the increase in the solid fraction curves is indeed rapid as result of the rapid solidification during recalescence once high undercooling or low nucleation temperature is attained. The smaller the droplet, the more rapid the solid fraction increases

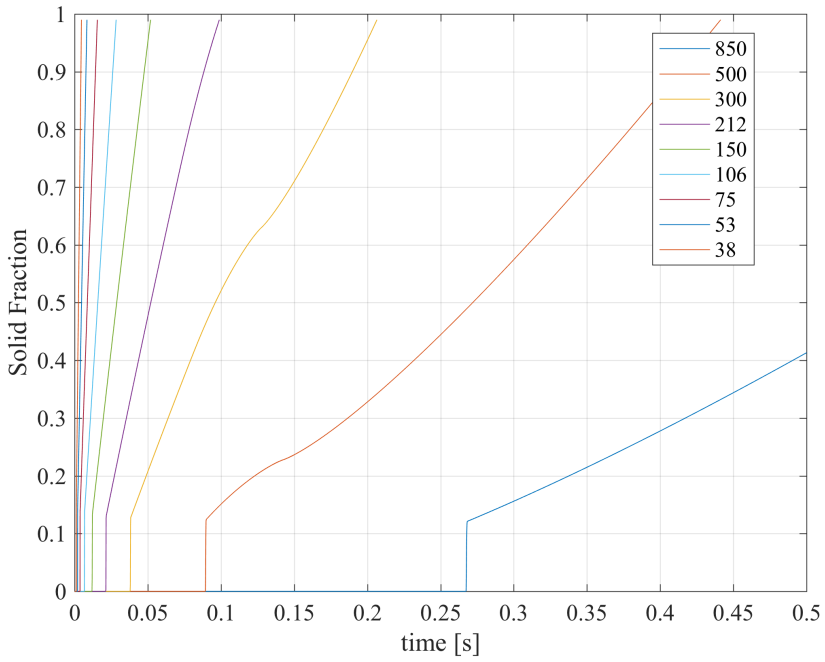

Figure 7.1.1: Variation on solid fraction against time for different droplet sizes

The extensive experimental images are shown in Fig. 7.1.2. It is clearly seen there are the pore in Fig. 7.1.2a opened on the droplet surface and the internal void in Fig. 7.1.2b inside the droplet. Both solidification defeats can give rise to the gas filled in or occupied on these regions prior to the

liquid, thereby having the poor atomization during rapid solidification.

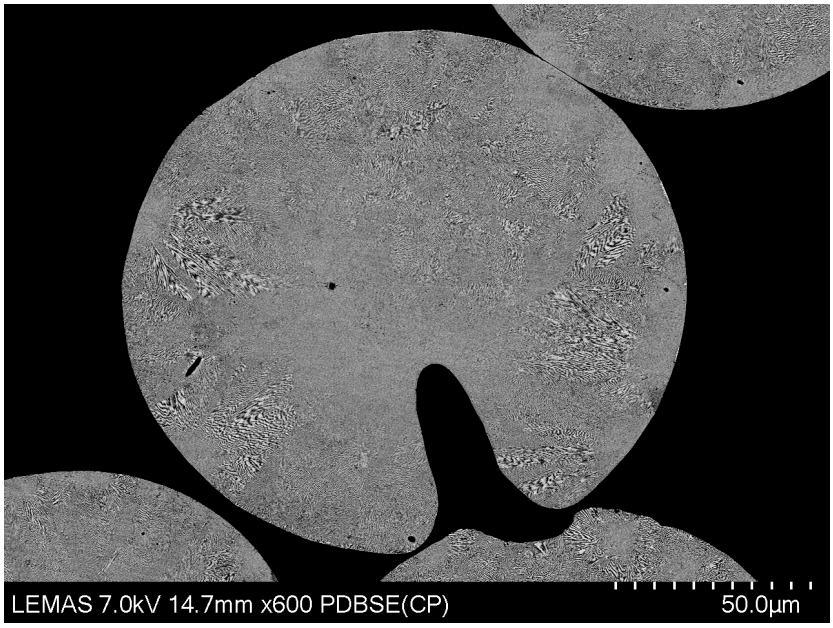

(a) 106 ~ 150 μm

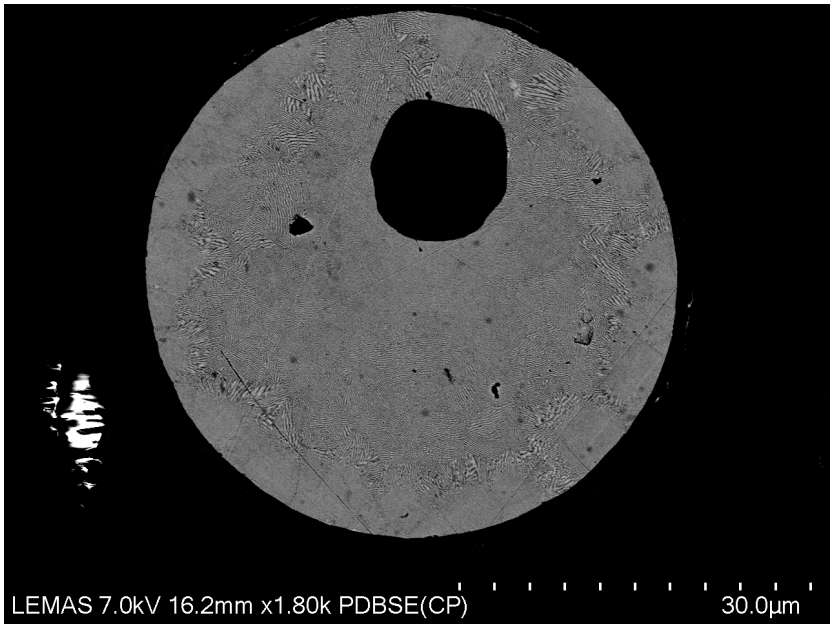

(b) 53 ~ 75 μm

Figure 7.1.2: Solidification defects attained in the smaller droplet size

7.2 LIQUID COOLING

Assumed the various sizes of droplet atomized from the melt immediately after the ejection, then the widely used starting point for modelling the cooling process is the balance of heat fluxes as also used in Section 3.1. The difficulty of predicting the temperature change by this modelling in this cooling process is related to the definition of the gas velocity and the interaction between the gas and the spherical melt. To simplify the calculation of this theoretical model, the well-known *Ranz and Marshall* correlation is then used to interpret the incompressible fluid flow past the droplet, which might become the largest uncertainty of calculated result. In [59], estimates of the cooling rate by measuring secondary dendrite arm spacing (SDAS) in the resulting powder product is adopted, which indicates the macroscopic heat transfer modelling with the *Ranz and Marshall* correlation can only overestimate the cooling rate that droplets are subject with.

In order to justify the heat extraction on the drop-tube processed sample, the second modelling is introduced in Section 3.2 and the relevant local Nu number is calculated in Section 6.3.2. This numerical result in Fig. 6.3.16 and Fig. 6.3.17 is highly suggestive that, at low Pe number, the cooling process might be reduced significantly due to the reverse heat transfer at the rear stagnation point. According to Eq. (3.2.3) with the diameter-determined uniform free-stream fluid velocity along z-axis in Table B.2.1, Pe can be obtained as shown in Table 7.2.1 The Pe number at size range 38 ~ 75 μm seems to be small enough for reducing the heat extraction rate of in-flight droplet. It should be also noted that Pe number at 500 ~ 850 μm is too large to apply in the unsteady heat transfer modelling. Therefore the calculation is only conducted at the range between 38 and 300 μm.

The local Nu shown in Fig. 7.2.1 at $\xi \to \infty$, however fails to reduce down below 0 for the reverse heat transfer from the fluid to the droplet. The reason for small Pe of all polar angles greater than 1 could be resulted from the small ratio between $c_f \rho_f$ and $c_s \rho_s$, which is approximately equal to 0.00034.

Considering a heat conduction equation in Eq. (4.2.4) to describe the heat conductivity inside the Ag-Cu alloy with the *Neumann* boundary condition as

$$\kappa_f \frac{\mathrm{d}T}{\mathrm{d}n} = h\,(T - T_\infty) \tag{7.2.1}$$

where the left-hand side of Eq. (7.2.1) is for the rate of flow across the spherical surface and the heat transfer coefficient is calculated by

$$h = \frac{\mathrm{Nu}_\theta\, \kappa_f}{2\, r_0} \tag{7.2.2}$$

Although there would be a temperature gradient, for example (Fig. 7.2.1), inside a 300-μm droplet at any instant of time by using Eq. (7.2.1), the reverse heat transfer might be unlikely to take place even at the rear part of droplet to slow the cooling process.

Table 7.2.1: Pe number of different droplet sizes

Diameter (μm)	Pe
38	0.70
53	1.89
75	5.37
106	15.16
150	42.95
212	121.25
300	343.59
500	1590.69
850	7815.07

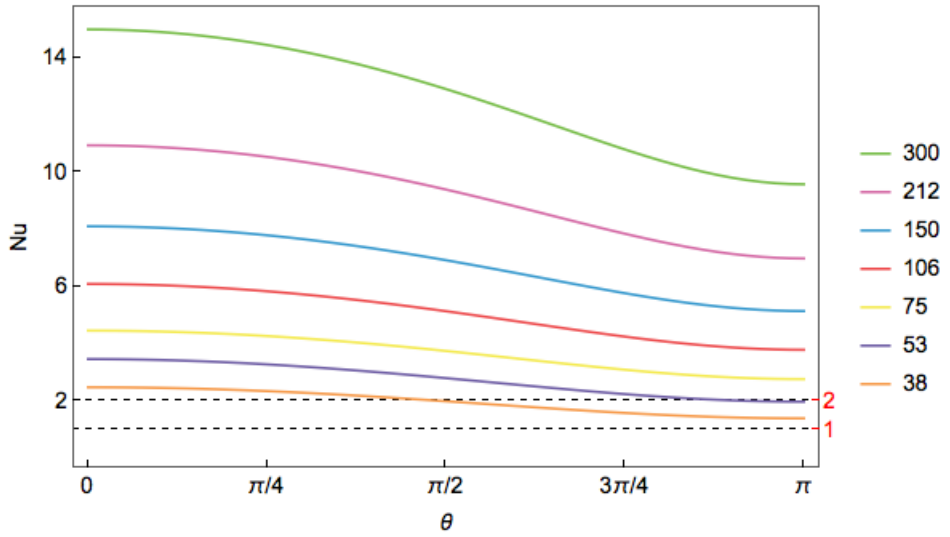

Figure 7.2.1: Variation on local ıNu along the polar angle θ for different size ranges at $\xi \to \infty$

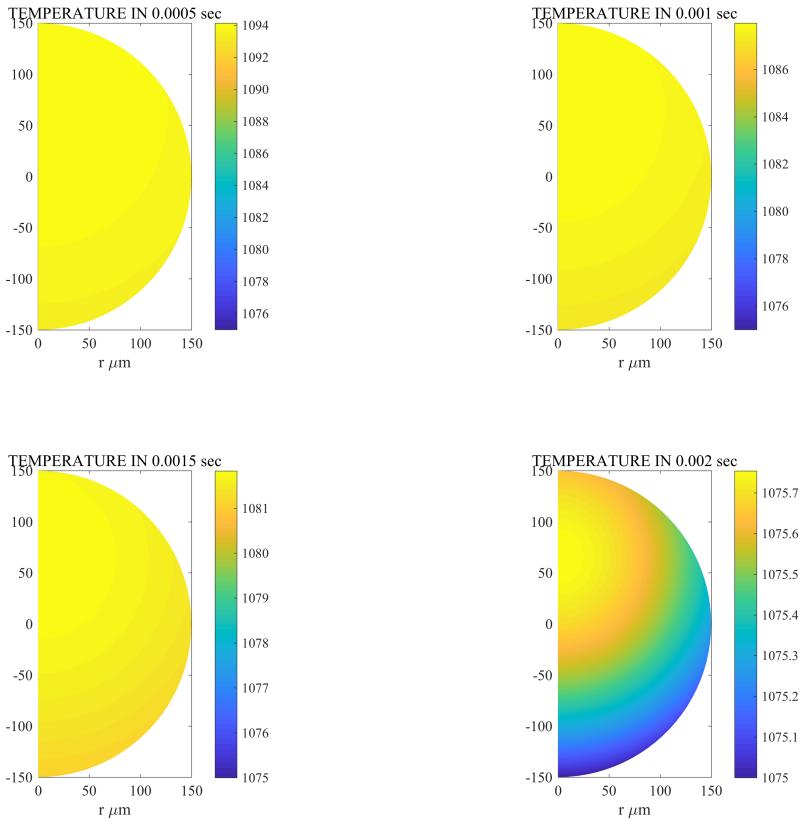

Figure 7.2.2: Temperature gradient inside a 300-μm droplet at different times

Moreover, the average cooling rate generated by the macroscopic heat transfer modelling is smaller than that by the unsteady convective heat transfer modelling as shown in Fig. 7.2.3. The possible reason for this estimation by the unsteady convective heat transfer modelling can be explained by high average Nu number at the beginning of drop-tube processing, whereas the asymptotic distribution of Nu along θ coordinate in Fig. 7.2.1 could only take place at the last stage of solidification. In the case of 38-μm droplet, average Nu at $\xi \rightarrow \infty$ which is stabilization of the thermal field around the droplet is nearly equal to 2 but actually close to 18.3 at the onset of cooling process. Nevertheless, average Nu is around 3 in the beginning of cooling process in Fig. 6.3.8, which is yet far below 18.33.

Because the calculated cooling rates by both modelling share the same change tendency, the smaller the size range, the more likely the droplets are subject with the higher cooling rate Such a small heat input to the system from the molten metal in the drop-tube processing should achieve the high limit end of cooling rate, the value of which might be largely determined by the differential velocity between the gas and the melt due to the overpressure to force the melt out of the orifice.

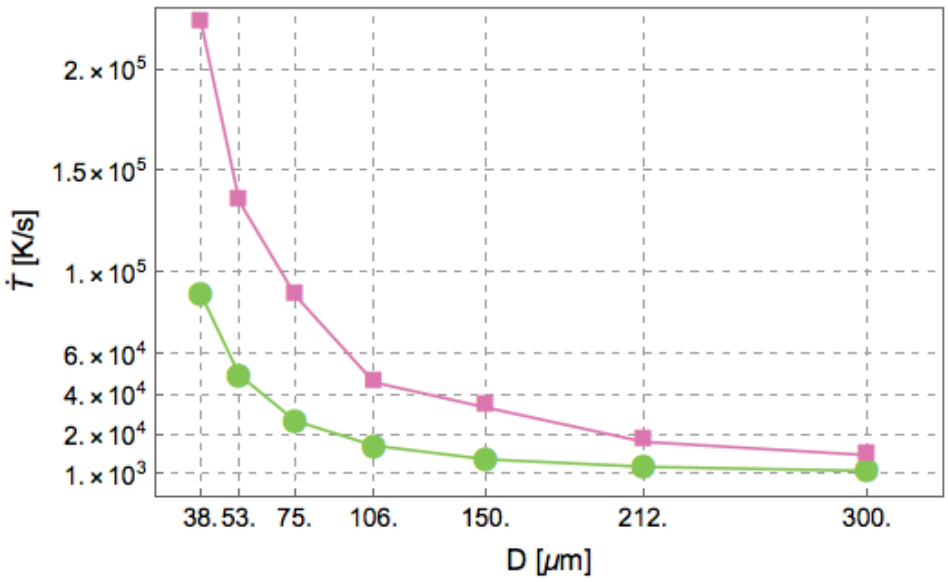

Figure 7.2.3: Cooling rate of all size ranges generated by the macroscopic heat transfer modelling (green) and the unsteady convective heat transfer modelling (pink)

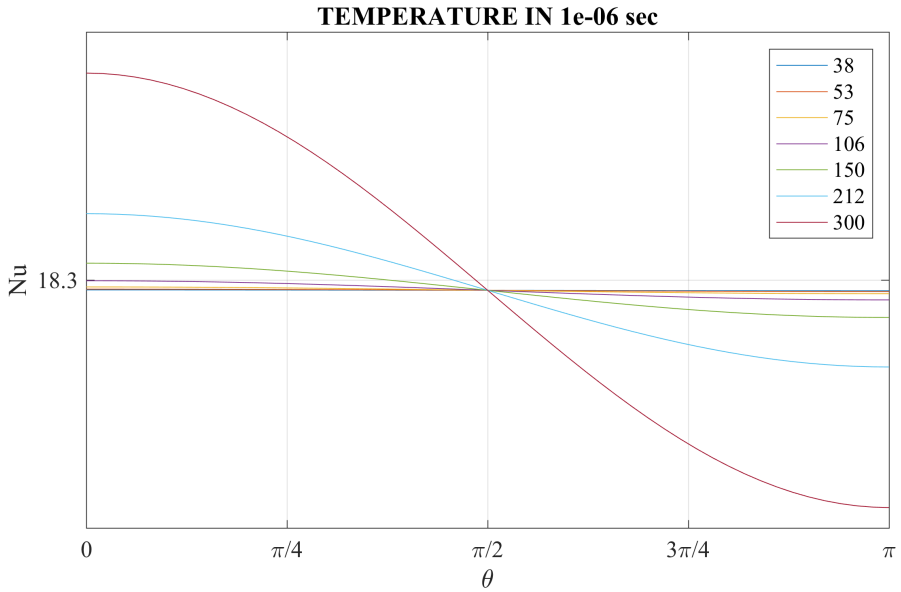

Figure 7.2.4: Variation on local ıNu along the polar angle θ for different size ranges in liquid cooling process

7.3 NUCLEATION

The nucleation event is of importance to understand the subsequent solidification. Lack of directly thermal measurement in drop-tube processing however causes the difficulty to interpret the morphology of as-solidified droplet. In order to estimate a possible nucleation temperature (undercooling), the classical heterogeneous nucleation theory in [3] with calculated cooling rate is applied in Section 3.1.2 in the macroscopic heat transfer modelling. The result was shown in Fig. 6.3.4.

In order to compare with the cooling rate by the unsteady heat transfer modelling, different cooling rates are applied in Eq. (3.1.9) for the same size of droplet as shown in Fig. 7.3.1. The cooling rates from 10^2 to 10^5 are chosen in this calculation since the 300-μm droplet has the order of 2×10^3 K/s in the macroscopic modelling and the order of 1×10^4 K/s in the unsteady one. Hence, the possible nucleation temperature should be attained within the range of temperatures in Fig. 7.3.1. As can be seen, the variation on nucleation temperatures in response to the range of cooling rates is around 5 K. Because of such a small change from the large range of cooling rates, we conjecture that, according to Fig. 6.3.4 ,the undercooling of smallest size range of droplet (38 ~ 53 K) may not be greater than 60 K. More importantly, the nucleation change by the contact angle in Fig. 6.3.6 is indicative that the order of undercooling is less dependent on the gas interruption, but more dependent on the nucleation condition. Therefore, small contamination inclusions or outer surface could catalyse nucleation at low undercoolings.

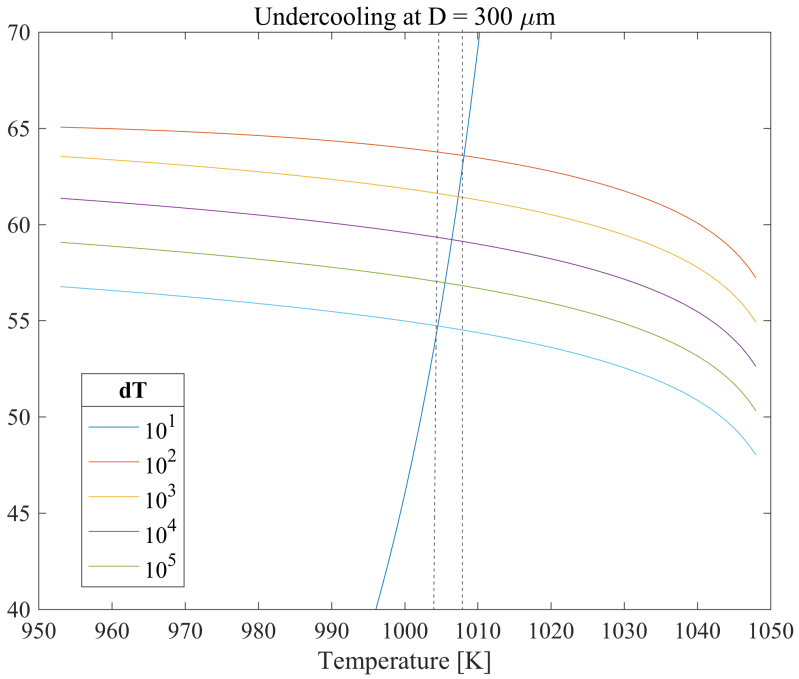

Figure 7.3.1: Undercooling of 300-μm droplet achieved by different cooling rates

7.4 RECALESCENCE

The thermal profile at recalescence is possible to be calculated by Eq. (3.1.13) as the temperature rapidly rises up to or near the eutectic temperature within 5 ms in Fig. 6.3.3. However this estimated thermal profile might be unlikely valid in the drop-tube processed Ag-Cu sample.

Once the nucleation event initiates, the heating rate due to the recalescence is mainly dependent on the kinetics of the primary phase or the ratio of releasing latent heat to the undercooled melt. In [27, 7], a simple radiation pyrometer is used to determine the nucleation temperature of Ag-Cu alloy in the glass fluxing processing. For glass-fluxing Ag-Cu morphology having anomalous eutectic embraced with lamellar eutectic at the undercooling between 10 and 70 K, the recalescence rate detected by the pyrometer showed no greater than 100 K/s. More importantly, the glass-fluxing sample is subjected with the cooling rate less than 50 K/s. If this is the case with an accuracy of ± 3 K as mentioned in [27], then the drop-tube processed sample initiated with the same primary phase should have the recalescence rate less than 100 K/s since the sample is subjected with much higher cooling rate in the drop-tube processing.

Therefore, the drop-tube processed sample experiencing high cooling rate initiates the surface nucleation as shown in the experimental result in Section 6.1 due to the possible temperature gradient in Fig. 7.2.2. The undercooled melt ahead of branched interface act as a heat sink to absorb the external releasing heat during the primary solidification in the drop-tube processing. Because of such a low recalescence rate against high cooling rate around spherical droplet, the primary phase might grow all over the droplet, especially with the larger size ranges prior to the lamellar eutectic in the remaining melt. In Fig. 6.2.14, the image processing also reveals the other distribution in which anomalous eutectic is more retained at outer surface of the droplet. The possible reason is that the primary phase branching into undercooled melt ahead, was stopped by the subsequent recalescence of lamellar eutectic attached on the larger surface area of the primary phase. With the decrease of droplet size, the space of undercooled melt ahead acting as a heat sink decreases, giving no place for coarsening of anomalous region at the smaller size ranges. As a result, more equilibrium eutectic develops in the inner region of droplet as shown in Fig. 6.2.9b, Fig. 6.2.10b, Fig. 6.2.11b, and Fig. 6.2.12b.

Based on the previous discussion, the morphology of Ag-Cu microstructure has two main factors, that is, undercooling and cooling rate. The order of undercoolings determines the formation of primary phase, including eutectic dendrite at $10 \sim 70$ K and single-phase dendrite at > 70 K, which results in different final microstructures. The order of cooling rates, on the one hand, has less influence on the level of undercoolings as shown in Fig. 7.3.1. On the other hand, the more efficient heat extraction on the smaller size ranges of droplet takes place at the upwind surface region than the inner droplet region as shown in Fig. 7.2.2. Because of this, the more intensive non-equilibrium eutectic populated at the surface gives more rapid release of latent heat to warm up small spacial undercooled melt ahead of primary phase interface during recalescence, which eventually leads to

more lamellar eutectic in the centre of droplet.

In [7], before the critical undercooling (70 K) is attained, the volume fraction of anomalous eutectic is believed to increase monotonically with the undercooling in glass fluxing technique. However this is partially true in the drop-tube processed samples in Section 6.2, since the droplets ranging from 38 to 106 have lower volume fraction of anomalous eutectic than those at larger size. The reason can be explained that undercooing prompts the formation of anomalous eutectic whereas cooling rate hinders from the growth of anomalous eutectic. Due to their joint action, the maximum fraction at size might be more likely to occur at the 106 ~ 212 μm droplets as shown in Fig. 6.2.13.

7.5 EUTECTIC SOLIDIFICATION

When the release rate of the latent heat is compatible with the heat extraction rate to the environment, the subsequent eutectic solidification occurs. In Section 6.1.3, microstructure of all size ranges are investigated and the lamellar eutectic is growing as a result of the subsequent solidification after the primary phase. To understand the thermal variation at this stage, each data range of lamellar spacings are obtained by measuring unique locations on the droplet of the same size range, except for the first column of data that represents the spacing of raw material. Because the raw material was made under no undercooling, its lamellar spacing formed during equilibrium solidification thereby provides a good reference in comparison with the lamellar spacing of drop-tube processed samples. As can seen in Fig. 7.5.1, the spacing of lamellar eutectic is changed, even for the one solidified under the equilibrium condition, despite the general tendency that the smaller droplet size has smaller lamellar spacing.

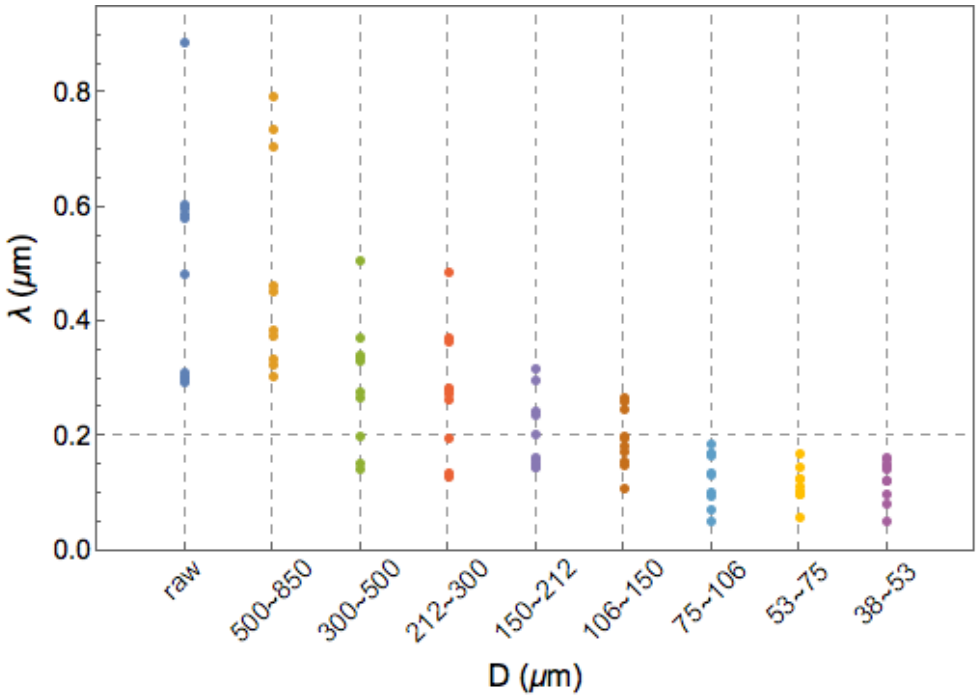

Figure 7.5.1: Lamellar spacing range for equilibrium solidification and for different size ranges of droplet

According to HJ and TMK theoretical model in Section 2.3.1, the eutectic growth can take place under low undercoolings. For Ag-Cu eutectic alloy, it is possible to have the local undercooling ahead of the eutectic interface and the higher undercooling ahead of the local interface could cause the smaller spacing of lamellar eutectic as shown in Fig. 2.3.3 and Fig. 2.3.4 respectively. The variation of the spacing is somehow consistent with Fig. 6.3.4 that smaller droplet size range subjected with

higher cooling rate in general give rise to higher undercooling in the melt. Although the undercooling during the eutectic growth is not as significant as that prior to the nucleation event, the high heat extraction effect on individual droplets constantly during their free falling down to the bottom of tube thereby affects on the eutectic solidification stage.

To interpret the recalescence kinetics in the subsequent solidification, the theoretical model of Jackson and Hunt is adapted to estimate the growth velocity of the eutectic. Although the eutectic growth under high undercooling departs from that under low undercooling [38], the outcomes of HJ model in Eq. (2.3.3) with HJ model with temperature dependent diffusion coefficient in Eq. (2.3.5) as well as TMK model in Eq. (2.3.17), shown in Fig. 2.3.5, are approximately the same at the order of undercooling below 10 K. Therefore, the scaling laws developed by JH model illustrated in Eq. (2.3.1) and Eq. (2.3.2) are used here.

Because each size range has a specific spacing range of lamellar eutectic in Fig. 7.5.1 and every spacing range can produce a undercooling range due to the relationship between the undercooling and the lamellar spacing. In Fig. 7.5.2, only the smallest spacing of each size range of droplets is selected in calculation of the possible undercooling locally since the smallest spacing of lamellar eutectic is more likely to occur at the final stage of eutectic solidification as no or less latent heat released during this transformation keep warming up the remaining undercooled liquid. For this reason, undercooling of each size range in Fig. 7.5.2 could indicate the possible undercooling ahead of eutectic interface and be compared with each other.

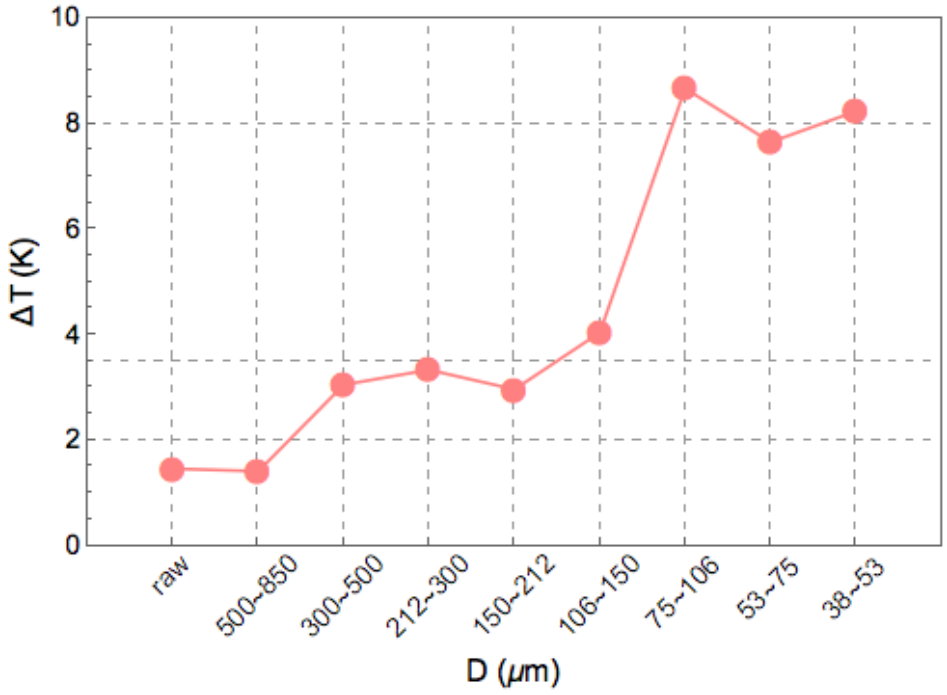

Figure 7.5.2: Undercooling for equilibrium solidification and for different size ranges of droplet

In [27, 7], the lamellar spacings measured from the fluxing melt sample under different undercooling remain roughly unchanged in comparison with that from the reference sample with notionally no undercooling. The drop-tube processed samples of different size ranges, on the other hand, show different undercooling in Fig. 7.5.2. The difference of these two can be attributed to the cooling rate introduced on each samples. Typically the cooling rate less than 50 K/s by using fluxing technique reported in the previous publication [27]. At such a low cooling rate, once the undercooled melt warmed up to the eutectic temperature, the remaining liquid is more likely to remain this temperature until the melt being fully solid. In contrast, drop-tube processed samples have various cooling rates from 2000 to 10^6 K/s shown in Fig. 7.2.3. At such a high cooling rate, the temperature increased at recalescence is possible to reduce again in the following solidification, especially at the smaller size range of droplets. As a result, apart from 500 ~ 850-μm droplet which keeps the similar order of undercooling as the raw material formed under equilibrium condition, the undercooling generally increases with the decrease of droplet size. Clearly the higher undercooling applied in the eutectic growth takes place at the smaller size range from 38 ~ 53 to 75 ~ 106 μm, which is in agreement with the finer lamellar eutectic populated in the centre of those droplets in Fig. 6.1.16 and Fig. 6.1.17.

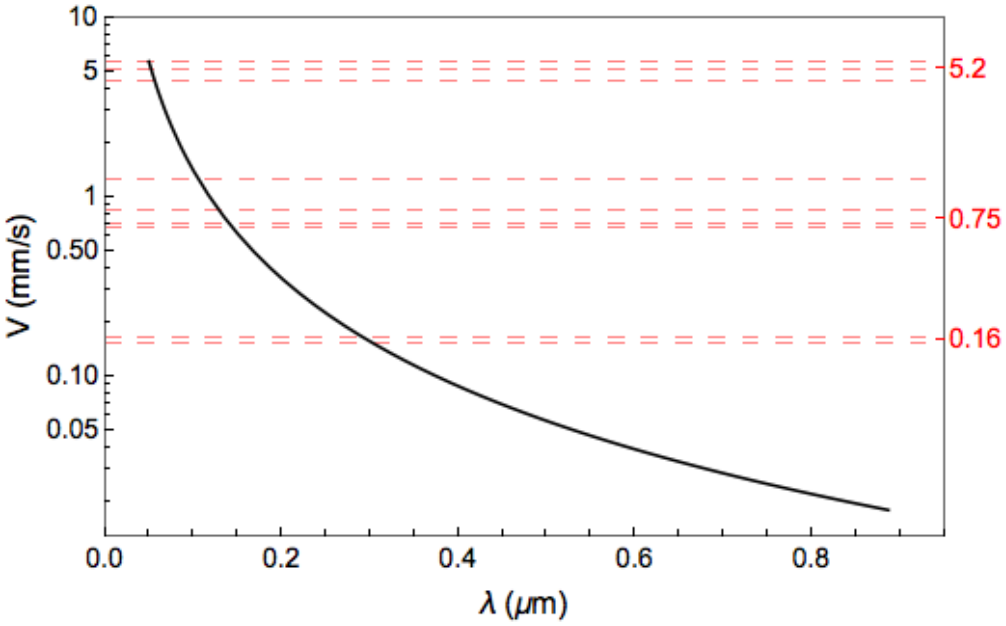

Figure 7.5.3: Growth velocity of lamellar eutectic against different lamellar spacing

Furthermore, those measured lamellar spacings in Fig. 7.5.1 are also applied to estimate of the growth velocity as shown in Fig. 7.5.3. The slowest value of growth velocity (~ 0.16 mm) is obtained by using the lamellar spacing of raw material. Based on the profile of growth velocity against lamel-

lar spacing, it is clearly that the smaller the droplet, the faster the growth speed, which is consistent with the changes of solid fraction in Fig. 7.1.1.

At last, there are certain regions believed as finest lamellar eutectic in the smallest size range 38 ~ 53 since the BSE image shows the mixed grey level between the Ag-rich region and the Cu-rich region inside the white cycle in Fig. 7.5.4. However further investigation might be required to identify this planar, space-filling phase. As indicated by Fig. 7.5.2 and Fig. 7.5.3, the smaller the lamellar space, the higher the undercooling and the faster the growth velocity. Once the undercooling exceeds the critical undercooling ΔT_0 [16], the undercooled melt has too low temperature to perform the diffusion during the eutectic solidification and leads to partitionless planar growth instead.

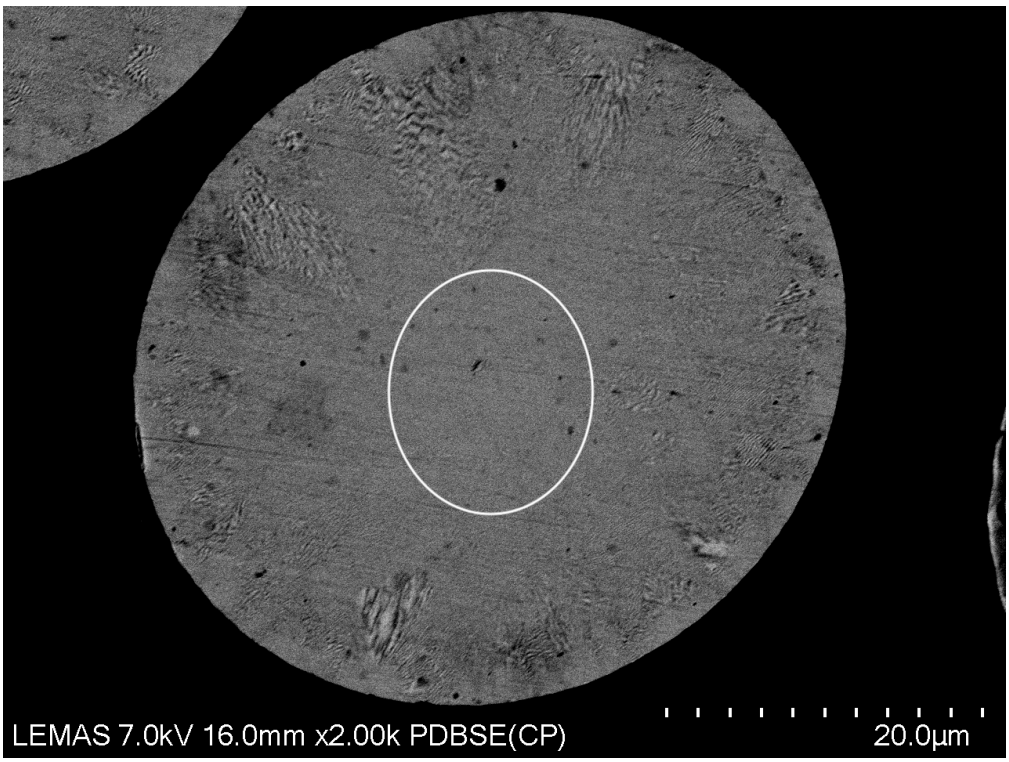

Figure 7.5.4: Lamellar eutectic in the smallest size range of droplet

7.6 SEGREGATED SOLIDIFICATION

In the microstructure of size ranges shown in Section 6.1.3, it is clearly seen that the Ag-rich inclusions are randomly distributed within the larger droplets (212 ~ 850 μm). In contrast, there is no such inclusions in smaller ranges, such as 38 ~ 53 μm in Fig. 6.1.17, 53 ~ 75 μm in Fig. 6.1.16, and 75 ~ 106 μm in Fig. 6.1.15.

In order to predict the amount of micro-segregation, the amount of eutectic must be known at first. The lever rule is widely used in estimation of the amount of eutectic in the equilibrium solidification, but is impossible to do so for non-equilibrium eutectic since the local conditions, such as cooling rate and subsequently recalescence rate, largely determine the morphology of final microstructure. For a larger size ranges, these observed inclusions can be explained by *Scheil's model* wherein only diffusion of the liquid is taken into account. Using equilibrium partitioning at the solid-liquid interface, the anomalous eutectic formed at the composition departing from the equilibrium eutectic composition leads to an enrichment of solute in the liquid, such that the final solidification ends at the Ag-rich inclusions.

However, the original *Scheil's model* fails to explain the rather homogeneous microstructure in smaller size ranges. The possible explanation for this morphology change can be attributed to back diffusion in the solid, which directly influences, not only on the evolution of type, amount, and composition of the interdendritic phases and the formation of non-equilibrium eutectic in the final eutectic fraction [76]. In the previous study of hypoeutectic Al-Cu alloys, Sarreal and Abbaschian [77], who found that the amount of non-equilibrium eutectic increases monotonically up to a cooling rate of 190 K/s, followed by a strongly reduced fraction of non-equilibrium eutectic at 1700 K/s. They believed that with increasing cooling rate, the increase of volumetric back diffusion rate could restrain non-equilibrium eutectic from growth. Therefore, at large cooling rates, back diffusion becomes an important factor to interrupt the final morphology.

As a result, the homogeneous microstructures in a smaller size ranges of droplets subjected with higher cooling rates could be attributed to larger amount of volumetric back diffusion taking place in the eutectic dendrite, and leads to the composition of eutectic dendrite close to that of equilibrium eutectic. With less or no enrichment of solute left in liquid, the distinct Ag-rich inclusions are impossible to form in the end of solidification. Higher undercooling attained in smaller droplet however is of no help to explain the microsegregation free at smaller size range of droplets.

According to above discussion, two different morphologies in the drop-tube proceeded samples can give rise to different reasons. The larger size range is essentially undercooling controlled whereas the smalller one is more cooling rate controlled.

CHAPTER 8

CONCLUSION

1. At the fixed superheat temperature, a size range of droplet formed from one spray, might have solidification defects attained as discussed in Section 7.1. Depending on cooling rates, the solid fraction might be excessive in the initial solidification so that the surface layer is no longer interconnected due to lack of liquid to fill pores.

2. The local Nu number around sphere is proved to change from the forward stagnation points to the rear stagnation points as shown in Fig. 6.3.14. The assumption of minimum Nu at 2 under motionless flow is invalid for stoke flow as the local Nu can become negative. For $Ag-40at\%Cu$ alloy, the reverse heat transfer due to $Nu < 0$, however, is only possible to take place at the smallest size range $38 \sim 53\ \mu m$ due to the low ratio of specific heat between fluid and solid at the end of solidification.

3. The morphology by which anomalous eutectic is embraced with lamellar eutectic occurs at all size ranges ($38 \sim 850\ \mu m$). Although droplets at the smaller size range are subjected with higher cooling rates, the undercooling or the temperature prior to nucleation is more contact angle dependent than cooling rate dependent. At fixed contact angle $\pi/4$, the undercooling value raises with the decrease of droplet size. The undercooling greater than 60 K might only take place upon the smallest droplet at $38 \sim 53\ \mu m$. As a result, there is no clearly transitive primary phase from anomalous eutectic to single-phase dendrite in drop-tube processed Ag-Cu samples.

4. There are two different distributions of anomalous eutectic within the droplets found by using *ImageJ* macro scripting to identify the number of anomalous eutectic in series of annuli. The anomalous eutectic is distributed evenly in every annulus region at larger size ranges $212 \sim 850\ \mu m$, , whereas the anomalous eutectic is retained more in the annulus nearest the surface at smaller size ranges $38 \sim 212\ \mu m$. It is believed that the primary phases was stopped by the recalescence when they branch into undercooled melt, followed by the nucleation of lamellar eutectic attached on the larger surface area of the primary phase gives no place act-

ing as the heat sink for further coarsening anomalous region, especially at the smaller size of droplets.

5. The higher the cooling rate is achieved in smaller droplet size, the higher possibility the high undercooling could be attained prior to solidification. At the smallest size range 38 ~ 53 μm, it is likely that the heat extraction rate up to (10^5 K/s) can neglect the influence of recalescence and the subsequent latent heat released during solidification. Under this circumstance, once the high undercooling is attained, the undercooled melt would keep undercooled till the end of solidification, which provides a necessary condition to have partitionless solidification at size 38 ~ 53 μm.

6. At the high cooling rate, the primary phases are not only subjected to a kind of heat treatment, but also receive back diffusion during the subsequent eutectic formation. As a result, the droplet with smaller size experiences higher cooling rate to be micro-segregation free. On the other hand, the type of droplet morphologies in Section 6.1.3 is largely dependent on the level of undercooling. Therefore, the larger size range is essentially undercooling controlled whereas the smalller one is more cooling rate controlled.

APPENDIX A

CONSERVATION EQUATIONS

Consider an arbitrary inertial frame in space of finite volume Ω enclosed by its bounding surface $\partial\Omega$, the *Reynolds Transport theorem* is used to assume that the amount of the changes Φ over a control volume Ω is equal to what is fluxed through the surface $\partial\Omega$ and what is created within the volume. Thus Φ is assumed to be constant on a scale to Ω and the average value of Φ is a good approximation to Φ anywhere over Ω.

$$\frac{\mathrm{d}}{\mathrm{d}t}\int_{\Omega}\Phi\ \mathrm{d}V = -\int_{\partial\Omega}F\cdot\vec{n}\ \mathrm{d}S - \int_{\partial\Omega}\Phi\,\vec{u}\cdot\vec{n}\ \mathrm{d}S - \int_{\Omega}Q\ \mathrm{d}V \tag{A.0.1}$$

where F is the flux of Φ in the absence of fluid transport, $\Phi\,\vec{u}$ is the flux across the layer due to the fluid transport and Q is a external source or sink of Φ.

According to the *Divergence Therorem*, the flux term of Eq. (A.0.1) is allowed to express a volume integal as

$$-\int_{\partial\Omega}F\cdot\vec{n}\ \mathrm{d}S - \int_{\partial\Omega}\Phi\,\vec{u}\cdot\vec{n}\ \mathrm{d}S = -\int_{\Omega}\nabla\cdot(F+\Phi\,\vec{u})\ \mathrm{d}V \tag{A.0.2}$$

Because the surface and volume are fixed in an inertial frame, the *Leibniz's Rule* is applied to the left-hand side of Eq. (A.0.1)

$$\frac{\mathrm{d}}{\mathrm{d}t}\int_{\Omega}\Phi\ \mathrm{d}V = \int_{\Omega}\frac{\mathrm{d}\Phi}{\mathrm{d}t}\ \mathrm{d}V \tag{A.0.3}$$

Combining Eq. (A.0.1) with Eq. (A.0.2) and Eq. (A.0.3),

$$\int_{\Omega}\left(\frac{\mathrm{d}\Phi}{\mathrm{d}t}+\nabla\cdot\left(F+\Phi\,\vec{u}\right)+Q\right)\mathrm{d}V = 0$$

This relation applies to an arbitrary control volume Ω. In order to remain valid for all volumes, the integrand should be zero

$$\frac{\mathrm{d}\Phi}{\mathrm{d}t}+\nabla\cdot\left(F+\Phi\,\vec{u}\right)+Q = 0 \tag{A.0.4}$$

This basic continuity equation is used to describe the change of an intensive property Φ in continuum mechanics. Three main intensive quantities, mass ρ, heat $\rho\,c\,T$, and force balance $\vec{u}$, are further discussed in the following sections based on the general form of continity equation in Eq. (A.0.4).

A.1 CONSERVATION OF MASS

With no source or sink of mass $Q = 0$ to create or destroy mass, the mass per unit volume (mass density $\Phi = \rho$) is put in Eq. (A.0.4)

$$\frac{\partial \rho}{\partial t} + \nabla \cdot \left(\rho \, \vec{u}\right) = 0 \tag{A.1.1}$$

where the flux F term is not involved since mass flux only attributes to the transport change.

In the case of an incompressible fluid, the density along the path of a fluid is constant

$$\frac{\mathrm{d}\rho}{\mathrm{d}t} = 0$$

Eq. (A.1.1) can reduce to

$$\nabla \cdot \left(\rho \, \vec{u}\right) = 0 \Longleftrightarrow \nabla \cdot \vec{u} = 0 \tag{A.1.2}$$

A.2 CONSERVATION OF HEAT

For a single phase material, heat per unit volume $\Phi = \rho \, c \, T$

$$\frac{\partial \rho \, c \, T}{\partial t} + \nabla \cdot \left(\rho \, c \, T \, \vec{u}\right) = \nabla \cdot F + Q \tag{A.2.1}$$

where heat flux is consist of two components, the one due to conduction F and the other $\rho \, c \, T \, \vec{u}$ due to transport as well as heat source Q may give rise to radioactive decay or viscous dissipation and shear heating.

The heat flux of conduction raised by a temperature gradient within a control volume can be expressed

$$F = -\kappa \nabla T \tag{A.2.2}$$

Inserting Eq. (A.2.2) in Eq. (A.2.1), the general conservation of heat is

$$\frac{\partial \rho \, c \, T}{\partial t} + \nabla \cdot \left(\rho \, c \, T \, \vec{u}\right) = \nabla \cdot \left(\kappa \nabla T\right) + Q \tag{A.2.3}$$

For a material with constant c and κ being the hotest source and in the absence of fluid transport, Eq. (A.2.3) becomes

$$\rho \, c \frac{\partial T}{\partial t} = \kappa \nabla^2 T \tag{A.2.4}$$

A.3 CONSERVATION OF MOMENTUM

In general, conservation of momentum (force balance) can be derived in the same way as shown in Appendix A.1 and Appendix A.2, but the amount of momentum per unit volume $\rho \, \vec{u}$ is substituted into Φ in Eq. (A.0.4).

$$\frac{\partial \rho \, \vec{u}}{\partial t} + \nabla \cdot \left(\rho \, \vec{u} \, \vec{u}\right) = \nabla \cdot \sigma + \rho \, \vec{g} \tag{A.3.1}$$

where the flux of force (the Cauchy stress tensor) $F = -\sigma$ acts on the surface of the control volume Ω and the source $Q = \rho\,\vec{g}$ is the net external force.

Unlike heat and mass as scalar field in Eq. (A.1.1) and Eq. (A.2.3) respectively, mementum is a vector field due to fluid flow velocity $\vec{u} = (u, v, w)$. To solve a dyad $\vec{u}\,\vec{u}$ in Eq. (A.3.1), the divergence of a second rank tensor is applied

$$\vec{u}\frac{\partial \rho}{\partial t} + \rho\frac{\partial \vec{u}}{\partial t} + \vec{u}\,\vec{u}\cdot\nabla\rho + \rho\,\vec{u}\cdot\nabla\vec{u} + \rho\,\vec{u}\nabla\cdot\vec{u} = \nabla\cdot\sigma + \rho\,\vec{g}$$

$$\vec{u}\left(\frac{\partial \rho}{\partial t} + \vec{u}\cdot\nabla\rho + \rho\nabla\cdot\vec{u}\right) + \rho\left(\frac{\partial \vec{u}}{\partial t} + \vec{u}\cdot\nabla\vec{u}\right) = \nabla\cdot\sigma + \rho\,\vec{g} \tag{A.3.2}$$

Because of mass continuity in Eq. (A.1.1), the first term in the right-hand side of Eq. (A.3.2) is

$$\vec{u}\left(\frac{\partial \rho}{\partial t} + \vec{u}\cdot\nabla\rho + \rho\nabla\cdot\vec{u}\right) \Longleftrightarrow \vec{u}\left(\frac{\partial \rho}{\partial t} + \nabla\cdot(\rho\,\vec{u})\right) = \vec{u}\,0 = 0$$

Therefore, Eq. (A.3.1) can be written as

$$\frac{\partial \vec{u}}{\partial t} + \vec{u}\cdot\nabla\vec{u} = \frac{1}{\rho}\nabla\cdot\sigma + \vec{g} \tag{A.3.3}$$

For completion, the stress tensor σ (see Fig. A.3.1) must be evaluated and is often divided into two terms, the volumetric stress tensor and the stress deviator tensor.

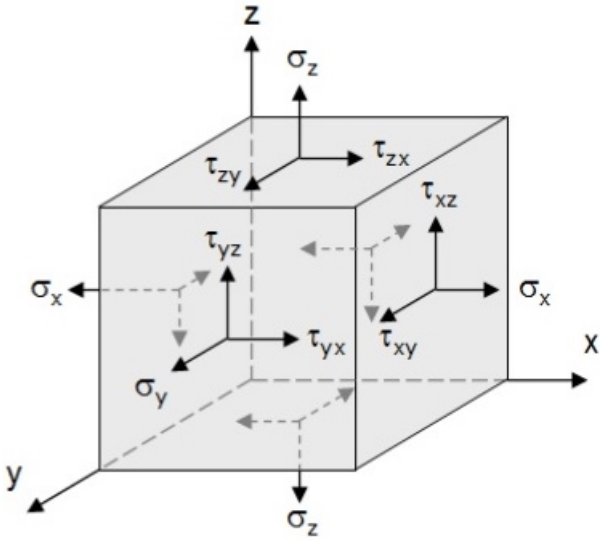

Figure A.3.1: components of Cauchy stress tensor in three dimensions

The volumetric stress tensor tends to change the volume of the body, such as the pressure force. The stress deviator tensor on the other hand represents the tendency of the body deformation and movement.

Thus, σ in the Cartesian coordinates can be broken down into

$$\begin{aligned}
\sigma &= \begin{pmatrix} \sigma_{xx} & \tau_{xy} & \tau_{xz} \\ \tau_{yx} & \sigma_{yy} & \tau_{yz} \\ \tau_{zx} & \tau_{zy} & \sigma_{zz} \end{pmatrix} \\
&= -\begin{pmatrix} p & 0 & 0 \\ 0 & p & 0 \\ 0 & 0 & p \end{pmatrix} + \begin{pmatrix} \sigma_{xx}+p & \tau_{xy} & \tau_{xz} \\ \tau_{yx} & \sigma_{yy}+p & \tau_{yz} \\ \tau_{zx} & \tau_{zy} & \sigma_{zz}+p \end{pmatrix} \\
&= -pI + \tau
\end{aligned} \tag{A.3.4}$$

Combining with Eq. (A.3.3) and Eq. (A.3.4), the general form of the *Navier-Stokes* equation is

$$\frac{\partial \vec{u}}{\partial t} + \vec{u}\cdot\nabla\vec{u} = -\frac{1}{\rho}\nabla p + \frac{1}{\rho}\nabla\cdot\tau + \vec{g} \tag{A.3.5}$$

In the right-hand side of Eq. (A.3.5), $-\nabla p$ is the pressure term for preventing from volume motion due to normal stresses and $\nabla\cdot\tau$ is the stress (viscous) term giving rise to surface motion in the direction of the flow due to horizontal friction and shear stresses. In practice, a specific fluid and its associated mass continuity are required to determine the pressure p and the stress deviator tensor τ in Eq. (A.3.5),

A.3.1 INCOMPRESSIBLE NEWTONIAN FLUID

For an isotropic incompressible fluids, the stress tensor τ in Eq. (A.3.4) is proportional to the rate of deformation in the direction of fluid velocity $\vec{u} = (u, v, w)$

$$\tau_{ij} = \mu\left(\frac{\partial u_i}{\partial x_j} + \frac{\partial u_j}{\partial x_i}\right) \Longleftrightarrow \tau = \mu\left(\nabla\vec{u} + (\nabla\vec{u})^T\right) = \mu\begin{pmatrix} 2\dfrac{\partial u}{\partial x} & \dfrac{\partial u}{\partial y}+\dfrac{\partial v}{\partial x} & \dfrac{\partial u}{\partial z}+\dfrac{\partial w}{\partial x} \\ \dfrac{\partial u}{\partial y}+\dfrac{\partial v}{\partial x} & 2\dfrac{\partial v}{\partial y} & \dfrac{\partial v}{\partial z}+\dfrac{\partial w}{\partial y} \\ \dfrac{\partial u}{\partial z}+\dfrac{\partial w}{\partial x} & \dfrac{\partial v}{\partial z}+\dfrac{\partial w}{\partial y} & 2\dfrac{\partial w}{\partial z} \end{pmatrix} \tag{A.3.6}$$

where the viscosity of the fluid μ defines the resistance to gradual deformation by shear stress when the fluid flows is subjected to body forces.

The stress term of the x momentum equation with a constant viscosity μ in Eq. (A.3.5) is derived by considering with the incompressible mass continuity in Eq. (A.1.2)

$$\begin{aligned}
\left(\nabla\cdot\tau\right)_i &= \mu\left(\frac{\partial}{\partial x}\left(2\frac{\partial u}{\partial x}\right)+\frac{\partial}{\partial y}\left(\frac{\partial u}{\partial y}+\frac{\partial v}{\partial x}\right)+\frac{\partial}{\partial z}\left(\frac{\partial u}{\partial z}+\frac{\partial w}{\partial x}\right)\right)\\
&= \mu\left(\frac{\partial^2 u}{\partial x^2}+\frac{\partial^2 u}{\partial y^2}+\frac{\partial^2 u}{\partial z^2}\right)+\mu\left(\frac{\partial^2 u}{\partial x^2}+\frac{\partial^2 u}{\partial x\partial y}+\frac{\partial^2 u}{\partial x\partial z}\right)\\
&= \mu\nabla^2 u+\mu\frac{\partial}{\partial x}\left(\nabla\cdot\vec{u}\right)\\
&= \mu\nabla^2 u+0=\mu\nabla^2 u
\end{aligned}$$

Similarly for the y and z term of the divergence,

$$\left(\nabla\cdot\tau\right)_j=\mu\nabla^2 v \qquad \left(\nabla\cdot\tau\right)_k=\mu\nabla^2 w$$

Thus, the divergence of the stress tensor

$$\nabla\cdot\tau=\left(\nabla\cdot\tau\right)_i+\left(\nabla\cdot\tau\right)_j+\left(\nabla\cdot\tau\right)_k=\mu\nabla^2\vec{u} \tag{A.3.7}$$

Substituting Eq. (A.3.7) into Eq. (A.3.5), the Navier-Stokes equation is obtained to describe an incompressible Newtonian fluid [67] as

$$\frac{\partial\vec{u}}{\partial t}+\vec{u}\cdot\nabla\vec{u}=-\frac{1}{\rho}\nabla p+\frac{\mu}{\rho}\nabla^2\vec{u}+\vec{g} \tag{A.3.8}$$

APPENDIX B

STOKES FLOW PAST A SPHERE

For an incompressible *Stokes flow* with no concern to external body force, the general dimensional form of the *Navier-Stokes equation* for a Newtonian viscous fluid of constant density ρ_f and constant viscosity ν can be derived from Eq. (A.3.8) as

$$\frac{\partial \vec{u}}{\partial t} + (\vec{u} \cdot \nabla)\, \vec{u} - \nu \nabla^2 \vec{u} = -\frac{1}{\rho_f} \nabla p \tag{B.0.1}$$

where the kinematic viscosity

$$\nu = \frac{\mu}{\rho_f} \tag{B.0.2}$$

At the small *Reynolds number Re*, the inertia terms as the first two terms in the left-hand side of Eq. (B.0.1) are neglected.

$$-\nu \nabla^2 \vec{u} = -\frac{1}{\rho_f} \nabla p \tag{B.0.3}$$

Because Eq. (B.0.1) is assumed to have a Newtonian viscous fluid of constant ρ_f and constant ν,

$$\frac{\mathrm{d}\rho}{\mathrm{d}t} = 0$$

The continuity equation is derived from the conservation of mass in Eq. (A.1.2) as

$$\nabla \cdot \vec{u} = 0 \tag{B.0.4}$$

Therefore, the steady incompressible Stokes flow is characteristic with

$$-\nu \nabla^2 \vec{u} = -\frac{1}{\rho_f} \nabla p \tag{B.0.5a}$$

$$\nabla \cdot \vec{u} = 0 \tag{B.0.5b}$$

B.1 STOKES' SOLUTION FOR A SPHERE

Considering melt sphere moving in axisymmetric steady Stokes flow for the spherical polar coordinates system (r,θ,ϕ) satisfies Eq. (B.0.5b)

$$\nabla\cdot\vec{u}=\frac{1}{r^2}\frac{\partial r^2 u_r}{\partial r}+\frac{1}{r\sin\theta}\frac{\partial \sin\theta\, u_\theta}{\partial\theta}+\frac{1}{r\sin\theta}\frac{\partial u_\phi}{\partial\phi}=0$$

then the flow velocity components, u_r, u_θ and u_ϕ related to the stream function Ψ have the general solution as

$$u_r=\frac{1}{r^2\sin\theta}\frac{\partial\Psi}{\partial\theta} \tag{B.1.1a}$$

$$u_\theta=-\frac{1}{r\sin\theta}\frac{\partial\Psi}{\partial r} \tag{B.1.1b}$$

$$u_\phi=0; \tag{B.1.1c}$$

According to the vector identity, any vector $\vec{G}$ has

$$\nabla\times(\nabla\times\vec{G})=\nabla(\nabla\cdot\vec{G})-\nabla^2\vec{G} \tag{B.1.2a}$$

$$\nabla\times(\nabla\vec{G})\equiv 0 \tag{B.1.2b}$$

$$\nabla^2(\nabla\times\vec{G})=\nabla\times(\nabla^2\vec{G})=-\nabla\times\left(\nabla\times(\nabla\times\vec{G})\right) \tag{B.1.2c}$$

Because of Eq. (B.0.5b),

$$\nabla(\nabla\cdot\vec{u})=\nabla(0)=0$$

Then

$$\nabla\times(\nabla\times\vec{u})=\nabla(\nabla\cdot\vec{u})-\nabla^2\vec{u}=-\nabla^2\vec{u}=-\frac{1}{\nu\rho_f}\nabla p \tag{B.1.3}$$

Due to Eq. (B.1.2b) and

$$\nabla\times\left(\frac{\Psi}{r\sin\theta}\vec{e}_\phi\right)=\frac{1}{r^2\sin\theta}\begin{vmatrix}\vec{e}_r & r\vec{e}_\theta & r\sin\theta\,\vec{e}_\phi\\ \frac{\partial}{\partial r} & \frac{\partial}{\partial\theta} & \frac{\partial}{\partial\phi}\\ 0 & 0 & r\sin\theta\frac{\Psi}{r\sin\theta}\end{vmatrix}=u_r\vec{e}_r+u_\theta\vec{e}_\theta+0\vec{e}_\phi$$

Eq. (B.1.3) becomes

$$\nabla\times\nabla\times(\nabla\times\vec{u})=\nabla\times\nabla\times\left(\nabla\times\left(\nabla\times\frac{\Psi}{r\sin\theta}\vec{e}_\phi\right)\right)=\nabla\times\left(-\frac{1}{\nu\rho_f}\nabla p\right)\equiv 0$$

$$\left(\frac{\partial^2}{\partial r^2}+\frac{\sin\theta}{r^2}\frac{\partial}{\partial\theta}\left(\frac{1}{\sin\theta}\frac{\partial}{\partial\theta}\right)\right)^2\Psi=0 \tag{B.1.4}$$

BOUNDARY CONDITION

In the case of steady Stokes flow in the spherical polar coordinates (r,θ,ϕ), the fluid velocity is assumed to be constant , say w_f along z axis, at $r\to\infty$. The radial and polar components of w_f are

$$u_r = w_f\cos\theta = \frac{1}{r^2\sin\theta}\frac{\partial\Psi}{\partial\theta} \qquad u_\theta = w_f\sin\theta = -\frac{1}{r\sin\theta}\frac{\partial\Psi}{\partial r} \qquad \text{at } r\to\infty$$

Integration of either velocity components above can obtain the stream function

$$\Psi = \frac{w_f}{2}r^2\sin^2\theta \qquad \text{at } r\to\infty \tag{B.1.5}$$

Moreover, the flow adjacent to the sphere surface (sphere radius a) is assumed to be motionless

$$u_r = 0 \qquad u_\theta = 0 \qquad \text{at } r = a \tag{B.1.6}$$

Provided there is a solution of Eq. (B.1.4) in the form

$$\Psi = \sin^2\theta\, f(r) \tag{B.1.7}$$

then

$$\left(\frac{\partial^2}{\partial r^2} - \frac{2}{r^2}\right)^2 f(r) = 0 \tag{B.1.8}$$

Putting $f(r) = r^\lambda$ in Eq. (B.1.8), $(\lambda^2-1)(\lambda-2)(\lambda-4)=0$ suggests the general solution is

$$f(r) = \frac{A}{r} + B\,r + C\,r^2 + D\,r^4$$

Combining with boundary condition of Eq. (B.1.5) and Eq. (B.1.6)

$$A = \frac{1}{4}w_f\,a^3 \qquad B = -\frac{3}{4}w_f\,a \qquad C = \frac{1}{2}w_f \qquad D = 0$$

With Eq. (B.1.7), the Stokes steam function is written

$$\Psi(r,\theta) = \frac{1}{2}w_f\sin^2\theta\left(r^2 + \frac{a^3}{2\,r} - \frac{3\,a\,r}{2}\right) \tag{B.1.9}$$

Therefore, the resulting flow in spherical polar coordinates (Eq. (B.1.1a) and Eq. (B.1.1b)) is given by

$$u_r = w_f\cos\theta\left(1 + \frac{a^3}{2\,r^3} - \frac{3\,a}{2\,r}\right) \tag{B.1.10a}$$

$$u_\theta = -w_f\sin\theta\left(1 - \frac{a^3}{4\,r^3} - \frac{3\,a}{4\,r}\right) \tag{B.1.10b}$$

B.2 PHYSICAL DEDUCTIONS

In spherical coordinates, the vector laplacian is

$$\nabla^2\vec{G}=\begin{pmatrix} \frac{1}{r}\frac{\partial^2(r\,G_r)}{\partial r^2}+\frac{1}{r^2}\frac{\partial^2 G_r}{\partial\theta^2}+\frac{1}{r^2\sin^2\theta}\frac{\partial^2 G_r}{\partial\phi^2}+\frac{\cot\theta}{r^2}\frac{\partial G_r}{\partial\theta}-\frac{2}{r^2}\frac{\partial G_\theta}{\partial\theta}-\frac{2}{r^2\sin\theta}\frac{\partial G_\phi}{\partial\phi}-\frac{2\,G_r}{r^2}-\frac{2\cot\theta\,G_\theta}{r^2} \\ \frac{1}{r}\frac{\partial^2(r\,G_\theta)}{\partial r^2}+\frac{1}{r^2}\frac{\partial^2 G_\theta}{\partial\theta^2}+\frac{1}{r^2\sin^2\theta}\frac{\partial^2 G_\theta}{\partial\phi^2}+\frac{\cot\theta}{r^2}\frac{\partial G_\theta}{\partial\theta}-\frac{2}{r^2}\frac{\cot\theta}{\sin\theta}\frac{\partial G_\phi}{\partial\phi}+\frac{2}{r^2}\frac{\partial G_r}{\partial\theta}-\frac{G_\theta}{r^2\sin^2\theta} \\ \frac{1}{r}\frac{\partial^2(r\,G_\phi)}{\partial r^2}+\frac{1}{r^2}\frac{\partial^2 G_\phi}{\partial\theta^2}+\frac{1}{r^2\sin^2\theta}\frac{\partial^2 G_\phi}{\partial\phi^2}+\frac{\cot\theta}{r^2}\frac{\partial G_\phi}{\partial\theta}+\frac{2}{r^2\sin\theta}\frac{\partial G_r}{\partial\phi}+\frac{2}{r^2}\frac{\cot\theta}{\sin\theta}\frac{\partial G_\theta}{\partial\phi}-\frac{G_\phi}{r^2\sin^2\theta} \end{pmatrix} \tag{B.2.1}$$

For the flow velocity components $(u_r,u_\theta,0)$, Eq. (B.1.3) combined with Eq. (B.2.1) is

$$\begin{pmatrix} \frac{1}{\mu}\frac{\partial p}{\partial r} \\ \frac{1}{\mu r}\frac{\partial p}{\partial\theta} \end{pmatrix}=\begin{pmatrix} \frac{1}{r}\frac{\partial^2(r\,u_r)}{\partial r^2}+\frac{1}{r^2}\frac{\partial^2 u_r}{\partial\theta^2}+\frac{\cot\theta}{r^2}\frac{\partial u_r}{\partial\theta}-\frac{2}{r^2}\frac{\partial u_\theta}{\partial\theta}-\frac{2\,u_r}{r^2}-\frac{2\cot\theta\,u_\theta}{r^2} \\ \frac{1}{r}\frac{\partial^2(r\,u_\theta)}{\partial r^2}+\frac{1}{r^2}\frac{\partial^2 u_\theta}{\partial\theta^2}+\frac{\cot\theta}{r^2}\frac{\partial u_\theta}{\partial\theta}+\frac{2}{r^2}\frac{\partial u_r}{\partial\theta}-\frac{u_\theta}{r^2\sin^2\theta} \end{pmatrix} \tag{B.2.2}$$

B.2.1 PRESSURE

The pressure p is determined by Eq. (B.2.2) with Eq. (B.1.10a) and Eq. (B.1.10b).

$$p=p_\infty-\frac{3}{2}\mu\,w_f\frac{a}{r^2}\cos\theta \tag{B.2.3}$$

where p_∞ is the constant pressure far away from the sphere.

B.2.2 SURFACE STRESSES

The expression of the normal and shear stress tensor components

$$\sigma_{ij}=-p\,\delta_{ij}+\mu\left(\nabla_i\,u_j+\nabla_j\,u_i\right) \tag{B.2.4}$$

can find the radial stress σ_{rr} and the shear stress $\sigma_{\theta r}$ as

$$\sigma_{rr}=-p+2\mu\frac{\partial u_r}{\partial r}=-p_\infty+\frac{3}{2}\mu\frac{a}{r^2}\left(3-2\frac{a^2}{r^2}\right)w_f\cos\theta \tag{B.2.5a}$$

$$\sigma_{\theta r}=\mu\left(r\frac{\partial}{\partial r}\left(\frac{u_\theta}{r}\right)+\frac{1}{r}\frac{\partial\,u_r}{\partial\theta}\right)=-\frac{3}{2}\mu\frac{a^3}{r^4}\,w_f\sin\theta \tag{B.2.5b}$$

The stress components on the sphere surface at $r=a$,

$$\sigma_{rr}|_{r=a}=-p_\infty+\frac{3}{2a}\mu\,w_f\cos\theta \tag{B.2.6a}$$

$$\sigma_{\theta r}|_{r=a}=-\frac{3}{2a}\mu\,w_f\sin\theta \tag{B.2.6b}$$

B.2.3 Drag Force

The force of drag is generated by the interaction and contact of a solid with a fluid. For a large *Reynolds number Re* to produce turbulence behind the sphere, the celebrated *drag equation* is used to estimate the drag force by a moving object through a fully enclosing fluid.

$$F_D = \frac{1}{2}\rho_f\, w_f^2\, C_D\, A \tag{B.2.7}$$

where the reference area A is characteristic with the cross-sectional area, πa^2, in the case of a sphere with radius a and C_D is the *Drag coefficient*.

At the Stokes flow, the net drag force exerted by the sphere on the fluid is

$$F_D = \int_S \Big(\sigma_{rr}\cos\theta - \sigma_{\theta r}\sin\theta\Big)\ \mathrm{d}S \tag{B.2.8}$$

In substitution of the parallel resultant stress to the z-axis on the sphere $r = a$ from Eq. (B.2.6a) and Eq. (B.2.6b), Eq. (B.2.8) becomes

$$\begin{aligned} F_D &= \int_0^\pi 2\pi a^2 \Big(\sigma_{rr}\cos\theta - \sigma_{\theta r}\sin\theta\Big)_{r=a}\sin\theta\ \mathrm{d}\theta \\ &= 2\pi a^2 \int_0^\pi -p_\infty \cos\theta\sin\theta + \frac{3}{2a}\mu\, w_f \sin\theta\ \mathrm{d}\theta \\ &= 6\pi\mu a\, w_f \end{aligned} \tag{B.2.9}$$

B.2.4 Drag Coefficient

Connecting Eq. (B.2.7) with Eq. (B.2.9),

$$\begin{aligned} &\frac{1}{2}\rho_f\, w_f^2\, C_D\, \pi a^2 = 6\pi\mu a\, w_f \\ &\qquad\qquad \therefore \\ &C_D = \frac{12\pi\mu a\, w_f}{\rho_f\, w_f^2\, \pi a^2} = \frac{12\mu}{\rho_f\, w_f\, a} = \frac{24}{\dfrac{\rho_f\, w_f\, (2a)}{\mu}} = \frac{24}{Re} \end{aligned} \tag{B.2.10}$$

a drag coefficient C_D is obtained, which is a dimensionaless quantity to quantify the resistance of an object in a fluid environment.

B.2.5 Falling Velocity

In the assumption of Stokes flow, the ambient velocity w_f is constant passing the rest system of the sphere. However, it is also valid for a sphere falling with the constant velocity w_s to the rest system of the asymptotic fluid.

Equating the Stokes drag with the force of gravity minus buoyancy weight of the sphere $r = a$, the terminal velocity of a falling sphere is

$$\begin{aligned} \left(\rho_s - \rho_f\right) V_s\, g &= 6\pi\,\mu\, a\, w_s \\ w_s = \frac{\rho_s - \rho_f}{6\pi\,\mu\, a}\,\frac{4}{3}\,\pi\, a^3\, g &= \frac{2}{9}\, g\, a^2\,\frac{\rho_s - \rho_f}{\mu} \end{aligned} \tag{B.2.11}$$

B.2.6 STOKES' SOLUTION FOR A AG-CU SPHERE

Considering the rigid sphere of Ag-Cu alloy experiences *Stokes' flow* in flight at Nitrogen gas,

Table B.2.1: Fall velocity of a particle through a fluid

Diameter (μm)	Velocity (m/s)	Drag Coefficient (-)	Drag (N)
38	0.41	24.0596	2.60×10^{-9}
53	0.79	8.8677	7.05×10^{-9}
75	1.58	3.1294	19.97×10^{-9}
106	3.15	1.1085	56.36×10^{-9}
150	6.31	0.3912	159.72×10^{-9}
212	12.61	0.1386	450.92×10^{-9}
300	25.25	0.0489	1277.77×10^{-9}
500	70.13	0.0106	5915.62×10^{-9}
850	202.68	0.0021	29063.4×10^{-9}

APPENDIX C

ANALYTIC SOLUTION OF ONE-DIMENSIONAL HEAT TRANSFER

C.1 SOLID SPHERE

Consider the heat transfer problem where a sphere with radius $r = b$, initially at a uniform temperature $T(r,0) = T_0$,

$$\frac{1}{r^2}\frac{\partial}{\partial r}\left(r^2\frac{\partial T}{\partial r}\right) = \frac{1}{\kappa}\frac{\partial T}{\partial t} \tag{C.1.1}$$

subject to

$$\frac{\partial T(0,t)}{\partial r} = 0 \tag{C.1.2a}$$

$$T(b,t) = T_1 \tag{C.1.2b}$$

In order to apply the method of separation of variables, the non-homogeneous boundary condition in Eq. (C.1.2b) is transformed into,

$$T^* = T(r,t) - T_1 \tag{C.1.3}$$

Substituting T with T^* in Eq. (C.1.1), Eq. (C.1.2a) and Eq. (C.1.2b), the problem is modified

$$\frac{1}{\kappa}\frac{\partial T^*}{\partial t} = \frac{1}{r^2}\frac{\partial}{\partial r}\left(r^2\frac{\partial T^*}{\partial r}\right) \tag{C.1.4}$$

$$\frac{\partial T^*(0,t)}{\partial r} = 0 \tag{C.1.5a}$$

$$T^*(b,t) = 0 \tag{C.1.5b}$$

Assumed there would be a solution in the form of the product,

$$T^*(r,t) = R(r)\,\Gamma(t)$$

Eq. (C.1.4) becomes

$$\frac{1}{r^2 R}\frac{\mathrm{d}}{\mathrm{d}r}\left(r^2\frac{\mathrm{d}R}{\mathrm{d}r}\right)=\frac{1}{\kappa\Gamma}\frac{\mathrm{d}\Gamma}{\mathrm{d}t} \tag{C.1.6}$$

Since $R(t)$ and $\Gamma(t)$ are independent of each other, the derivative of R equal to the derivative of Γ gives rise to a fixed constant, such as $-\lambda^2$, in each side of Eq. (C.1.6).

$$\frac{\mathrm{d}\Gamma}{\mathrm{d}t}=-\lambda^2\kappa\Gamma$$

$$\Gamma(t)=C\exp\left(-\kappa\lambda^2 t\right) \tag{C.1.7}$$

$$\frac{1}{r^2}\frac{\mathrm{d}}{\mathrm{d}r}\left(r^2\frac{\mathrm{d}R}{\mathrm{d}r}\right)=-\lambda^2 R$$

$$R(r)=A\frac{\sin\lambda r}{r}+B\frac{\cos\lambda r}{r} \tag{C.1.8}$$

To satisify with boundary condition Eq. (C.1.5a), B must be equal to 0 in Eq. (C.1.8). Because $R(0)$ at $t=0$ would be a constant after $B=0$ as

$$\lim_{r\to 0} A\frac{\sin\lambda r}{r}=A\lambda$$

Also, to satisfy with boundary condition Eq. (C.1.5b), Eq. (C.1.8) at $r=b$ should be

$$A\frac{\sin\lambda b}{b}=0$$

$$\lambda=\frac{n\pi}{b} \tag{C.1.9}$$

The product of Eq. (C.1.7) and Eq. (C.1.8) with constant A, B, C,

$$T^*(r,t)=\frac{A}{r}\sin\left(\frac{n\pi}{b}r\right)\exp\left\{-\kappa\left(\frac{n\pi}{b}\right)^2 t\right\} \tag{C.1.10}$$

where constant A is the multiplication of A and C

Applying the initial condition

$$T^*(r,0)=T(r,0)-T_1=T_0-T_1=\frac{A}{r}sin\left(\frac{n\pi}{b}r\right) \tag{C.1.11}$$

According to the property of orthogonality,

$$\int_0^L \sin\left(m\pi\frac{x}{L}\right)\sin\left(n\pi\frac{x}{L}\right)\,\mathrm{d}x=\begin{cases}0 & m\neq n\\ \dfrac{L}{2} & m=n\end{cases} \tag{C.1.12}$$

Multiplying with an integration of

$$\int_0^b \sin\left(\frac{m\pi}{b}r\right)\,\mathrm{d}r$$

Eq. (C.1.11) is

$$(T_0 - T_1)\int_0^b r\sin\left(\frac{m\pi}{b}r\right)\,\mathrm{d}r = A\int_0^b sin\left(\frac{n\pi}{b}r\right)\sin\left(\frac{m\pi}{b}r\right)\,\mathrm{d}r$$

$$\frac{b}{2}A = (T_0 - T_1)\int_0^b r\sin\left(\frac{n\pi}{b}r\right)\,\mathrm{d}r$$

$$A = 2\frac{T_0 - T_1}{b}\int_0^b r\sin\left(\frac{n\pi}{b}r\right)\,\mathrm{d}r$$

$$= 2b\frac{T_0 - T_1}{n^2\pi^2}(-\pi n\cos n\pi + \sin n\pi)$$

$$\therefore \quad A = -(-1)^n 2b\frac{T_0 - T_1}{n\pi} \qquad n = 1, 2, \ldots \tag{C.1.13}$$

The general solution of the sphere, therefore, initially at a uniform temperature T_0 and the surface temperature T_1 at $r = b$ is

$$T(r,t) = T^* + T_1 = T_1 - (T_0 - T_1)\frac{2b}{\pi r}\sum_{n=1}^{\infty}\frac{(-1)^n}{n}\sin\left(\frac{n\pi}{b}r\right)\exp\left\{-\kappa\left(\frac{n\pi}{b}\right)^2 t\right\} \tag{C.1.14}$$

C.2 Hollow Sphere

Consider the heat transfer where a hollow sphere with the surface $r = a$ maintained at a constant temperature U_1 and $r = b$ at U_2, when the initial temperature remains U_0 in the region $a \le r \le b$. On putting

$$V(r,t) = r\,U(r,t) \tag{C.2.1}$$

Eq. (C.1.1) with its initial and boundary conditions becomes

$$\frac{1}{\kappa}\frac{\partial V}{\partial t} = \frac{\partial^2 V}{\partial r^2} \tag{C.2.2a}$$

$$V(r,0) = r\,U_0 \tag{C.2.2b}$$

$$V(a,t) = a\,U_1 \tag{C.2.2c}$$

$$V(b,t) = b\,U_2 \tag{C.2.2d}$$

In order to apply Eq. (C.2.2a) by separation of variables, the non-homogeneous boundary is required to be transferred into a new homogeneous one by concerning with a steady-state solution that only varies linearly along the change of r between the boundary temperatures $a\,U_1$ and $b\,U_2$ when $t = \infty$ as shown in Eq. (C.2.3).

$$v(r,t) = a\,U_1 + \frac{b\,U_2 - a\,U_1}{b - a}(r - a) \tag{C.2.3}$$

Combining Eq. (C.2.3) with Eq. (C.2.2a), Eq. (C.2.2b), Eq. (C.2.2c) and Eq. (C.2.2d), the transient

$$Z(r,t) = V(r,t) - v(r,t)$$

is used to obtain

$$\frac{1}{\kappa}\frac{\partial Z}{\partial t} = \frac{\partial^2 Z}{\partial r^2} \tag{C.2.4a}$$

$$\begin{aligned} Z(r,0) &= V(r,0) - v(r,0) \\ &= r\,U_0 - \left(a\,U_1 + \frac{b\,U_2 - a\,U_1}{b-a}\,(r-a)\right) \end{aligned} \tag{C.2.4b}$$

$$Z(a,t) = 0; \tag{C.2.4c}$$

$$Z(b,t) = 0; \tag{C.2.4d}$$

Provided there is a solution of the form

$$Z(r,t) = R(r)\,\Gamma(t)$$

substituting this into Eq. (C.2.4a) yields

$$\frac{1}{R}\frac{\mathrm{d}^2 R}{\mathrm{d}r^2} = \frac{1}{\kappa\,\Gamma}\frac{\mathrm{d}\Gamma}{\mathrm{d}t} \tag{C.2.5}$$

Again, Eq. (C.2.5) shows there would be a fixed constant to make both sides equivalent as Appendix C.1. Eq. (C.2.2a) becomes two seperated ordinary differential equations, which have the general solution as same as those in Appendix C.1.

$$\Gamma(t) = C\exp(-\kappa\lambda_n^2\,t) \tag{C.2.6a}$$

$$R(r) = A_n \sin\lambda_n\,(r-a) + B_n\cos\lambda_n\,(r-a) \tag{C.2.6b}$$

By a good observation of the boundary condition Eq. (C.2.4c) and Eq. (C.2.4d), B_n in Eq. (C.2.6b) is equal to zero and

$$\lambda_n = \frac{n\,\pi}{b-a} \qquad n = 1, 2, 3, \ldots \tag{C.2.7}$$

Thus, the general solution of $Z(r,t)$ consists of an infinite number of functions

$$Z_n(x,t) = A_n \sin\left(n\,\pi\,\frac{r-a}{b-a}\right)\exp\left\{-\kappa\left(\frac{n\pi}{b-a}\right)^2 t\right\} \qquad n = 1, 2, 3, \ldots \tag{C.2.8}$$

To determine A_n, the given initial condition in Eq. (C.2.4d) is applied in Eq. (C.2.8)

$$r\,U_0 - \left(a\,U_1 + \frac{b\,U_2 - a\,U_1}{b-a}\,(r-a)\right) = \sum_{n=1}^{\infty} A_n \sin\left(n\,\pi\,\frac{r-a}{b-a}\right)$$

By multiplying both sides by

$$\sin\left(m\pi\,\frac{r-a}{b-a}\right)$$

and integrating from $r = a$ to b to vanish the sin term when $m = n$, due to orthogonality

$$\int_a^b \left(r\,U_0 - a\,U_1 - \frac{b\,U_2 - a\,U_1}{b-a}(r-a) \right) \sin\left(n\pi \frac{r-a}{b-a} \right) \mathrm{d}r = \sum_{m=1}^{\infty} A_n \int_a^b \sin\left(n\pi \frac{r-a}{b-a} \right) \sin\left(m\pi \frac{r-a}{b-a} \right) \mathrm{d}r$$

$$\int_a^b \left(r\,U_0 - a\,U_1 - \frac{b\,U_2 - a\,U_1}{b-a}(r-a) \right) \sin\left(n\pi \frac{r-a}{b-a} \right) \mathrm{d}r = A_n \frac{b-a}{2}$$

$$A_n = \frac{2}{b-a} \int_a^b \left(r\,U_0 - a\,U_1 - \frac{b\,U_2 - a\,U_1}{b-a}(r-a) \right) \sin\left(n\pi \frac{r-a}{b-a} \right) \mathrm{d}r$$

$$A_n = 2 \left(\frac{a\,(U_0 - U_1) - b\,(U_0 - U_2)\cos(n\pi)}{n\pi} \right) \tag{C.2.9}$$

The finial solution of $Z(r,t)$ is therefore

$$Z(r,t) = 2 \sum_{n=1}^{\infty} \left(\frac{a\,(U_0 - U_1) - b\,(U_0 - U_2)\cos(n\pi)}{n\pi} \right) \sin\left(n\pi \frac{r-a}{b-a} \right) \exp\left\{ -\kappa \left(\frac{n\pi}{b-a} \right)^2 t \right\} \tag{C.2.10}$$

Considering with the previous substitution in Eq. (C.2.1) and Eq. (C.2.3), the original problem is equivalent to

$$U(r,t) = \frac{Z(r,t) + v(r,t)}{r}$$

Thus

$$\begin{aligned} U(r,t) = & \frac{1}{r} \left(a\,U_1 + \frac{b\,U_2 - a\,U_1}{b-a}(r-a) \right) \\ & + \frac{2}{\pi r} \sum_{n=1}^{\infty} \left(\frac{a\,(U_0 - U_1) - b\,(U_0 - U_2)\cos(n\pi)}{n} \right) \sin\left(n\pi \frac{r-a}{b-a} \right) \exp\left\{ -\kappa \left(\frac{n\pi}{b-a} \right)^2 t \right\} \end{aligned} \tag{C.2.11}$$

In the special case of a constant initial temperature, U_0 and when $U_1 = U_2$, the solution [78] is

$$U(r,t) = U_1 + (U_0 - U_1) \frac{2}{\pi r} \sum_{n=1}^{\infty} \frac{a - b\cos(n\pi)}{n} \sin\left(n\pi \frac{r-a}{b-a} \right) \exp\left\{ -\kappa \left(\frac{n\pi}{b-a} \right)^2 t \right\} \tag{C.2.12}$$

APPENDIX D

NUMERICAL SOLUTION OF TWO-DIMENSIONAL HEAT TRANSFER

When temperature gradients within a body are concerned with spatially varying boundary conditions or boundary layer flow, the multidimensional effects in finite sized bodies become more important than the effect in one direction of interest. For bodies with simple boundary condition, multidimensional, linear heat transfer problems can be solved by analytical methods, such as laplace transform or Fourier series transform, which are introduced in elsewhere. In the case of either complicated boundary conditions, or temperature dependent properties in irregular body shapes, the numerical computation of multidimensional parabolic systems is preferred.

The explicit, the fully implicit, and the ADI stencils introduced in Section 4.2.1 now is extended into the two-dimensional problems in Appendix D.1. Also the brief introduction about the solution of two-dimensional unsteady heat transfer modelling in Section 3.2.1 is given in Appendix D.2.

D.1 CARTESIAN COORDINATES

Provided two-dimensional (2D), linear heat transfer in isotropic solids, the temperature fields inside the medium is governed by the partial differential equation, as introduced in Eq. (A.2.4) for cartesian coordinates system

$$\frac{\partial U}{\partial t} = \alpha \left(\frac{\partial^2 U}{\partial x^2} + \frac{\partial^2 U}{\partial y^2} \right) \tag{D.1.1}$$

subject to Dirichlet boundary condition on the right and left sides and Neumann boundary condition on the top and bottom sides.

D.1.1 Explicit Scheme

The use of explicit method is to discretize $U(x, y, t)$ in Eq. (D.1.1) as an explicit discretization scheme

$$\frac{U_{i,j}^{n+1} - U_{i,j}^{n}}{\Delta t} = \alpha \left(\frac{U_{i-1,j}^{n} - 2U_{i,j}^{n} + U_{i+1,j}^{n}}{\Delta x^2} + \frac{U_{i,j-1}^{n} - 2U_{i,j}^{n} + U_{i,j+1}^{n}}{\Delta y^2} \right) \tag{D.1.2}$$

$U(i\Delta x, j\Delta y, n\Delta t)$ in Eq. (D.1.2) is rearranged in the form

$$U_{i,j}^{n+1} = U_{i,j}^{n} + r_x \left(U_{i-1,j}^{n} - 2U_{i,j}^{n} + U_{i+1,j}^{n} \right) + r_y \left(U_{i,j-1}^{n} - 2U_{i,j}^{n} + U_{i,j+1}^{n} \right) \tag{D.1.3a}$$

$$r_x = \alpha \frac{\Delta t}{\Delta x^2} \qquad r_y = \alpha \frac{\Delta t}{\Delta y^2} \tag{D.1.3b}$$

for the internal nodes $i = 1, 2, \ldots, M-1$ and $j = 1, 2, \ldots, N-1$.

Eq. (D.1.3a) provides M and N relations to x and y direction but yet exists unknown node potential 0 and $M+1$ (0 and $N+1$) for $T_{i,j}^{n}$ at the time level n. Thus, an additional relationship at boundaries is required to develop a full discretization scheme in numerical computation.

Both prescribed surface temperature and heat flux are considered at the left outer surface $x = 0$, which is $i = 0$ in Eq. (D.1.3a).

$$U_{0,j}^{n+1} = U_{0,j}^{n} + r_x \left(U_{-1,j}^{n} - 2U_{0,j}^{n} + U_{1,j}^{n} \right) + r_y \left(U_{0,j-1}^{n} - 2U_{0,j}^{n} + U_{0,j+1}^{n} \right) \tag{D.1.4}$$

where $U_{-1,j}^{n}$ is a fictitious node in the central difference representation.

Dirichlet Boundary Condition

The left side surface temperature at $i = 0$ for $j = 1, 2, \ldots, N-1$ at all time levels is

$$U_{0,j}^{n} = U_b \tag{D.1.5}$$

Neumann Boundary Condition

$$\frac{U_{1,j}^{n} - U_{-1,j}^{n}}{2\Delta x} = c_1 \tag{D.1.6}$$

where c_1 represents an arbitrary constant heat flux.

Combined with Eq. (D.1.4) and Eq. (D.1.6), the fictitious node can be eliminated for the node at $i = 0$

$$U_{0,j}^{n+1} = U_{0,j}^{n} + 2r_x \left(-U_{0,j}^{n} + U_{1,j}^{n} - c_1 \Delta x \right) + r_y \left(U_{0,j-1}^{n} - 2U_{0,j}^{n} + U_{0,j+1}^{n} \right) \tag{D.1.7}$$

The stability is concerned in order to obtain meaningful results from the solution of Eq. (D.1.4) with related boundary conditions

$$\left(r_x + r_y \right) \leq \frac{1}{2} \tag{D.1.8}$$

The explicit method is applied at the cost of severe restrictions imposed on the size of the marching step Δx and Δy for its conditional stability, but it is nevertheless the best choice for the general heat transfer equations.

D.1.2 Implicit Scheme

The fully implicit discretization scheme of Eq. (D.1.1) is

$$\frac{U_{i,j}^{n+1}-U_{i,j}^{n}}{\Delta t}=\alpha\left(\frac{U_{i-1,j}^{n+1}-2U_{i,j}^{n+1}+U_{i+1,j}^{n+1}}{\Delta x^2}+\frac{U_{i,j-1}^{n+1}-2U_{i,j}^{n+1}+U_{i,j+1}^{n+1}}{\Delta y^2}\right) \tag{D.1.9}$$

Rearranging crefeq:appdx-sph-08 gives $U(i\Delta x, j\Delta y, n\Delta t)$ of next time level $n+1$ on the left side of equation and those of current time level n on the right side

$$U_{i,j}^{n+1}-r_x\left(U_{i-1,j}^{n+1}-2U_{i,j}^{n+1}+U_{i+1,j}^{n+1}\right)-r_y\left(U_{i,j-1}^{n+1}-2U_{i,j}^{n+1}+U_{i,j+1}^{n+1}\right)=U_{i,j}^{n}$$

$$-r_xU_{i-1,j}^{n+1}-r_yU_{i,j-1}^{n+1}+\left(1+2r_x+2r_y\right)U_{i,j}^{n+1}-r_yU_{i,j+1}^{n+1}-r_xU_{i+1,j}^{n+1}=U_{i,j}^{n} \tag{D.1.10a}$$

$$r_x=\alpha\frac{\Delta t}{\Delta x^2}\qquad r_y=\alpha\frac{\Delta t}{\Delta y^2} \tag{D.1.10b}$$

for the internal nodes $i=1,2,\ldots,M-1$ and $j=1,2,\ldots,N-1$.

2D implicit scheme with N interior nodes in each direction involves a total N^2 interior points such that $N^2\times N^2$ matrix is involved at each time step of calculation. For example, 7×5 interior nodes need to deal with 35×35 matrix A as

$$\begin{pmatrix}
1 & 0 & \cdots & 0 & 0 & 0 & 0 & 0 & 0 & 0 & 0 & \cdots & 0 & 0\\
0 & 1 & \cdots & 0 & 0 & 0 & 0 & 0 & 0 & 0 & 0 & \cdots & 0 & 0\\
\vdots & & \ddots & & \vdots & & \vdots & \vdots & & \vdots & & \ddots & & \vdots\\
0 & 0 & \cdots & -r_y & \cdots & -r_x & 1+2r_x+2_y & -r_x & \cdots & -r_y & 0 & \cdots & 0 & 0\\
0 & 0 & \cdots & 0 & -r_y & \cdots & -r_x & 1+2r_x+2_y & -r_x & \cdots & -r_y & \cdots & 0 & 0\\
\vdots & & \ddots & & \vdots & & \vdots & \vdots & & \vdots & & \ddots & & \vdots\\
0 & 0 & \cdots & 0 & 0 & 0 & 0 & 0 & 0 & 0 & 0 & \cdots & 1 & 0\\
0 & 0 & \cdots & 0 & 0 & 0 & 0 & 0 & 0 & 0 & 0 & \cdots & 0 & 1
\end{pmatrix}$$

The vector x and b in $A\dot{x} = b$ are given by temperature $U_{i,j}$ of time level n and $n+1$ respectively.

$$x = \begin{pmatrix} U_1^{n+1} \\ U_2^{n+1} \\ \vdots \\ U_{18}^{n+1} \\ U_{19}^{n+1} \\ \vdots \\ U_{34}^{n+1} \\ U_{35}^{n+1} \end{pmatrix} \qquad b = \begin{pmatrix} U_1^{n} \\ U_2^{n} \\ \vdots \\ U_{18}^{n} \\ U_{19}^{n} \\ \vdots \\ U_{34}^{n} \\ U_{35}^{n} \end{pmatrix} \begin{matrix} \\ \\ \\ \\ \Rightarrow \text{ center} \\ \\ \\ \Rightarrow \text{ top} \end{matrix}$$

D.1.3 ADI SCHEME

With the modification of Eq. (D.1.1),

$$\frac{U_{i,j}^{n+0.5} - U_{i,j}^{n}}{0.5\Delta t} = \alpha \left(\frac{U_{i-1,j}^{n+0.5} - 2U_{i,j}^{n+0.5} + U_{i+1,j}^{n+0.5}}{\Delta x^2} + \frac{U_{i,j-1}^{n} - 2U_{i,j}^{n} + U_{i,j+1}^{n}}{\Delta y^2} \right) \tag{D.1.11a}$$

$$\frac{U_{i,j}^{n+1} - U_{i,j}^{n+0.5}}{0.5\Delta t} = \alpha \left(\frac{U_{i-1,j}^{n+0.5} - 2U_{i,j}^{n+0.5} + U_{i+1,j}^{n+0.5}}{\Delta x^2} + \frac{U_{i,j-1}^{n+1} - 2U_{i,j}^{n+1} + U_{i,j+1}^{n+1}}{\Delta y^2} \right) \tag{D.1.11b}$$

Rearranging Eq. (D.1.11a) and Eq. (D.1.11b),

$$-\frac{r_x}{2} U_{i-1,j}^{n+0.5} + \left(1 + r_x\right) U_{i,j}^{n+0.5} - \frac{r_x}{2} U_{i+1,j}^{n+0.5} = \frac{r_y}{2} U_{i,j-1}^{n} + \left(1 - r_y\right) U_{i,j}^{n} + \frac{r_y}{2} U_{i,j+1}^{n} \tag{D.1.12a}$$

$$-\frac{r_y}{2} U_{i,j-1}^{n+1} + \left(1 + r_y\right) U_{i,j}^{n+1} - \frac{r_y}{2} U_{i,j+1}^{n+1} = \frac{r_x}{2} U_{i-1,j}^{n+0.5} + \left(1 - r_x\right) U_{i,j}^{n+0.5} + \frac{r_x}{2} U_{i+1,j}^{n+0.5} \tag{D.1.12b}$$

$$r_x = \frac{\alpha \Delta t}{\Delta x^2} \qquad r_y = \frac{\alpha \Delta t}{\Delta y^2} \tag{D.1.12c}$$

To advance from the time level n to $n+1$, Eq. (D.1.12a) is used to solve in N_y times and Eq. (D.1.12b) in N_x times.

Therefore, ADI method only requires to solve $N_x \times N_y$ matrix twice instead of to solve $N_x \cdot N_y \times N_y \cdot N_x$ matrix once at the same level of time. Comparing with the explicit and the fully implicit scheme,

the computation of ADI scheme is efficient but yet accurate by using Thomas algorithm, due to the symmetric and tri-diagonal system in both Eq. (D.1.12a) and Eq. (D.1.12b).

ADI Scheme in the x-Direction

To obtain unknown $U_{i,j}^{n+0.5}$ in Eq. (D.1.12a), the tri-diagonal matrix $N_x \times N_x$ with relevant known $U_{i,j}^{n}$ for $i = 0, 1, \ldots, N_x - 1$ is solved at fixed $j = 0, 1, \ldots, N_y - 1$. The entries at row 0 and $N_x - 1$ in tri-diagonal matrix may vary, depending on the left-side and the right-side boundary condition.

To simplify Eq. (D.1.12a) in compact matrix notation,r a horizontal slice from left to right through 2D temperature gradient is defined as vector

$$\mathbf{U}_{N_x-1,j}^{n+0.5} = \left(U_{0,j}^{n+0.5}, U_{1,j}^{n+0.5}, \ldots, U_{N_x-1,j}^{n+0.5}\right)$$

The ADI linear system in the x-direction can be obtained as

$$A_{N_x \times N_x} \cdot \left(\mathbf{U}_{N_x-1,j}^{n+0.5}\right)' = b_j \qquad j = 0, 1, \ldots, N_y - 1 \tag{D.1.13}$$

where

$$A_{N_x \times N_x} = \begin{pmatrix} 1 & 0 & 0 & 0 & 0 & \cdots & 0 & 0 & 0 & 0 \\ -\frac{r_x}{2} & 1+r_x & -\frac{r_x}{2} & 0 & 0 & \cdots & 0 & 0 & 0 & 0 \\ 0 & -\frac{r_x}{2} & 1+r_x & -\frac{r_x}{2} & 0 & \cdots & 0 & 0 & 0 & 0 \\ \vdots & & & & & \ddots & & & & \\ 0 & 0 & 0 & 0 & 0 & \cdots & 0 & -\frac{r_x}{2} & 1+r_x & -\frac{r_x}{2} \\ 0 & 0 & 0 & 0 & 0 & \cdots & 0 & 0 & 0 & 1 \end{pmatrix}$$

$A_{0,0} = 1$ and $A_{N_x-1,N_y-1} = 1$ because Dirichlet boundary conditions happen on the far left and right with $i = 0$ and $N_x - 1$ as the description of heat transfer problem above. Neumann boundary conditions on the top and the bottom side of temperature gradient also requires

$$b_j = \begin{pmatrix} \frac{r_y}{2} U^n_{0,j-1} + (1-r_y) U^n_{0,j} + \frac{r_y}{2} U^n_{0,j+1} \\ \frac{r_y}{2} U^n_{1,j-1} + (1-r_y) U^n_{1,j} + \frac{r_y}{2} U^n_{1,j+1} \\ \vdots \\ \frac{r_y}{2} U^n_{N_x-2,j-1} + (1-r_y) U^n_{N_x-2,j} + \frac{r_y}{2} U^n_{N_x-2,j+1} \\ \frac{r_y}{2} U^n_{N_x-1,j-1} + (1-r_y) U^n_{N_x-1,j} + \frac{r_y}{2} U^n_{N_x-1,j+1} \end{pmatrix}$$

Further modification at $j = 0$ and $N_y - 1$,

$$b_0 = \begin{pmatrix} \frac{r_y}{2} U^n_{0,-1} + (1-r_y) U^n_{0,0} + \frac{r_y}{2} U^n_{0,1} & = & U^n_{0,0} \\ \frac{r_y}{2} U^n_{1,-1} + (1-r_y) U^n_{1,0} + \frac{r_y}{2} U^n_{1,1} & = & (1-r_y) U_{1,0} + r_y U_{1,1} \\ \vdots & = & \vdots \\ \frac{r_y}{2} U^n_{N_x-2,-1} + (1-r_y) U^n_{N_x-2,0} + \frac{r_y}{2} U^n_{N_x-2,1} & = & (1-r_y) U^n_{N_x-2,0} + r_y U^n_{N_x-2,1} \\ \frac{r_y}{2} U^n_{N_x-1,-1} + (1-r_y) U^n_{N_x-1,0} + \frac{r_y}{2} U^n_{N_x-1,1} & = & U^n_{N_x-1,0} \end{pmatrix}$$

$$b_{N_y-1} = \begin{pmatrix} \frac{r_y}{2} U^n_{0,N_y-2} + (1-r_y) U^n_{0,N_y-1} + \frac{r_y}{2} U^n_{0,N_y} & = & U^n_{0,N_y-1} \\ \frac{r_y}{2} U^n_{1,N_y-2} + (1-r_y) U^n_{1,N_y-1} + \frac{r_y}{2} U^n_{1,N_y} & = & r_y U^n_{1,N_y-2} + (1-r_y) U^n_{1,N_y-1} \\ \vdots & = & \vdots \\ \frac{r_y}{2} U^n_{N_x-2,N_y-2} + (1-r_y) U^n_{N_x-2,N_y-1} + \frac{r_y}{2} U^n_{N_x-2,N_y} & = & r_y U^n_{N_x-2,N_y-2} + (1-r_y) U^n_{N_x-2,N_y-1} \\ \frac{r_y}{2} U^n_{N_x-1,N_y-2} + (1-r_y) U^n_{N_x-1,N_y-1} + \frac{r_y}{2} U^n_{N_x-1,N_y} & = & U^n_{N_x-1,N_y-1} \end{pmatrix}$$

ADI Scheme in the y-Direction

To obtain unknown $U_{i,j}^{n+1}$ in Eq. (D.1.12b), the tri-diagonal matrix $N_y \times N_y$r with relevant known $U_{i,j}^{n+0.5}$ for $j = 0, 1, \ldots, N_y - 1$ is solved at fixed $i = 0, 1, \ldots, N_x - 1$. The entries at row 0 and $N_y - 1$ in tri-diagonal matrix may vary, depending on the bottom-side and the top-side boundary condition.

Again, a simplified vertical vector from bottom to top through two-dimensional temperature gradient is

$$\mathbf{U}_{i,N_y-1}^{n+1} = \left(U_{i,0}^{n+1}, U_{i,1}^{n+1}, \ldots, U_{i,N_y-1}^{n+1}\right)$$

The ADI linear system in the y-direction can be obtained as

$$A_{N_y \times N_y} \cdot \mathbf{U}_{i,N_y-1}^{n+1} = b_i \qquad i = 0, 1, \ldots, N_x - 1 \tag{D.1.14}$$

Because Neumann boundary conditions happen on the bottom and the top side, Eq. (D.1.12b) at $j = 0$ and $N_y - 1$ is written in Eq. (D.1.15) and Eq. (D.1.16) respectively.

$$\begin{aligned} -\frac{r_y}{2} U_{i,-1}^{n+1} + (1 + r_y) U_{i,0}^{n+1} - \frac{r_y}{2} U_{i,1}^{n+1} &= \frac{r_x}{2} U_{i-1,0}^{n+0.5} + (1 - r_x) U_{i,0}^{n+0.5} + \frac{r_x}{2} U_{i+1,0}^{n+0.5} \\ (1 + r_y) U_{i,0}^{n+1} - r_y U_{i,1}^{n+1} &= \frac{r_x}{2} U_{i-1,0}^{n+0.5} + (1 - r_x) U_{i,0}^{n+0.5} + \frac{r_x}{2} U_{i+1,0}^{n+0.5} \end{aligned} \tag{D.1.15}$$

$$\begin{aligned} -\frac{r_y}{2} U_{i,N_y-2}^{n+1} + (1 + r_y) U_{i,N_y-1}^{n+1} - \frac{r_y}{2} U_{i,N_y}^{n+1} &= \frac{r_x}{2} U_{i-1,N_y-1}^{n+0.5} + (1 - r_x) U_{i,N_y-1}^{n+0.5} + \frac{r_x}{2} U_{i+1,N_y-1}^{n+0.5} \\ -r_y U_{i,N_y-2}^{n+1} + (1 + r_y) U_{i,N_y-1}^{n+1} &= \frac{r_x}{2} U_{i-1,N_y-1}^{n+0.5} + (1 - r_x) U_{i,N_y-1}^{n+0.5} + \frac{r_x}{2} U_{i+1,N_y-1}^{n+0.5} \end{aligned} \tag{D.1.16}$$

Combining Eq. (D.1.12b) with Eq. (D.1.15) and Eq. (D.1.16),

$$A_{N_y \times N_y} = \begin{pmatrix} 1 + r_y & -r_y & 0 & 0 & 0 & \ldots & 0 & 0 & 0 & 0 \\ -\frac{r_y}{2} & 1 + r_y & -\frac{r_y}{2} & 0 & 0 & \ldots & 0 & 0 & 0 & 0 \\ 0 & -\frac{r_y}{2} & 1 + r_y & -\frac{r_y}{2} & 0 & \ldots & 0 & 0 & 0 & 0 \\ \vdots & & & & & \ddots & & & & \\ 0 & 0 & 0 & 0 & 0 & \ldots & 0 & -\frac{r_y}{2} & 1 + r_y & -\frac{r_y}{2} \\ 0 & 0 & 0 & 0 & 0 & \ldots & 0 & 0 & -r_y & 1 + r_y \end{pmatrix}$$

where $A_{N_y \times N_y}$ can only be satisfied with $i = 1, 2, \ldots, N_x - 2$, due to the Dirichlet boundary conditions on the right and left side of temperature plane. At both $i = 0$ and $N_x - 1$,

$$A_{N_y \times N_y} = \begin{pmatrix} 1 & 0 & 0 & \cdots & 0 & 0 \\ 0 & 1 & 0 & \cdots & 0 & 0 \\ \vdots & & & \ddots & & \\ 0 & 0 & 0 & \cdots & 0 & 1 \end{pmatrix}$$

The form of vector b_i in Eq. (D.1.14) with $i = 1, 2, \ldots, N_x - 2$ is

$$b_i = \begin{pmatrix} \frac{r_x}{2} U_{i-1,0}^{n+0.5} + (1 - r_x) U_{i,0}^{n+0.5} + \frac{r_x}{2} U_{i+1,0}^{n+0.5} \\ \frac{r_x}{2} U_{i-1,1}^{n+0.5} + (1 - r_x) U_{i,1}^{n+0.5} + \frac{r_x}{2} U_{i+1,1}^{n+0.5} \\ \vdots \\ \frac{r_x}{2} U_{i-1,N_y-1}^{n+0.5} + (1 - r_x) U_{i,N_y-1}^{n+0.5} + \frac{r_x}{2} U_{i+1,N_y-1}^{n+0.5} \end{pmatrix}$$

At $i = 0$ and $N_x - 1$, vector b_i is written as the same form of vector with different subscript i, depending on its location.

$$b_0 = \begin{pmatrix} U_{0,0}^{n+0.5} \\ U_{0,1}^{n+0.5} \\ \vdots \\ U_{0,N_y-1}^{n+0.5} \end{pmatrix} \qquad b_{N_x-1} = \begin{pmatrix} U_{N_x-1,0}^{n+0.5} \\ U_{N_x-1,1}^{n+0.5} \\ \vdots \\ U_{N_x-1,N_y-1}^{n+0.5} \end{pmatrix}$$

D.2 Spherical Polar Coordinates

The expansion of governing dimensionless equation $Z_f(\tau, \xi, \theta)$ in Eq. (3.2.5) by chain rule is

$$\frac{\partial Z_f}{\partial \tau} + Pe \left(v_\xi \frac{\partial Z_f}{\partial \xi} + \frac{v_\theta}{\xi} \frac{\partial Z_f}{\partial \theta} \right) = \frac{\partial^2 Z_f}{\partial \xi^2} + \frac{2}{\xi} \frac{\partial Z_f}{\partial \xi} + \frac{1}{\xi^2} \frac{\partial^2 Z_f}{\partial \theta^2} + \frac{\cot\theta}{\xi^2} \frac{\partial Z_f}{\partial \theta} \tag{D.2.1}$$

Also, the singularities along the stagnation Line at $\theta = 0$ and π are solved by using L'Hôpital's rule

$$\frac{\partial Z_f}{\partial \tau} + Pe\left(v_\xi \frac{\partial Z_f}{\partial \xi} + \frac{v_\theta}{\xi}\frac{\partial Z_f}{\partial \theta}\right) = \frac{\partial^2 Z_f}{\partial \xi^2} + \frac{2}{\xi}\frac{\partial Z_f}{\partial \xi} + \frac{2}{\xi^2}\frac{\partial^2 Z_f}{\partial \theta^2} \tag{D.2.2}$$

D.2.1 Grid Construction

To construct a mesh grid (τ, ξ, θ) for Eq. (D.2.1),

$$\tau_n = n\,\Delta\tau \qquad n = 0, \ldots, N_\tau \tag{D.2.3a}$$

$$\xi_i = 1 + i\,\Delta\xi \qquad i = 0, \ldots, N_\xi \tag{D.2.3b}$$

$$\theta_j = j\,\Delta\theta \qquad j = 0, \ldots, N_\theta \tag{D.2.3c}$$

where $\Delta\tau$, $\Delta\xi$, and $\Delta\theta$ are defined as

$$\Delta\tau = \frac{\tau}{N_\tau} \qquad \Delta\xi = \frac{\xi_{bdy} - 1}{N_\xi} \qquad \Delta\theta = \frac{\pi}{N_\theta}$$

The numerical approximations of $Z_f(\tau, \xi, \theta)$ is

$$Z_f(\tau, \xi, \theta) \approx Z_f(n\Delta\tau, 1 + i\,\Delta\xi, j\,\Delta\theta) = {Z_f}^n_{i,j} \tag{D.2.4}$$

D.2.2 The Alternating Direction Implicit Stencils

The construction of the ADI method is to split the time step $\Delta\tau$ into two parts. In each half time step, two different stencils are applied, such as computing $Z_f^{n+0.5}$ and then Z_f^{n+1} to form one increment time step between n and $n+1$.

Eq. (D.2.1) is represented

$$\begin{aligned}
&\frac{Z^{n+0.5}_{i,j} - Z^n_{i,j}}{0.5\,\Delta\tau} + Pe\, v^\xi_{i,j}\frac{Z^{n+0.5}_{i+1,j} - Z^{n+0.5}_{i-1,j}}{2\,\Delta\xi} + Pe\,\frac{v^\theta_{i,j}}{\xi_i}\frac{Z^n_{i,j+1} - Z^n_{i,j-1}}{2\,\Delta\theta} \\
&= \frac{Z^{n+0.5}_{i+1,j} - 2\,Z^{n+0.5}_{i,j} + Z^{n+0.5}_{i-1,j}}{\Delta\xi^2} + \frac{2}{\xi_i}\frac{Z^{n+0.5}_{i+1,j} - Z^{n+0.5}_{i-1,j}}{2\,\Delta\xi} + \frac{1}{\xi_i^2}\frac{Z^n_{i,j+1} - 2\,Z^n_{i,j} + Z^n_{i,j-1}}{\Delta\theta^2} + \frac{\cot\theta_j}{\xi_i^2}\frac{Z^n_{i,j+1} - Z^n_{i,j-1}}{2\,\Delta\theta}
\end{aligned} \tag{D.2.5a}$$

$$\begin{aligned}
&\frac{Z^{n+1}_{i,j} - Z^{n+0.5}_{i,j}}{0.5\,\Delta\tau} + Pe\, v^\xi_{i,j}\frac{Z^{n+0.5}_{i+1,j} - Z^{n+0.5}_{i-1,j}}{2\,\Delta\xi} + Pe\,\frac{v^\theta_{i,j}}{\xi_i}\frac{Z^{n+1}_{i,j+1} - Z^{n+1}_{i,j-1}}{2\,\Delta\theta} \\
&= \frac{Z^{n+0.5}_{i+1,j} - 2\,Z^{n+0.5}_{i,j} + Z^{n+0.5}_{i-1,j}}{\Delta\xi^2} + \frac{2}{\xi_i}\frac{Z^{n+0.5}_{i+1,j} - Z^{n+0.5}_{i-1,j}}{2\,\Delta\xi} + \frac{1}{\xi_i^2}\frac{Z^{n+1}_{i,j+1} - 2\,Z^{n+1}_{i,j} + Z^{n+1}_{i,j-1}}{\Delta\theta^2} + \frac{\cot\theta_j}{\xi_i^2}\frac{Z^{n+1}_{i,j+1} - Z^{n+1}_{i,j-1}}{2\,\Delta\theta}
\end{aligned} \tag{D.2.5b}$$

Stagnation Lines

Eq. (D.2.2) is

$$\frac{Z_{i,j}^{n+0.5}-Z_{i,j}^{n}}{0.5\,\Delta\tau}+Pe\,v_{i,j}^{\xi}\,\frac{Z_{i+1,j}^{n+0.5}-Z_{i-1,j}^{n+0.5}}{2\,\Delta\xi}+Pe\,\frac{v_{i,j}^{\theta}}{\xi_i}\,\frac{Z_{i,j+1}^{n}-Z_{i,j-1}^{n}}{2\,\Delta\theta}$$
$$=\frac{Z_{i+1,j}^{n+0.5}-2\,Z_{i,j}^{n+0.5}+Z_{i-1,j}^{n+0.5}}{\Delta\xi^2}+\frac{2}{\xi_i}\,\frac{Z_{i+1,j}^{n+0.5}-Z_{i-1,j}^{n+0.5}}{2\,\Delta\xi}+\frac{2}{\xi_i^2}\,\frac{Z_{i,j+1}^{n}-2\,Z_{i,j}^{n}+Z_{i,j-1}^{n}}{\Delta\theta^2} \tag{D.2.6a}$$

$$\frac{Z_{i,j}^{n+1}-Z_{i,j}^{n+0.5}}{0.5\,\Delta\tau}+Pe\,v_{i,j}^{\xi}\,\frac{Z_{i+1,j}^{n+0.5}-Z_{i-1,j}^{n+0.5}}{2\,\Delta\xi}+Pe\,\frac{v_{i,j}^{\theta}}{\xi_i}\,\frac{Z_{i,j+1}^{n+1}-Z_{i,j-1}^{n+1}}{2\,\Delta\theta}$$
$$=\frac{Z_{i+1,j}^{n+0.5}-2\,Z_{i,j}^{n+0.5}+Z_{i-1,j}^{n+0.5}}{\Delta\xi^2}+\frac{2}{\xi_i}\,\frac{Z_{i+1,j}^{n+0.5}-Z_{i-1,j}^{n+0.5}}{2\,\Delta\xi}+\frac{2}{\xi_i^2}\,\frac{Z_{i,j+1}^{n+1}-2\,Z_{i,j}^{n+1}+Z_{i,j-1}^{n+1}}{\Delta\theta^2} \tag{D.2.6b}$$

Referring to Eq. (3.2.7c) and Eq. (3.2.7d), Eq. (D.2.6a) and Eq. (D.2.6b) have an excess relationship

$$Z_{i,j+1}=Z_{i,j-1} \tag{D.2.7}$$

D.2.3 The Alternating Direction Implicit Linear System

Define

$$cvdr_{i,j}=\frac{Pe}{4}\,\frac{\Delta\tau}{\Delta\xi}\,v_{i,j}^{\xi} \tag{D.2.8a}$$

$$cvdth_{i,j}=\frac{Pe}{4}\,\frac{\Delta\tau}{\Delta\theta}\,\frac{v_{i,j}^{\theta}}{\xi_i} \tag{D.2.8b}$$

$$c1dr_i=\frac{1}{2}\,\frac{\Delta\tau}{\Delta\xi}\,\frac{1}{\xi_i} \tag{D.2.8c}$$

$$c2dr=\frac{1}{2}\,\frac{\Delta\tau}{\Delta\xi^2} \tag{D.2.8d}$$

$$c1dth_{i,j}=\frac{1}{4}\,\frac{\Delta\tau}{\Delta\theta}\,\frac{\cot\theta_j}{\xi_i^2} \tag{D.2.8e}$$

$$c2dth_i=\frac{1}{2}\,\frac{\Delta\tau}{\Delta\theta^2}\,\frac{1}{\xi_i^2} \tag{D.2.8f}$$

Linear Systems in the $\xi-$Direction

$$(cvdr_{i,j}-c1dr_i-c2dr)\,Z_{i+1,j}^{n+0.5}+(1+2\,c2dr)\,Z_{i,j}^{n+0.5}+(c1dr_i-c2dr-cvdr_{i,j})\,Z_{i-1,j}^{n+0.5}$$
$$=$$
$$(c1dth_{i,j}+c2dth_i-cvdth_{i,j})\,Z_{i,j+1}^{n}+(1-2\,c2dth_i)\,Z_{i,j}^{n}+(cvdth_{i,j}-c1dth_{i,j}+c2dth_i)\,Z_{i,j-1}^{n} \tag{D.2.9}$$

Linear Systems in the $\theta-$Direction

$$\begin{aligned}(cvdth_{i,j} - c1dth_{i,j} - c2dth_i)\, Z_{i,j+1}^{n+1} + (1 + 2\,c2dth_i)\, Z_{i,j}^{n+1} + (c1dth_{i,j} - c2dth_i - cvdth_{i,j})\, Z_{i,j-1}^{n+1} \\ = \\ (c1dr_i + c2dr - cvdr_{i,j})\, Z_{i+1,j}^{n+0.5} + (1 - 2\,c2dr)\, Z_{i,j}^{n+0.5} + (cvdr_{i,j} - c1dr_i + c2dr)\, Z_{i-1,j}^{n+0.5}\end{aligned} \tag{D.2.10}$$

Along the stagnation lines, Eq. (D.2.6a) and Eq. (D.2.6b) are

$$\begin{aligned}(cvdr_{i,j} - c1dr_i - c2dr)\, Z_{i+1,j}^{n+0.5} + (1 + 2\,c2dr)\, Z_{i,j}^{n+0.5} + (c1dr_i - c2dr - cvdr_{i,j})\, Z_{i-1,j}^{n+0.5} \\ = \\ 4\,c2dth_i\, Z_{i,j+1}^{n} + (1 - 4\,c2dth_i)\, Z_{i,j}^{n}\end{aligned} \tag{D.2.11}$$

$$\begin{aligned}-4\,c2dth_i\, Z_{i,j+1}^{n+1} + (1 + 4\,c2dth)\, Z_{i,j}^{n+1} \\ = \\ (c1dr_i + c2dr - cvdr_{i,j})\, Z_{i+1,j}^{n+0.5} + (1 - 2\,c2dr)\, Z_{i,j}^{n+0.5} + (cvdr_{i,j} - c1dr_i + c2dr)\, Z_{i-1,j}^{n+0.5}\end{aligned} \tag{D.2.12}$$

BIBLIOGRAPHY

[1] D.A. Porter, K.E. Easterling, and M. Sherif. *Phase Transformations in Metals and Alloys, Third Edition (Revised Reprint)*. CRC Press, 2009. Available at https://books.google.co.uk/books?id=axDSBQAAQBAJ.

[2] W.F. Gale and T.C. Totemeier. *Smithells Metals Reference Book*. Elsevier Science, 2003. Available at https://www.sciencedirect.com/science/book/9780750675093.

[3] W. Kurz and D. J. Fisher. *Fundamentals of solidification*. Trans Tech Publications, 1986. Available at https://books.google.co.uk/books?id=AR1RAAAAMAAJ.

[4] Eon-Sik Lee and S. Ahn. Solidification progress and heat transfer analysis of gas-atomized alloy droplets during spray forming. *Acta Metallurgica et Materialia*, 42(9):3231–3243, 1994. Available at http://www.sciencedirect.com/science/article/pii/0956715194904219.

[5] K. A. Jackson and J. D. Hunt. Lamellar and rod eutectic growth. *Transactions of the Metallurgical Society of Aime*, 236(8):1129–1142, 1966. Available at https://www.researchgate.net/profile/Kenneth_Jackson4/publication/265004384_Lamellar_and_Rod_Eutectic_Growth/links/5696796d08ae1c427903caad/Lamellar-and-Rod-Eutectic-Growth.pdf.

[6] V. Seetharaman and R. Trivedi. Eutectic growth: Selection of interlamellar spacings. *Metallurgical Transactions A*, 19(12):2955–2964, 1988. Available at http://dx.doi.org/10.1007/BF02647722.

[7] C. R. Clopet, R. F. Cochrane, and A. M. Mullis. The origin of anomalous eutectic structures in undercooled ag–cu alloy. *Acta Materialia*, 61(18):6894–6902, 2013. Available at http://www.sciencedirect.com/science/article/pii/S1359645413005879.

[8] J.S. Langer and J. Müller-Krumbhaar. Stability effects in dendritic crystal growth. *Journal of Crystal Growth*, 42(C):11–14, 1977. Available at https://www.scopus.com/inward/record.uri?eid=2-s2.0-49449127862&doi=10.1016%2f0022-0248%2877%2990171-3&partnerID=40&md5=545bc478ecc1c42b2bbfed99757690a3.

[9] W. Kurz, B. Giovanola, and R. Trivedi. Theory of microstructural development during rapid solidification. *Acta Metallurgica*, 34(5):823 – 830, 1986. Available at http://www.sciencedirect.com/science/article/pii/0001616086900568.

[10] B. Abramzon and C. Elata. Unsteady heat transfer from a single sphere in stokes flow. *International Journal of Heat and Mass Transfer*, 27(5):687–695, 1984. Available at http://www.sciencedirect.com/science/article/pii/0017931084901388.

[11] William E Ranz. Evaporation from drops 1. *Chem. Eng. Prog.*, 48:141, 1952. Available at http://dns2.asia.edu.tw/~ysho/YSHO-English/1000%20CE/PDF/Che%20Eng%20Pro48,%20141.pdf.

[12] R. M. Young and E. Pfender. Nusselt number correlations for heat transfer to small spheres in thermal plasma flows. *Plasma Chemistry and Plasma Processing*, 7(2):211–229, 1987. Available at http://dx.doi.org/10.1007/BF01019179.

[13] Stephen Whitaker. Forced convection heat transfer correlations for flow in pipes, past flat plates, single cylinders, single spheres, and for flow in packed beds and tube bundles. *AIChE Journal*, 18(2):361–371, 1972. Available at http://dx.doi.org/10.1002/aic.690180219.

[14] Otto Redlich and AT Kister. Algebraic representation of thermodynamic properties and the classification of solutions. *Industrial & Engineering Chemistry*, 40(2):345–348, 1948. Available at https://www.researchgate.net/publication/231384572_Algebraic_Representation_of_Thermodynamic_Properties_and_Classification_of_Solutions.

[15] KN Ishihara and PH Shingu. Calculation of t0 curves and metastable phase equilibria in connection with rapid solidification. *Materials Science and Engineering*, 63(2):251–256, 1984. Available at http://www.sciencedirect.com/science/article/pii/0025541684901265.

[16] J. L. Murray. Calculations of stable and metastable equilibrium diagrams of the ag-cu and cd-zn systems. *Metallurgical Transactions a-Physical Metallurgy and Materials Science*, 15(2):261–268, 1984. Available at https://link.springer.com/article/10.1007/BF02645110.

[17] PR Subramanian and JH Perepezko. The ag-cu (silver-copper) system. *Journal of Phase Equilibria*, 14(1):62–75, 1993. Available at https://link.springer.com/article/10.1007/BF02652162.

[18] M Baricco, M Palumbo, D Baldissin, E Bosco, and L Battezzati. Metastable phases and phase diagrams. In *Paper presented at the seminar: Phase transformations and phase diagrams*, volume 23, 2003. Available at http://www.gruppofrattura.it/pdf/ext/AIM/Anno%202004/11/003.pdf.

[19] H. Fredriksson, Y. Arai, T. Emi, M. Haddad-Sabsevar, and H. Shibata. Melting temperature, transformation and metastable phase diagram of rapidly solidified ag-cu alloys. *Materials Transactions, JIM*, 39(5):587–595, 1998. Available at https://www.jstage.jst.go.jp/article/matertrans1989/39/5/39_5_587/_article.

[20] R.W. Cahn and P. Haasen. *Physical Metallurgy*. Number v. 1 in Physical metallurgy. Elsevier Science, 1996. Available at https://books.google.co.uk/books?id=-uj80fqU8LEC.

[21] P. G. Boswell and G. A. Chadwick. The structure of the γ extended solid solution in a splat-cooled ag-50 at.% cu alloy. *Journal of Materials Science*, 12(9):1879–1894, 1977. Available at http://dx.doi.org/10.1007/BF00566250.

[22] Sigemako Nagakura, Seiji Toyama, and Shiguéo Oketani. Lattice parameter and structure of silver-copper alloys rapidly quenched from liquid state. *Acta Metallurgica*, 14(1):73 – 75, 1966. Available at http://www.sciencedirect.com/science/article/pii/0001616066902835.

[23] V. Franetović, O. Milat, D. Ivček, and A. Bonefačić. Quenching efficiency of some splat-cooling devices. *Journal of Materials Science*, 14(2):498–500, 1979. Available at http://dx.doi.org/10.1007/BF00589850.

[24] S Mader, A.S Nowick, and H Widmer. Metastable evaporated thin films of cu-ag and co-au alloys—i occurrence and morphology of phases. *Acta Metallurgica*, 15(2):203 – 214, 1967. Available at http://www.sciencedirect.com/science/article/pii/0001616067901939.

[25] K H J Buschow. Short-range order and thermal stability in amorphous alloys. *Journal of Physics F: Metal Physics*, 14(3):593, 1984. Available at http://stacks.iop.org/0305-4608/14/i=3/a=005.

[26] D. M. Herlach, R. F. Cochrane, I. Egry, H. J. Fecht, and A. L. Greer. Containerless processing in the study of metallic melts and their solidification. *International Materials Reviews*, 38(6):273–347, 1993. Available at http://www.maneyonline.com/doi/abs/10.1179/095066093790326267.

[27] S. Walder and P. L. Ryder. Nonequilibrium solidication in undercooled melts of the alloy ag-39.9 at. *Journal of Applied Physics*, 73(4):1965–1970, 1993. Available at http://aip.scitation.org/doi/abs/10.1063/1.353187.

[28] Kalin I. Dragnevski, Andrew M. Mullis, and Robert F. Cochrane. The effect of experimental variables on the levels of melt undercooling. *Materials Science and Engineering: A*, 375:485 – 487, 2004. Available at http://www.sciencedirect.com/science/article/pii/S0921509303010542.

[29] S. Walder and P. L. Ryder. Critical solidification behavior of undercooled ag-cu alloys. *Journal of Applied Physics*, 74(10):6100–6106, 1993. Available at http://scitation.aip.org/content/aip/journal/jap/74/10/10.1063/1.355172.

[30] John H. Perepezko. Nucleation in undercooled liquids. *Materials Science and Engineering*, 65(1):125 – 135, 1984. Available at http://www.sciencedirect.com/science/article/pii/0025541684902064.

[31] A. L. Greer. Nucleation and solidification studies using drop-tubes. *Materials Science and Engineering: A*, 178(1–2):113–120, 1994. Available at http://www.sciencedirect.com/science/article/pii/0921509394905282.

[32] J. Gao, T. Volkmann, S. Reutzel, and D.M. Herlach. Characterization of the microstructure of gas-atomized nd–fe–b alloy particles of non-peritectic chemical compositions. *Journal of Alloys and Compounds*, 388(2):235 – 240, 2005. Available at http://www.sciencedirect.com/science/article/pii/S0925838804009570.

[33] Y. Yu, A. M. Mullis, and R. F. Cochrane. Rapidly solidified ag-cu eutectics: A comparative study using drop-tube and melt fluxing techniques. *IOP Conference Series: Materials Science and Engineering*, 117(1):012053, 2016. Available at http://stacks.iop.org/1757-899X/117/i=1/a=012053.

[34] R Rablbauer, G Frommeyer, and F Stein. Determination of the constitution of the quasi–binary eutectic nial–re system by dta and microstructural investigations. *Materials Science and Engineering: A*, 343(1):301 – 307, 2003. Available at https://www.sciencedirect.com/science/article/pii/S092150930200388X#FIG3.

[35] CG Rhodes and G Garmong. The aging response of al-cu and al-cu-mg directionally solidified eutectics. *Metallurgical Transactions*, 3(7):1861–1868, 1972. Available at https://link.springer.com/article/10.1007/BF02642571.

[36] W. J. Boettinger, D. Shechtman, R. J. Schaefer, and F. S. Biancaniello. The effect of rapid solidification velocity on the microstructure of ag-cu alloys. *Metallurgical Transactions A*, 15(1):55–66, 1984. Available at http://dx.doi.org/10.1007/BF02644387.

[37] N. Wang, C. D. Cao, and B. Wei. Solidification behaviour of silver-copper alloys in a drop tube. *Advances in Space Research*, 24(10):1257–1261, 1999. Available at http://www.sciencedirect.com/science/article/pii/S0273117799007292.

[38] R. Trivedi, P. Magnin, and W. Kurz. Theory of eutectic growth under rapid solidification conditions. *Acta Metallurgica*, 35(4):971–980, 1987. Available at http://www.scopus.com/inward/record.url?eid=2-s2.0-0023326682&partnerID=40&md5=e18b36a341cbb05a67a736d7f5c45b7b.

[39] David G Beck, Stephen M Copley, and Michael Bass. The constitution and phase stability of overlapping melt trails in ag-cu alloys produced by continuous laser melt quenching. *Metallurgical and Materials Transactions A*, 13(11):1879–1889, 1982. Available at https://link.springer.com/article/10.1007%2FBF02645931.

[40] Su Zhao, Jinfu Li, Li Liu, and Yaohe Zhou. Solidification of undercooled ag–cu eutectic alloy with the sb addition. *Journal of Alloys and Compounds*, 478(1–2):252–256, 2009. Available at http://www.sciencedirect.com/science/article/pii/S0925838808021932.

[41] CR Clopet, RF Cochrane, and AM Mullis. Spasmodic growth during the rapid solidification of undercooled ag-cu eutectic melts. *Applied Physics Letters*, 102(3):031906–031906–4, 2013. Available at http://aip.scitation.org/doi/full/10.1063/1.4775670.

[42] Su Zhao, Jinfu Li, Li Liu, and Yaohe Zhou. Eutectic growth from cellular to dendritic form in the undercooled ag–cu eutectic alloy melt. *Journal of Crystal Growth*, 311(5):1387–1391, 2009. Available at http://www.sciencedirect.com/science/article/pii/S0022024808013468.

[43] M. Erol, U. Böyük, T. Volkmann, and D. M. Herlach. Containerless solidification of ag–al and ag–cu eutectic alloys in a drop tube. *Journal of Alloys and Compounds*, 575(0):96–103, 2013. Available at http://www.sciencedirect.com/science/article/pii/S0925838813009092.

[44] R Goetzinger, M Barth, and DM Herlach. Mechanism of formation of the anomalous eutectic structure in rapidly solidified ni–si, co–sb and ni–al–ti alloys. *Acta materialia*, 46(5):1647–1655, 1998. Available at http://www.sciencedirect.com/science/article/pii/S135964549700339X.

[45] N. Zeoli, S. Gu, and S. Kamnis. Numerical modelling of metal droplet cooling and solidification. *International Journal of Heat and Mass Transfer*, 51(15–16):4121–4131, 2008. Available at http://www.sciencedirect.com/science/article/pii/S0017931008000173.

[46] S. Zhao, J. F. Li, L. Liu, and Y. H. Zhou. Cellular growth of lamellar eutectics in undercooled ag–cu alloy. *Materials Characterization*, 60(6):519–524, 2009. Available at http://www.sciencedirect.com/science/article/pii/S1044580308003446.

[47] Ronald K. Linde. Lattice parameters of metastable silver-copper alloys. *Journal of Applied Physics*, 37(2):934–934, 1966. Available at http://scitation.aip.org/content/aip/journal/jap/37/2/10.1063/1.1708298.

[48] W. Kurz, B. Giovanola, and R. Trivedi. Theory of microstructural development during rapid solidification. *Acta Metallurgica*, 34(5):823–830, 1986. Available at http://www.sciencedirect.com/science/article/pii/0001616086900568.

[49] JS Langer and J Müller-Krumbhaar. Stability effects in dendritic crystal growth. *Journal of Crystal Growth*, 42:11–14, 1977. Available at http://www.sciencedirect.com/science/article/pii/0022024877901713?via%3Dihub.

[50] J. Lipton, W. Kurz, and R. Trivedi. Rapid dendrite growth in undercooled alloys. *Acta Metallurgica*, 35(4):957–964, 1987. Available at http://www.sciencedirect.com/science/article/pii/000161608790174X.

[51] MJ Aziz. Model for solute redistribution during rapid solidification. *Journal of Applied Physics*, 53(2):1158–1168, 1982. Available at http://aip.scitation.org/doi/pdf/10.1063/1.329867.

[52] R. Trivedi, J. Lipton, and W. Kurz. Effect of growth rate dependent partition coefficient on the dendritic growth in undercooled melts. *Acta Metallurgica*, 35(4):965 – 970, 1987. Available at http://www.sciencedirect.com/science/article/pii/0001616087901751.

[53] R Stoering and H Conrad. Metastable structures in liquid quenched and vapor quenched ag-cu alloys. *Acta Metallurgica*, 17(8):933–948, 1969. Available at http://www.sciencedirect.com/science/article/pii/0001616069900388.

[54] PG Boswell and GA Chadwick. The structure of the γ' extended solid solution in a splat-cooled ag-50 at.% cu alloy. *Journal of Materials Science*, 12(9):1879–1894, 1977. Available at https://link.springer.com/article/10.1007%2FBF00566250?LI=true.

[55] Sigemako Nagakura, Seiji Toyama, and Shiguéo Oketani. Lattice parameter and structure of silver-copper alloys rapidly quenched from liquid state. *Acta Metallurgica*, 14(1):73–75, 1966. Available at http://www.sciencedirect.com/science/article/pii/0001616066902835.

[56] N. Konopliv and E. M. Sparrow. Unsteady heat transfer and temperature for stokesian flow about a sphere. *Journal of Heat Transfer*, 94(3):266–272, 1972. Available at http://0-dx.doi.org.wam.leeds.ac.uk/10.1115/1.3449926.

[57] Horatio Scott Carslaw, John Conrad Jaeger, and Herman Feshbach. Conduction of heat in solids. *Physics Today*, 15(11):74–76, 1962. Available at https://global.oup.com/academic/product/conduction-of-heat-in-solids-9780198533689?cc=gb&lang=en&.

[58] Ho Brauer. Unsteady state mass transfer through the interface of spherical particles—i: Physical and mathematical description of the mass-transfer problem. *International Journal of Heat and Mass Transfer*, 21(4):445–453, 1978. Available at http://www.sciencedirect.com/science/article/pii/0017931078900789.

[59] AndrewM Mullis, Leane Farrell, RobertF Cochrane, and NicholasJ Adkins. Estimation of cooling rates during close-coupled gas atomization using secondary dendrite arm spacing mea-

surement. *Metallurgical and Materials Transactions B*, 44(4):992–999, 2013. Available at http://dx.doi.org/10.1007/s11663-013-9856-2.

[60] J.F. Li, W.Q. Jie, S. Zhao, and Y.H. Zhou. Structural evidence for the transition from coupled to decoupled growth in the solidification of undercooled ni-sn eutectic melt. *Metallurgical and Materials Transactions A*, 38(8):1806–1816, 2007. Available at http://dx.doi.org/10.1007/s11661-007-9198-2.

[61] KP Young and DH Kerkwood. The dendrite arm spacings of aluminum-copper alloys solidified under steady-state conditions. *Metallurgical Transactions A*, 6(1):197–205, 1975. Available at https://link.springer.com/article/10.1007/BF02673688.

[62] P. S. Grant. Spray forming. *Progress in Materials Science*, 39(4–5):497–545, 1995. Available at http://www.sciencedirect.com/science/article/pii/0079642595000046.

[63] A. M. Mullis, T. D. Bigg, and N. J. Adkins. A microstructural investigation of gas atomized raney type al-27.5 at. *Journal of Alloys and Compounds*, 648:139–148, 2015. Available at http://www.sciencedirect.com/science/article/pii/S0925838815014474.

[64] DH St John and LM Hogan. A simple prediction of the rate of the peritectic transformation. *Acta Metallurgica*, 35(1):171–174, 1987. Available at http://www.sciencedirect.com/science/article/pii/0001616087902264.

[65] SK. Friedlander. Mass and heat transfer to single spheres and cylinders at low reynolds numbers. *AIChE Journal*, 3(1):43–48, 1957. Available at http://onlinelibrary.wiley.com/doi/10.1002/aic.690030109/abstract.

[66] Dirk Bergmann, Udo Fritsching, and Klaus Bauckhage. A mathematical model for cooling and rapid solidification of molten metal droplets. *International Journal of Thermal Sciences*, 39(1):53–62, 2000. Available at http://www.sciencedirect.com/science/article/pii/S1290072900001951.

[67] T. Kambe. *Elementary Fluid Mechanics*. World Scientific, 2007. Available at https://books.google.co.uk/books?id=L9nICgAAQBAJ.

[68] N. Ozisik. *Finite Difference Methods in Heat Transfer*. Heat Transfer. Taylor & Francis, 1994. Available at https://books.google.co.uk/books?id=M-Jun14kdxcC.

[69] Jules Thibault, Simon Bergeron, and Hugues W Bonin. On finite-difference solutions of the heat equation in spherical coordinates. *Numerical Heat Transfer, Part A: Applications*, 12(4):457–474, 1987. Available at http://www.tandfonline.com/doi/pdf/10.1080/10407788708913597?needAccess=true.

[70] O. D. Momoh, M. N. Sadiku, and S. M. Musa. Finite difference analysis of time-dependent spherical problems. In *2013 Proceedings of IEEE Southeastcon*, pages 1–4. Available at http://ieeexplore.ieee.org/document/6567468/metrics.

[71] Dieter M. Herlach. Metastable solids from undercooled melts. In *THERMEC 2006*, volume 539 of *Materials Science Forum*, pages 1977–1982. Trans Tech Publications, 2 2007. Available at https://www.elsevier.com/books/metastable-solids-from-undercooled-melts/herlach/978-0-08-043638-8.

[72] D. Dollimore. Thermal analysis. *Analytical Chemistry*, 64(12):147–153, 1992. Available at https://www.elsevier.com/books/thermal-analysis/wunderlich/978-0-12-765605-2.

[73] P.J. Goodhew, J. Humphreys, and R. Beanland. *Electron Microscopy and Analysis, Third Edition*. Taylor & Francis, 2000. Available at https://books.google.co.uk/books?id=zuxPIVmGLGsC.

[74] X. X. Wei, X. Lin, W. Xu, Q. S. Huang, M. Ferry, J. F. Li, and Y. H. Zhou. Remelting-induced anomalous eutectic formation during solidification of deeply undercooled eutectic alloy melts. *Acta Materialia*, 95:44–56, 2015. Available at http://www.sciencedirect.com/science/article/pii/S1359645415003353.

[75] C. Yang, J. Gao, Y. K. Zhang, M. Kolbe, and D. M. Herlach. New evidence for the dual origin of anomalous eutectic structures in undercooled ni–sn alloys: In situ observations and ebsd characterization. *Acta Materialia*, 59(10):3915–3926, 2011.

[76] G. Kasperovich, T. Volkmann, L. Ratke, and D. Herlach. Microsegregation during solidification of an al-cu binary alloy at largely different cooling rates (0.01 to 20,000 k/s): Modeling and experimental study. *Metallurgical and Materials Transactions A: Physical Metallurgy and Materials Science*, 39 A(5):1183–1191, 2008. Available at https://link.springer.com/article/10.1007/s11661-008-9505-6.

[77] J. A. Sarreal and G. J. ABbaschian. The effect of solidification rate on microsegregation. *Metallurgical Transactions A*, 17(11):2063–2073, Nov 1986. Available at https://link.springer.com/article/10.1007/BF02645003.

[78] J. Crank. *The Mathematics of Diffusion*. Oxford science publications. Clarendon Press, 1979. Available at https://books.google.co.uk/books?id=eHANhZwVouYC.